On the lifecycle of Antarctic Bottom Water

Casimir de Lavergne

THÈSE DE DOCTORAT
DE L'UNIVERSITÉ PIERRE ET MARIE CURIE

Spécialité : **Océanographie physique**

École doctorale : "129 - Science de l'environnement"

réalisée au

Laboratoire d'Océanographie et du Climat

présentée par

Casimir de LAVERGNE

pour obtenir le grade de :

DOCTEUR DE L'UNIVERSITÉ PIERRE ET MARIE CURIE

Titre de la thèse :

Eléments du cycle de vie de l'Eau Antarctique de Fond

Soutenance prévue le 23/09/16

devant le jury composé de :

M.	David Marshall	(University of Oxford)	*Rapporteur*
M.	Jonas Nycander	(MISU, Stockholm)	*Rapporteur*
Mme	Pascale Bouruet-Aubertot	(UPMC, Paris)	*Examinateur*
M.	Gilles Reverdin	(LOCEAN, Paris)	*Examinateur*
M.	Bruno Ferron	(LPO, Brest)	*Examinateur*
M.	Gurvan Madec	(LOCEAN, Paris)	*Directeur de thèse*
M.	Patrice Klein	(Caltech, Pasadena)	*Co-directeur de thèse*

Eléments du cycle de vie de l'Eau Antarctique de Fond

Résumé : L'Eau Antarctique de Fond constitue la principale masse d'eau océanique par son volume, et nourrit la composante la plus profonde et la plus lente de la circulation océanique. Les processus qui régissent son cycle de vie sont donc clé pour la capacité de stockage de l'océan en carbone et chaleur aux échelles centennales à multi-millénaires. Cette thèse tente de caractériser et quantifier les principaux processus responsables de la destruction (synonyme d'allègement et de remontée) de l'Eau Antarctique de Fond dans l'océan abyssal. A partir d'une estimée issue d'observations de la structure thermohaline de l'océan mondial et de diagnostics fondés sur le budget de densité des eaux profondes, les rôles respectifs du chauffage géothermal, du mélange turbulent par déferlement d'ondes internes et de la géométrie des bassins sont évalués. Il est montré que la géométrie de l'océan gouverne la structure de la circulation de l'Eau Antarctique de Fond. La contribution du déferlement des ondes internes, bien que mal contrainte, est estimée insuffisante pour maintenir un rythme de destruction de l'Eau Antarctique de Fond comparable à celui de sa formation. Le chauffage géothermal a quant à lui un rôle important pour la remontée des eaux recouvrant une large surface du lit océanique. Les résultats suggèrent une réévaluation de l'importance du mélange au niveau des détroits et seuils profonds, mais aussi du rôle fondamental de la forme des bassins, pour l'allègement et le transport des eaux abyssales.

Mots clés : Masses d'eau, Océan abyssal, Circulation thermohaline, Chauffage géothermal, Mélange, Ondes internes, Turbulence, Paramétrisation, Modélisation, NEMO

On the lifecycle of Antarctic Bottom Water

Abstract : Antarctic Bottom Water is the most voluminous water mass of the World Ocean, and it feeds the deepest and slowest component of ocean circulation. The processes that govern its lifecycle are therefore key to the ocean's carbon and heat storage capacity on centennial to multi-millennial timescales. This thesis aims at characterizing and quantifying processes responsible for the destruction (synonymous of lightening and upwelling) of Antarctic Bottom Water in the abyssal ocean. Using an observational estimate of the global ocean thermohaline structure and diagnostics based on the density budget of deep waters, we explore the roles of basin geometry, geothermal heating and mixing by breaking internal waves for the abyssal circulation. We show that the shape of ocean basins largely controls the structure of abyssal upwelling. The contribution of mixing powered by breaking internal waves, though poorly constrained, is estimated to be insufficient to destroy Antarctic Bottom Water at a rate comparable to that of its formation. Geothermal heating plays an important role for the upwelling of waters covering large seafloor areas. The results suggest a reappraisal of the role of mixing in deep straits and sills, but also of the fundamental role of basin geometry, for the lightening and transport of abyssal waters.

Keywords : Water masses, Abyssal ocean, Thermohaline circulation, Geothermal heating, Mixing, Internal waves, Turbulence, Parameterization, Modelling, NEMO

Contents

Introduction

Earth's climate system is composed of different interconnected media: the atmosphere, the ocean, sea ice, land ice, the seabed (both sediments and bedrock) and continental surfaces (soils, vegetation, rivers and lakes). Climate dynamics are driven by exchanges of energy, momentum and matter between these media and with the outer space. Describing, understanding and modelling climate therefore hinges upon characterizing and quantifying these exchanges.

Central to the climate system is the atmosphere, which regulates radiative exchanges with the outer space, shuffles heat and freshwater around the globe and across media, and largely sets surface properties of continents and oceans. But the atmosphere's ability to exchange and redistribute properties over large spatial and short temporal scales goes at the expense of its storage capacity and memory, both of which are limited relative to other media (Fig. 1). Instead, storage and memory functions are largely attributes of the other main fluid of the climate system: the ocean.

Two defining properties of the ocean distinguish it from the overlying atmosphere: its thermal inertia and its opacity. Because the ocean is nearly 300 times heavier than the atmosphere, and because it costs four times more energy to warm by one Celsius degree a given mass of water relative to the same mass of air, the total heat capacity of the ocean is over 1,000 times that of the atmosphere. Its total heat capacity is also much larger than that of Earth's frozen water, whose volume is only about 2 % that of the ocean. Hence, the ocean is the primary heat reservoir of the climate system.

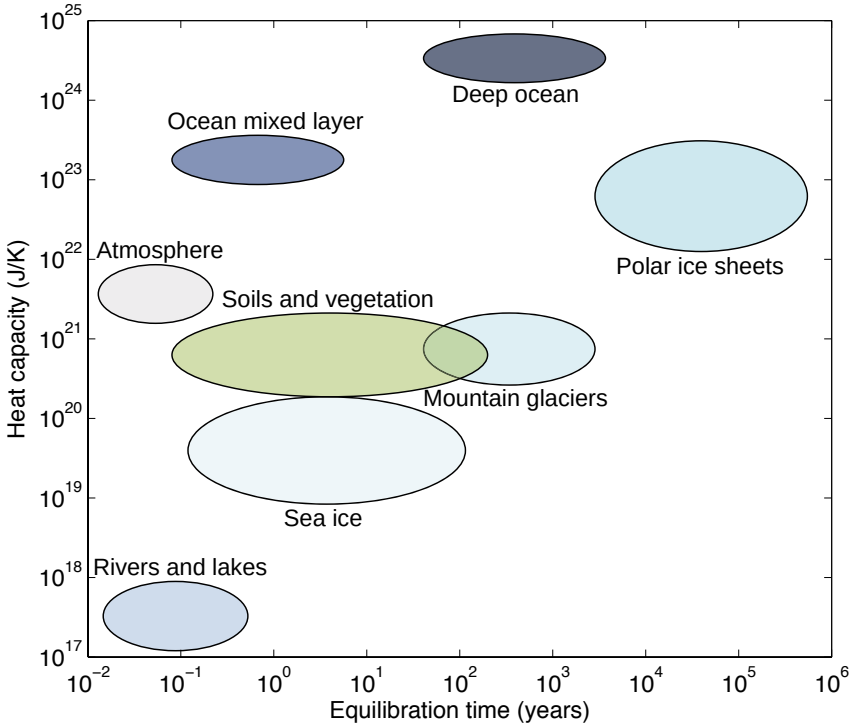

Figure 1: Typical equilibration time and total heat capacity of various components of the climate system. The total heat capacity [J/K] is the amount of energy required to raise by one Celsius degree the mean temperature of each component. The equilibration timescale is the typical duration for a component to adjust to modified boundary conditions. Values from McGuffie and Henderson-Sellers (2014).

Yet most of this reservoir is not readily accessible. Indeed, whereas solar radiation is able to penetrate throughout the atmosphere, the opacity of seawater prevents it from reaching ocean depths greater than 200 meters. As a result, the incoming solar energy warms preferentially the land and ocean surface. This surface warming is a destabilizing force for the atmosphere but a stabilizing force for the ocean, because gravity needs warmer, lighter fluid to rest above colder, denser fluid. Solar heating thus stimulates a rapid vertical rearrangement of atmospheric properties, but inhibits this vertical redistribution and the downward penetration of atmospheric forcing in the ocean. The ocean's opacity thus contributes to isolate the large deep ocean reservoir from the remainder of the climate system. Together with the ocean's tremendous thermal inertia, the inefficient oceanic redistribution explains why it may

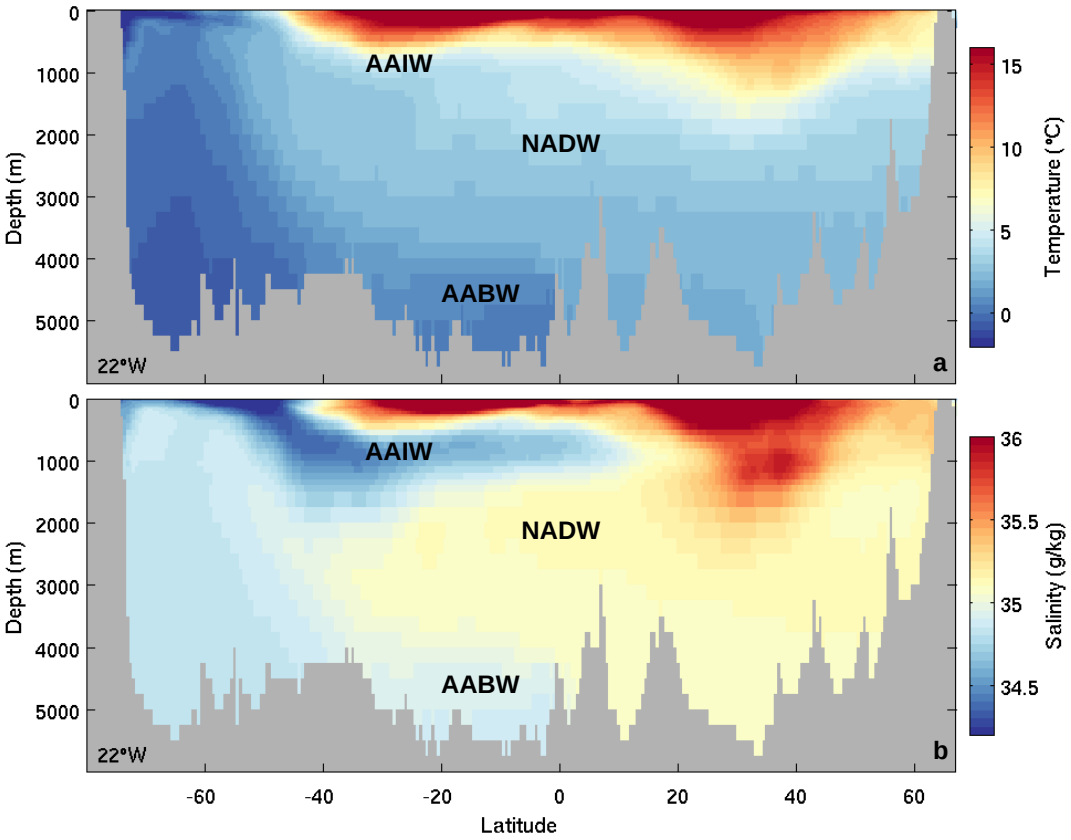

Figure 2: Longitudinal section across the Atlantic Ocean at 22°W showing the annual mean (**a**) potential temperature and (**b**) salinity of seawater. Major deep water masses are labelled: Antarctic Bottom Water (AABW), North Atlantic Deep Water (NADW) and Antarctic Intermediate Water (AAIW). Data from the WOCE hydrographic atlas (Gouretski and Koltermann 2004).

take centuries to millennia before deep ocean layers fully adjust to new boundary conditions. More generally, the restricted penetration of atmospheric forcing into the ocean gives the latter its characteristic memory and organized global property distributions in distinct, stable water masses.

A water mass can be defined as a body of water with coherent temperature, salinity and biochemical attributes. Major deep ocean water masses are clearly identifiable in a latitude-depth view of seawater salinity and temperature (Fig. 2): a cold, relatively fresh body of water extends from the Antarctic continent to northern basins along the ocean floor (Antarctic Bot-

tom Water); a warmer, saltier water mass spreads southward from the North Atlantic at mid-depths (North Atlantic Deep Water); and a distinctly fresh tongue of water that originates at the Southern Ocean surface protrudes northward at shallower depths (Antarctic Intermediate Water).

Crucially, it is apparent that these water masses inherit their core characteristics near the surface, under the influence of air-sea exchanges, and only thereafter carry their acquired properties into the ocean interior. By contrast with the short-lived air masses of the atmosphere, the absence of direct radiative forcing of the deep ocean allows water masses to retain their defining characteristics for decades to thousands of years and to span planetary spatial scales. Yet the gradual erosion of deep water mass properties following their pathways shows that they are not entirely sheltered from forcing. This erosion is primarily the result of turbulent mixing, which works to suppress the property gradients that delineate water masses.

The overall structure, the lifetime and flowing pathways of water masses thus depend both on their formation and export by air-sea fluxes, and on their subsequent modification and destruction in the ocean interior. In turn, the lifecycle of water masses determines ocean physical and biochemical property distributions, how they evolve under changing boundary conditions and how their evolution feeds back on the changing climate state. In particular, characterizing and quantifying processes governing the lifecycle of the voluminous deep water masses is key to understanding and modelling the ocean's role in low-frequency climate variability and change.

This thesis explores some of the processes involved in the millennial journey of the densest global-scale water mass: Antarctic Bottom Water (AABW). Two sections of the AABW lifecycle have been considered: its formation in open waters of the Weddell Sea, as a continuation of my master's project, and its destruction in the global ocean abyss, as the core of this PhD work. For cohesion and brevity, I choose to focus this thesis on the abyssal itinerary of AABW, and present investigations of formation processes only in the Appendix. Despite this choice, the two facets of the AABW lifecycle are in close connection to each other: AABW formation and injection through deep convective mixing provides a conduit from the surface to the

abyss, while AABW destruction through abyssal lightening provides the return path to the upper ocean. Together, the injection into and return from the abyss regulate exchanges between the atmosphere and the vast abyssal pools of carbon and heat, participating in century-scale to glacial-interglacial climate variations (Sigman et al. 2010; Ferrari et al. 2014).

The following pages set the stage for the journey by situating and formulating questions to be examined (Physical problem). In chapter I, we assess the roles of internal ocean waves (the subsurface analogue of surface waves that break on beaches) and geothermal heating for the density transformation of AABW. We show that the slow but steady heating from below significantly helps homogeneous abyssal waters to climb back to lighter layers. The impact of turbulent mixing fed by breaking internal waves is found to be strongly dependent on its spatial distribution but weaker than previously suggested, especially when accounting for variations of the efficiency of mixing (chapter II). In chapter III, we show that the concentration of density loss along the bottom boundary implies that the geometry of ocean basins exerts a strong control on the volume and return route of AABW. A discussion of the under-appreciated role and lack of observations of the bottom boundary layer is provided in chapter IV. Next, we construct new three-dimensional maps of internal wave-driven turbulence and refine estimates of deep water mass transformation by breaking internal waves (chapter V). The improved maps demonstrate that internal waves are unlikely to be a dominant contributor to AABW destruction. Main results and stirred questions are summarized in the concluding chapter.

Two articles focused on near-surface processes make up the Appendix. In the first study (de Lavergne et al. 2014), we analyse historical observations of Antarctic subpolar seas and model simulations to document a plausible but previously overlooked shift in AABW ventilation following the mid-1970s. Deep winter convection in the open Weddell Sea was observed in 1974-1976 thanks to newly-available satellite observations of Antarctic sea ice (Gordon 1978; Carsey 1980), but has not reoccurred since, and is now assumed to be an insignificant mode of AABW formation (Heuzé et al. 2013). However, model simulations indicate that the measured decrease in surface ocean salinity around Antarctica over recent decades is sufficient to impede the onset of deep convection, suggesting that the frequency of Weddell Sea

convective events could have been stronger in the past. Is the surface freshening and resulting stabilization of subpolar Southern Ocean waters part of a long-term climate trend? Is it a manifestation of natural variability, or is it largely human-induced? Such questions are examined in the second study (Jones et al. 2016).

References

Carsey, F. D. (1980). Microwave observation of the Weddell Polynya. *Monthly Weather Review*, 108(12):2032–2044.

de Lavergne, C., Palter, J. B., Galbraith, E. D., Bernardello, R., and Marinov, I. (2014). Cessation of deep convection in the open Southern Ocean under anthropogenic climate change. *Nature Climate Change*, 4:278–282.

Ferrari, R., Jansen, M. F., Adkins, J. F., Burke, A., Stewart, A. L., and Thompson, A. F. (2014). Antarctic sea ice control on ocean circulation in present and glacial climates. *Proceedings of the National Academy of Sciences*, 111(24):8753–8758.

Gordon, A. L. (1978). Deep Antarctic convection west of Maud Rise. *Journal of Physical Oceanography*, 8(4):600–612.

Gouretski, V. and Koltermann, K. P. (2004). Woce global hydrographic climatology. Technical Report 35, Berichte des Bundesamtes für Seeschiffahrt und Hydrographie.

Heuzé, C., Heywood, K. J., Stevens, D. P., and Ridley, J. K. (2013). Southern Ocean bottom water characteristics in CMIP5 models. *Geophysical Research Letters*, 40(7):1409–1414.

Jones, J. M., Gille, S. T., Goosse, H., Abram, N. J., Canziani, P. O., Charman, D. J., Clem, K. R., Crosta, X., de Lavergne, C., Eisenman, I., England, M. H., Fogt, R. L., Frankcombe, L. M., Marshall, G. J., Masson-Delmotte, V., Morrison, A. K., Orsi, A. J., Raphael, M. N., Renwick, J. A., Schneider, D. P., Simpkins, G. R., Steig, E. J., Stenni, B., Swingedouw, D., and Vance, T. R. (2016). Assessing recent trends in high latitude Southern Hemisphere surface climate. *Nature Climate Change*, in press.

McGuffie, K. and Henderson-Sellers, A. (2014). *The climate modelling primer, 4th Edition*. Wiley Blackwell.

Sigman, D. M., Hain, M. P., and Haug, G. H. (2010). The polar ocean and glacial cycles in atmospheric CO2 concentration. *Nature*, 466(7302):47–55.

Physical problem

The densest ocean waters are produced in the surface high latitudes through freshwater loss to freezing seawater and/or heat and freshwater loss to the colder, dryer atmosphere. Gravity allows some of these dense waters to sink to abyssal depths, where they become largely isolated from strong surface atmospheric forcing. This relative isolation from surface density and momentum fluxes slows their transformation and transport, increases their residence time, and thus favours their gradual accumulation in the deep ocean. As a result, 75 % of the ocean volume is filled with waters colder than 4°C that originate in the Antarctic and Arctic regions (Fig. 1a).

But the nonetheless finite volume of cold deep waters implies that the filling process from the poles must be balanced by some emptying process. What provides for the required sink of dense waters? This long-standing oceanographic question (Munk 1966) remains an active area of research, and is the subject of this thesis. We next consider three types of mechanisms able to convert dense waters into lighter ones: deep ocean mixing, near-surface thermodynamic forcing and mixing, and bottom thermodynamic forcing. We conclude with a summary of recent developments and key unresolved questions.

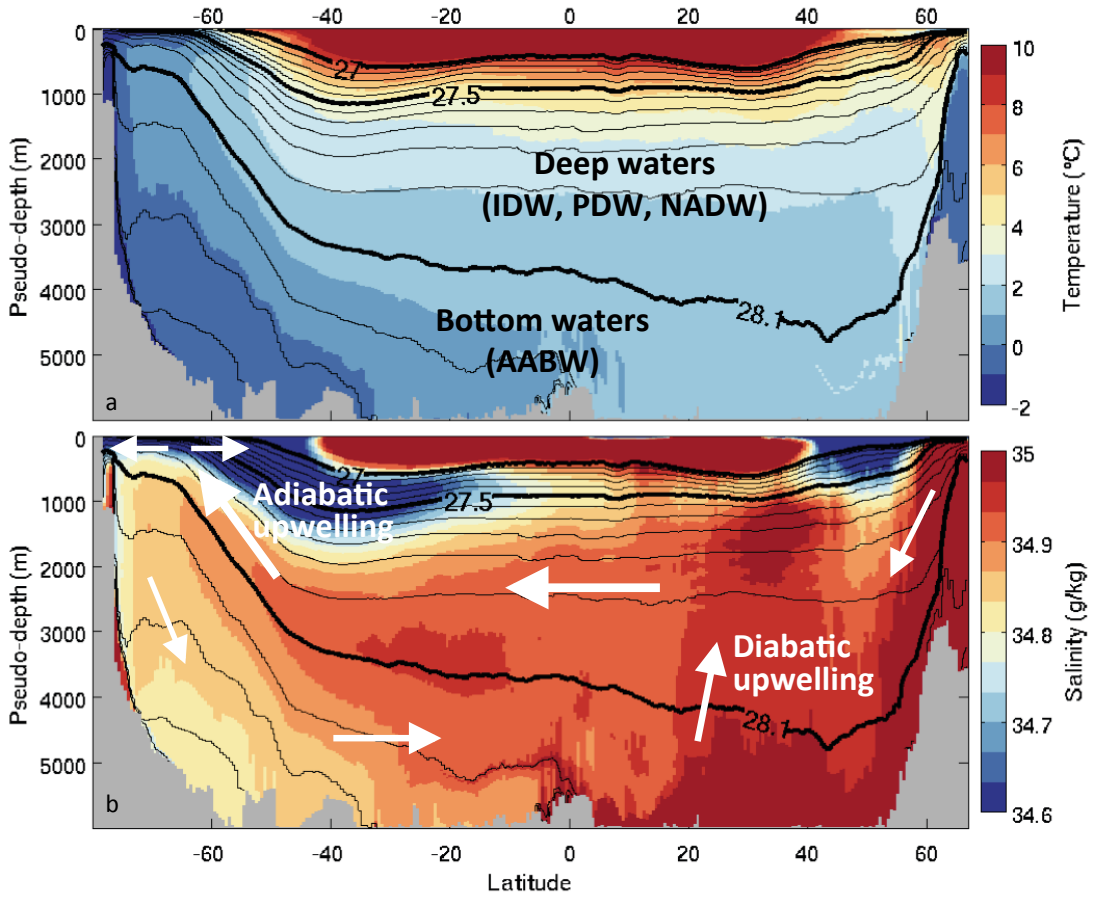

Figure 1: Zonal average (**a**) potential temperature and (**b**) salinity as a function of neutral density (contoured every 0.1 kg m^{-3}) and latitude. For visual purposes, the density-binned values are remapped to pseudo-depth using a bottom-up filling of each latitude band with ocean waters ordered from dense to light. Deep waters, composed of Indian Deep Water (IDW), Pacific Deep Water (PDW) and North Atlantic Deep Water (NADW), embody the 27.5-28.1 kg m^{-3} neutral density range. Denser waters are defined as Antarctic Bottom Water (AABW). Schematic transports of the overturning circulation are shown in (**b**). Flow across (along) density surfaces is termed diabatic (adiabatic). Data from the WOCE hydrographic atlas (Gouretski and Koltermann 2004). The neutral density variable is that of Jackett and McDougall (1997).

1. Deep mixing

Away from ocean boundaries, only two processes can modify the density of seawater: mixing, and frictional heat production by sheared motions. Though significant in nearshore surf zones (Sinnett and Feddersen 2014), frictional heating is quasi-negligible in the subsurface ocean, whose scarcer energetic small-scale motions are unable to overwhelm the high volumetric heat capacity of seawater (Eden et al. 2014). Therefore, density transformation in the ocean interior is almost exclusively the result of mixing.

Interior sinks of dense waters must then rely on their mixing with lighter waters. Molecular mixing rates of heat and salt are 1.4×10^{-7} and $1.4 \times 10^{-9}\,\mathrm{m^2\,s^{-1}}$, respectively (e.g., Stern 1960). The time for molecular diffusion to communicate a surface temperature anomaly to the abyssal ocean, say to 4,000 m depth, scales as $(4000\,\mathrm{m})^2/(1.4 \times 10^{-7}\,\mathrm{m^2\,s^{-1}}) \approx 4$ millions of years. It is two orders of magnitude larger still for a salt anomaly. Alone, such slow rates of mixing would let the whole ocean interior fill with the densest ocean waters.

Observed ocean properties and basin-scale property budgets suggest that effective deep ocean mixing rates rather average about $10^{-4}\,\mathrm{m^2\,s^{-1}}$ (Munk 1966; Ganachaud and Wunsch 2000; Lumpkin and Speer 2007; Talley 2013). Such elevated mixing relative to molecular levels requires that turbulent stirring enhances and renews small-scale property gradients. In turn, the presence of ocean turbulence requires sources of turbulent kinetic energy. The search for interior sinks of dense waters is thus tied to the search of energy sources able to sustain sufficient turbulent mixing (Munk 1966; Munk and Wunsch 1998).

Abyssal Recipes

In his pioneering *Abyssal Recipes*, Munk (1966) showed that observed vertical property profiles $\lambda(z)$ of the deep Pacific, between 1,000 and 4,000 m depth, are consistent with a balance between vertical advection and diffusion, $w\,\partial_z\lambda = \partial_z(K_z\,\partial_z\lambda)$, provided the upwelling velocity w and the vertical diffusivity K_z near values of $1.2 \times 10^{-7}\,\mathrm{m\,s^{-1}}$ and $1.3 \times 10^{-4}\,\mathrm{m^2\,s^{-1}}$, respectively. Scaled to the entire Pacific, the implied upwelling rate of $\sim 20\,\mathrm{Sv}$erdrups ($1\,\mathrm{Sv} \equiv 10^6\,\mathrm{m^3\,s^{-1}}$) was found to be comparable to the estimated polar downwelling (and subsequent northward inflow) of dense Antarctic Bottom Water. Hence, it appeared that a constant deep Pacific mixing rate of about $10^{-4}\,\mathrm{m^2\,s^{-1}}$ could lighten Pacific bottom waters at a rate sufficient to prevent their filling of the entire basin.

Munk (1966) considered a number of mechanisms that could allow for the inferred turbulent mixing rate: intensified mixing near the bottom boundary, due to interactions of currents with topography; double-diffusive mixing, arising from the differential in heat and salt molecular diffusivities; the cabbeling effect, a densification process involving the non-linearity of the equation of state of seawater; shear instability of internal ocean waves, particularly internal ocean tides, which are generated by tidal currents over sloping topography; and mixing by

swimming and migrating organisms. Quantification of the latter two processes was attempted. Using energetic considerations and an analysis of internal wave stability, he suggested that biological mixing should be negligible, but that breaking internal tides could possibly provide for a fraction of the inferred mixing.

Half a century later, results and proposals of *Abyssal Recipes* remain central to discussions of deep ocean mixing. Double-diffusive instabilities can drive significant density fluxes in regions of unstable salinity (S) or temperature (T) stratification and relatively weak background small-scale turbulence allowing for differential T, S mixing (Schmitt 1994; Merryfield et al. 1998; Inoue et al. 2007; Jackson and Rehmann 2014). However, they are mostly active in upper-ocean waters characterized by sharp gradients and/or strong water mass variability (Schmitt 1994; Merrifield et al. 2016). Because of these spatial restrictions, their impact on large-scale ocean transports and the less variable deep ocean water masses is modest (Merryfield et al. 1999). Moreover, by extracting potential energy stored in the unstable T or S stratification, double-diffusive instabilities increase the density of waters underlying instability locales and lower the ocean's centre of mass (Inoue et al. 2007), in opposition to the requisite lightening and potential energy gain of the abyss. Similarly, the cabbeling and thermobaric effects, both related to the non-linear dependence of density on T and S, have been shown to be a net density source for the deep ocean (Iudicone et al. 2008a,b; Klocker and McDougall 2010): they contribute to the formation rather than to the destruction of dense waters. Hence, purely thermodynamic, interior sources of density fluxes are implausible sinks of cold abyssal waters.

Estimates of the energy spent into swimming by marine organisms (Dewar et al. 2006) and observations of turbulence bursts triggered by migrating krill (Kunze et al. 2006) recently attracted attention to biological mixing. But whether fluid displaced (Huntley and Zhou 2004) or dragged (Katija and Dabiri 2009) by swimming animals causes significant, efficient mixing is unclear (Visser 2007; Rousseau et al. 2010; Thiffeault and Childress 2010; Kunze 2011; Noss and Lorke 2014). Above all, the bulk of swimming-driven turbulence and transports, like biomass, is confined to the biologically productive upper-ocean waters (Munk 1966; Kunze et al. 2006; Rousseau et al. 2010), with virtually all of the available energy concentrated above

the maximum depth of the diel vertical migration of zooplankton, about 700 m (Bianchi et al. 2013). By confining the solar energy flux that feeds the marine biosphere to a thin surface layer, the opacity of seawater restricts biological mixing to shallow waters, much as it restricts the penetration of atmospheric forcing.

We are thus left with two of the abyssal mixing processes considered by Munk (1966): near-boundary turbulence fed by ocean currents, and breaking internal waves away from topography. The former mechanism is presently thought to be the leading contributor to deep ocean mixing, and the latter to mixing in stratified open waters (Munk and Wunsch 1998; Garrett and Laurent 2002; Bryden and Nurser 2003; Nikurashin and Ferrari 2013; Waterhouse et al. 2014). Both of them rely on sources of oceanic kinetic energy, which must ultimately derive from one or several of: surface momentum fluxes, gravitational interaction with the Moon and Sun, and boundary density fluxes. Surface winds directly impart momentum to the ice-free ocean, and indirectly to frozen seas via sea ice momentum transfers. Gravitational interaction with the Moon and Sun drives ocean tidal currents. Heat, freshwater and salt exchanges at ocean boundaries modify the density of seawater, and the resulting density gradients set the fluid in motion through gravity and pressure differences.

Abyssal Recipes II

In 1998, Munk and Wunsch revisited Munk's *Abyssal Recipes* in light of new observations. Decades of oceanographic cruises had made available global estimates of the ocean's mean thermohaline structure (Levitus et al. 1994; Levitus and Boyer 1994). Developing methods to measure mixing rates *in situ* had shown that interior diffusivities average only about $10^{-5}\,\mathrm{m^2\,s^{-1}}$ (Osborn and Cox 1972; Stigebrandt 1979; Schmit et al. 1988; Gregg 1989; Ledwell et al. 1993; Toole et al. 1994), but can attain values of up to $10^{-1}\,\mathrm{m^2\,s^{-1}}$ in specific boundary regions (Polzin et al. 1996, 1997). In particular, vertical profiles of velocity and temperature microstructure taken along a longitudinal section of the Brazil Basin had revealed a marked enhancement of diffusivities near the rough topography of the Mid-Atlantic Ridge (Fig. 2; Polzin et al. 1997). It was suspected that the elevated mixing was maintained by the local generation and subsequent breaking of internal tides, as later confirmed (Ledwell et al. 2000; Nikurashin and Legg 2011).

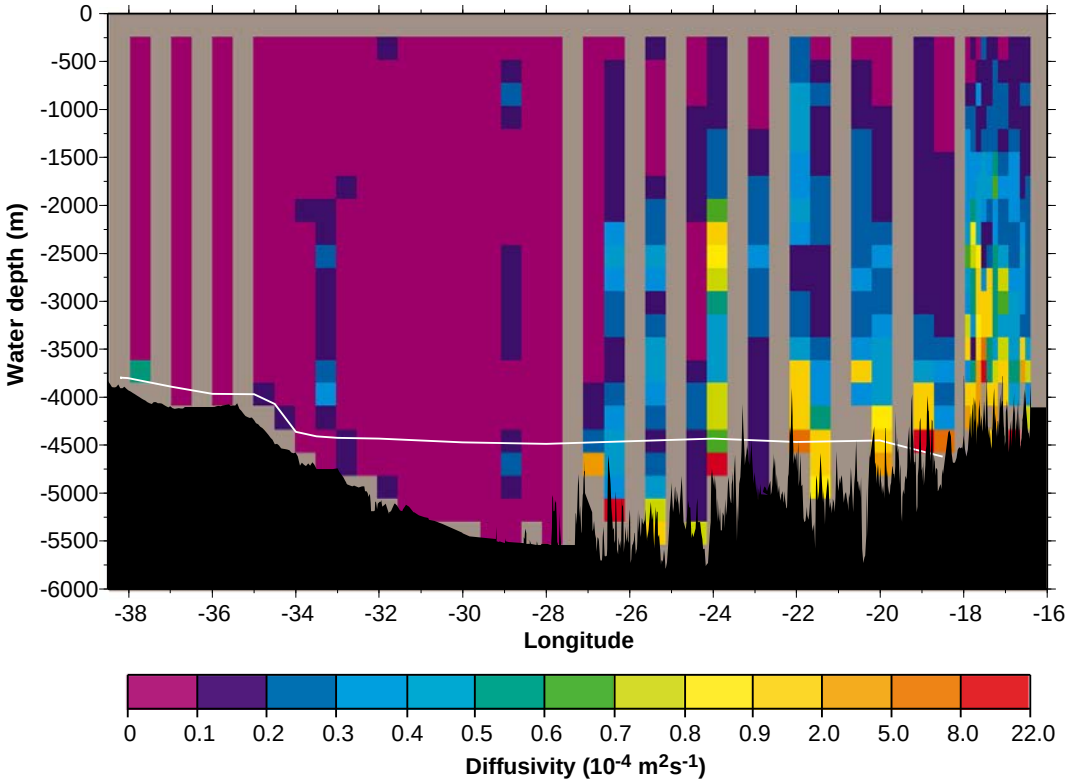

Figure 2: Depth-longitude section of turbulent diffusivity across the Brazil Basin. The diffusivity was estimated from velocity microstructure data along two longitudinal transects sampled in 1996. The white line marks the 0.8°C isotherm. From Polzin et al. (1997).

These observations meant that assumptions of uniform diffusivity and upwelling and the restriction to a few local property profiles were no longer justified. To estimate large-scale mean diffusivities, Munk and Wunsch (1998) considered the horizontally-averaged density balance of the 40°S-48°N ocean domain, between 1,000 and 4,000 m depth, under given boundary transports. Assuming the northern plus southern inflow of dense waters below 4,000 m depth to be 30 Sv, and that all of it upwells across density surfaces to 1,000 m depth, they obtained a mean vertical profile of the diffusivity (Fig. 3). The mean diffusivity was found to be almost independent of depth and just over $10^{-4}\,\mathrm{m^2\,s^{-1}}$. Though matching the previous estimate of Munk (1966), the value was no more interpreted as a uniformly-acting diffusivity but rather as an effective diffusivity resulting from concentrated density fluxes along boundaries.

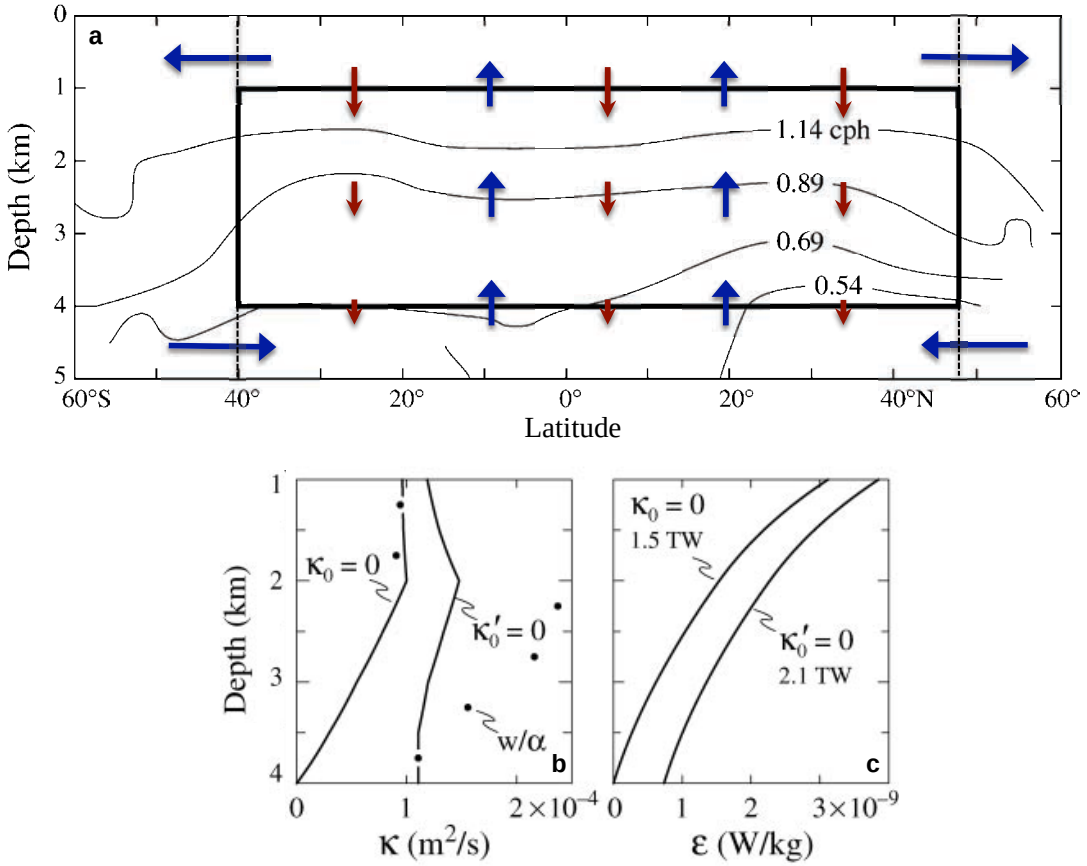

Figure 3: Domain and results of the *Abyssal Recipes II* calculation. (**a**) Zonal mean stratification ($N^2 = (g/\rho)\,\partial_z\rho$, in cycles per hour) contours from the Levitus et al. (1994) climatology. Arrows schematize the transports (blue) and downward buoyancy fluxes (red) implied by the calculation: depth-decreasing, convergent buoyancy fluxes cause lightening and cross-density upwelling of dense waters. (**b**,**c**) Calculated profiles of mean (**b**) diffusivity and (**c**) turbulent kinetic production. The preferred solution (right curves) uses the boundary condition $\partial_z K_z = 0$ at $z = 4000$ m. From Munk and Wunsch (1998).

But central to the new recipe was the discussion of energy sources able to maintain such density fluxes and thereby confine the dense inflowing waters to depths greater than 4,000 m. The density flux, equal to the vertical (more precisely, diapycnal) diffusivity times the density gradient, can be related to the rate of turbulent kinetic production ε_T [W kg^{-1}] through a mixing efficiency R_f (Osborn 1980):

$$(g/\rho) K_z\, \partial_z \rho = R_f\, \varepsilon_T \ ,$$

with g the gravitational acceleration and ρ the potential density of seawater. The above equation states that a fraction R_f of the energy flux into small-scale turbulence performs work against gravity, causing mixing and potential energy gain. The rest of the energy is converted into (quasi-negligible amounts of) heat by friction. Choosing a commonly-used upper-bound value $R_f = 0.2$, Munk and Wunsch deduced the 1,000-4,000 m depth profile of the horizontally-averaged ε_T (Fig. 3c). Vertical integration and multiplication by the global surface area of the ocean yielded a total rate of turbulent kinetic energy production of 2.1 TW.

Which forcing supplies the required 2.1 TW of energy? Arguing that air-sea density fluxes alone would produce only a very shallow convectively-driven ocean circulation, as suggested by early theoretical and laboratory work (Sandström 1908; see Coman et al. 2006), Munk and Wunsch (1998) asserted that the required deep mixing must be powered by winds and tides. Estimating the global kinetic energy supply from winds and tides is non-trivial. Determining the proportion of that energy which ultimately feeds small-scale turbulence in the deep ocean is even more difficult, because it demands a precise understanding and quantification of energy routes from forcing to dissipation. A preliminary budget was nonetheless attempted by Munk and Wunsch (Fig. 4).

Several sources of information constrain the energy available from tidal forcing. Retroreflectors placed on the Moon during the Apollo mission allow precise laser ranging measurements of the Earth-Moon distance (Dickey et al. 1994). The measurements show that the Moon recedes from the Earth by almost four centimetres per year, diminishing the energy of the Earth-Moon gravitational system at the rate of 3.2 TW (Munk and Wunsch 1997). This energy loss corresponds to the power input to lunar tides. Additional information comes from gravity perturbations of the orbits of man-made satellites, indicating notably that solar tides receive another 0.5 TW (Marsh et al. 1990). Altimetry observations further allow spatially-resolved estimates of the work done by tidal forces on the ocean (Cartwright and Ray 1991) and of the rate at which ocean tidal currents dissipate (Egbert 1997; Egbert and Ray 2000). They show that the total power input to barotropic ocean tides nears 3.5 TW (the remaining 0.2 TW drives solid earth and atmospheric tides), about two-thirds of which are lost to bottom friction at continental margins and one-third to baroclinic or internal tides (e.g., Egbert and Ray 2003). Through wave instabilities near topography or in the interior, internal tides may then provide for ~ 1 TW of turbulent kinetic energy production (Fig. 4).

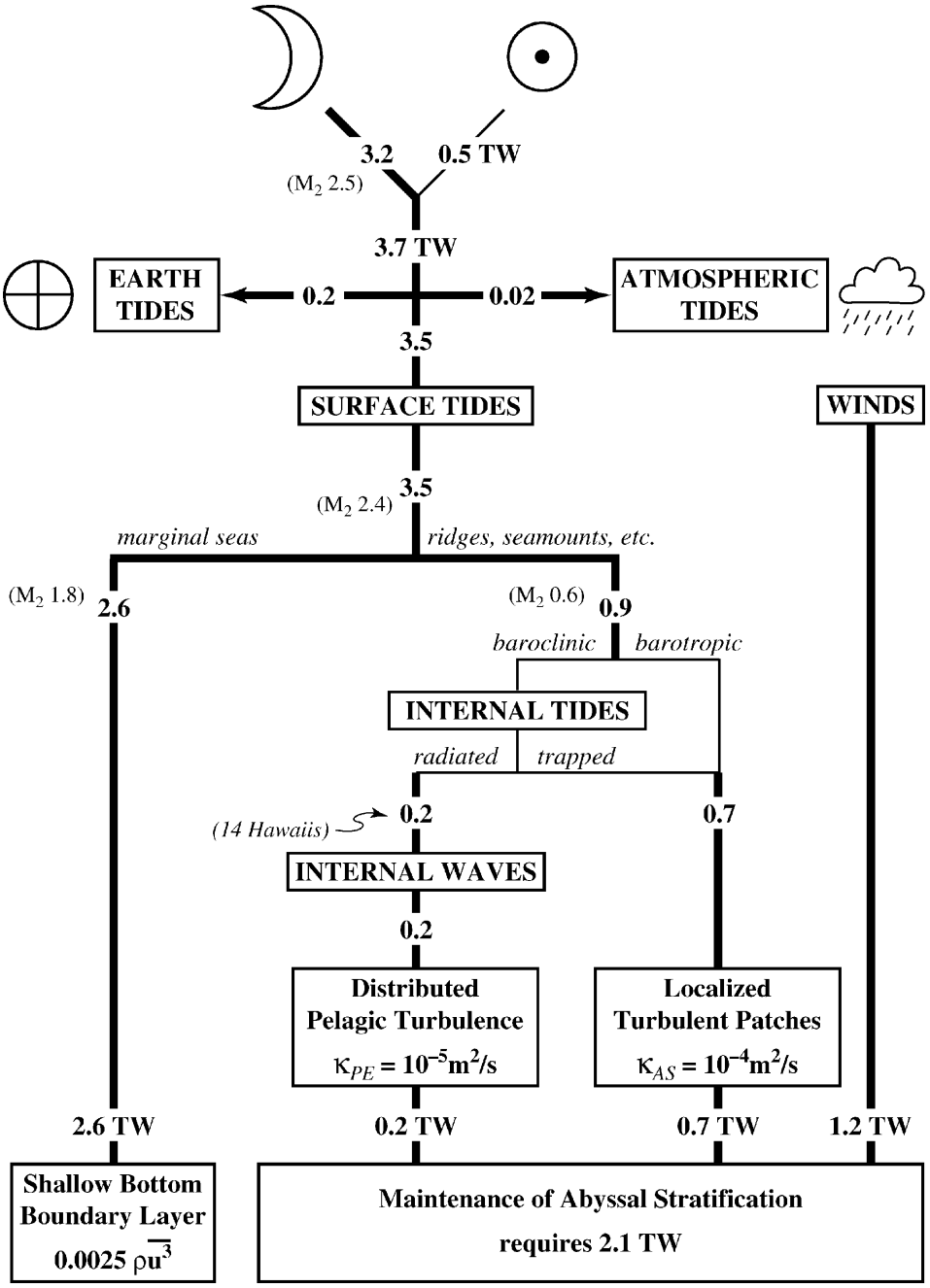

Figure 4: Energy budget proposed by Munk and Wunsch (1998). Winds contribute 1.2 TW to deep mixing and, thereby, to the maintenance of abyssal density gradients. Tides lose most of their energy in the bottom boundary layer of marginal seas. The remaining 0.9 TW contributes to distributed interior ("pelagic") turbulence, associated with a diffusivity of about $10^{-5}\,\mathrm{m^2\,s^{-1}}$, and to concentrated mixing along boundaries producing a large-scale mean diffusivity of about $10^{-4}\,\mathrm{m^2\,s^{-1}}$.

The rates and routes of wind-driven deep turbulence production are less well known. Like solar radiation, the vast majority of the wind energy input is absorbed in the surface boundary layer (Wunsch and Ferrari 2004; Wang and Huang 2004a,b). A small fraction directly excites internal waves, notably near-inertial internal waves, with an estimated ~ 0.1 TW of near-inertial wave energy escaping the surface mixed layer and (potentially) contributing to deeper mixing (Townsend 1965; Large and Crawford 1995; Alford 2003a; Furuichi et al. 2008; Rimac et al. 2013, 2016). A larger contribution, thought to lie in the 0.75-1 TW range, powers large-scale and mesoscale geostrophic flows of the ocean interior (Wunsch 1998; Huang et al. 2006; von Storch et al. 2007; Scott and Xu 2009; Roquet et al. 2011; Rimac et al. 2016). The energy of geostrophic flows must eventually dissipate at small scales, but the location and mixing efficiency of the induced small-scale turbulence depend on the dissipation pathways of these flows (e.g., Molemaker et al. 2005; Dewar and Hogg 2010; Molemaker et al. 2010; Zhai et al. 2010; Nikurashin and Ferrari 2010; Dewar et al. 2011; Wright et al. 2013). Because the relative contributions of the various dissipative mechanisms are poorly quantified, the amount of deep mixing powered by winds is largely unknown. Guided by the estimated ~ 1 TW of wind input to the general circulation (Wunsch 1998), Munk and Wunsch (1998) closed their budget by assigning a 1.2 TW wind contribution to the cross-density upwelling of dense waters via mixing (Fig. 4).

Beyond the recipes

Stommel (1958) first argued that the high-latitude sinking of dense waters must be balanced by upwelling across density surfaces at lower latitudes. Munk (1966) showed that the maintenance of vertical property gradients of the abyssal Pacific requires turbulent diffusivities of order $10^{-4}\,\mathrm{m^2\,s^{-1}}$. Munk and Wunsch (1998) further emphasized the reliance of the cross-density low-latitude upwelling on mechanical energy input by winds and tides. Because this cross-density upwelling joins the abyssal equatorward flow of cold dense waters with the compensating upper-ocean poleward flow of warmer, lighter waters (Fig. 3a), they argued that the poleward heat transport accomplished by the circulation connecting sources and sinks of

dense waters is ultimately driven by wind- and tide-powered mixing. They so contributed to change the view of this circulation, referred to as the meridional overturning circulation, from one driven by surface density forcing and high-latitude sinking to one driven by momentum forcing and deep mixing (Kuhlbrodt et al. 2007).

The influential work of Munk and Wunsch (1998) arouses a number of questions. First, are winds and tides "the only possible source of mechanical energy to drive the interior mixing"? Surface density fluxes generate flows, whose kinetic energy must eventually cascade to small-scales, causing turbulence and mixing. In particular, high-latitude surface densification generates descending plumes of dense waters which entrain and mix with ambient waters, causing strong transformation of the dense waters along their route from the surface to the abyssal ocean (e.g., Killworth 1977; Hughes and Griffiths 2006). This transformation is largely responsible for the significant salinity, temperature and density gradients observed along the bottom sinking and spreading branches of the overturning (Fig. 1; Polzin et al. 1996; Bryden and Nurser 2003). Though unable to lift abyssal waters back to the surface, mixing in sinking plumes thus contributes to lighten dense waters and participates to the overall density and temperature contrasts of the meridional overturning circulation. More generally, since both boundary density forcing and momentum forcing supply mechanical energy to the ocean (Oort et al. 1994; Hughes et al. 2009; Hogg 2010; Saenz et al. 2012; Howard et al. 2015), both could be expected to contribute to deep ocean mixing.

Second, how important is the distribution of the required turbulent kinetic energy production? The oft-quoted global number of 2 TW masks the restricted domain of the *Abyssal Recipes II* calculation (Fig. 3a) as well as the vertical structure of the horizontally-averaged power density (Fig. 3c). What fraction of the power available from internal tides and winds dissipates above 1,000 m depth, or deeper than 4,000 m? Given that internal wave energy dissipation is generally observed to scale with stratification $\partial_z \rho$ in the open sea (Gregg 1989; Polzin et al. 1995; Kunze and Sanford 1996), the possibility that a majority of tidal dissipation occurs in the upper-ocean cannot be ruled out. What if a large fraction of the available power dissipates south of 40°S, where most of the large-scale wind work is located (Wunsch 1998)? The latitudinal distribution of upwelling should affect the meridional extent and structure of the overturning, and therefore the associated heat, salt and passive tracer transports. Distribution matters also within the low-latitude, abyssal domain of the calculation. In order to have

density loss (equivalently, buoyancy gain) and upwelling throughout the 1,000-4,000 m depth range, the density flux $K_z\,\partial_z\rho$ must decrease with depth. Given a fixed mixing efficiency, so does the turbulent production ε_T. Hence, the 2 TW of turbulence production should not be randomly distributed, but rather follow the depth-decreasing curve of Fig. 3c on a horizontal average. In general, the three-dimensional distribution of density fluxes should govern the locations of dense water sinks, and thereby the circulation linking sinks to sources.

Third, the horizontally-averaged framework of the recipe raises the question of basin geometry. Perhaps to account for the mixing occurring in regions outside of their domain, Munk and Wunsch (1998) used the global surface ocean area to convert their average ε_T profile into a total energy requirement. But the overall procedure dismisses the depth-decrease of the ocean area. Between 1,000 and 4,000 m depth, the 40°S-48°N wet area shrinks by almost a factor of two. To compensate for the decrease in basin area, the mean density flux should decrease less rapidly with depth, distorting and shifting to higher values the diffusivity profile of Fig. 3b. By assuming the mean velocity to be vertically uniform and ignoring geometry, Munk and Wunsch (1998) thus underestimated the mean diffusivity and its vertical variation. Puzzlingly, they neglected the presence of the same sloping boundaries that they hypothesized as hosting the bulk of density fluxes. Yet without these slopes, concentrated mixing along the flat ocean bottom would disallow a top-to-bottom buoyancy transfer and concomitant bottom-to-top cross-density upwelling (rather, such mixing would be expected to erase the near-bottom stratification). Given concentrated sources of mixing along the seafloor, could the shape of the bottom boundary affect the distribution of these sources, and thereby the energy, diffusivity, and upwelling profiles?

The one-dimensional, horizontally-averaged calculation also neglects co-variations between diffusivities and stratification. Munk and Wunsch (1998) assumed that vigorous heat and salt exchanges between the mixing boundaries and the interior effectively maintain a horizontally homogeneous stratification. But in regions such as above the rough Brazil Basin topography (Fig. 2), where strong near-bottom turbulence is sustained by steady tidal forcing, one might expect the near-bottom stratification to be weaker than in more quiescent surroundings. If abyssal mixing is dominated by tidally-forced, bottom-enhanced turbulence, one could expect an anti-correlation between mixing and stratification levels, so that mean diffusivities are no longer representative of the mean density flux. Further, if a significant fraction of the

near-bottom turbulence dissipates within the well-mixed bottom boundary layer, where density fluxes must vanish, the overall mixing efficiency associated with such boundary processes may be well below the upper-bound 20 % value. As a result, the energy requirement could be significantly underestimated – or, equivalently, the effective power availability overestimated. What are the implications of mixing efficiency variations for the energetics of the overturning?

2. Near-surface transformation

Following Stommel (1958), Munk and Wunsch (1998) proposed that cross-density upwelling at temperate latitudes closes the circulation of northern-sourced and southern-sourced dense waters by returning them to the upper-ocean as lighter waters. The resulting overturning circulation may be pictured as consisting of two symmetric cells (Fig. 3a): a southern cell associated with the lifecycle of Antarctic Bottom Water (AABW) and a northern cell fed by North Atlantic Deep Water (NADW) formation. Yet Toggweiler and Samuels (1993b) had challenged this view by showing that observed radiocarbon activities are not compatible with bottom-to-top, low-latitude upwelling of dense waters. Instead, Toggweiler and Samuels argued that most of the upwelling occurs near the Antarctic continent (Fig. 1b). There, surface westerlies drive northward Ekman flow in a shallow surface layer. South of the position of maximum zonal wind stress, the divergent Ekman transport raises deep waters towards the surface, where they can be destroyed locally by air-sea fluxes or transported northward in the Ekman flow to be transformed elsewhere (Toggweiler and Samuels 1993b,a, 1995; Döös and Coward 1997). No deep mixing is required, it was argued, because the upwelling is *adiabatic* rather than *diabatic* (Toggweiler and Samuels 1998): that is, it occurs *along* rather than *across* density surfaces (Fig. 1b).

Toggweiler and Samuels (1993a, 1995) further argued that the presence of a zonally continuous band of water within Drake Passage latitudes helps to select relatively deep waters as a replacement for the shallow northward Ekman transport. Indeed, above the $\approx 2{,}000\,\mathrm{m}$ deep Drake Passage sill, the zonal mean zonal pressure gradient must vanish, disallowing any net meridional geostrophic transport. Only deep waters located below the sill depth are allowed to flow in geostrophic balance towards or away from the Antarctic continent. This dynamical constraint, combined to the required southward mass transport to compensate for the

surface Ekman (and bottom AABW) northward flow, ultimately favours the southward import of relatively dense, deep waters (Toggweiler and Samuels 1995). Nonetheless, ageostrophic dynamics also allow the southward and upward transport of deep waters, as necessitated by the surface divergence within (and not only south of) Drake Passage latitudes (Marshall 1997; Gnanadesikan 1999; Marshall and Radko 2003; Olbers and Visbeck 2005; Nikurashin and Vallis 2011). Below the Ekman layer and above the sill depth, this mass transport is accomplished by mesoscale eddies acting to flatten out the slant density surfaces of the Antarctic Circumpolar Current (see Fig. 1; Gent and Mcwilliams 1990; Marshall 1997). Both geostrophic and ageostrophic upwelling pathways are thought to be primarily adiabatic, involving little density transformation below the direct influence of air-sea density fluxes (Marshall and Speer 2012). Nonetheless, the presence of significant salinity and temperature along-density gradients (Fig. 1) implies that significant interior mixing and water mass property modification does occur along the upwelling path (Naveira Garabato et al. 2007, 2016).

The Southern Ocean adiabatic upwelling route, which is primarily wind-forced (Toggweiler and Samuels 1993b; Marshall and Speer 2012), alleviates the requirement for density transformation and diabatic upwelling at temperate latitudes (Webb and Suginohara 2001). Indeed, it is presently thought that the bulk of southward-flowing NADW upwells along isopycnals in the Southern Ocean rather than into the main thermocline (Lumpkin and Speer 2007; Talley 2013). On the other hand, the denser, northward-flowing AABW does need to upwell diabatically, but only until it reaches the mid-depth density layers which connect southward to the Ekman divergence of the Southern Ocean. The deep ocean meridional circulation may then be conceptualized as composed of two dynamically distinct branches (Figs. 1b and 5; Talley 2013): a northward, diabatic branch that carries AABW from Antarctica to the abyss of the Indian, Pacific and Atlantic basins, along which AABW is gradually lightened until converted into one of North Atlantic, Indian or Pacific Deep Water; and a southward, adiabatic branch that carries these lighter deep waters along density surfaces to the Southern Ocean surface, where near-surface thermodynamic forcing and mixing convert them into denser (AABW) or lighter waters. In the remainder of this thesis, we focus on density transformation processes in the abyssal ocean and, therefore, on the AABW limb of the overturning.

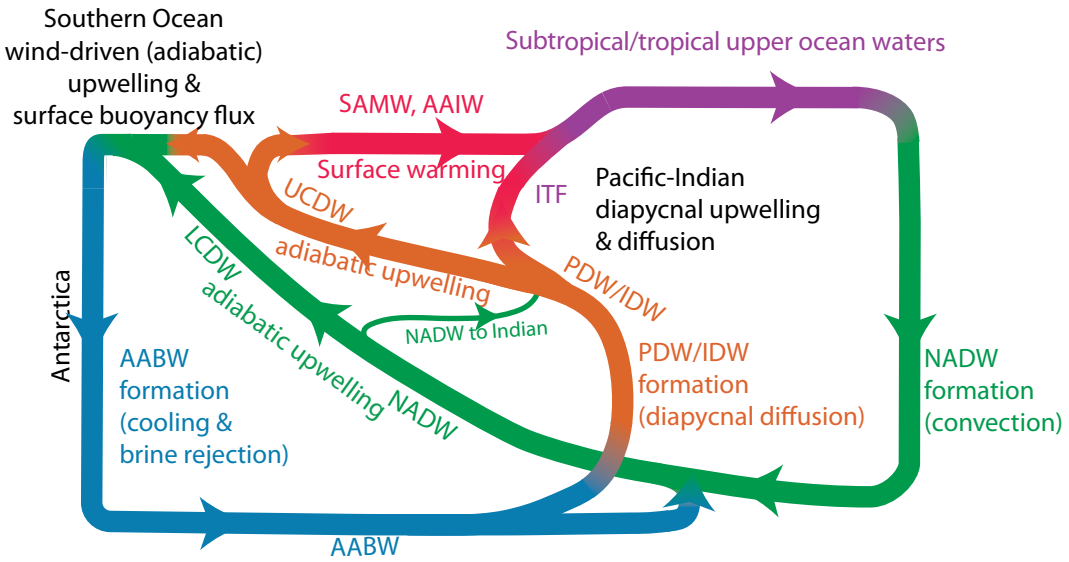

Figure 5: Schematic of the overturning circulation by Talley (2013). The densest water mass, Antarctic Bottom Water (AABW), is formed around Antarctica and spreads northward along the bottom. It is lightened into Indian Deep Water (IDW), Pacific Deep Water (PDW) and North Atlantic Deep Water (NADW). Deep waters move southward primarily adiabatically and upwell in the Southern Ocean. The densest of upwelled waters are recycled into AABW. The remainder is lightened into Antarctic Intermediate Water (AAIW), Subantarctic Mode Water (SAMW) or lighter upper-ocean waters, ultimately feeding North Atlantic sinking.

3. Geothermal heating

Thermodynamic forcing of the ocean is not restricted to its upper boundary: geothermal heat diffuses from Earth's interior into the ocean bottom (Munk 1966). The global heat supply through the ocean floor amounts to $\sim 30\,\mathrm{TW}$, corresponding to an average flux near $80\,\mathrm{mW\,m^{-2}}$ (Stein and Stein 1992; Pollack et al. 1993; Huang 1999). This heat flux is much smaller than typical surface fluxes of 10-100 $\mathrm{W\,m^{-2}}$, but is always of the same sign and ideally placed to supply potential energy to the abyss (Huang 1999; Hofmann and Morales Maqueda 2009). Munk (1966) and Munk and Wunsch (1998) estimated that this heat flux would only warm by 0.1-0.3°C abyssal waters renewed at a rate of about 30 Sv. Because this temperature difference is small compared with the ~ 10°C temperature changes across the overturning, they concluded that geothermal heating plays a negligible role in the overturning circulation.

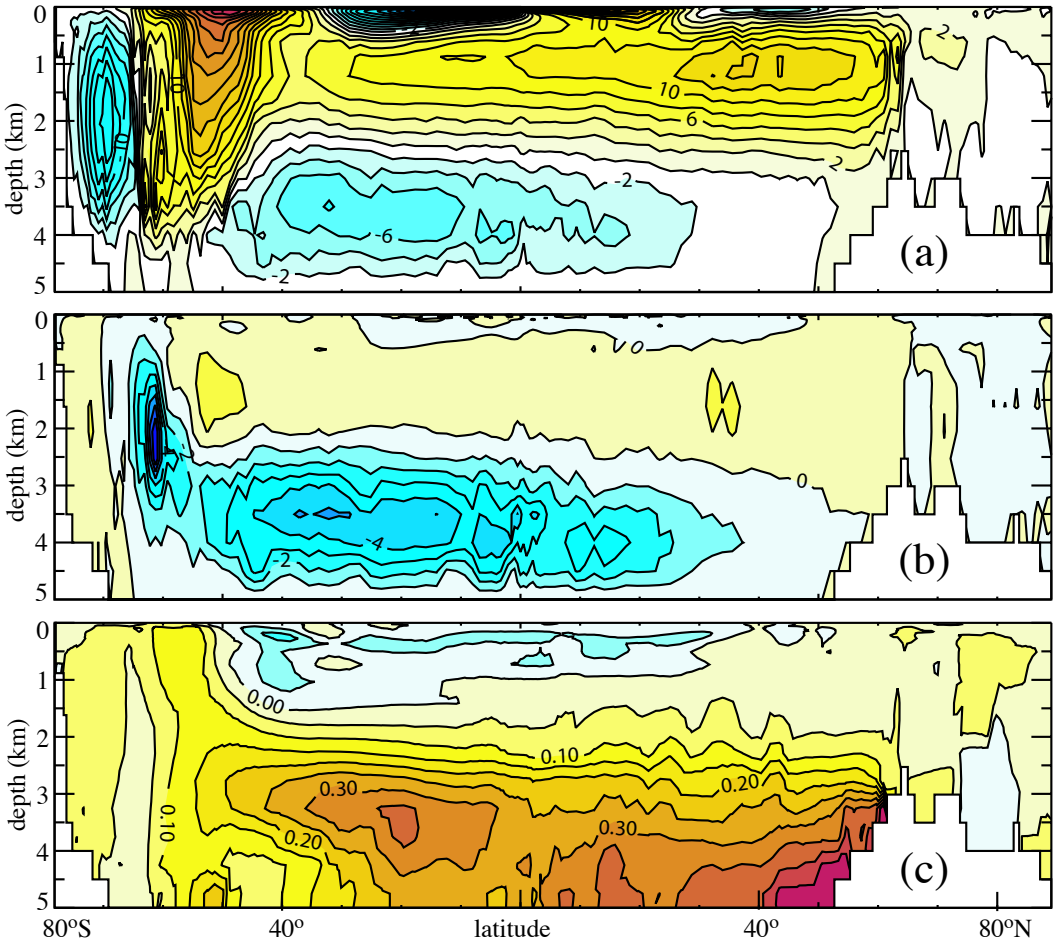

Figure 6: Impact of geothermal heating in a global ocean model. (**a**) Meridional overturning streamfunction [Sv] in a standard configuration without geothermal heating. (**b**,**c**) Change in the (**b**) overturning streamfunction [Sv] and (**c**) zonal mean potential temperature [°C] due to the addition of geothermal forcing. From Emile-Geay and Madec (2009).

However, experiments using ocean general circulation models later showed that the addition of bottom geothermal forcing, while warming AABW by less than 0.5°C, may strengthen the AABW circulation by up to 5 Sv (Fig. 6; Adcroft et al. 2001; Scott et al. 2001; Hofmann and Morales Maqueda 2009; Emile-Geay and Madec 2009). Using an observational estimate of the bottom density distribution, Emile-Geay and Madec (2009) further showed that the density balance of bottom ocean waters requires a cross-density advective transport of up to 6 Sv to counter the geothermal lightening. This relatively large transport is a consequence of the weak bottom density gradients of northern basins: there, advection over a large distance is necessary to equilibrate a small geothermal heat input (Emile-Geay and Madec 2009). Hence,

because of the relative homogeneity and large seafloor coverage of AABW (Johnson 2008), geothermal heating seems to contribute significantly to the AABW limb of the overturning. Emile-Geay and Madec (2009) noted that, near the ocean bottom, the upward geothermal heat flux is of comparable magnitude to the downward heat flux induced by a $10^{-4}\,\mathrm{m^2\,s^{-1}}$ diffusivity. Could bottom density forcing be as important a sink of AABW as abyssal mixing?

4. Overturning circulation driven by breaking internal waves?

Internal gravity waves, which represent the oceanic dynamical regime closest to small-scale turbulence in terms of time and space scales, are thought to be the primary pathway to turbulent mixing in the stratified ocean (Garrett and Munk 1979; Garrett and Laurent 2002; Alford 2003b; Gregg et al. 2003; Waterhouse et al. 2014; Eden et al. 2014). Sources of internal waves include: baroclinic tide generation over irregular ocean topography (Munk 1966); lee wave radiation by geostrophic flows impinging on rough, small-scale topography (Nikurashin and Ferrari 2010); surface generation of near-inertial waves by atmospheric storms (Alford 2003a); spontaneous generation by imbalanced flow (Williams et al. 2008; Vanneste 2013; Nagai et al. 2015; Sugimoto and Plougonven 2016). Observations and theory suggest that bottom-generated internal tides and lee waves dominate in the deep ocean (Polzin et al. 1997; Egbert and Ray 2000; Ledwell et al. 2000; Garrett and Laurent 2002; Naveira Garabato et al. 2004; Nycander 2005; Nikurashin and Ferrari 2011; Sheen et al. 2013).

In order to represent internal wave-driven mixing in ocean climate models and estimate its contribution to the transformation of dense waters, it is necessary to map the production of turbulent kinetic energy by breaking internal waves. Such three-dimensional maps have recently been constructed for the dissipation of internal tides and lee waves (St. Laurent et al. 2002; Polzin 2009; Niwa and Hibiya 2011; Nikurashin and Ferrari 2013; Oka and Niwa 2013). As a first step, the bottom energy flux into these waves is estimated. Most accurate maps of energy sources have been obtained by applying linear wave theory (Bell 1975; Llewellyn Smith and Young 2002) to recent bathymetry products (Smith and Sandwell 1997; Goff and Arbic 2010; Goff 2010) and climatologies of ocean stratification and tidal or geostrophic currents (Fig. 7; Nycander 2005; Scott et al. 2011; Nikurashin and Ferrari 2011; Green and Nycander 2013; Melet et al. 2013; Falahat et al. 2014). Next, it is assumed that a fraction of the energy source

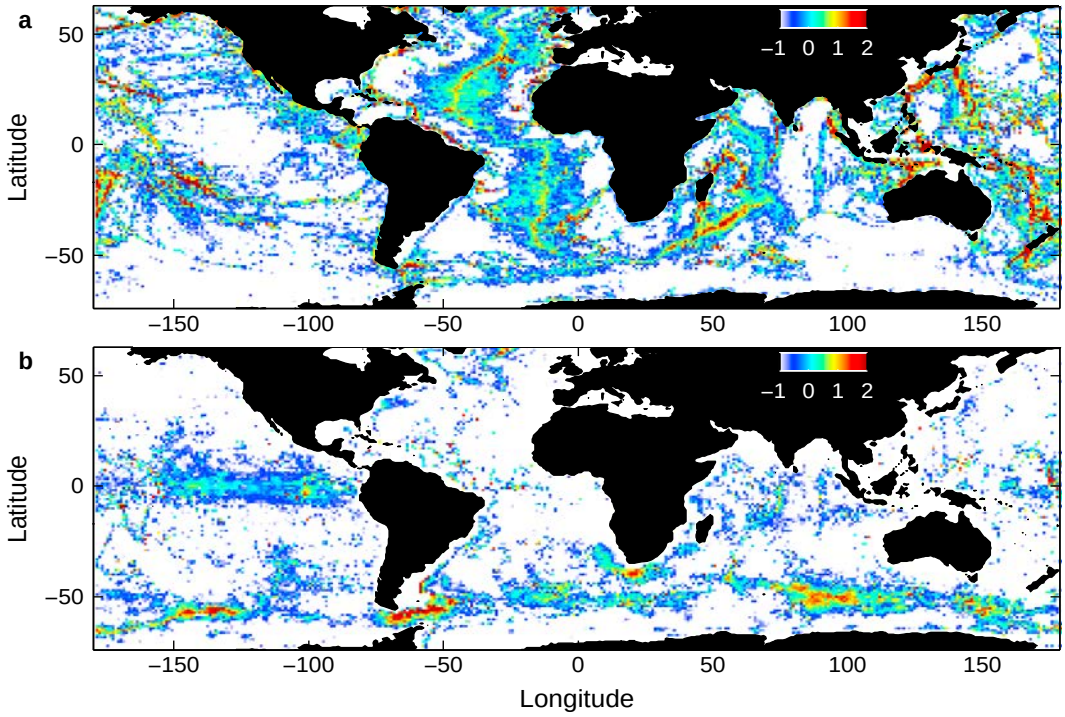

Figure 7: Energy flux [log(mW m^{-2})] into (**a**) internal tides and (**b**) lee waves estimated by Nycander (2005) and Nikurashin and Ferrari (2011), respectively. The global power input is 1 TW for internal tides and 0.2 TW for lee waves. From Nikurashin and Ferrari (2013).

contributes to local or near-field wave breaking, with a turbulent kinetic production generally taken as decreasing exponentially with height above bottom, consistent with Brazil Basin microstructure observations (St. Laurent et al. 2002). The remote or far-field internal wave energy dissipation, whose distribution is largely unknown, is generally ignored or assumed to sustain an interior diffusivity of 10^{-5} m^2 s^{-1} (Simmons et al. 2004; Nikurashin and Ferrari 2013).

Using constructed three-dimensional maps of local internal tide and lee wave dissipation and an observation-based hydrographic climatology, Nikurashin and Ferrari (2013) recently calculated the global cross-density transports required to balance the density tendencies caused by near-field internal wave breaking. They found that locally-dissipating internal tides and lee waves can balance diabatic upwelling transports of up to 17 and 9 Sv, respectively (Fig. 8). The peak total transport of about 25 Sv across the 28.1 kg m^{-3} neutral density surface roughly matches the strength and depth of the AABW circulation suggested by inverse estimates of ocean transports (Ganachaud and Wunsch 2000; Talley et al. 2003; Lumpkin and Speer 2007;

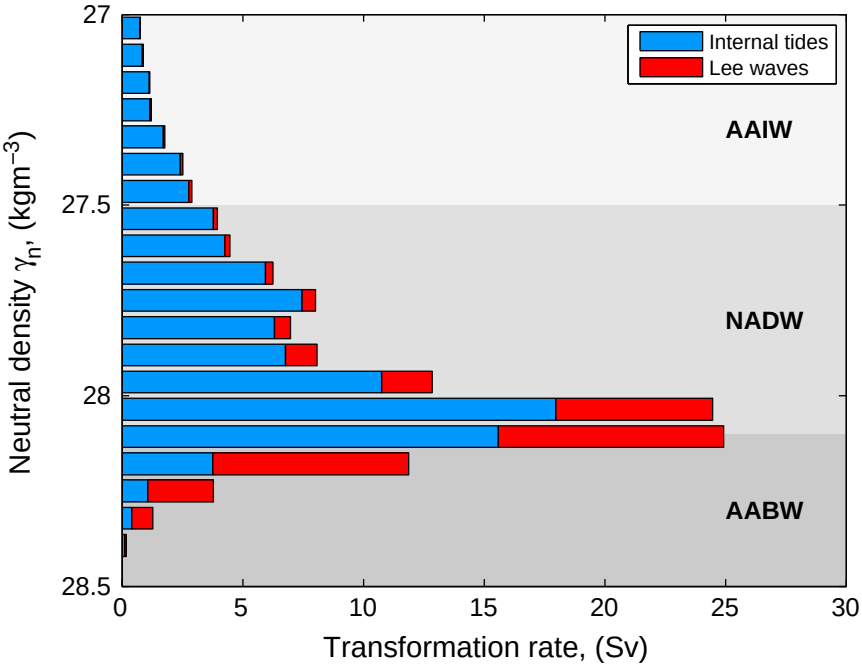

Figure 8: Cross-density upwelling transports induced by near-field (blue) internal tide and (red) lee wave breaking as a function of neutral density, calculated by Nikurashin and Ferrari (2013). As shown in chapter I, the calculation is erroneous and the transports actually correspond to the downwelling of interior waters that are densified by bottom-enhanced turbulence.

Talley 2013). Consistent with predominantly adiabatic upwelling of deep waters, diabatic upwelling rates fall below 8 Sv at neutral densities lesser than 27.9 kg m^{-3} (corresponding to depths shallower than 2,000 m north of the Antarctic Circumpolar Current). Nikurashin and Ferrari (2013) thus argued that bottom-intensified mixing by breaking internal tides and lee waves, combined to wind-forced upwelling in the Southern Ocean, is able to return 25 Sv of AABW to the surface.

The results of Nikurashin and Ferrari (2013) concur with the prevailing view that the diabatic component of the overturning is primarily sustained by breaking internal waves in the deep ocean (Munk and Wunsch 1998; Garrett and Laurent 2002; MacKinnon 2013; Waterhouse et al. 2014). Yet the inferred upwelling rates appear surprisingly large in light of evidence from other studies. First, the response of global ocean models to similar bottom-intensified mixing is relatively modest: its inclusion enhances the AABW volume transport by less than 5 Sv (Simmons et al. 2004; Saenko and Merryfield 2005; Jayne 2009; Oka and Niwa 2013; Melet et al. 2014). Second, observed levels of internal wave-driven turbulence in the

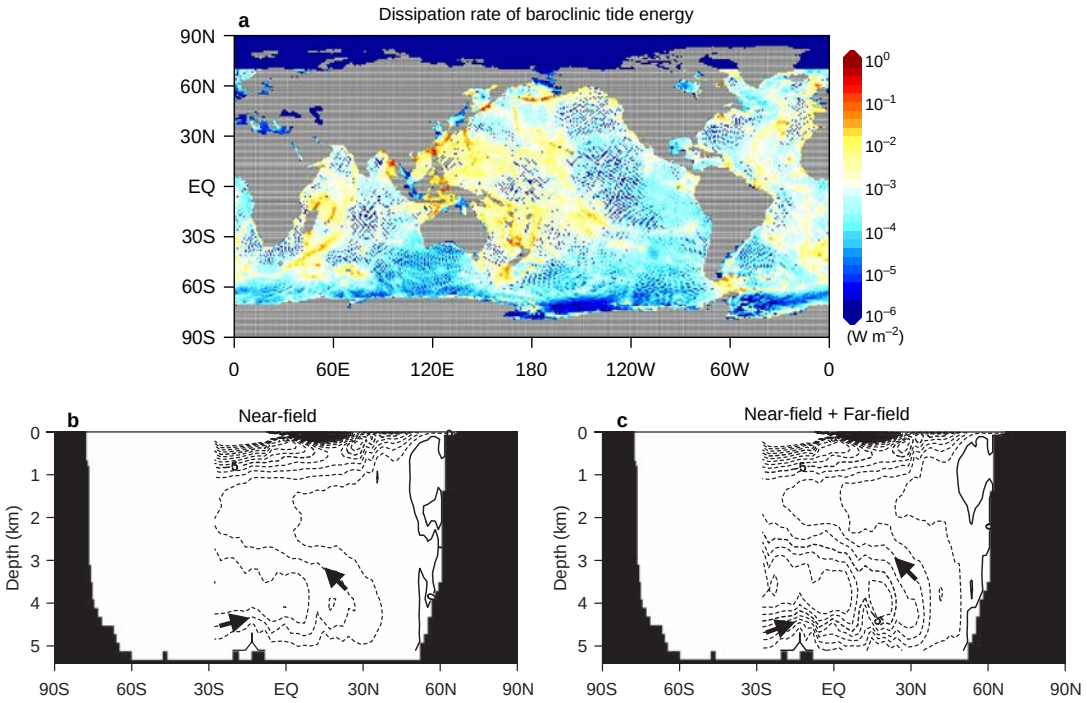

Figure 9: Impact of remote tidal mixing in a global ocean model. (**a**) Depth-integrated dissipation rate of internal tides diagnosed from global three-dimensional numerical experiments (Niwa and Hibiya 2011). (**b**,**c**) Meridional streamfunction in the Pacific Ocean for simulations including parameterized (**b**) local tidal mixing and (**c**) local and remote tidal mixing. The contour interval is 1 Sv. From Oka and Niwa (2013).

Indian Ocean are insufficient to explain the estimated ~ 10 Sv of deep circulation in this basin, suggesting that additional bottom boundary mixing must be at play (Huussen et al. 2012). Third, basin-scale diffusivity profiles implied by the parameterized local tidal dissipation are a factor of 3 to 10 weaker than analogous profiles inferred from inversions of hydrographic observations (Decloedt and Luther 2012). Last, the results of Nikurashin and Ferrari (2013) suggest that other sources of abyssal water mass transformation, such as remotely-dissipating internal tides, geothermal heating or mixing in deep overflows, are of secondary importance. In contrast, Oka and Niwa (2013) argue that mixing due to remotely-breaking internal tides is key to the Pacific overturning circulation: using a recent model estimate of the two-dimensional distribution of remote tidal dissipation (Fig. 9a; Niwa and Hibiya 2011) and the assumption of vertically-uniform turbulent kinetic energy production, they showed that the addition of far-field tidal mixing raises the strength of the simulated Pacific deep circulation from 4 to 8 Sv (Fig. 9b,c).

As suggested by Melet et al. (2014), the gap between model results and the climatological transport estimates of Nikurashin and Ferrari (2013) could be a consequence of the erosion of the simulated stratification by bottom-intensified mixing. This would suggest that the mixing efficiency of 20 % employed in those studies leads to overestimate the density fluxes maintained by bottom-enhanced internal wave breaking. Should the mixing efficiency be reduced in the weakly stratified abyss? But closer examination of the modelled response to lee wave-driven mixing (Melet et al. 2014) brings up an additional puzzle: bottom-enhanced lee wave dissipation significantly homogenizes the model AABW but barely affects lighter, shallower waters. Given that 90 % of the lee wave generation occurs at depths greater than 3,000 m (Melet et al. 2014), mostly in the Antarctic Circumpolar Current (Fig. 7b), this response matches that expected from boundary mixing along the deep Southern Ocean floor. However, it implies that lee wave breaking causes density loss of the densest AABW but density *gain* of the lighter AABW. In turn, this density gain should be balanced by diabatic downwelling, rather than upwelling. How to explain the net upwelling throughout the deep ocean density range (Fig. 8) diagnosed by Nikurashin and Ferrari (2013)? As we will show in chapter I, omission of the no-density-flux bottom boundary condition led the authors to miscalculate and misinterpret diabatic transports: their values reflect the downwelling caused by interior density gain and exclude the upwelling due to near-bottom density loss.

These recent disparate results call for clarification of the role of local and remote internal wave breaking for deep ocean density transformation. How does internal wave-driven mixing compare with geothermal heating and other processes? How important is the distribution of turbulence relative to different water masses and basins? Do variations of the mixing efficiency matter? These and earlier questions may be summarized as follows:

1. **What drives the destruction of Antarctic Bottom Water?** In other words, which **processes** and which **energy sources** contribute to the upwelling of dense waters across the deep ocean stratification?

2. **What are the implications of mixing being intensified along boundaries for the structure and strength of abyssal upwelling?** In particular, how does the heterogeneous distribution of turbulence impact the **efficiency of mixing**, the distribution of density losses and gains and the associated **upwelling and downwelling patterns**?

In the following chapter, we set out the water mass transformation framework (Walin 1982; Iudicone et al. 2008b) employed throughout this thesis and reassess the contributions of geothermal heating and bottom-generated internal waves to AABW upwelling. The sensitivity of diagnosed upwelling rates to varying mixing efficiencies is explored in chapter II. Next, we highlight the relationship between the large-scale overturning structure and the depth distribution of ocean floor (chapter III) as well as the need for more observations of bottom boundary processes (chapter IV). In chapter V, we refine the energy distributions of chapters I and II to narrow down uncertainties in the density transformation accomplished by breaking internal waves. We conclude with a summary of key findings and perspectives for further work.

References

Adcroft, A., Scott, J. R., and Marotzke, J. (2001). Impact of geothermal heating on the global ocean circulation. *Geophysical Research Letters*, 28(9):1735–1738.

Alford, M. H. (2003a). Improved global maps and 54-year history of wind-work on ocean inertial motions. *Geophysical Research Letters*, 30(8):1424.

Alford, M. H. (2003b). Redistribution of energy available for ocean mixing by long-range propagation of internal waves. *Nature*, 423(6936):159–162.

Bell, T. H. (1975). Topographically generated internal waves in the open ocean. *Journal of Geophysical Research*, 80(3):320–327.

Bianchi, D., Galbraith, E. D., Carozza, D. A., Mislan, K. A. S., and Stock, C. A. (2013). Intensification of open-ocean oxygen depletion by vertically migrating animals. *Nature Geoscience*, 6(7):545–548.

Bryden, H. L. and Nurser, A. J. G. (2003). Effects of strait mixing on ocean stratification. *Journal of Physical Oceanography*, 33(8):1870–1872.

Cartwright, D. E. and Ray, R. D. (1991). Energetics of global ocean tides from Geosat altimetry. *Journal of Geophysical Research*, 96(C9):16897–16912.

Coman, M. A., Griffiths, R. W., and Hughes, G. O. (2006). Sandström's experiments revisited. *Journal of Marine Research*, 64(6):783–796.

Decloedt, T. and Luther, D. S. (2012). Spatially heterogeneous diapycnal mixing in the abyssal ocean: A comparison of two parameterizations to observations. *Journal of Geophysical Research*, 117(C11):C11025.

Dewar, W. K., Berloff, P., and Hogg, A. M. (2011). Submesoscale generation by boundaries. *Journal of Marine Research*, 69(4-6):501–522.

Dewar, W. K., Bingham, R. J., Iverson, R. L., Nowacek, D. P., St Laurent, L. C., and Wiebe, P. H. (2006). Does the marine biosphere mix the ocean? *Journal of Marine Research*, 64(4):541–561.

Dewar, W. K. and Hogg, A. M. (2010). Topographic inviscid dissipation of balanced flow. *Ocean Modelling*, 32(1–2):1–13.

Dickey, J. O., Bender, P. L., Faller, J. E., Newhall, X. X., Ricklefs, R. L., Ries, J. G., Shelus, P. J., Veillet, C., Whipple, A. L., Wiant, J. R., Williams, J. G., and Yoder, C. F. (1994). Lunar laser ranging: A continuing legacy of the Apollo program. *Science*, 265(5171):482–490.

Döös, K. and Coward, A. (1997). The Southern Ocean as the major upwelling zone of North Atlantic Deep Water. *International WOCE newsletter*, 27:3–4.

Eden, C., Czeschel, L., and Olbers, D. (2014). Toward energetically consistent ocean models. *Journal of Physical Oceanography*, 44(12):3160–3184.

Egbert, G. D. (1997). Tidal data inversion: interpolation and inference. *Progress in Oceanography*, 40(1):53–80.

Egbert, G. D. and Ray, R. D. (2000). Significant dissipation of tidal energy in the deep ocean inferred from satellite altimeter data. *Nature*, 405(6788):775–778.

Egbert, G. D. and Ray, R. D. (2003). Semi-diurnal and diurnal tidal dissipation from TOPEX/Poseidon altimetry. *Geophysical Research Letters*, 30(17):1907.

Emile-Geay, J. and Madec, G. (2009). Geothermal heating, diapycnal mixing and the abyssal circulation. *Ocean Science*, 5(2):203–217.

Falahat, S., Nycander, J., Roquet, F., and Zarroug, M. (2014). Global calculation of tidal energy conversion into vertical normal modes. *Journal of Physical Oceanography*, 44(12):3225–3244.

Furuichi, N., Hibiya, T., and Niwa, Y. (2008). Model-predicted distribution of wind-induced internal wave energy in the world's oceans. *Journal of Geophysical Research*, 113(C9):C09034.

Ganachaud, A. and Wunsch, C. (2000). Improved estimates of global ocean circulation, heat transport and mixing from hydrographic data. *Nature*, 408(6811):453–457.

Garrett, C. and Laurent, L. S. (2002). Aspects of deep ocean mixing. *Journal of oceanography*, 58(1):11–24.

Garrett, C. and Munk, W. (1979). Internal waves in the ocean. *Annual Review of Fluid Mechanics*, 11(1):339–369.

Gent, P. R. and Mcwilliams, J. C. (1990). Isopycnal mixing in ocean circulation models. *Journal of Physical Oceanography*, 20(1):150–155.

Gnanadesikan, A. (1999). A simple predictive model for the structure of the oceanic pycnocline. *Science*, 283(5410):2077–2079.

Goff, J. A. (2010). Global prediction of abyssal hill root-mean-square heights from small-scale altimetric gravity variability. *Journal of Geophysical Research*, 115(B12):B12104.

Goff, J. A. and Arbic, B. K. (2010). Global prediction of abyssal hill roughness statistics for use in ocean models from digital maps of paleo-spreading rate, paleo-ridge orientation, and sediment thickness. *Ocean Modelling*, 32(1–2):36–43.

Gouretski, V. and Koltermann, K. P. (2004). Woce global hydrographic climatology. Technical Report 35, Berichte des Bundesamtes für Seeschiffahrt und Hydrographie.

Green, J. A. M. and Nycander, J. (2013). A comparison of tidal conversion parameterizations for tidal models. *Journal of Physical Oceanography*, 43(1):104–119.

Gregg, M. C. (1989). Scaling turbulent dissipation in the thermocline. *Journal of Geophysical Research*, 94(C7):9686–9698.

Gregg, M. C., Sanford, T. B., and Winkel, D. P. (2003). Reduced mixing from the breaking of internal waves in equatorial waters. *Nature*, 422(6931):513–515.

Hofmann, M. and Morales Maqueda, M. A. (2009). Geothermal heat flux and its influence on the oceanic abyssal circulation and radiocarbon distribution. *Geophysical Research Letters*, 36(3):L03603.

Hogg, A. M. (2010). An Antarctic Circumpolar Current driven by surface buoyancy forcing. *Geophysical Research Letters*, 37(23):L23601.

Howard, E., McC. Hogg, A., Waterman, S., and Marshall, D. P. (2015). The injection of zonal momentum by buoyancy forcing in a Southern Ocean model. *Journal of Physical Oceanography*, 45(1):259–271.

Huang, R. X. (1999). Mixing and energetics of the oceanic thermohaline circulation. *Journal of Physical Oceanography*, 29(4):727–746.

Huang, R. X., Wang, W., and Liu, L. L. (2006). Decadal variability of wind-energy input to the world ocean. *Deep Sea Research*, 53(1-2):31–41.

Hughes, G. O. and Griffiths, R. W. (2006). A simple convective model of the global overturning circulation, including effects of entrainment into sinking regions. *Ocean Modelling*, 12(1–2):46–79.

Hughes, G. O., Hogg, A. M. C., and Griffiths, R. W. (2009). Available potential energy and irreversible mixing in the meridional overturning circulation. *Journal of Physical Oceanography*, 39(12):3130–3146.

Huntley, M. and Zhou, M. (2004). Influence of animals on turbulence in the sea. *Marine Ecology Progress Series*, 273:65–79.

Huussen, T. N., Naveira-Garabato, A. C., Bryden, H. L., and McDonagh, E. L. (2012). Is the deep Indian Ocean MOC sustained by breaking internal waves? *Journal of Geophysical Research*, 117(C8):C08024.

Inoue, R., Yamazaki, H., Wolk, F., Kono, T., and Yoshida, J. (2007). An estimation of buoyancy flux for a mixture of turbulence and double diffusion. *Journal of Physical Oceanography*, 37(3):611–624.

Iudicone, D., Madec, G., Blanke, B., and Speich, S. (2008a). The role of Southern Ocean surface forcings and mixing in the global conveyor. *Journal of Physical Oceanography*, 38(7):1377–1400.

Iudicone, D., Madec, G., and McDougall, T. J. (2008b). Water-mass transformations in a neutral density framework and the key role of light penetration. *Journal of Physical Oceanography*, 38(7):1357–1376.

Jackett, D. R. and McDougall, T. J. (1997). A neutral density variable for the World's oceans. *Journal of Physical Oceanography*, 27(2):237–263.

Jackson, P. R. and Rehmann, C. R. (2014). Experiments on differential scalar mixing in turbulence in a sheared, stratified flow. *Journal of Physical Oceanography*, 44(10):2661–2680.

Jayne, S. R. (2009). The impact of abyssal mixing parameterizations in an ocean general circulation model. *Journal of Physical Oceanography*, 39(7):1756–1775.

Johnson, G. C. (2008). Quantifying Antarctic Bottom Water and North Atlantic Deep Water volumes. *Journal of Geophysical Research*, 113(C5).

Katija, K. and Dabiri, J. O. (2009). A viscosity-enhanced mechanism for biogenic ocean mixing. *Nature*, 460(7255):624–626.

Killworth, P. D. (1977). Mixing on the Weddell Sea continental slope. *Deep Sea Research*, 24(5):427–448.

Klocker, A. and McDougall, T. J. (2010). Influence of the nonlinear equation of state on global estimates of dianeutral advection and diffusion. *Journal of Physical Oceanography*, 40(8):1690–1709.

Kuhlbrodt, T., Griesel, A., Montoya, M., Levermann, A., Hofmann, M., and Rahmstorf, S. (2007). On the driving processes of the Atlantic meridional overturning circulation. *Reviews of Geophysics*, 45(2):RG2001.

Kunze, E. (2011). Fluid mixing by swimming organisms in the low-Reynolds-number limit. *Journal of Marine Research*, 69(4-5):591–601.

Kunze, E., Dower, J. F., Beveridge, I., Dewey, R., and Bartlett, K. P. (2006). Observations of biologically generated turbulence in a coastal inlet. *Science*, 313(5794):1768–1770.

Kunze, E. and Sanford, T. B. (1996). Abyssal mixing: Where it is not. *Journal of Physical Oceanography*, 26(10):2286–2296.

Large, W. G. and Crawford, G. B. (1995). Observations and simulations of upper-ocean response to wind events during the Ocean Storms Experiment. *Journal of Physical Oceanography*, 25(11):2831–2852.

Ledwell, J. R., Montgomery, E. T., Polzin, K. L., Laurent, L. C. S., Schmitt, R. W., and Toole, J. M. (2000). Evidence for enhanced mixing over rough topography in the abyssal ocean. *Nature*, 403(6766):179–182.

Ledwell, J. R., Watson, A. J., and Law, C. S. (1993). Evidence for slow mixing across the pycnocline from an open-ocean tracer-release experiment. *Nature*, 364(6439):701–703.

Levitus, S. and Boyer, T. P. (1994). World Ocean Atlas 1994. Volume 4. Temperature. Technical Report PB–95-270112/XAB; NESDIS–4, National Environmental Satellite, Data, and Information Service, Washington, DC (United States).

Levitus, S., Burgett, R., and Boyer, T. P. (1994). World Ocean Atlas 1994. Volume 3. Salinity. Technical Report PB–95-270104/XAB; NESDIS–3, National Environmental Satellite, Data, and Information Service, Washington, DC (United States).

Llewellyn Smith, S. G. and Young, W. R. (2002). Conversion of the barotropic tide. *Journal of Physical Oceanography*, 32(5).

Lumpkin, R. and Speer, K. (2007). Global ocean meridional overturning. *Journal of Physical Oceanography*, 37(10):2550–2562.

MacKinnon, J. (2013). Oceanography: Mountain waves in the deep ocean. *Nature*, 501(7467):321–322.

Marsh, J. G., Lerch, F. J., Putney, B. H., Felsentreger, T. L., Sanchez, B. V., Klosko, S. M., Patel, G. B., Robbins, J. W., Williamson, R. G., Engelis, T. L., Eddy, W. F., Chandler, N. L., Chinn, D. S., Kapoor, S., Rachlin, K. E., Braatz, L. E., and Pavlis, E. C. (1990). The GEM-T2 gravitational model. *Journal of Geophysical Research*, 95(B13):22043–22071.

Marshall, D. (1997). Subduction of water masses in an eddying ocean. *Journal of Marine Research*, 55(2):201–222.

Marshall, J. and Radko, T. (2003). Residual-mean solutions for the Antarctic Circumpolar Current and its associated overturning circulation. *Journal of Physical Oceanography*, 33(11):2341–2354.

Marshall, J. and Speer, K. (2012). Closure of the meridional overturning circulation through Southern Ocean upwelling. *Nature Geoscience*, 5(3):171–180.

Melet, A., Hallberg, R., Legg, S., and Nikurashin, M. (2014). Sensitivity of the ocean state to lee wave–driven mixing. *Journal of Physical Oceanography*, 44(3):900–921.

Melet, A., Nikurashin, M., Muller, C., Falahat, S., Nycander, J., Timko, P. G., Arbic, B. K., and Goff, J. A. (2013). Internal tide generation by abyssal hills using analytical theory. *Journal of Geophysical Research*, 118(11):6303–6318.

Merrifield, S. T., Laurent, L. S., Owens, B., Thurnherr, A. M., and Toole, J. M. (2016). Enhanced diapycnal diffusivity in intrusive regions of the Drake Passage. *Journal of Physical Oceanography*, 46(4):1309–1321.

Merryfield, W. J., Holloway, G., and Gargett, A. E. (1998). Differential vertical transport of heat and salt by weak stratified turbulence. *Geophysical Research Letters*, 25(15):2773–2776.

Merryfield, W. J., Holloway, G., and Gargett, A. E. (1999). A global ocean model with double-diffusive mixing. *Journal of Physical Oceanography*, 29(6):1124–1142.

Molemaker, M. J., Mcwilliams, J. C., and Capet, X. (2010). Balanced and unbalanced routes to dissipation in an equilibrated Eady flow. *Journal of Fluid Mechanics*, 654:35–63.

Molemaker, M. J., McWilliams, J. C., and Yavneh, I. (2005). Baroclinic instability and loss of balance. *Journal of Physical Oceanography*, 35(9):1505–1517.

Munk, W. and Wunsch, C. (1997). The Moon, of course... *Oceanography*, 10:132–134.

Munk, W. and Wunsch, C. (1998). Abyssal recipes II: Energetics of tidal and wind mixing. *Deep-Sea Research*, 45(12):1977–2010.

Munk, W. H. (1966). Abyssal recipes. *Deep Sea Research*, 13(4):707–730.

Nagai, T., Tandon, A., Kunze, E., and Mahadevan, A. (2015). Spontaneous generation of near-inertial waves by the Kuroshio front. *Journal of Physical Oceanography*, 45(9):2381–2406.

Naveira Garabato, A. C., Polzin, K. L., Ferrari, R., Zika, J. D., and Forryan, A. (2016). A microscale view of mixing and overturning across the Antarctic Circumpolar Current. *Journal of Physical Oceanography*, page 151111130934007.

Naveira Garabato, A. C., Polzin, K. L., King, B. A., Heywood, K. J., and Visbeck, M. (2004). Widespread intense turbulent mixing in the Southern Ocean. *Science*, 303(5655):210–213.

Naveira Garabato, A. C., Stevens, D. P., Watson, A. J., and Roether, W. (2007). Short-circuiting of the overturning circulation in the Antarctic Circumpolar Current. *Nature*, 447(7141):194–197.

Nikurashin, M. and Ferrari, R. (2010). Radiation and dissipation of internal waves generated by geostrophic motions impinging on small-scale topography: Theory. *Journal of Physical Oceanography*, 40(5):1055–1074.

Nikurashin, M. and Ferrari, R. (2011). Global energy conversion rate from geostrophic flows into internal lee waves in the deep ocean. *Geophysical Research Letters*, 38(8):L08610.

Nikurashin, M. and Ferrari, R. (2013). Overturning circulation driven by breaking internal waves in the deep ocean. *Geophysical Research Letters*, 40(12):3133–3137.

Nikurashin, M. and Legg, S. (2011). A mechanism for local dissipation of internal tides generated at rough topography. *Journal of Physical Oceanography*, 41(2):378–395.

Nikurashin, M. and Vallis, G. (2011). A theory of deep stratification and overturning circulation in the ocean. *Journal of Physical Oceanography*, 41(3):485–502.

Niwa, Y. and Hibiya, T. (2011). Estimation of baroclinic tide energy available for deep ocean mixing based on three-dimensional global numerical simulations. *Journal of Oceanography*, 67(4):493–502.

Noss, C. and Lorke, A. (2014). Direct observation of biomixing by vertically migrating zooplankton. *Limnol. Oceanogr*, 59(3):724–732.

Nycander, J. (2005). Generation of internal waves in the deep ocean by tides. *Journal of Geophysical Research*, 110(C10).

Oka, A. and Niwa, Y. (2013). Pacific deep circulation and ventilation controlled by tidal mixing away from the sea bottom. *Nature Communications*, 4.

Olbers, D. and Visbeck, M. (2005). A model of the zonally averaged stratification and overturning in the Southern Ocean. *Journal of Physical Oceanography*, 35(7):1190–1205.

Oort, A. H., Anderson, L. A., and Peixoto, J. P. (1994). Estimates of the energy cycle of the oceans. *Journal of Geophysical Research*, 99(C4):7665.

Osborn, T. R. (1980). Estimates of the local rate of vertical diffusion from dissipation measurements. *Journal of Physical Oceanography*, 10(1):83–89.

Osborn, T. R. and Cox, C. S. (1972). Oceanic fine structure. *Geophysical Fluid Dynamics*, 3(1):321–345.

Pollack, H. N., Hurter, S. J., and Johnson, J. R. (1993). Heat flow from the Earth's interior: Analysis of the global data set. *Reviews of Geophysics*, 31(3):267–280.

Polzin, K. L. (2009). An abyssal recipe. *Ocean Modelling*, 30(4):298–309.

Polzin, K. L., Speer, K. G., Toole, J. M., and Schmitt, R. W. (1996). Intense mixing of Antarctic Bottom Water in the equatorial Atlantic Ocean. *Nature*, 380(6569):54–57.

Polzin, K. L., Toole, J. M., Ledwell, J. R., and Schmitt, R. W. (1997). Spatial variability of turbulent mixing in the abyssal ocean. *Science*, 276(5309):93–96.

Polzin, K. L., Toole, J. M., and Schmitt, R. W. (1995). Finescale parameterizations of turbulent dissipation. *Journal of Physical Oceanography*, 25(3):306–328.

Rimac, A., von Storch, J.-S., and Eden, C. (2016). The total energy flux leaving the ocean's mixed layer. *Journal of Physical Oceanography*.

Rimac, A., von Storch, J.-S., Eden, C., and Haak, H. (2013). The influence of high-resolution wind stress field on the power input to near-inertial motions in the ocean. *Geophysical Research Letters*, 40(18):4882–4886.

Roquet, F., Wunsch, C., and Madec, G. (2011). On the patterns of wind-power input to the ocean circulation. *Journal of Physical Oceanography*, 41(12):2328–2342.

Rousseau, S., Kunze, E., Dewey, R., Bartlett, K., and Dower, J. (2010). On turbulence production by swimming marine organisms in the open ocean and coastal waters. *Journal of Physical Oceanography*, 40(9):2107–2121.

Saenko, O. A. and Merryfield, W. J. (2005). On the effect of topographically enhanced mixing on the global ocean circulation. *Journal of Physical Oceanography*, 35(5).

Saenz, J. A., Hogg, A. M., Hughes, G. O., and Griffiths, R. W. (2012). Mechanical power input from buoyancy and wind to the circulation in an ocean model. *Geophysical Research Letters*, 39(13):L13605.

Sandström, J. W. (1908). Dynamische versuche mit meerwasser. *Annalen der Hydrographie und Maritimen Meteorologie*, 36:6–23.

Schmit, R. W., Toole, J. M., Koehler, R. L., Mellinger, E. C., and Doherty, K. W. (1988). The development of a fine- and microstructure profiler. *Journal of Atmospheric and Oceanic Technology*, 5(4):484–500.

Schmitt, R. W. (1994). Double diffusion in oceanography. *Annual Review of Fluid Mechanics*, 26(1):255–285.

Scott, J. R., Marotzke, J., and Adcroft, A. (2001). Geothermal heating and its influence on the meridional overturning circulation. *Journal of Geophysical Research*, 106(C12):31141–31154.

Scott, R. B., Goff, J. A., Naveira Garabato, A. C., and Nurser, A. J. G. (2011). Global rate and spectral characteristics of internal gravity wave generation by geostrophic flow over topography. *Journal of Geophysical Research*, 116(C9).

Scott, R. B. and Xu, Y. (2009). An update on the wind power input to the surface geostrophic flow of the World Ocean. *Deep Sea Research*, 56(3):295–304.

Sheen, K. L., Brearley, J. A., Naveira Garabato, A. C., Smeed, D. A., Waterman, S., Ledwell, J. R., Meredith, M. P., St. Laurent, L., Thurnherr, A. M., Toole, J. M., and Watson, A. J. (2013). Rates and mechanisms of turbulent dissipation and mixing in the Southern Ocean: Results from the Diapycnal and Isopycnal Mixing Experiment in the Southern Ocean (DIMES): Turbulent Dissipation Results from Dimes. *Journal of Geophysical Research*, 118(6):2774–2792.

Simmons, H. L., Jayne, S. R., Laurent, L. C., and Weaver, A. J. (2004). Tidally driven mixing in a numerical model of the ocean general circulation. *Ocean Modelling*, 6(3-4):245–263.

Sinnett, G. and Feddersen, F. (2014). The surf zone heat budget: The effect of wave heating. *Geophysical Research Letters*, 41(20):7217–7226.

Smith, W. H. F. and Sandwell, D. T. (1997). Global sea floor topography from satellite altimetry and ship depth soundings. *Science*, 277(5334):1956–1962.

St. Laurent, L. C., Simmons, H. L., and Jayne, S. R. (2002). Estimating tidally driven mixing in the deep ocean. *Geophysical Research Letters*, 29(23).

Stein, C. A. and Stein, S. (1992). A model for the global variation in oceanic depth and heat flow with lithospheric age. *Nature*, 359(6391):123–129.

Stigebrandt, A. (1979). Observational evidence for vertical diffusion driven by internal waves of tidal origin in the Oslofjord. *Journal of Physical Oceanography*, 9(2):435–441.

Stommel, H. (1958). The abyssal circulation. *Deep Sea Research*, 5(1):80–82.

Sugimoto, N. and Plougonven, R. (2016). Generation and backreaction of spontaneously emitted inertia-gravity waves. *Geophysical Research Letters*, 43(7):3519–3525.

Talley, L. (2013). Closure of the global overturning circulation through the Indian, Pacific, and Southern Oceans: Schematics and transports. *Oceanography*, 26(1):80–97.

Talley, L. D., Reid, J. L., and Robbins, P. E. (2003). Data-based meridional overturning streamfunctions for the global ocean. *Journal of Climate*, 16(19):3213–3226.

Thiffeault, J.-L. and Childress, S. (2010). Stirring by swimming bodies. *Physics Letters A*, 374(34):3487–3490.

Toggweiler, J. R. and Samuels, B. (1993a). Is the magnitude of the deep outflow from the Atlantic Ocean actually governed by Southern Hemisphere winds? In Heimann, M., editor, *The Global Carbon Cycle*, number 15 in NATO ASI Series, pages 303–331. Springer Berlin Heidelberg.

Toggweiler, J. R. and Samuels, B. (1993b). New radiocarbon constraints on the upwelling of abyssal water to the ocean's surface. In Heimann, M., editor, *The Global Carbon Cycle*, number 15 in NATO ASI Series, pages 333–366. Springer Berlin Heidelberg.

Toggweiler, J. R. and Samuels, B. (1995). Effect of drake passage on the global thermohaline circulation. *Deep Sea Research*, 42(4):477–500.

Toggweiler, J. R. and Samuels, B. (1998). On the ocean's large-scale circulation near the limit of no vertical mixing. *Journal of Physical Oceanography*, 28(9):1832–1852.

Toole, J. M., Schmitt, R. W., and Polzin, K. L. (1994). Estimates of diapycnal mixing in the abyssal ocean. *Science*, 264(5162):1120–1123.

Townsend, A. A. (1965). Excitation of internal waves by a turbulent boundary layer. *Journal of Fluid Mechanics*, 22(02):241–252.

Vanneste, J. (2013). Balance and spontaneous wave generation in geophysical flows. *Annual Review of Fluid Mechanics*, 45(1):147–172.

Visser, A. W. (2007). Biomixing of the oceans? *Science*, 316(5826):838.

von Storch, J.-S., Sasaki, H., and Marotzke, J. (2007). Wind-generated power input to the deep ocean: An estimate using a 1/10-degree general circulation model. *Journal of Physical Oceanography*, 37(3):657–672.

Walin, G. (1982). On the relation between sea-surface heat flow and thermal circulation in the ocean. *Tellus*, 34(2):187–195.

Wang, W. and Huang, R. X. (2004a). Wind energy input to the Ekman layer. *Journal of Physical Oceanography*, 34(5):1267–1275.

Wang, W. and Huang, R. X. (2004b). Wind energy input to the surface waves. *Journal of Physical Oceanography*, 34(5):1276–1280.

Waterhouse, A. F., MacKinnon, J. A., Nash, J. D., Alford, M. H., Kunze, E., Simmons, H. L., Polzin, K. L., St. Laurent, L. C., Sun, O. M., Pinkel, R., Talley, L. D., Whalen, C. B., Huussen, T. N., Carter, G. S., Fer, I., Waterman, S., Naveira Garabato, A. C., Sanford, T. B., and Lee, C. M. (2014). Global patterns of diapycnal mixing from measurements of the turbulent dissipation rate. *Journal of Physical Oceanography*, 44(7):1854–1872.

Webb, D. J. and Suginohara, N. (2001). Oceanography: Vertical mixing in the ocean. *Nature*, 409(6816):37–37.

Williams, P. D., Haine, T. W. N., and Read, P. L. (2008). Inertia–gravity waves emitted from balanced flow: Observations, properties, and consequences. *Journal of the Atmospheric Sciences*, 65(11):3543–3556.

Wright, C. J., Scott, R. B., Furnival, D., Ailliot, P., and Vermet, F. (2013). Global observations of ocean-bottom subinertial current dissipation. *Journal of Physical Oceanography*, 43(2):402–417.

Wunsch, C. (1998). The work done by the wind on the oceanic general circulation. *Journal of Physical Oceanography*, 28(11):2332–2340.

Wunsch, C. and Ferrari, R. (2004). Vertical mixing, energy, and the general circulation of the oceans. *Annual Review of Fluid Mechanics*, 36(1):281–314.

Zhai, X., Johnson, H. L., and Marshall, D. P. (2010). Significant sink of ocean-eddy energy near western boundaries. *Nature Geoscience*, 3(9):608–612.

CHAPTER

I On the consumption of Antarctic Bottom Water in the abyssal ocean

For the ocean to achieve a steady state, all water masses must be consumed at the same rate they are produced. Although a complete steady state is never achieved, an approximate balance between the formation and destruction of main water masses would be expected to establish under relatively stable climatic conditions. More simply, the observation that oceanic flows frequently cross salinity, temperature or density isosurfaces implies that some degree of water mass modification maintains property gradients along flow paths. In particular, the northward flow of Antarctic Bottom Water (AABW) in the abyssal ocean coexists with a northward descent and ultimate grounding of density surfaces, indicating that lightening occurs along its northward path. However, the rates of, and processes contributing to, AABW lightening are not clearly identified and quantified.

Two main complementary approaches have been followed to estimate the abyssal cross-density circulation. First, inversions of ship-based hydrographic observations taken along basin sections have been used to estimate transports through these sections and across density layers (e.g., Talley et al. 2003; Ganachaud and Wunsch 2000; Lumpkin and Speer 2007; Talley 2013; Naveira Garabato et al. 2014). These large-scale budgets provide guiding ranges for the AABW flow rate and its overall density transformation, but do not provide information on individual process contributions nor on regional patterns.

A second, forward approach consists in estimating the cross-density transports implied by specified sources of density transformation. Adding process-based sources of density transformation in global ocean models allows to quantify process contributions and their non-linear interplay in a self-consistent manner, bearing in mind inevitable limitations of the numerical ocean laboratory. This strategy has been adopted by many authors, exploring for example the impact of geothermal heat fluxes (Adcroft et al. 2001; Emile-Geay and Madec 2009), breaking internal tides (Simmons et al. 2004; Saenko and Merryfield 2005; Oka and Niwa 2013; Melet et al. 2016), breaking lee waves (Melet et al. 2014) or cabbeling and thermobaricity (Iudicone et al. 2008a; Klocker and McDougall 2010). Alternatively, the cross-density circulation can be diagnosed analytically by applying the same process-specific sources of density transformation to an observational climatology, with the advantage of avoiding model representation issues but with the drawback of losing interactivity. Emile-Geay and Madec (2009), Klocker and McDougall (2010) and Nikurashin and Ferrari (2013) employed this strategy to assess the roles of geothermal heating, along-density mixing and breaking internal waves, respectively. However, differing methodologies disallow a straightforward comparison of process contributions across the latter studies.

In this chapter, following Iudicone et al. (2008b), we present a unified framework to assess water mass transformation in the ocean interior, accounting for non-linearity in the equation of state and the presence of bottom geothermal heat fluxes. Applying this framework to an observational climatology and recent estimates of density fluxes induced by internal wave-driven mixing and geothermal heating, we bring together different process contributions and answer questions regarding the Nikurashin and Ferrari (2013) estimate. We confirm the significant role of geothermal heating (Emile-Geay and Madec 2009) but disprove the estimated foremost role of local, bottom-intensified internal tide and lee wave breaking (Nikurashin and Ferrari 2013) for the AABW circulation. We further highlight the key role of the vertical structure of local and basin-wide density fluxes in setting the strength and patterns of abyssal upwelling.

On the Consumption of Antarctic Bottom Water in the Abyssal Ocean

CASIMIR DE LAVERGNE

Sorbonne Universités (University Pierre et Marie Curie Paris 6)-CNRS-IRD-MNHN, LOCEAN Laboratory, Paris, France

GURVAN MADEC

Sorbonne Universités (University Pierre et Marie Curie Paris 6)-CNRS-IRD-MNHN, LOCEAN Laboratory, Paris, France, and National Oceanography Centre, Southampton, United Kingdom

JULIEN LE SOMMER

CNRS-Université Grenoble Alpes, Laboratoire de Glaciologie et Géophysique de l'Environnement, Grenoble, France

A. J. GEORGE NURSER

National Oceanography Centre, Southampton, United Kingdom

ALBERTO C. NAVEIRA GARABATO

University of Southampton, National Oceanography Centre, Southampton, United Kingdom

(Manuscript received 24 September 2014, in final form 24 November 2015)

ABSTRACT

The abyssal ocean is primarily filled by cold, dense waters formed around Antarctica and collectively referred to as Antarctic Bottom Water (AABW). At steady state, AABW must be consumed in the ocean interior at the same rate it is produced, but how and where this consumption is achieved remains poorly understood. Here, estimates of abyssal water mass transformation by geothermal heating and parameterized internal wave–driven mixing are presented. This study uses maps of the energy input to internal waves by tidal and geostrophic motions interacting with topography combined with assumptions about the distribution of energy dissipation to evaluate dianeutral transports induced by breaking internal tides and lee waves. Geothermal transformation is assessed based on a map of geothermal heat fluxes. Under the hypotheses underlying the constructed climatologies of buoyancy fluxes, the authors calculate that locally dissipating internal tides and geothermal heating contribute, respectively, about 8 and 5 Sverdrups (Sv; $1\,\mathrm{Sv} \equiv 10^6\,\mathrm{m^3\,s^{-1}}$) of AABW consumption (upwelling), mostly north of 30°S. In contrast, parameterized lee wave–driven mixing causes significant transformation only in the Southern Ocean, where it forms about 3 Sv of AABW, decreasing the mean density but enhancing the northward flow of abyssal waters. The possible role of remotely dissipating internal tides in complementing AABW consumption is explored based on idealized distributions of mixing energy. Depending mostly on the chosen vertical structure, such mixing could drive 1 to 28 Sv of additional AABW upwelling, highlighting the need to better constrain the spatial distribution of remote dissipation. Though they carry large uncertainties, these climatological transformation estimates shed light on the qualitative functioning and key unknowns of the diabatic overturning.

1. Introduction

The abyssal ocean is primarily filled by Antarctic Bottom Water (AABW), a cold, dense water mass produced around Antarctica that spreads northward to cover most of the World Ocean floor (Johnson 2008). While sinking and spreading along the seabed, the densest, newly formed AABW entrain and mix with ambient Southern Ocean waters to reach a maximum northward flow of about 20–30 Sverdrups (Sv; $1\,\mathrm{Sv} \equiv 10^6\,\mathrm{m^3\,s^{-1}}$) near 30°S (Ganachaud and Wunsch 2000; Lumpkin and Speer 2007; Talley et al. 2003; Talley 2008, 2013). To close the abyssal overturning circulation and reach a steady state, the northward-flowing AABW

Corresponding author address: Casimir de Lavergne, LOCEAN Laboratory, 4 Place Jussieu, F-75005 Paris, France.
E-mail: casimir.delavergne@gmail.com

DOI: 10.1175/JPO-D-14-0201.1

must gain buoyancy and upwell across isopycnals in the Pacific, Indian, and Atlantic basins. In the deep ocean, this buoyancy gain can only be achieved through two processes: mixing and geothermal heating. Were the cold bottom waters not consumed by such diabatic processes, they would gradually fill the whole ocean interior. In contrast, the overlying, southward-flowing deep waters may upwell mostly adiabatically in the Antarctic Divergence, allowing their consumption to rely largely on near-surface transformation (Toggweiler and Samuels 1995; Talley 2013).

Downward diffusion of buoyancy by turbulent mixing is considered to be the dominant mechanism allowing for AABW consumption and, thereby, for the maintenance of the abyssal stratification (Munk and Wunsch 1998; Wunsch and Ferrari 2004). The required diapycnal mixing is thought to be primarily driven by the breaking of internal waves. These ubiquitous waves in the ocean interior derive their energy from winds and tides and generate turbulence when they become unstable and break (Garrett and Munk 1979). Baroclinic tide and lee wave generation by tidal and geostrophic flows impinging on rough topography are among the most significant sources of internal wave energy for the deep ocean (Egbert and Ray 2000; Garrett and St. Laurent 2002). Some of these internal waves tend to break near their generation sites and contribute to mixing in the near field, whereas low-mode waves are able to propagate over large distances and may dissipate in the far field (St. Laurent and Garrett 2002).

According to a recent calculation (Nikurashin and Ferrari 2013), mixing driven by locally dissipating internal tides and lee waves is able to drive 25 Sv of AABW upwelling globally and could therefore account for the full strength of the abyssal overturning. Yet, experiments with ocean general circulation models (OGCM) have shown less of an impact of parameterized near-field mixing from internal tides and lee waves: only about 5 and 2 Sv of additional abyssal flow was simulated with the successive inclusion of near-field tidal mixing and lee wave–driven mixing (Simmons et al. 2004; Saenko and Merryfield 2005; Melet et al. 2014). In a recent OGCM study (Oka and Niwa 2013), it was suggested that the addition of far-field tidal mixing—that is, mixing driven by remotely dissipating internal tides—is key in simulating a Pacific overturning circulation of realistic strength. Meanwhile, although most studies focus on diapycnal mixing as the main buoyancy supply for AABW, geothermal heating was shown to be a rivalling heat source for the bottom-most waters of the ocean (Emile-Geay and Madec 2009). Indeed, it has been estimated that 2 to 6 Sv of abyssal flow may be sustained by geothermal heat fluxes alone (Adcroft et al. 2001; Hofmann and Morales Maqueda 2009; Emile-Geay and Madec 2009). These recent disparate results show that it remains largely unclear which processes control the strength of the lower branch of the overturning and how and where the diabatic return of northward-flowing bottom waters is accomplished.

In the past decades, much attention has been directed to the identification of mechanical energy sources able to sustain sufficient internal wave activity and deep mixing. Munk and Wunsch (1998) calculated that 2.1 TW are required to upwell 30 Sv of dense waters across isopycnals from 4000- to 1000-m depth. Considering that AABW need only upwell until it joins the southward adiabatic route to the Southern Ocean outcrop region (Talley 2013), this number could be substantially reduced. On the other hand, deep-ocean power availability from tides and lee-wave radiation has been estimated as 0.9–1.3 (Egbert and Ray 2000; Nycander 2005; Melet et al. 2013b) and 0.15–0.75 TW (Scott et al. 2011; Nikurashin and Ferrari 2011; Wright et al. 2014; Nikurashin et al. 2014), respectively. But though these global estimates of power availability and requirement may compare favorably, they do not discriminate between different water masses, despite different return pathways. Indeed, differing spatial distributions of wave-breaking energy can have radically different implications for ocean circulation (Simmons et al. 2004; Saenko et al. 2012; Oka and Niwa 2013).

The water mass transformation framework (Walin 1982; Nurser et al. 1999; Marshall et al. 1999; Iudicone et al. 2008b) enables us to translate the energy available for mixing into diapycnal transports that can be meaningfully compared to rates of dense water input. Here, we address some of the questions regarding AABW consumption by evaluating climatological rates of water mass conversion in the ocean interior by internal wave breaking and geothermal heating. We describe the water mass transformation framework and the dataset employed in the following section. In section 3, we outline some qualitative properties of dianeutral transports induced by mixing and geothermal heating and justify the choice of the 28.11 kg m^{-3} neutral surface as the upper boundary of AABW based on the climatological density structure of the ocean. Transformation estimates are presented in section 4. Results from earlier and present studies are compared and reconciled in section 5. Conclusions make up the last section. Further discussion on the role of nonlinearities in the equation of state and on the importance of hypsometry for water mass transformation can be found in appendixes A and B, respectively.

2. Methods

a. *Water mass transformation in the neutral density framework*

We denote by $K_\perp$ and $K_\parallel$ the turbulent diapycnal and isopycnal diffusivities, respectively. For a given oceanic

property λ, we define the diapycnal diffusive flux of λ as $F^{\lambda} = K_{\perp}\partial_{\perp}\lambda$, where $\partial_{\perp}$ is the gradient along the diapycnal direction. The isopycnal diffusive flux of λ is given by $K_{\parallel}\nabla_{\parallel}\lambda$, with $\nabla_{\parallel}$ as the spatial gradient in the tangent isopycnal plane. In a reference frame that follows instantaneous isopycnals and in the absence of external forcings from the surface, the rate of change of the locally referenced potential density ρ due to diffusive fluxes of Conservative Temperature Θ and Absolute Salinity S_A must be balanced by the advection across isopycnals (McDougall 1984; Iudicone et al. 2008b):

$$\omega\partial_{\perp}\rho = \partial_{\Theta}\rho[\partial_{\perp}F^{\Theta} + \nabla_{\parallel}\cdot(K_{\parallel}\nabla_{\parallel}\Theta)] + \partial_{S_A}\rho[\partial_{\perp}F^{S_A} + \nabla_{\parallel}\cdot(K_{\parallel}\nabla_{\parallel}S_A)], \quad (1)$$

where we have introduced the diapycnal velocity ω. Note that, by convention, the diapycnal axis is oriented from low to high density, so that $\omega > 0$ corresponds to transport toward greater densities. For brevity, Conservative Temperature and Absolute Salinity will be referred to simply as "temperature" and "salinity" in all the following.

Water mass transformation by isopycnal mixing was estimated by Iudicone et al. (2008a,b) and Klocker and McDougall (2010), who showed that isopycnal diffusion results in significant net densification in the Southern Ocean, contributing to the production of abyssal waters but not to their consumption. Here, we focus on the consumption of AABW by internal wave–driven diapycnal mixing and geothermal heating and only diagnose the contribution of diapycnal mixing terms to the diapycnal velocity:

$$\omega\partial_{\perp}\rho = \partial_{\Theta}\rho\partial_{\perp}F^{\Theta} + \partial_{S_A}\rho\partial_{\perp}F^{S_A}. \quad (2)$$

Since neutral surfaces are tangent to local isopycnal surfaces by construction, the diapycnal velocity ω equates the local dianeutral velocity (Jackett and McDougall 1997). By integrating ω over a given neutral surface $A(\gamma)$, with γ neutral density, one obtains the total dianeutral transport or transformation rate $T(\gamma)$ (Walin 1982):

$$T(\gamma) = \iint_{A(\gamma)} \omega\, dA = \iint_{A(\gamma)} (\partial_{\perp}\rho)^{-1}(\partial_{\Theta}\rho\partial_{\perp}F^{\Theta} + \partial_{S_A}\rho\partial_{\perp}F^{S_A})\, dA. \quad (3)$$

Equation (3), though exact and relatively simple, is difficult to implement in a discrete calculation. To avoid sampling issues, reduce data noise, and allow more detailed diagnostics, we take advantage of the global character of neutral density to propose an equivalent, more robust formulation for computing the dianeutral transports. Multiplying (2) by the factor $b = \partial_{\perp}\gamma/\partial_{\perp}\rho$ (Iudicone et al. 2008b), we obtain the neutral density balance

$$\omega\partial_{\perp}\gamma = b\partial_{\Theta}\rho\partial_{\perp}F^{\Theta} + b\partial_{S_A}\rho\partial_{\perp}F^{S_A}. \quad (4)$$

From here, two different directions may be taken.

The simplest approach consists of neglecting spatial variations of the coefficients $b\partial_{\Theta}\rho$ and $b\partial_{S_A}\rho$ (i.e., neglecting effects related to the nonlinearity of the equation of state), allowing the diapycnal velocity to be expressed as

$$\omega^{\mathrm{lin}} = (\partial_{\perp}\gamma)^{-1}\partial_{\perp}(b\partial_{\Theta}\rho F^{\Theta} + b\partial_{S_A}\rho F^{S_A}) = \partial_{\gamma}(b\partial_{\Theta}\rho F^{\Theta} + b\partial_{S_A}\rho F^{S_A}). \quad (5)$$

Noting that $b\partial_{\Theta}\rho F^{\Theta} + b\partial_{S_A}\rho F^{S_A} = bF^{\rho} = F^{\gamma}$, (5) reduces to $\omega^{\mathrm{lin}} = \partial_{\gamma}F^{\gamma}$, giving

$$T^{\mathrm{lin}}(\gamma) = \iint_{A(\gamma)} \partial_{\gamma}F^{\gamma}\, dA. \quad (6)$$

Since the area of integration $A(\gamma)$ depends on γ, care must be taken when moving the γ derivative in (6) outside of the integral. Consider a neutral density layer $V(\gamma_1, \gamma_2)$ defined by $\gamma_1 \le \gamma \le \gamma_2$ (Fig. 1). The layer will intersect the surface and bottom of the ocean over two distinct surfaces, which we denote by $O(\gamma_1, \gamma_2)$ and $I(\gamma_1, \gamma_2)$ and refer to as the outcrop and incrop surfaces, respectively. Together with $A(\gamma_1)$ and $A(\gamma_2)$, these surfaces bound the considered layer volume. Using these definitions and Leibniz's integral rule, we obtain

$$T^{\mathrm{lin}}(\gamma) = \partial_{\gamma}\iint_{A(\gamma)} F^{\gamma}\, dA + \partial_{\gamma}\iint_{O(\gamma,+\infty)} F^{\gamma}\, dA - \partial_{\gamma}\iint_{I(\gamma,+\infty)} F^{\gamma}\, dA. \quad (7)$$

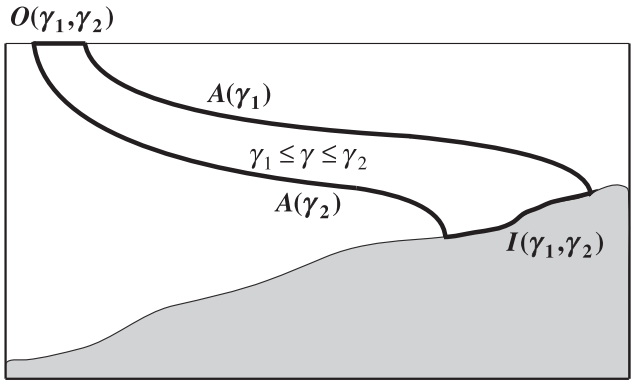

FIG. 1. Sketch of a neutral density layer $\gamma_1 \le \gamma \le \gamma_2$ bounded by neutral surfaces $A(\gamma_1)$ and $A(\gamma_2)$ and by its outcrop and incrop surfaces $O(\gamma_1, \gamma_2)$ and $I(\gamma_1, \gamma_2)$.

Note that $A(\gamma)$, $O(\gamma, +\infty)$, and $I(\gamma, +\infty)$ enclose the volume of waters denser than γ, so that, using Gauss's theorem, one may also recast T^{lin} in terms of the volume-integrated divergence of the neutral density flux F^{γ}:

$$T^{\text{lin}}(\gamma) = -\partial_{\gamma}\iiint_{V(\gamma,+\infty)} \partial_{\perp} F^{\gamma}\, dV. \tag{8}$$

The discrete form of (7) reads

$$\begin{aligned} T^{\text{lin}}(\gamma)\Delta\gamma = &\iint_{A[\gamma+(\Delta\gamma/2)]} F^{\gamma}\, dA - \iint_{A[\gamma-(\Delta\gamma/2)]} F^{\gamma}\, dA \\ &- \iint_{O[\gamma-(\Delta\gamma/2),\gamma+(\Delta\gamma/2)]} F^{\gamma}\, dA \\ &+ \iint_{I[\gamma-(\Delta\gamma/2),\gamma+(\Delta\gamma/2)]} F^{\gamma}\, dA, \end{aligned} \tag{9}$$

where $\Delta\gamma$ is a small but finite density step. Implementation of (9) now solely requires the specification of surface and bottom boundary conditions. Since we only consider mixing in the ocean interior, air–sea exchanges are excluded and our surface boundary condition is $F^{\Theta}|_{\text{surf}} = 0$ and $F^{S_A}|_{\text{surf}} = 0$, implying $F^{\gamma}|_{\text{surf}} = 0$. At the ocean bottom, the diffusive salinity flux must vanish, $F^{S_A}|_{\text{bot}} = 0$, but the diffusive temperature flux must meet the geothermal boundary condition $F^{\Theta}|_{\text{bot}} = Q_{\text{geo}}/(\rho c_p^0)$, where Q_{geo} (W m^{-2}) is the geothermal heat flux, and c_p^0 is the appropriate (constant) heat capacity. The transformation rate T^{lin} can then be decomposed into contributions of mixing and geothermal heating:

$$\begin{aligned} T^{\text{lin}}_{\text{mix}}(\gamma)\Delta\gamma = &\iint_{A[\gamma+(\Delta\gamma/2)]} F^{\gamma}\, dA \\ &- \iint_{A[\gamma-(\Delta\gamma/2)]} F^{\gamma}\, dA, \quad \text{and} \end{aligned} \tag{10}$$

$$\begin{aligned} T^{\text{lin}}_{\text{geo}}(\gamma)\Delta\gamma = &\iint_{I[\gamma-(\Delta\gamma/2),\gamma+(\Delta\gamma/2)]} F^{\gamma}\, dA \\ = &-\iint_{I[\gamma-(\Delta\gamma/2),\gamma+(\Delta\gamma/2)]} \frac{b\alpha Q_{\text{geo}}}{c_p^0}\, dA, \end{aligned} \tag{11}$$

where we have introduced the thermal expansion coefficient $\alpha = -\partial_{\Theta}\rho/\rho$ in (11). Note that, in view of the ocean aspect ratio, F^{γ} is very well approximated by $-K_{\perp}\partial_z\gamma$ (e.g., Iudicone et al. 2008b), where height z increases upward and has its origin at the surface. The term $T^{\text{lin}}_{\text{mix}}$ can therefore be computed as

$$\begin{aligned} T^{\text{lin}}_{\text{mix}}(\gamma)\Delta\gamma = &\iint_{A[\gamma-(\Delta\gamma/2)]} K_{\perp}\partial_z\gamma\, dA \\ &- \iint_{A[\gamma+(\Delta\gamma/2)]} K_{\perp}\partial_z\gamma\, dA. \end{aligned} \tag{12}$$

Nonlinearity in the equation of state need not be neglected, however. Noting again that diapycnal gradients are well approximated by vertical gradients, we can integrate the neutral density tendency at the right-hand side of (4) from the seafloor ($z = -H$) to the level of a given neutral surface [$z = z_{A(\gamma)}$] to obtain an equivalent diffusive flux of neutral density F^{γ}_{eq} across $A(\gamma)$:

$$F^{\gamma}_{\text{eq}}(\gamma) = -\int_{-H}^{z_{A(\gamma)}} [b\partial_{\Theta}\rho\partial_z(K_{\perp}\partial_z\Theta) + b\partial_{S_A}\rho\partial_z(K_{\perp}\partial_z S_A)]\, dz. \tag{13}$$

The flux F^{γ}_{eq} represents the actual neutral density flux crossing the surface $A(\gamma)$ as a result of turbulent diapycnal mixing of salinity and temperature below the level of $A(\gamma)$, accounting for the full nonlinearity of the equation of state. Equating $\partial_{\perp}$ with $-\partial_z$, we have by construction $\partial_{\perp}F^{\gamma}_{\text{eq}} = b\partial_{\Theta}\rho\partial_{\perp}F^{\Theta} + b\partial_{S_A}\rho\partial_{\perp}F^{S_A}$, so that (4) becomes $\omega = (\partial_{\perp}\gamma)^{-1}\partial_{\perp}F^{\gamma}_{\text{eq}} = \partial_{\gamma}F^{\gamma}_{\text{eq}}$ and

$$T(\gamma) = \iint_{A(\gamma)} \partial_{\gamma}F^{\gamma}_{\text{eq}}\, dA. \tag{14}$$

Replacing F^{γ} by F^{γ}_{eq} in (7)–(9) gives continuous and discrete equivalents of (14). The bottom boundary condition is unchanged and

$$T_{\text{geo}}(\gamma)\Delta\gamma = T^{\text{lin}}_{\text{geo}}(\gamma)\Delta\gamma = -\iint_{I[\gamma-(\Delta\gamma/2),\gamma+(\Delta\gamma/2)]} \frac{b\alpha Q_{\text{geo}}}{c_p^0}\, dA. \tag{15}$$

While surface diffusive fluxes of salinity and temperature remain set to zero, the equivalent surface flux of neutral density may now differ significantly from zero (mixing in the ocean interior may be a net source or sink of volume and of volume-integrated neutral density). The dianeutral transport induced by diapycnal mixing is thus obtained as

$$\begin{aligned} T_{\text{mix}}(\gamma)\Delta\gamma = &\iint_{A[\gamma+(\Delta\gamma/2)]} F^{\gamma}_{\text{eq}}\, dA \\ &- \iint_{A[\gamma-(\Delta\gamma/2)]} F^{\gamma}_{\text{eq}}\, dA \\ &- \iint_{O[\gamma-(\Delta\gamma/2),\gamma+(\Delta\gamma/2)]} F^{\gamma}_{\text{eq}}\, dA, \end{aligned} \tag{16}$$

where the last term's integrand is

$$F^{\gamma}_{\text{eq}}|_{\text{surf}} = -\int_{-H}^{0} [b\partial_{\Theta}\rho\partial_z(K_{\perp}\partial_z\Theta) + b\partial_{S_A}\rho\partial_z(K_{\perp}\partial_z S_A)]\, dz.$$

In practice, to avoid irrelevant nonlinear effects resulting from strong diffusivities but finite $\partial_{\Theta}\rho$ and $\partial_{S_A}\rho$ gradients in unstratified surface waters [see (20) and appendix A], the no-flux surface boundary condition ($F^{\Theta}|_{\text{surf}} = 0$ and $F^{S_A}|_{\text{surf}} = 0$) is matched by linearly

reducing F^{Θ} and F^{S_A} to zero from the base of the mixed layer to the surface. This procedure is justified since we are interested in interior rather than near-surface transformation, thus excluding mixed layer processes, and since diapycnal gradients may no longer be accurately diagnosed as vertical gradients within vanishing stratification.

For diagnostic purposes, it is useful to rewrite the dianeutral transports T_{mix} and T_{geo} as the γ derivative of a total buoyancy flux into the volume of waters denser than γ. From (7), we identify

$$T_{\text{geo}}(\gamma) = \partial_\gamma \iint_{I(\gamma,+\infty)} (-F^{\gamma}_{\text{eq}})\, dA, \quad \text{and} \tag{17}$$

$$T_{\text{mix}}(\gamma) = \partial_\gamma \iint_{A(\gamma)\cup O(\gamma,+\infty)} F^{\gamma}_{\text{eq}}\, dA. \tag{18}$$

In (17) and (18), $I(\gamma, +\infty)$ and $A(\gamma) \cup O(\gamma, +\infty)$ correspond to the areas bounding the volume $V(\gamma, +\infty)$ from below and from above, respectively.

b. Climatologies

Annual climatologies of the required hydrographic properties, including neutral density, are taken from the World Ocean Circulation Experiment hydrographic atlas (Gouretski and Koltermann 2004). All variables are computed according to the International Thermodynamic Equation of Seawater—2010 (TEOS-10) framework (McDougall and Barker 2011).

A climatological distribution of the energy lost to the internal wave field ε_T ($\mathrm{W\,kg^{-1}}$) is constructed from published estimates of energy fluxes into baroclinic tides (Nycander 2005; Melet et al. 2013b; Fig. 2a) and lee waves (Scott et al. 2011; Fig. 2b) combined with the near-field mixing parameterization of St. Laurent et al. (2002):

$$\varepsilon_T(x,y,z) = \frac{1}{\rho}[q_{\text{LW}}E_{\text{LW}}(x,y) + q_{\text{IT}}E_{\text{IT}}(x,y) + q_{\text{ITAH}}E_{\text{ITAH}}(x,y)]\frac{\exp\{[-H(x,y)-z]/\zeta\}}{\zeta\{1-\exp[-H(x,y)/\zeta]\}}. \tag{19}$$

Parameterization (19) assumes that a fixed fraction q of generated internal waves contributes to near-field mixing and that the dissipating energy decays exponentially from the seabed with an e-folding length ζ. Here, E_{LW}, E_{IT}, and E_{ITAH} ($\mathrm{W\,m^{-2}}$) designate the power input to internal waves by geostrophic currents impinging on small-scale topography and by barotropic tidal flows interacting with topographic features of horizontal scales larger (E_{IT}) and smaller (E_{ITAH}) than 10 km, respectively. Topographic roughness at scales smaller than 10 km is dominated by abyssal hills, and though it is not deterministically resolved in current global bathymetric products, its contribution to internal tide generation has been recently estimated (Melet et al. 2013b) following the methodology of Nycander (2005). The barotropic to baroclinic conversion by abyssal hill roughness, with a global energy flux of 0.1 TW, represents a nonnegligible contribution to tidal mixing and will therefore be included in our water mass transformation estimates. The q_{LW}, q_{IT}, and q_{ITAH} parameters represent the fraction of the predicted internal wave generation power that dissipates close to generation sites, assumed to be constant in space for each flux. In the case of lee waves, which are stationary and thereby expected to dissipate only in the near field, the choice of a coefficient $q_{\text{LW}} < 1$ is justified by observational (Sheen et al. 2013; Waterman et al. 2013, 2014) and modeling (Nikurashin and Ferrari 2010a,b; Nikurashin et al. 2014) results showing that the predicted energy fluxes (Scott et al. 2011) tend to overestimate the water column dissipation by about a factor of 3 to 10.

Falahat et al. (2014) calculated that, on a global average, the first two vertical normal modes take up 59% of the energy flux into internal tides. Since near-field dissipation is thought to be quasi negligible for the lowest two modes, this places an upper bound for q_{IT} at 41%. On the other hand, the global data analysis of Waterhouse et al. (2014) suggests a minimum of 20% of local internal tide dissipation. Because small-scale bathymetry tends to favor the generation of small-scale, high-mode waves, a somewhat larger portion of local dissipation should apply to internal tides generated by abyssal hills, so that $q_{\text{ITAH}} \sim 0.5$ may be considered a reasonable reference value (A. Melet 2014, personal communication). The parameter q_{LW} is less well constrained, with a probable range of about 0.1–0.5 (Nikurashin and Ferrari 2010a,b; Sheen et al. 2013; Waterman et al. 2013, 2014; Nikurashin et al. 2014). Near-field dissipation is generally observed to decrease away from the seafloor with a decay scale ranging roughly between 300 and 1000 m (St. Laurent et al. 2002; St. Laurent and Nash 2004; Nikurashin and Ferrari 2010a,b). To allow comparison with earlier studies, we choose typical values $q_{\text{LW}} = q_{\text{IT}} = 1/3$ and $\zeta = 500$ m, and we set $q_{\text{ITAH}} = 1/2$.

We note that both q and the vertical structure of local dissipation must vary regionally depending on topographic and oceanographic conditions (St. Laurent and Garrett 2002; St. Laurent and Nash 2004; Polzin 2009; Nikurashin and Ferrari 2010a,b; Nikurashin and Legg 2011; Waterman et al. 2013, 2014; Nikurashin et al. 2014; Falahat et al. 2014). Though the present choices for q_{LW}, q_{IT}, and q_{ITAH} aim to be representative of global

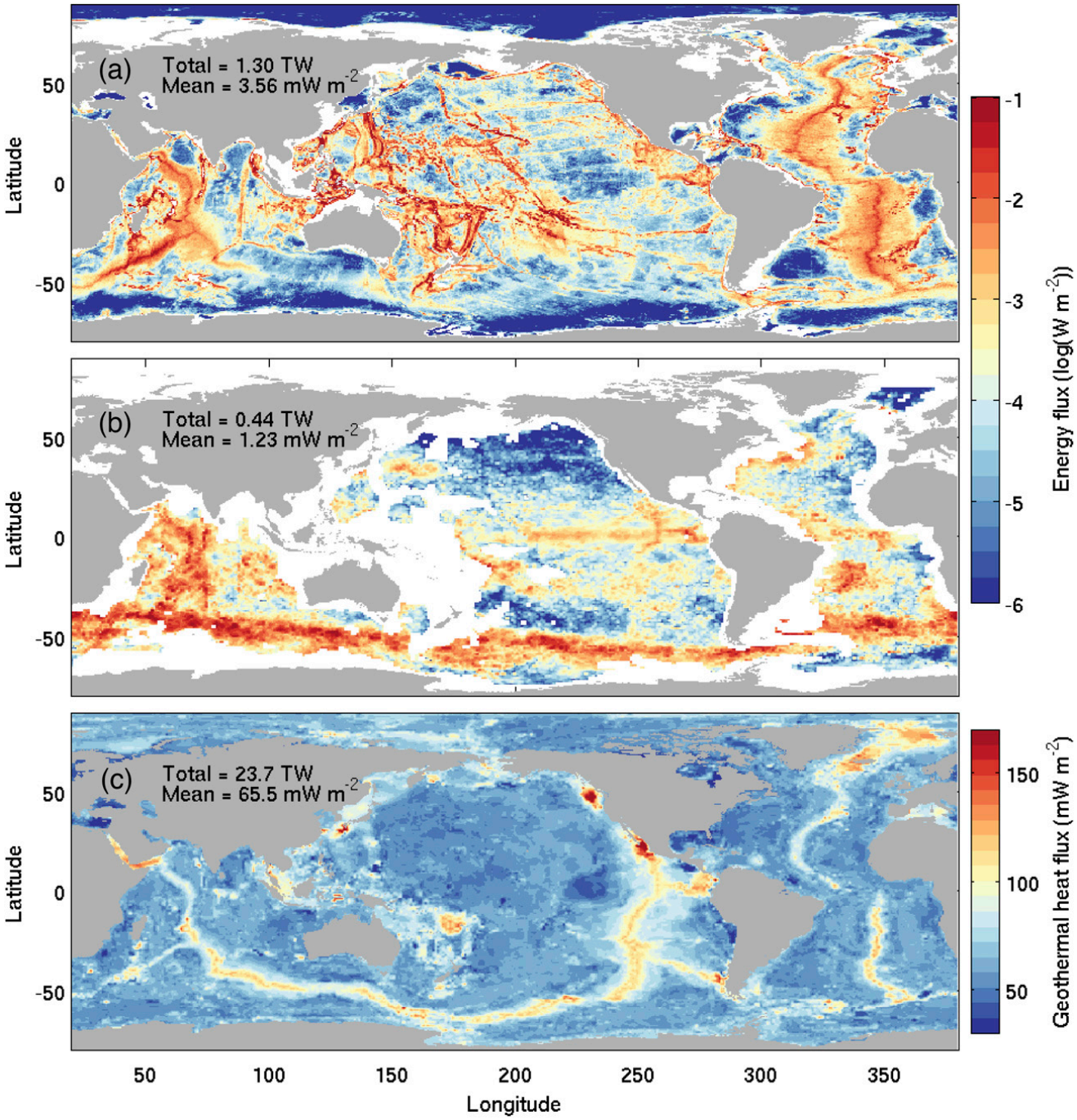

FIG. 2. Energy flux [log(W m^{-2})] into (a) internal tides (Nycander 2005; Melet et al. 2013b) and (b) lee waves (Scott et al. 2011). (c) Geothermal heat fluxes (mW m^{-2}) into the bottom ocean estimated by Goutorbe et al. (2011). Mean and globally integrated fluxes are indicated in the upper-left corner of each panel. The energy flux shown in (a) includes internal tide generation by topographic features with horizontal scales larger (Nycander 2005) and smaller (Melet et al. 2013b) than 10 km.

average values, they should be viewed as a somewhat arbitrary reference, facilitating comparison with earlier work (e.g., Simmons et al. 2004; Saenko and Merryfield 2005; Nikurashin and Ferrari 2013; Melet et al. 2014) while oversimplifying the energy partitioning of the real ocean. Nonetheless, the diagnosed dianeutral transports depend linearly on the chosen q values, and local-scale deviations from global averages should not strongly affect the general picture of the presented transformation estimates. On the other hand, because of the nonlinear dependence on ζ, we will examine the sensitivity of transformation rates to the vertical decay scale. Though we do not test alternative, nonexponential vertical distributions of local dissipation (e.g., Polzin 2009; Melet

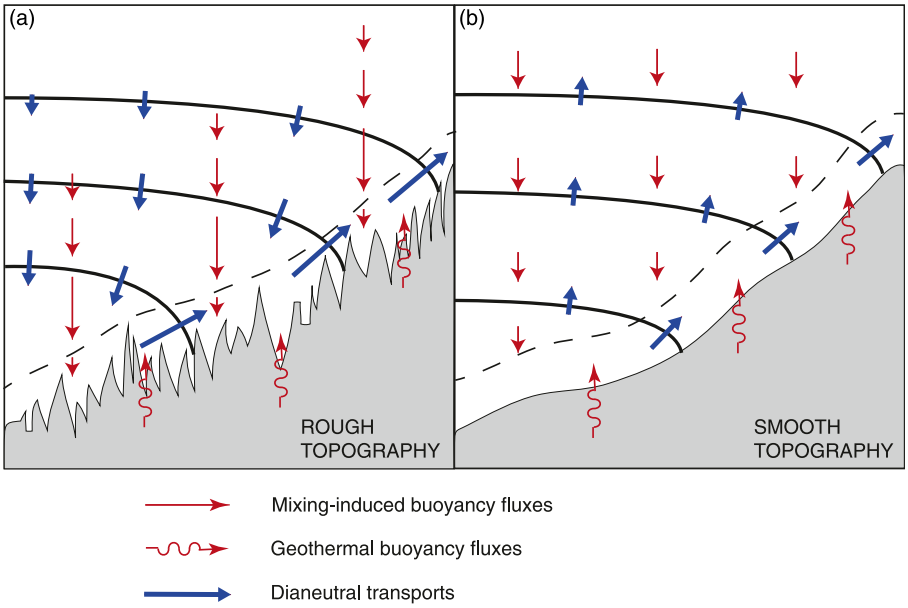

FIG. 3. Idealized schematic of local dianeutral transports induced by geothermal heat fluxes and internal wave breaking above (a) rough or (b) smooth bathymetry. In (a), the thin red arrows depict local downward buoyancy fluxes associated with bottom-intensified mixing parameterized by (19) and (20), accounting for their sharp decay in a relatively thin bottom layer (dashed line) of reduced mixing efficiency. The induced large-scale dianeutral transports (thick blue arrows) are directed toward higher (lower) density outside (within) the bottom layer. Thick black lines represent selected neutral surfaces. In (b), as a comparison example, buoyancy fluxes and dianeutral transports resulting from weaker internal wave activity and decreasing energy dissipation with depth are sketched. In this chosen situation, dianeutral upwelling occurs everywhere in the water column but preferentially along the seafloor. Note that we plot buoyancy fluxes as straight vertical arrows instead of dianeutral arrows so as to visualize the regions of divergent vs convergent buoyancy flux and to be consistent with the present methods where local density fluxes are approximated as vertical.

et al. 2013a), varying ζ should give some indication of the robustness of the diagnosed transports.

The turbulent diffusivity can be related to the buoyancy frequency $N^2 = -(g/\rho)\partial_z\rho$ and wave-breaking energy ε_T according to (Osborn 1980)

$$K_\perp N^2 = R_f \varepsilon_T, \tag{20}$$

where R_f is the mixing efficiency, taken to be one-sixth. Note that $R_f = 1/6$ corresponds to a flux coefficient $\Gamma = (K_\perp N^2)/(\varepsilon_T - K_\perp N^2) = 0.2$, the canonical upper-bound value postulated by Osborn (1980). Because mixing efficiency should approach zero in unstratified waters, we must remedy for unrealistically large values of the predicted eddy diffusivity in weak stratification. Therefore, following Simmons et al. (2004), $K_\perp$ is computed as

$$K_\perp = \min\left\{\left[\frac{R_f \varepsilon_T}{\max(N^2, 10^{-8}\,\mathrm{s}^{-2})}\right], 10^{-2}\mathrm{m}^2\,\mathrm{s}^{-1}\right\}. \tag{21}$$

The spatial distribution of geothermal heat fluxes $Q_{\mathrm{geo}}(x, y)$ ($\mathrm{W\,m^{-2}}$; Goutorbe et al. 2011) is depicted in Fig. 2c. The flux Q_{geo} averages $65.5\,\mathrm{mW\,m^{-2}}$ in the ocean and represents a global energy flux of 23.7 TW. We note that this average heat supply is somewhat weaker than most earlier estimates (Stein and Stein 1992; Pollack et al. 1993; Huang 1999), which fall within $80–100\,\mathrm{mW\,m^{-2}}$, possibly owing to a low bias in young oceanic crust (Goutorbe et al. 2011). Therefore, the presented transformation estimate by geothermal heating is likely to be a lower bound.

3. Preliminary remarks

The near-field mixing parameterization given by (19) and (20) aims at mimicking bottom-intensified mixing by breaking internal waves over rough topography (St. Laurent et al. 2002). The increase of energy dissipation with depth implied by (19) has some implications for the associated buoyancy forcing and circulation, as illustrated in Fig. 3a. Starting from the advective–diffusive balance of (2) and neglecting diapycnal variations of the thermal expansion and haline contraction coefficients (a rough but not unreasonable approximation in the deep

ocean, which has relatively weak Θ, S_A variations; see appendix A), the velocity induced by diapycnal mixing may be approximated by

$$\omega = (\partial_\perp \rho)^{-1} \partial_\perp (K_\perp \partial_\perp \rho) \approx -\frac{1}{N^2} \partial_z (K_\perp N^2)$$
$$= -\frac{1}{N^2} \partial_z (R_f \varepsilon_T). \quad (22)$$

Since $R_f \varepsilon_T$ decays away from the bottom, $\omega > 0$ and mixing drives transport toward higher densities (which we will refer to as downwelling or downward transport for simplicity, although this transport is not necessarily vertical). Indeed, the downward buoyancy flux associated with upward-decaying ε_T is divergent, and the resultant increase in density must be compensated by downward advection across isopycnals. Yet, in the approximation of a linear equation of state and ignoring the geothermal heat source at the seabed, mixing can only redistribute buoyancy, and sinks and sources of buoyancy must balance each other. Because of the zero stratification of the bottom boundary layer and the no-flux bottom boundary condition, the downward buoyancy flux induced by diapycnal mixing $K_\perp N^2$ must vanish at the seabed, implying a strong convergence of the buoyancy flux in the vicinity of the seafloor (Ledwell et al. 2000; St. Laurent et al. 2001; Simmons et al. 2004; Melet et al. 2013a). When geothermal heating is taken into account, buoyancy convergence near the bottom is increased as the net downward diffusive buoyancy flux induced by mixing must eventually match an opposite sign, upward bottom buoyancy flux.

Thus, in the presence of geothermal heating and a bottom-intensified mixing energy according to (19) and (20), the bottommost waters gain buoyancy, whereas the overlying waters lose buoyancy. Note that increasing the vertical decay scale ζ of energy dissipation will not modify the regions of buoyancy loss and buoyancy gain but will slightly reduce the buoyancy gain near the seabed and spread the compensating buoyancy loss higher in the water column. Rather than triggering convective instability, this buoyancy transfer is cancelled by diapycnal advection, with relatively weak but widespread downwelling away from the seabed and strong upwelling along topographic features (Fig. 3a). This behavior has been noted in observations of enhanced abyssal mixing near rough topography, such as in the Brazil basin (Polzin et al. 1997; Ledwell et al. 2000; St. Laurent et al. 2001). Note that the bottom layer that concentrates buoyancy deposition is characterized by a vanishing mixing efficiency, reconciling (19) and (22) with $\omega < 0$ near the seafloor (St. Laurent et al. 2001).

An increase of internal wave energy dissipation with depth does not systematically characterize the deep ocean (e.g., Toole et al. 1994; Waterhouse et al. 2014). Indeed, observations of internal wave activity over smooth bathymetry generally show no significant bottom intensification of energy dissipation (Toole et al. 1994; Kunze and Sanford 1996; Polzin et al. 1997). The induced buoyancy flux may then decrease toward the seafloor, causing buoyancy gain and upwelling over a wider depth range away from the seabed (Fig. 3b). Yet, because of geothermal heating and the need for the diffusive buoyancy flux to vanish close to the seabed, waters banked along topographic slopes are likely to experience increased buoyancy gain relative to horizontally adjacent waters (Fig. 3b). This effect, related to hypsometry (the decrease of the ocean's horizontal area with depth), implies that upwelling may occur preferentially along the sloping topography even in the absence of enhanced wave breaking near the seafloor.

Several consequences may be drawn from the previous remarks. First, it can be hypothesized that global AABW consumption and upwelling occur primarily along the bottom topography. This hypothesis is consistent with suggestions that diabatic upwelling of dense waters is mostly confined to below the crests of the major topographic ridges (Lumpkin and Speer 2007; Huussen et al. 2012; Ferrari et al. 2014). A focused upwelling along topography implies in turn that the circulation induced by such mixing would be very different in a flat bottom ocean. Second, it can be expected that water masses covering the largest portions of the seabed will exhibit the strongest consumption rates or, to rephrase, that dianeutral upwelling will peak within the neutral density layer that has the largest incrop area. Indeed, two related effects combine to reinforce potential upwelling rates within density layers occupying a large seafloor area: increased exposure to near-bottom buoyancy deposition by abyssal mixing and geothermal heating and weak bottom diapycnal density gradients requiring strong velocities to balance the buoyancy gain.

The incrop area, defined by

$$\mathcal{J}(\gamma) = (1/\Delta\gamma) \iint_{I[\gamma-(\Delta\gamma/2),\gamma+(\Delta\gamma/2)]} dA\,,$$

is plotted in Fig. 4a. The term $\mathcal{J}(\gamma)$ exhibits a maximum at $\gamma = 28.20\,\mathrm{kg\,m^{-3}}$ within the Southern Ocean (thick red line) and a much stronger peak at $\gamma = 28.11\,\mathrm{kg\,m^{-3}}$ within the 30°S–67°N region (thick blue line). Consequently, dianeutral upwelling north of 30°S may be expected to peak at $\gamma = 28.11\,\mathrm{kg\,m^{-3}}$. In addition, mass conservation dictates that the surface of maximum dianeutral transport north of 30°S must correspond to the level of maximum cumulated northward dense water transport at 30°S, except for potential, small additional inflow of waters denser than $28.11\,\mathrm{kg\,m^{-3}}$ from the north (see Figs. 5a,b; Ganachaud and Wunsch 2000). In

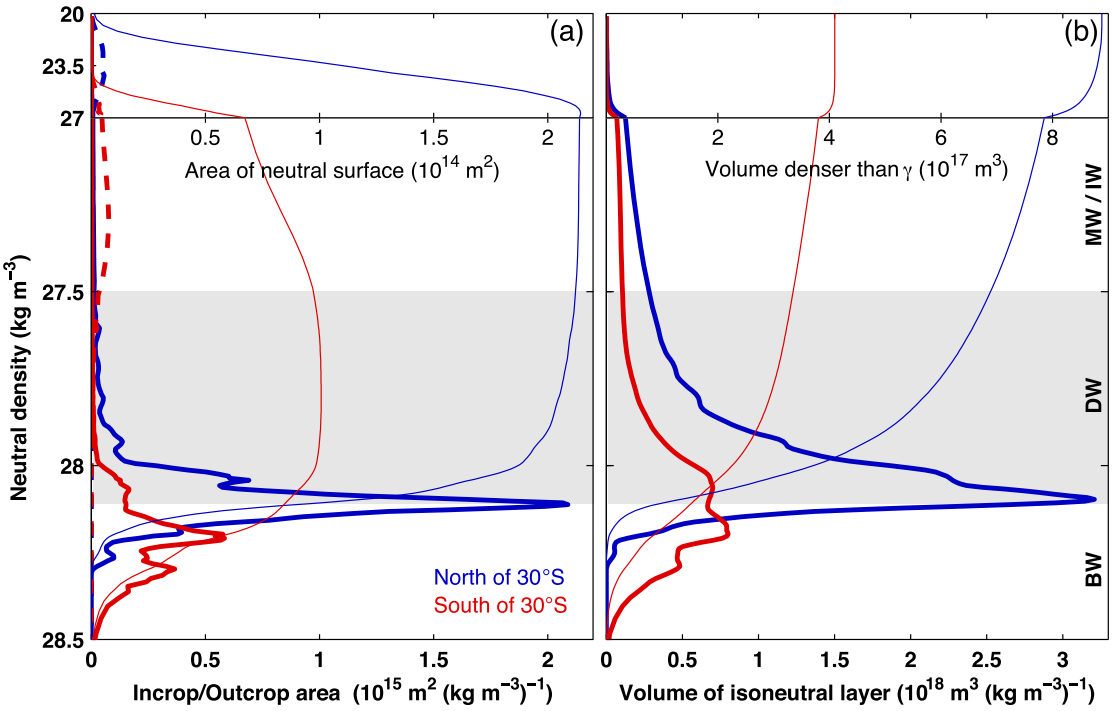

FIG. 4. Key characteristics of the climatological neutral density field, for ocean domains north (blue) and south (red) of 30°S. (a) Incrop (thick lines), outcrop (thick dashed lines), and neutral surface (thin lines) areas as a function of neutral density γ. (b) Isoneutral layer volume (thick lines) and volume of waters denser than γ (thin lines) as a function of neutral density γ. Note the different vertical scale above and below $\gamma = 27\,\mathrm{kg\,m^{-3}}$ and the upper x axis for thin lines. Neutral density ranges of bottom water (BW), deep water (DW), and mode/intermediate water (MW/IW) are indicated by the light gray shading and the right-side labels.

other words, if dianeutral transport north of 30°S peaks at $28.11\,\mathrm{kg\,m^{-3}}$, then the overturning streamfunction at 30°S should also peak near $28.11\,\mathrm{kg\,m^{-3}}$. Indeed, the $28.11\,\mathrm{kg\,m^{-3}}$ neutral surface is the approximate boundary between northward abyssal flow and southward deep-water flow at 30°S found by inverse studies (Ganachaud and Wunsch 2000; Lumpkin and Speer 2007), supporting our inference from the climatological density field. Defining the light end of AABW as the neutral density level at which the abyssal overturning streamfunction peaks, we will thus refer to AABW as waters characterized by $\gamma \geq 28.11\,\mathrm{kg\,m^{-3}}$.

A closer look at the latitudinal structure of the incrop area (Fig. 5a) reveals that $\sim 28.11\,\mathrm{kg\,m^{-3}}$ waters are in contact with the seafloor mostly in the Northern Hemisphere and that the maximum incrop area gradually moves toward lighter densities from south to north. (In Fig. 5a, the density-binned values of incrop area are reprojected to pseudodepth for visual purposes. The remapping procedure involves a simple bottom-up filling of each latitude band with ocean grid cells ordered from dense to light.) This supports the idea that the densest abyssal waters that cover the seafloor are gradually converted to lighter densities as they move northward. Preferential consumption of bottommost waters leads to progressive homogenization of AABW, reducing the abyssal stratification and thereby increasing the thickness and incrop area of the dominant neutral density layers (Figs. 4, 5). This in turn reinforces the efficiency of AABW consumption near the seabed, allowing potentially strong diabatic transport across the $28.11\,\mathrm{kg\,m^{-3}}$ neutral surface in northern basins.

4. Water mass transformation estimates

a. *Transformation by near-field mixing and geothermal heating*

1) LOCAL DIANEUTRAL TRANSPORTS

The spatial structure of dianeutral transports induced by locally dissipating internal tides, lee waves, and geothermal heating is illustrated in Figs. 6 and 7. Local dianeutral transports forced by mixing dominate those forced by geothermal heat fluxes (Fig. 6). Because lee-wave generation occurs mainly along the deep Southern Ocean floor, lee-wave-driven transformation appears dominated by a dipole of lightening below $28.15\,\mathrm{kg\,m^{-3}}$ and densification above. Internal tides are generated at various depths and densities, resulting in a more noisy

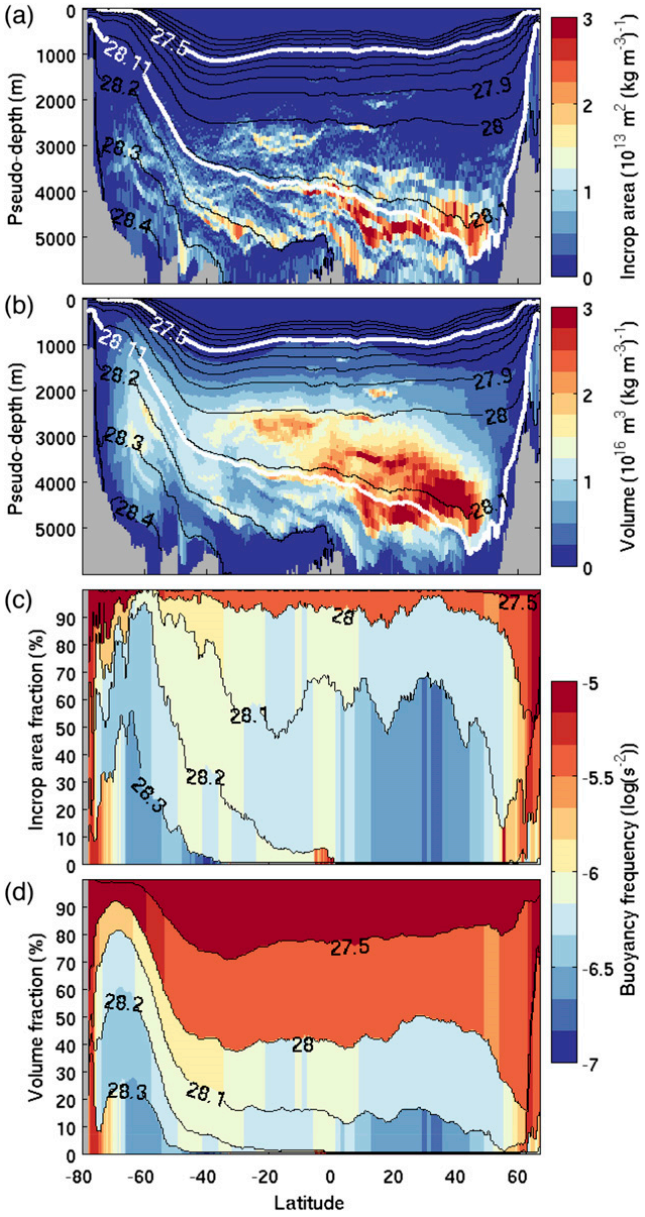

FIG. 5. (top) Along-isopycnal zonal sum of (a) incrop area and (b) isoneutral layer volume, where the density-binned values are reprojected to pseudodepth for visual purposes. The remapping procedure involves a simple bottom-up filling of each latitude band with ocean grid cells ordered from dense to light. Note that we use a variable density step $\Delta\gamma$ for appropriate sampling. (c),(d) Fraction of (c) seabed area and (d) ocean volume occupied by six neutral density layers and their volume-averaged stratification (shading) as a function of latitude, illustrating the gradual lightening and homogenization of AABW as it progresses northward. The Arctic Ocean and marginal seas are excluded from all calculations.

distribution of positive and negative transports. Whereas mixing transfers buoyancy across isoneutral layers, the geothermal heat flux causes only lightening and upward transport. In addition, the spatial pattern of the induced geothermal transports resembles closely that of the incrop area shown in Fig. 5a: geothermal heating consumes most efficiently water masses blanketing vast seafloor areas, so that dianeutral transports appear aligned along the 28.11 kg m^{-3} surface.

Figure 7 shows the horizontal pattern of upwelling and downwelling across specific neutral surfaces, chosen as the neutral density level of maximum net upwelling globally. Unsurprisingly, the level of maximum upwelling due to lee-wave breaking coincides with the peak incrop area south of 30°S ($\gamma = 28.20$ kg m^{-3}), while peak upwelling rates due to near-field tidal mixing and geothermal heating coincide with the peak incrop area north of 30°S ($\gamma = 28.11$ kg m^{-3}). Mixing driven by internal tides and lee waves results in downwelling across wide areas, including strong downwelling where the surface approaches the seafloor but upwelling where the neutral surface grounds. Geothermal heating acts only where the neutral density layer (of thickness $\Delta\gamma$) covers the ocean floor (Fig. 7c), which is also the area where near-field mixing causes upwelling (Fig. 7a). Upwelling across the 28.11 kg m^{-3} surface by geothermal heating and tidal mixing is concentrated on the sides of major oceanic ridges and along topographic slopes of the North Pacific.

2) TOTAL DIANEUTRAL TRANSPORTS

The water mass transformation rate as a function of neutral density is obtained by summing the local dianeutral transports over neutral surfaces (Fig. 8). The volume rate of water mass formation or consumption in a given density class [γ_1, γ_2] corresponds to the difference in transformation rates $T(\gamma_2) - T(\gamma_1)$. Any volume loss within one density class must be balanced by a volume gain in another density class.

Internal tides, lee waves, and geothermal heating have qualitatively different impacts on water mass transformation (Fig. 8a). Whereas geothermal heat fluxes induce only negative rates (buoyancy gain), diapycnal mixing must extract buoyancy from one water mass in order to supply buoyancy to another. This behavior is most clearly apparent in the lee-wave transformation curve, which exhibits a dipole of positive and negative transports: lee-wave-driven mixing is a net source (sink) of buoyancy for waters denser (lighter) than 28.15 kg m^{-3}. This results in the formation of 9 Sv of 28.05–28.20 kg m^{-3} waters, at the expense of denser and lighter water masses, which together lose volume at the same rate. In the case of baroclinic tides, buoyancy gain (upwelling) dominates for neutral densities greater than 27.20 kg m^{-3}, while buoyancy loss prevails for lighter waters. Indeed, the total downward buoyancy flux associated with near-field tidal mixing is convergent over most of the deep-ocean density range (Fig. 9a). In contrast, the buoyancy flux due to dissipating lee waves

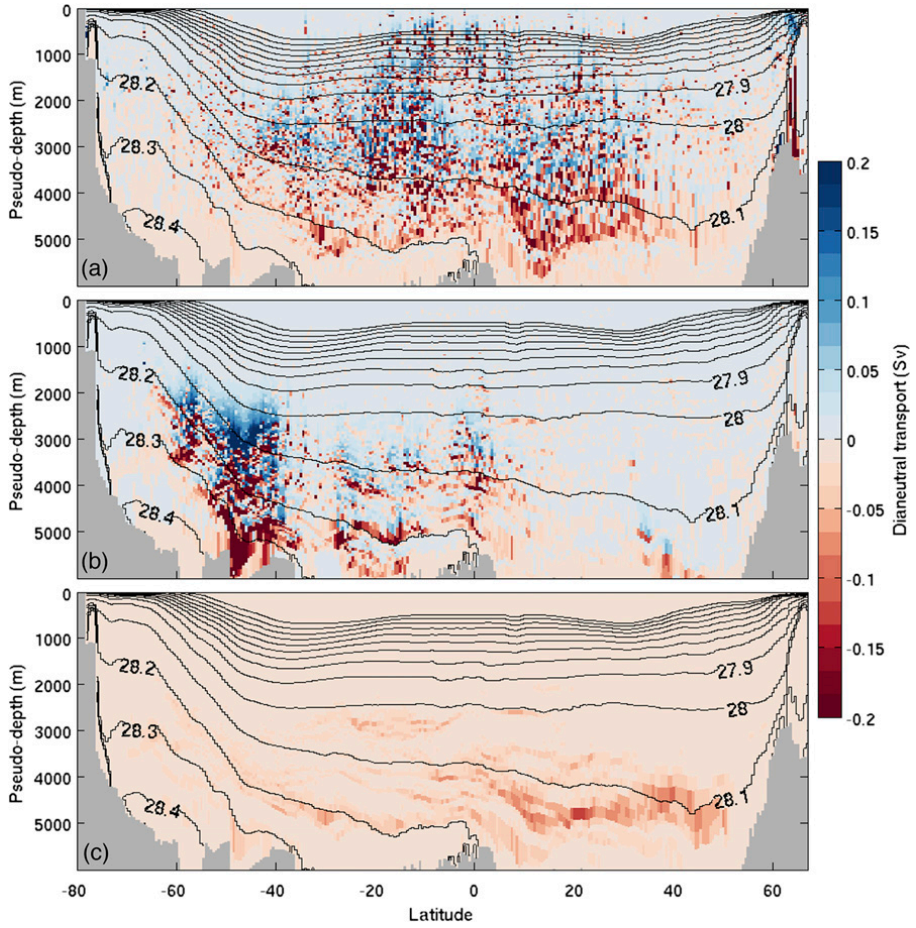

FIG. 6. Along-isopycnal zonal sum of dianeutral transports (Sv) induced by locally dissipating (a) internal tides and (b) lee waves and by (c) geothermal heating, where the density-binned values are reprojected to pseudodepth for visual purposes. Shaded cells depict the rate of upwelling (red) or downwelling (blue) within each neutral density layer and each latitude band.

peaks at 28.15 kg m^{-3}, well within the AABW layer (Fig. 9b).

Parameterized near-field tidal mixing drives ~9 Sv of upwelling across the 28.11 kg m^{-3} surface globally, of which 2 Sv are attributable to internal tides generated by abyssal hill roughness (Fig. 8a). Despite the relatively weak local transports due to geothermal heating (Figs. 6 and 7), its peak transformation rate of −5.5 Sv at γ = 28.11 kg m^{-3} is of comparable magnitude to the maximum upwelling rate due to locally dissipating internal tides. On the other hand, parameterized mixing from breaking lee waves results in net downwelling across the 28.11 kg m^{-3} surface, consuming about 6 Sv of waters denser than 28.20 kg m^{-3} but forming about 7 Sv of lighter AABW. Decomposing dianeutral transports between the Southern Ocean (80°S–30°S; Fig. 8c) and other basins (30°S–67°N; Fig. 8b) reveals that water mass transformation is dominated by tidal mixing and geothermal heating north of 30°S and by lee-wave-driven mixing south of 30°S. North of 30°S, tidal mixing and geothermal heating consume, respectively, about 8 and 5 Sv of AABW, whereas upwelling forced by lee waves remains weaker than 2 Sv, a contribution similar to that of internal tides generated by abyssal hills. Lee-wave-driven mixing is concentrated in the Antarctic Circumpolar Current (ACC), where it converts ~5 Sv of bottom waters heavier than 28.3 kg m^{-3} into lighter AABW and draws ~3 Sv of lighter, deep waters into the AABW density range. Hence, according to the present parameterization, mixing by breaking lee waves is little involved in the diabatic return of AABW flowing out of the Southern Ocean. Rather, it participates in the lightening of the densest AABW, while enhancing bottom-water flow by forming additional, lighter AABW prior to its escape into the Atlantic and Indo-Pacific basins.

The shape of the geothermal transformation and its narrow peak at 28.11 kg m^{-3} are not controlled by spatial contrasts in heat fluxes (Fig. 2c) but rather by the incrop area (Fig. 4a), as postulated in section 3 (see

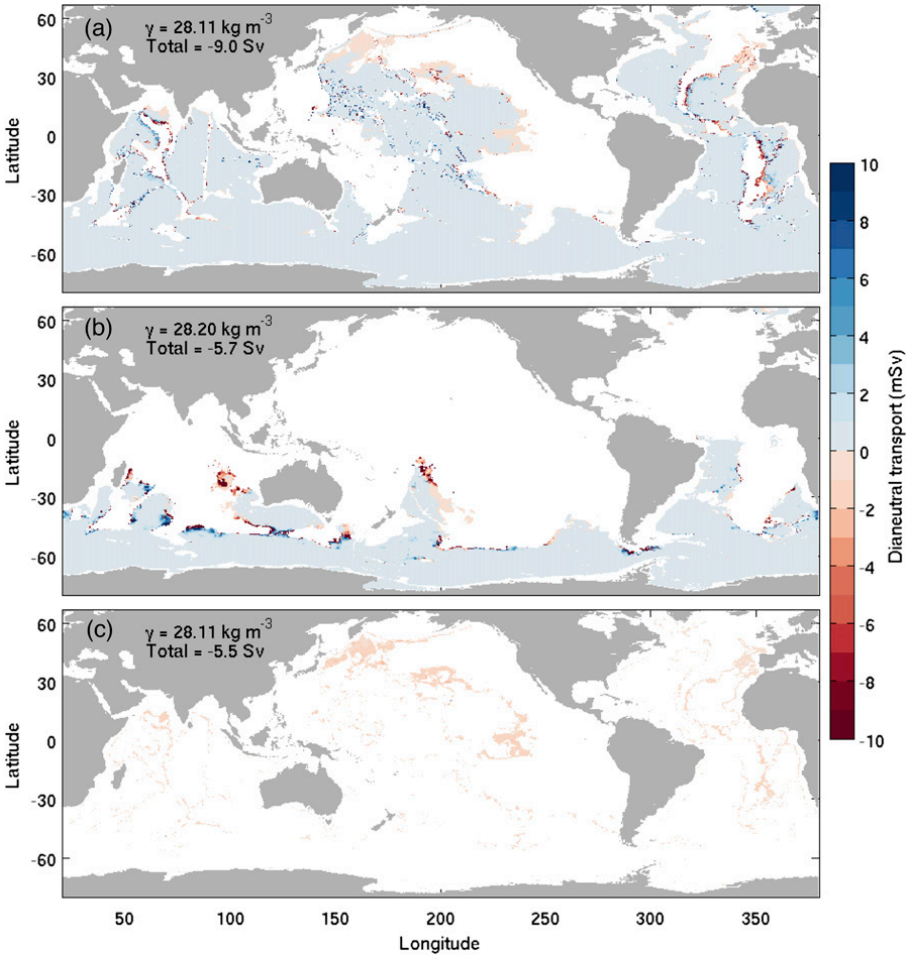

FIG. 7. Maps of dianeutral transport (mSv) induced by locally dissipating (a) internal tides and (b) lee waves and by (c) geothermal heating across neutral surfaces $\gamma = 28.11$, 28.20, and 28.11 kg m^{-3}, respectively. These neutral surfaces correspond to the respective density levels of maximum global upwelling. Mixing causes dianeutral transports toward both lighter (red) and denser (blue) water. Geothermal heating causes dianeutral transport toward lighter waters within the bottommost neutral density layer ($\Delta\gamma = 0.005$ kg m^{-3} at $\gamma = 28.11$ kg m^{-3}).

appendix B for further discussion). Similarly, the sharp decrease of the area of neutral surfaces at 28.11 kg m^{-3} (Fig. 4a), equivalent to the sharp peak of the incrop area, controls the peak tidal transformation by forcing a strong convergence of the total buoyancy flux near 28.11 kg m^{-3} (Fig. 9a). Hence, the concomitant maxima of geothermal and tidal transformations, and their correspondence with the approximate boundary between deep and bottom waters, must not be seen as fortuitous. Rather, a dynamic–thermodynamic equilibrium is reached in which AABW is gradually transformed into densities close to 28.11 kg m^{-3} as it progresses through the Southern Ocean and farther northward along the sea bottom, so that a voluminous, weakly stratified water mass occupies a vast portion of the World Ocean floor and maximizes its exposure to geothermal heating and abyssal mixing (Figs. 4, 5).

3) SENSITIVITY TO THE VERTICAL DECAY SCALE ζ

The overall efficiency of mixing energy in supplying buoyancy to the deep ocean depends on its distribution relative to the neutral density field and in particular on the degree of cancellation between convergent and divergent buoyancy fluxes. Parameterized near-field tidal mixing drives a net source of buoyancy over most of the ocean interior, fluxing buoyancy from the upper ocean down to deep and abyssal waters (Fig. 9a). On the other hand, because the energy of dissipating lee waves is placed at large depths (90% of the estimated lee-wave generation occurs below 3000 m), the resultant mixing is unable to bring heat from thermocline waters to the deep ocean (Fig. 9b). Nevertheless, the efficiency of buoyancy transfer from light to dense waters may be enhanced if the vertical decay scale ζ is increased, that is,

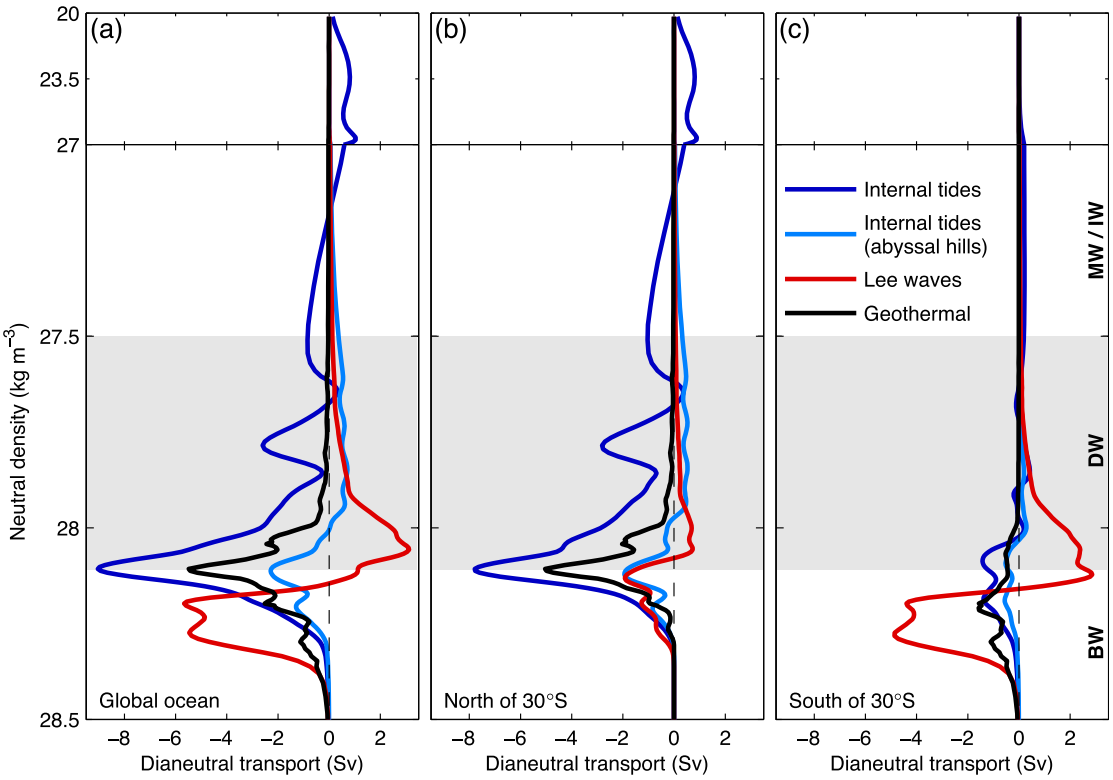

FIG. 8. Water mass transformation by near-field diapycnal mixing and geothermal heating. (a) Global, (b) 30°S–67°N, and (c) 80°–30°S dianeutral transports resulting from geothermal heating (black) and from near-field mixing by internal tides (blue), internal tides generated by abyssal hills only (pale blue), and lee waves (red). To minimize data noise resulting from the patchiness of mixing and induced transports (see Figs. 6 and 7), the transformation profiles shown are obtained using (17) and (18), where a small degree of smoothing is applied to the total buoyancy flux before taking the γ derivative. Note the different vertical scale above and below $\gamma = 27\,\mathrm{kg\,m^{-3}}$. Neutral density ranges of BW, DW, and MW/IW waters are indicated by the light gray shading and the right-end labels.

if internal wave energy tends to dissipate higher in the water column.

Figure 9 illustrates the sensitivity of transformation estimates to the ζ parameter. Different ζ values result in weak overall differences in buoyancy fluxes and dianeutral transports. A doubling of the decay scale increases the tidally driven buoyancy flux out of the thermocline and into the deep ocean, resulting in slightly greater upwelling rates within the 27–28.1 $\mathrm{kg\,m^{-3}}$ density range but virtually unchanged transformation within the AABW layer (Figs. 9a,d). Doubling ζ also slightly smoothens and shifts upward the peak buoyancy flux driven by lee waves, reducing downwelling across the deep/bottom-water boundary but leaving the transformation estimate largely unchanged (Figs. 9b,e). On the other hand, reducing the decay scale to 300 m tends to accentuate somewhat peak dianeutral transports, including a 1 Sv increase of tidally driven AABW consumption due to an increased buoyancy flux across $\gamma = 28.11\,\mathrm{kg\,m^{-3}}$ but deviations from the reference curve remain no greater than 2 Sv (Figs. 9a–f).

Hence, in our climatological setting, water mass transformation by near-field mixing is not set by the choice of vertical decay scale for energy dissipation but more so by the ocean's density structure and bathymetry, combined with the horizontal distribution of internal wave generation. While demonstrating the robustness of the present transformation estimates, this weak sensitivity contrasts with results from OGCM experiments showing enhanced abyssal flow under larger ζ (Saenko et al. 2012; Oka and Niwa 2013). The difference could arise from the response of stratification to mixing in numerical experiments: strong, focused, near-bottom mixing may weaken the simulated local stratification and ultimately reduce its ability to sustain a buoyancy flux.

b. *Transformation rates due to far-field mixing*

1) ENERGY DISTRIBUTION FOR REMOTE DISSIPATION

In the preceding subsection, we have examined transformation rates associated with the commonly used

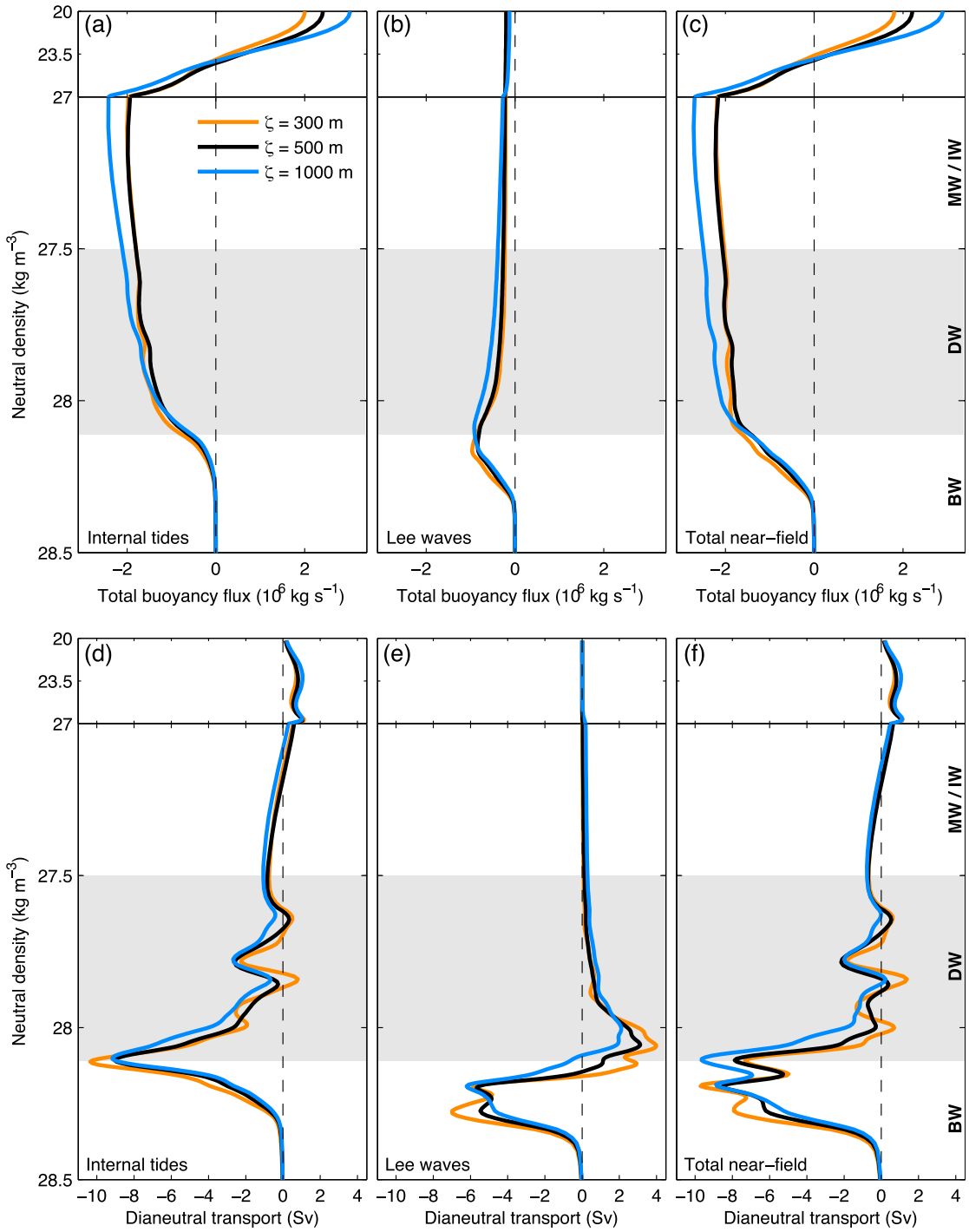

FIG. 9. Sensitivity of global water mass transformation by near-field mixing to the vertical decay scale of energy dissipation. Shown are (top) neutral density fluxes and (bottom) dianeutral transports induced by locally dissipating (a),(d) internal tides, (b),(e) lee waves, and (c),(f) both, using an e-folding length ζ of 300 (orange), 500 (black), and 1000 m (pale blue) in the vertical structure function of (19). Black curves correspond to the reference case shown in previous figures.

mixing parameterization for internal waves that dissipate near their generation sites. Because less is known about the dissipation of internal waves than about their generation, it is assumed that one-third of the wave energy dissipates where it is generated, while the other two-thirds are ignored or assumed to contribute to sustain a background vertical diffusivity of about $10^{-5}\,\mathrm{m^2\,s^{-1}}$ (St. Laurent et al. 2002; Simmons et al.

2004). Yet, using a map of the depth-integrated tidal energy dissipation diagnosed from global numerical simulations (Niwa and Hibiya 2011), Oka and Niwa (2013) recently extended the parameterization to include far-field tidal mixing. To specify the vertical structure of energy dissipation, the authors used an exponential decay from the bottom for the fraction q of locally dissipating energy but assumed a vertically uniform ε_T for remote dissipation.

To explore the implications of various assumptions about the distribution of far-field mixing energy, we calculate transformation rates due to remotely dissipating internal tides under various idealized scenarios. We construct two scenarios for the horizontal distributions of the energy flux $E_{\text{far-field}}(x, y)$ (W m^{-2}):

(Su) uniformly distributed energy over the whole ocean volume, where $E_{\text{far-field}}(x, y)$ is proportional to local water depth $H(x, y)$; and
(Sp) the horizontal spread of energy around generation sites, where $E_{\text{far-field}}(x, y)$ is obtained by uniformly redistributing the energy flux $(1 - q_{\text{IT}})E_{\text{IT}}(x, y) + (1 - q_{\text{ITAH}})E_{\text{ITAH}}(x, y)$ within a radius of 1000 km of each (x, y) grid point. This ad hoc procedure aims at grossly mimicking horizontal propagation of internal tide energy, as observed in maps produced by Niwa and Hibiya (2011).

Of particular interest for abyssal water mass transformation is the fraction of far-field energy dissipated in shallow versus deep areas of ocean basins. The percentage of mixing energy located in ocean areas deeper than 3000 m is 92% under scenario Su, dropping to 67% in scenario Sp. For comparison, the percentage of local tidal dissipation occurring within the same area is 30%. Both scenarios thus imply that far-field dissipation contributes more energy to deep oceanic regions than near-field dissipation, possibly departing from real conditions if most of the remote tidal dissipation was to occur at continental shelves and upper continental slopes (see, e.g., Nash et al. 2004; Martini et al. 2011; Kelly et al. 2013; Waterhouse et al. 2014). Nonetheless, the two distributions are sufficiently different that they should hint at the sensitivity to the fraction of remote dissipation taking place in shallow waters.

The vertical structure of energy dissipation is specified according to the following scenarios:

(S2) ε_T proportional to N^2, that is, constant $K_\perp$;
(S1) ε_T proportional to N, that is, $K_\perp$ proportional to N^{-1};
(S0) constant ε_T, that is, $K_\perp$ proportional to N^{-2}; and
(S−1) ε_T proportional to N^{-1}, that is, $K_\perp$ proportional to N^{-3}.

The numbering of the scenarios corresponds to exponents of N in the assumed dependence of dissipation to stratification. Scenario S2 is believed to be typical of nonlinear energy transfer and dissipation in a uniform internal wave field described by a Garrett–Munk spectrum (Garrett and Munk 1972; Müller et al. 1986) and was the form used by Koch-Larrouy et al. (2007). Scenario S1 corresponds to the vertical structure suggested by Gargett (1984) and subsequently used in ocean modeling (Cummins et al. 1990). Scenario S0 was used in simulations of Oka and Niwa (2013). Scenario S−1 is the only scenario for which the far-field energy dissipation increases with depth.

By combining the proposed horizontal and vertical distributions, we obtain eight scenarios with identical overall power available for mixing, equal to 0.85 TW. Scenario S2u (the combination of Su and S2) results in a globally uniform eddy diffusivity of 1.23×10^{-5} m^2 s^{-1}. We stress here that these scenarios are not meant to provide realistic parameterizations of far-field tidal mixing nor to span all possible outcomes for the energy of low-mode internal tides. Rather, they are meant to achieve preliminary understanding and to explore the sensitivity to key choices in constructing the energy distribution.

2) DIANEUTRAL TRANSPORTS

The resulting transformation curves are shown in Fig. 10. The differing horizontal distributions across scenarios Su (upper panels) and Sp (lower panels) have a relatively modest impact on water mass transformation north of 30°S (Figs. 10b,e). Significant qualitative differences appear only in the Southern Ocean, where the weak internal tide generation results in negligible mixing under scenario Sp but in significant mixing under Su (Figs. 10c,f). Yet, even under Su, Southern Ocean dianeutral transports induced by far-field tidal mixing remain quite weak overall, with peak upwelling rates not exceeding 6 Sv. Except under scenario S1u, for which far-field mixing drives 4 Sv of AABW consumption south of 30°S, AABW transformation in the Southern Ocean is dominated by the parameterized lee-wave dissipation. The weak Southern Ocean transports relative to those occurring north of 30°S can be largely explained by the stronger stratification of the Southern Ocean abyss and the associated lack of large incrop areas. In the following, we refer exclusively to dianeutral transports for the 30°S–67°N region (Figs. 10b,e).

North of 30°S, peak transformation rates tend to be enhanced under the uniform volume distribution Su compared with the horizontally spread distribution Sp, as might be expected from the former's greater power availability in the open ocean and over abyssal plains in particular. The transformation estimates remain qualitatively similar,

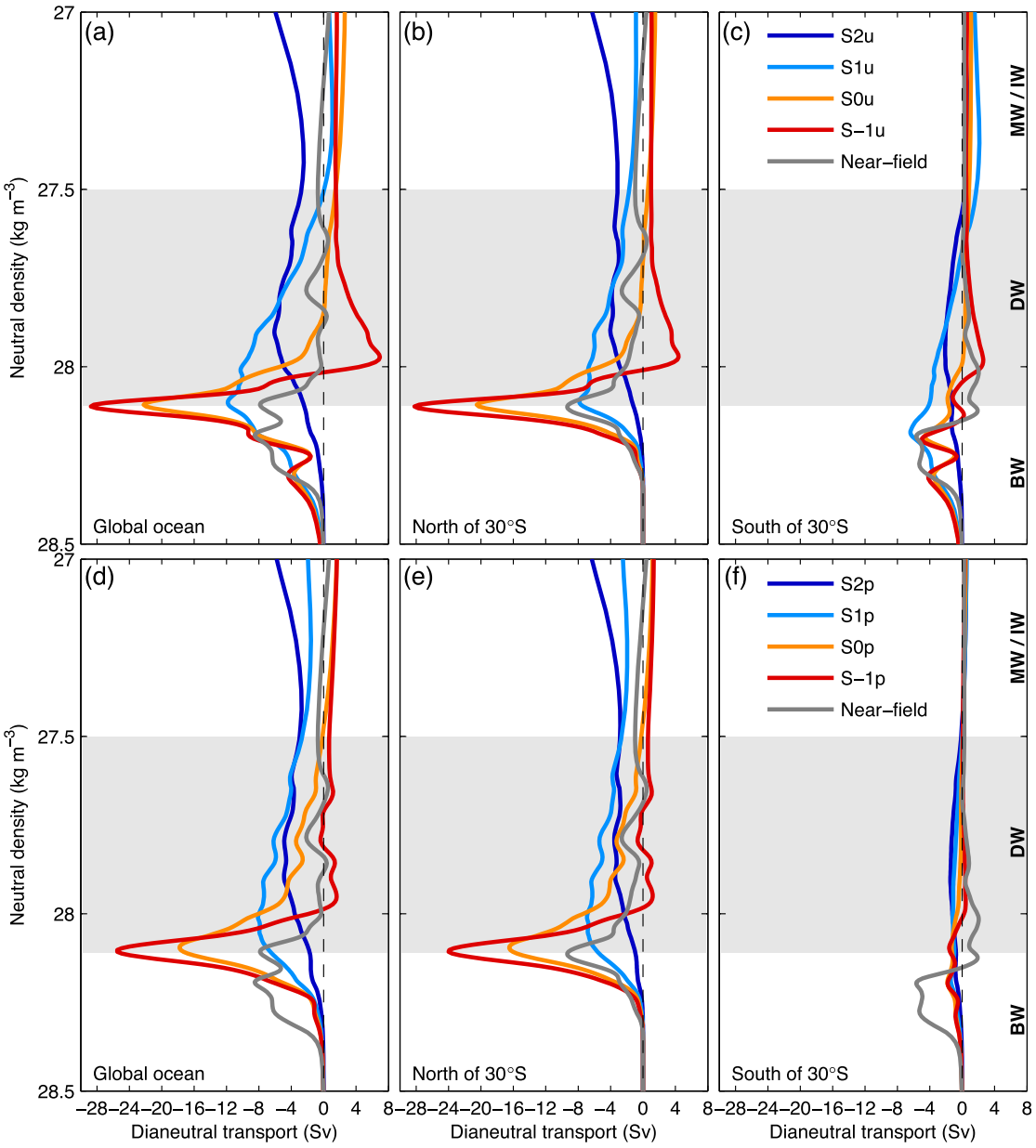

FIG. 10. Water mass transformation by far-field tidal mixing under eight idealized scenarios for (a),(d) global, (b),(e) 30°S–67°N, and (c),(f) 80°–30°S ocean domains. The horizontal energy distribution is specified according to assumption (top) Su or (bottom) Sp and the vertical energy structure scales either as N^2 (S2, blue), N (S1, pale blue), 1 (S0, orange), or $1/N$ (S−1, red). Transformation by near-field mixing (both lee waves and internal tides) is plotted in gray for comparison.

however, suggesting that the details of the horizontal distribution of the open-ocean dissipation are not crucial to the large-scale water mass conversion. In contrast, dianeutral transports forced by parameterized far-field mixing are strongly sensitive to the vertical structure given to energy dissipation.

The uniform diffusivity of scenario S2 results in ~3 Sv of upwelling within deep-water masses, but the upwelling rate drops to only 1 Sv at the deep/bottom-water boundary, implying negligible AABW consumption. Under scenario S1, a maximum dianeutral transport of −7 to −8 Sv appears at or near the 28.11 kg m^{-3} neutral density level, with gradually decreasing upwelling toward lighter and denser waters. Thus, under the assumption that remote dissipation scales as N, far-field mixing could balance a significant portion of the estimated northward abyssal flow at 30°S.

The vertically homogenous energy dissipation rate of scenario S0 has radically different implications for the overturning circulation. Indeed, aside from effects

associated with the nonlinearity of the equation of state (see appendix A for a discussion of these effects), a vertically uniform buoyancy flux implies that convergence occurs only at the seafloor, with no impact on the remainder of the water column except for compensating divergence at the surface. Thus, under such mixing, buoyancy is extracted at the base of the mixed layer and fluxed directly to the bottom boundary layer, with nonlinearity in the equation of state contributing some additional buoyancy loss in upper waters and some additional buoyancy gain at depths (appendix A). Consequently, the resultant water mass transformation displays a shape quite similar to that associated with geothermal heating, with upwelling reaching a maximum of 16–21 Sv at the boundary between deep and abyssal waters. Hence, given a constant mixing efficiency of one-sixth, 0.85 TW of uniformly distributed energy dissipation may provide for ~20 Sv of bottom-water consumption.

Even stronger AABW consumption can be obtained by applying a vertical profile of wave-breaking energy proportional to $1/N$ as assumed in scenario S−1. Here, efficient lightening of abyssal waters is achieved at the expense of waters lighter than 28 kg m^{-3}, most of which undergo densification. Dianeutral transport across $\gamma = 28.11$ kg m^{-3} reaches −23 Sv in S−1p and −28 Sv in S−1u. This scenario highlights the result that rates of deep-water mass conversion and the implied ocean circulation do not depend as much on the overall consumed power as they do on the spatial—and especially vertical—distribution of energy lost to the internal wave field.

In summary, by carrying energy away from major topographic features toward deeper parts of ocean basins, low-mode internal tides could be more efficient than their locally dissipating counterpart in supplying buoyancy to bottom water masses. However, the actual impact of low-mode internal tides on AABW consumption depends on the (largely unknown) location of their ultimate decay into small-scale turbulence. Results from the tested idealized scenarios suggest that the fraction of remote dissipation occurring in the open ocean and the vertical structure of the open-ocean dissipation are key uncertainties in the far-field energy distribution. Insignificant AABW consumption is to be expected if remote dissipation occurs primarily at continental margins or within the pycnocline, whereas a leading role of far-field tidal mixing in consuming AABW is possible if the associated mixing energy is more evenly distributed over the ocean's volume.

5. Relation with previous studies

a. *Diapycnal mixing*

The present transformation estimate due to near-field mixing is consistent with previous OGCM studies but inconsistent with the analogous estimate of Nikurashin and Ferrari (2013). We show that, excluding the added contribution of abyssal hill roughness, parameterized tidal mixing according to (19) and (21) drives the upwelling of 6 Sv of bottom waters north of 30°S, in broad agreement with a ~5-Sv enhancement of the lower branch of the overturning circulation in numerical experiments (Saenko and Merryfield 2005). Melet et al. (2014) show that including lee-wave radiation as a second source of mixing slightly strengthens the abyssal overturning and shifts it toward lower densities, a response that closely matches our results. In contrast, Nikurashin and Ferrari (2013) estimated that the local dissipation of baroclinic tide and lee-wave energy drives 16 and 9 Sv of global AABW upwelling, respectively. The discrepancy with the present estimate comes from the contribution of the bottom layer of buoyancy gain. Their calculation excluded the near-bottom convergence of the buoyancy flux so that their values reflect the global diabatic sinking rates of interior waters in response to the divergent buoyancy flux associated with depth-increasing dissipation (R. Ferrari and M. Nikurashin 2014, personal communication). Problematically, they seemed to imply that their estimates of interior transformation pertained to the upwelling rather than the downwelling of water masses. Our results are consistent with theirs for the interior transformation, but we find that the bottom layer contribution is as large and needs to be considered to compute the overall transformation rates. In particular, their estimate implied that both sources of mixing force net upwelling throughout the 27–28.5 kg m^{-3} neutral density range, whereas mixing due to breaking lee waves is expected to cause both negative and positive rates of transformation within this density range (Fig. 8). Given that other sources of mixing and buoyancy may contribute to AABW consumption, such as low-mode internal tides, geothermal heating, deep overflow mixing, or alternate dissipation routes of balanced flows, their values might also have appeared uncomfortably high.

Our idealized estimates of water mass transformation by far-field mixing shed light on the recent findings of Oka and Niwa (2013), who report a doubling of the simulated strength of the Pacific overturning circulation with the addition of vertically uniform dissipation for remotely breaking internal tides. It is shown that this assumption, a priori most simple, results in almost exclusive consumption of waters covering the seafloor, causing strong diabatic upwelling within the voluminous, weakly stratified water mass that occupies most of the seabed area of northern basins.

b. Geothermal heating

The role of geothermal heating in converting abyssal waters has been quantified in a manner consistent with that of diapycnal mixing and is shown to be non-negligible. This agrees with a previous water mass transformation estimate (Emile-Geay and Madec 2009) and with earlier numerical studies reporting a significant geothermal influence on the lower overturning cell and North Pacific abyssal temperatures (Adcroft et al. 2001; Hofmann and Morales Maqueda 2009; Emile-Geay and Madec 2009). Despite relatively weak local buoyancy fluxes, geothermal heating efficiently consumes the thick, homogenous water mass that covers large seafloor areas of the North Pacific and eastern Atlantic (Fig. 7c). With about 5 Sv of induced AABW upwelling across the 28.11 kg m^{-3} neutral surface north of 30°S, geothermal heating almost rivals parameterized near-field tidal mixing in maintaining the northward AABW flow out of the Southern Ocean. This result suggests that geothermal heat fluxes have a nonnegligible part in the energy flows that sustain the abyssal overturning. The respective roles of diapycnal mixing and geothermal heating for ocean energetics can be compared by calculating their potential energy supply to the global ocean (e.g., Huang 1999; Nycander et al. 2007):

$$\partial_t E_p = g \iiint \partial_t \rho z \, dV, \tag{23}$$

$$(\partial_t E_p)_{\text{geo}} = g \iint_{I(0,+\infty)} \left(\frac{-Q_{\text{geo}} \alpha}{c_p^0} \right) (-H) \, dA, \quad \text{and} \tag{24}$$

$$(\partial_t E_p)_{\text{mix}} = g \iiint [\partial_\Theta \rho \partial_\perp F^\Theta + \partial_{S_A} \rho \partial_\perp F^{S_A}] z \, dV, \tag{25}$$

where no-flux surface and bottom boundary conditions must be applied in (25), as required for interior mixing alone. Equating $\partial_\perp$ with $-\partial_z$ and integrating by parts, (25) may be rewritten as

$$(\partial_t E_p)_{\text{mix}} = \iiint \rho K_\perp N^2 \, dV + g \iiint [F^\Theta \partial_z (\partial_\Theta \rho) + F^{S_A} \partial_z (\partial_{S_A} \rho)] z \, dV,$$

showing that $(\partial_t E_p)_{\text{mix}}$ differs from $\iiint \rho K_\perp N^2 \, dV = \iiint \rho R_f \varepsilon_T \, dV$ when accounting for spatial variations in $\partial_\Theta \rho$ and $\partial_{S_A} \rho$.

Near-field mixing parameterized by (19) and (21) supplies potential energy at a total rate of 97 GW, with internal tides and lee waves contributing 64 and 33 GW, respectively. The geothermal contribution is of comparable magnitude, amounting to 35 GW. Geothermal heating efficiently raises the ocean's center of mass by supplying buoyancy directly to the ocean bottom. On the other hand, of the 600 GW of internal wave energy assumed to be lost near generation sites, only 16.2% is ultimately converted to potential energy. This percentage, though close to $R_f = 1/6$ in the present case, needs not be equal to the assumed mixing efficiency because of nonlinearity in the equation of state (which contributes −5 and +9 GW in the potential energy supply by internal tides and lee waves, respectively) and because of the upper-bound imposed on vertical diffusivity (which induces a net total loss of 7 GW). Note that the $1 - R_f$ fraction of lee-wave and internal tide energy that dissipates through viscosity represents a quasi-negligible heat source for the ocean, with a total heat supply of 1.45 TW comparing to 23.7 TW of geothermal input globally.

6. Conclusions

A hydrographic climatology and estimates of available power from lee and tidally generated internal waves and from geothermal heating have been used to quantify rates of water mass transformation in the ocean interior. It was shown that parameterized near-field mixing under typical assumptions cannot account for the full strength of the abyssal overturning. The specified local dissipation of internal tide energy consumes about 8 Sv of AABW north of 30°S. Breaking lee waves, most energetic in the Southern Ocean, instead precondition abyssal waters prior to their escape north of the ACC, reducing their density but increasing their northward volume transport. In addition, geothermal heating, estimated to sustain about 5 Sv of AABW flow, was found to be a significant component of the abyssal overturning.

High mixing rates observed or inferred to prevail in the deep Southern Ocean (Olbers and Wenzel 1989; Heywood et al. 2002; Naveira Garabato et al. 2004; Sloyan 2005; Kunze et al. 2006) are often suggested to contribute prominently to the diabatic closure of the abyssal overturning circulation (Ito and Marshall 2008; Nikurashin and Ferrari 2013). However, inverse estimates and model simulations generally show an increase of the maximum northward abyssal flow as AABW crosses the ACC (e.g., Lumpkin and Speer 2007; Jayne 2009; Melet et al. 2014), indicating that the ACC is most likely a positive contributor to the northward dense water volume transport. This picture is consistent with isoneutral mixing (Iudicone et al. 2008a,b; Klocker and McDougall 2010) and near-field diapycnal mixing representing net sources of waters denser than 28.11 kg m^{-3} in the ACC region. We show that parameterized lee-wave-driven mixing, which largely dominates the estimated total water mass transformation by near-field

mixing and geothermal heating in the Southern Ocean, has an ambiguous role on the diabatic return of AABW; as well as augmenting the AABW input to northern basins, lee-wave radiation contributes to the homogenization of AABW and so facilitates its subsequent consumption by tidal mixing and geothermal heating. Additionally, we stress that diapycnal mixing can densify a water mass if the associated downward buoyancy flux is divergent within its density range; in particular, parameterized near-field mixing is a buoyancy sink for 27.7–28.15 $\mathrm{kg\,m^{-3}}$ waters in the Southern Ocean. A portion of Lower Circumpolar Deep Water, mainly of North Atlantic origin, may thus be transformed into denser AABW class waters by topographically enhanced mixing in the ACC, short-circuiting the overturning from the upper to the lower branch (Naveira Garabato et al. 2007). This short circuit could provide for some of the interior consumption of deep waters and further intertwines both branches of the circulation.

Given fixed spatial distributions of energy dissipation and geothermal heat fluxes, the density field and topography of the ocean exert strong controls on the implied water mass transformation. Density classes that cover large portions of the seafloor are ideally placed to receive buoyancy from overlying water masses and the solid Earth through abyssal mixing and geothermal heating. In the present climate, AABW, which covers roughly two-thirds of the sea bottom (Fig. 5c; Johnson 2008), and its most voluminous variety ($\gamma \approx 28.11\,\mathrm{kg\,m^{-3}}$) in particular are most efficiently consumed by such diabatic processes. Yet, under a different climate, rates of water mass transformation by geothermal heating and near-field mixing may strongly deviate from the present estimates. For instance, the geothermal circulation would be reduced in a more stratified abyssal ocean because individual density layers would have access to narrower seabed areas or, equivalently, because the stronger density gradients would require weaker dianeutral advection to balance the geothermal buoyancy gain (Emile-Geay and Madec 2009). In addition, if AABW upwelling is mostly confined to actively mixing ocean boundaries, the height distribution of the topographically complex seafloor may provide a strong constraint on the vertical extent and overall strength of the abyssal overturning.

Conversely, given fixed ocean topography and density structure, as well as fixed overall power available for mixing, transformation rates strongly depend on the specified spatial distribution of energy sinks. The vertical structure of the energy lost to the internal wave field has particularly important implications. In the deep ocean, away from strong gradients of the thermal expansion coefficient, an increasing mixing energy with depth implies mostly buoyancy gain within a thin bottom layer and buoyancy loss elsewhere, driving strong, localized upwelling along topography. In contrast, a mixing energy that decreases with depth distributes buoyancy more evenly over the water column, driving only upward deep transport. On the other hand, a vertically homogenous mixing energy is highly efficient at driving a diabatic abyssal circulation, acting somewhat like a geothermal heat flux for the abyss and selectively consuming waters draping the ocean floor.

Important limitations to the present work must be underlined. First, uncertainty in the abyssal stratification, inherent to the sparse observations available at abyssal depths and especially close to the seabed, is a significant source of uncertainty for the estimated transformation rates. Second, the parameterization of near-field mixing relies on simplifying assumptions about the fraction of local internal wave dissipation, taken to be globally uniform for each wave type, and its vertical distribution, uniformly specified as an exponential decay from the bottom. In particular, the q_{LW} parameter and the overall amount of lee-wave dissipation remain poorly constrained so that the estimated transformation by breaking lee waves should be regarded as qualitatively representative of the real ocean but quantitatively accurate only to within a factor of ~3. On the other hand, the uncertainty in tidally forced dianeutral transports associated with q_{IT} and q_{ITAH} values is estimated to be a factor of ~1.5. Nonetheless, the impact of spatial variability in the mode partitioning of internal tide generation deserves further investigation. Third, presently used maps of internal wave generation rates contain uncertainty, primarily associated with imperfect knowledge of bathymetry and bottom flows and with shortcomings of the linear wave theory (Nycander 2005; Scott et al. 2011; Melet et al. 2013b), which may introduce further errors in the constructed dissipation fields. Inaccuracies in the field of geothermal heat fluxes (Goutorbe et al. 2011) could also bias the geothermal transformation estimate. However, it is the relatively well-constrained background flux of about 55 $\mathrm{mW\,m^{-2}}$, typical of abyssal plains, together with incrop areas that controls peak geothermal transports (see appendix B). Therefore, we do not expect uncertainties in geothermal heat fluxes to translate into strong biases in geothermal transformation rates. Next, it was assumed that one-sixth of the energy lost to the internal wave field contributes to irreversible mixing, except when this assumption led to unrealistic vertical diffusivities ($>100\,\mathrm{cm^2\,s^{-1}}$). Although the present assumption of a constant mixing efficiency allowed comparison with earlier studies, refinements could be considered in

future work (e.g., St. Laurent et al. 2001; Melet et al. 2013a). Fifth, as opposed to numerical experiments, such static, climatological transformation estimates prohibit the response of stratification to vertical mixing and geothermal heating. In particular, this approach masks possible incompatibilities between the observed stratification and the estimated mixing levels, such as may result from overestimated mixing efficiencies. Further, the climatological approach neglects possible time correlations between fluctuations of hydrographic properties and mixing rates at the resolved spatial scales. Last, the present estimates do not allow quantification of the interplay between different processes. What would be the induced geothermal circulation if no mixing from lee waves and internal tides had contributed to shape the observed bottom density distribution? Such questions may find answers in OGCM studies (Emile-Geay and Madec 2009).

Nevertheless, we note that the climatological dianeutral transports diagnosed here are in broad agreement with earlier results from OGCM simulations using similar parameterizations or geothermal forcing (e.g., Simmons et al. 2004; Saenko and Merryfield 2005; Emile-Geay and Madec 2009; Oka and Niwa 2013; Melet et al. 2014), lending support to our conclusions. Such consistency also suggests that water mass transformation estimates provide a powerful tool to test parameterizations of diapycnal mixing and anticipate their impact on the simulated water mass structure and overturning circulation.

Whereas observations suggest a total AABW input to the Pacific, Indian, and Atlantic basins of about 20–30 Sv (Ganachaud and Wunsch 2000; Lumpkin and Speer 2007; Talley et al. 2003; Talley 2008, 2013), hereinestimated contributions of near-field mixing and geothermal heating only sum to about 15 Sv of AABW upwelling north of 30°S. Far-field mixing from the breakdown of low-mode internal tides radiating away from generation sites could provide the required additional buoyancy supply. However, how and where nonlocal energy dissipation occurs is still largely unknown, so that gross assumptions must be made to represent this source of mixing (Oka and Niwa 2013). We explored the potential contribution of far-field mixing to deep-water mass conversion using idealized distributions of mixing energy. Depending mostly on the assumed vertical energy profile, AABW upwelling rates of 1 to 28 Sv were found compatible with a global power consumption of 0.85 TW. Such different rates of transformation imply radically different overturning circulations, highlighting the need for better constraints on the vertical distribution of remote energy dissipation and, ultimately, for an accurate three-dimensional mapping of energy sinks. Other sources of mixing also require quantification. In particular, turbulence and entrainment in narrow passages, known to be important controls on the abyssal density distribution, could also be important contributors to AABW consumption (Polzin et al. 1996; Thurnherr and Speer 2003; Bryden and Nurser 2003; Thurnherr et al. 2005; Huussen et al. 2012). Candidate sources of mixing energy for the abyss also include the loss of balance of meso- to large-scale motions as they develop frontal instabilities near topography (Zhai et al. 2010; Dewar et al. 2011) or in the interior (Molemaker et al. 2010).

Despite the limitations and uncertainties attached to the present transformation estimates and the correspondingly incomplete closure of the AABW life cycle, a qualitative picture of the diabatic, abyssal branch of the overturning can be proposed based on previously established and present results:

1) Intense buoyancy loss near Antarctica drives gravitational sinking of cold, relatively fresh surface waters. Aided by thermobaricity in their descent (Killworth 1977; McPhee 2003), the sinking waters entrain surrounding waters, thereby increasing the dense water input to the deep Southern Ocean (Orsi et al. 2002).
2) Mixing with ambient waters and topographic constraints contribute to reduce the density of abyssal waters allowed to enter the ACC (Orsi et al. 1999; Johnson 2008).
3) Further mixing occurs within the ACC, where turbulence from breaking lee waves consumes some of the densest AABW but also converts some of the overlying Circumpolar Deep Water into AABW class waters.
4) A fairly homogenous, weakly stratified bottom-water mass is transported northward into the Indo-Pacific and Atlantic basins at a rate of about 20–30 Sv. As it progresses and recirculates along the seafloor and through constrictive passages, AABW undergoes further homogenization and gradually gains buoyancy through deep mixing and heating from below.
5) Geothermal heating and abyssal mixing force AABW upwelling, preferentially along topographic features. The diabatic return of AABW occurs predominantly in regions of weak abyssal stratification and/or fractured topography.

Acknowledgments. We thank F. Roquet and A. Melet for helpful discussions and for sharing the tidal conversion estimates of Nycander (2005) and Melet et al. (2013b).

APPENDIX A

On the Role of the Nonlinearity of the Equation of State

Locally dissipating internal tides and lee waves both induce a nonzero buoyancy flux into the global ocean: lee waves result in a volume-integrated neutral density loss of $-2.0 \times 10^5\,\mathrm{kg\,s^{-1}}$, whereas internal tides cause a net neutral density gain of $2.4 \times 10^6\,\mathrm{kg\,s^{-1}}$ (Figs. 9a,b). Indeed, because of nonlinearity in the equation of state, mixing can be a net source or sink of neutral density and a strict balance between buoyancy gain and buoyancy loss need not be achieved.

We examine the role of nonlinearity by decomposing the total dianeutral transports T_{mix} into a linear component $T_{\mathrm{mix}}^{\mathrm{lin}}$ and a nonlinear component $T_{\mathrm{mix}}^{\mathrm{nonlin}} = T_{\mathrm{mix}} - T_{\mathrm{mix}}^{\mathrm{lin}}$ (Fig. A1). Total buoyancy fluxes and transformation rates resulting from near-field mixing are shown for the regions north (Figs. A1b,c) and south (Figs. A1e,f) of 30°S. The impact of nonlinearity on dianeutral transports induced by parameterized near-field mixing appears relatively modest. Significant effects can be noted, however. First, upward transport across the $28.11\,\mathrm{kg\,m^{-3}}$ is increased by 1 Sv both north and south of 30°S, meaning that nonlinearity causes additional buoyancy gain (more precisely, neutral density loss) in the abyss. This effect is mostly explained by the increase with depth of the thermal expansion coefficient α below about 2000 m (or $\gamma = 27.8\,\mathrm{kg\,m^{-3}}$) due to its pressure dependence (Figs. A1a,d; Palter et al. 2014).

Using (4) and (5), we can write the diapycnal velocity induced by nonlinear effects as

$$\omega^{\mathrm{nonlin}} = \omega - \omega^{\mathrm{lin}} = -(\partial_\perp \gamma)^{-1}[\partial_\perp(b\partial_\Theta \rho)F^\Theta + \partial_\perp(b\partial_{S_A}\rho)F^{S_A}]. \quad \text{(A1)}$$

Equation (A1) shows that net neutral density loss (corresponding to upwelling, $\omega^{\mathrm{nonlin}} < 0$) occurs when mixing transfers heat toward lower $b\partial_\Theta\rho = -\rho b\alpha$ or transfers salt toward lower $b\partial_\Theta\rho = \rho b\beta$ and conversely. Because the haline contraction coefficient β has relatively weak spatial variations relative to α, ω^{nonlin} is dominated by the first term. Variations in the b factor are most significant south of 55°S (Iudicone et al. 2008b), so that its effect is secondary here except for some amplification of the nonlinear α effect in the Southern Ocean (Fig. A1d). Thus, the increase of α with depth in the abyss enhances neutral density loss and thereby the efficiency of AABW consumption. This shows up as increased buoyancy gain and upwelling for waters denser than $27.8\,\mathrm{kg\,m^{-3}}$ (Figs. A1b,c,e,f).

The tendency is reversed for lighter waters, however, since α decreases sharply with depth within the tropical thermocline. For mode, intermediate, and tropical waters ($\gamma \le 27.5\,\mathrm{kg\,m^{-3}}$), nonlinearity in the equation of state becomes a first-order effect. In the linear approximation, buoyancy gain by waters denser than $25\,\mathrm{kg\,m^{-3}}$ is exactly balanced by buoyancy loss for waters lighter than $25\,\mathrm{kg\,m^{-3}}$ (Figs. A1b,e). Including the full nonlinearity of the equation of state causes the buoyancy loss of waters lighter than $27.2\,\mathrm{kg\,m^{-3}}$ to amount to more than twice the buoyancy gain of denser waters. Indeed, by fluxing heat toward smaller α, diapycnal mixing causes strong additional buoyancy loss (neutral density gain) in the upper ocean. Note that this effect will be greatly amplified when other sources of upper-ocean mixing are taken into account. Here, diapycnal temperature and salinity fluxes F^Θ and F^{S_A} arise only from near-field mixing below the mixed layer driven by bottom-generated internal waves. Including mixed layer turbulence and processes such as direct wind mixing and surface-generated waves would greatly enhance the diapycnal fluxes F^Θ and F^{S_A} and thereby the buoyancy loss and associated downwelling in (A1). Indeed, the herein-estimated, volume-integrated buoyancy loss owing to parameterized near-field mixing is $1.9 \times 10^6\,\mathrm{kg\,s^{-1}}$, about 50 times weaker than that required to balance the global buoyancy gain from air–sea buoyancy fluxes (Schanze and Schmitt 2013; Palter et al. 2014).

APPENDIX B

On the Role of the Incrop Area

The total geothermal and mixing-induced buoyancy fluxes entering the volume $V(\gamma, +\infty)$ of waters denser than γ, defined by (17) and (18), can be written as the product between a mean buoyancy flux and the corresponding area of integration (Figs. B1a–c):

$$T_{\mathrm{geo}}(\gamma) = \partial_\gamma \iint_{I(\gamma,+\infty)} (-F_{\mathrm{eq}}^\gamma)\, dA = \partial_\gamma \left[\overline{F_{\mathrm{geo}}^\gamma} \iint_{I(\gamma,+\infty)} dA\right], \quad \text{and} \quad \text{(B1)}$$

$$T_{\mathrm{mix}}(\gamma) = \partial_\gamma \iint_{A(\gamma)\cup O(\gamma,+\infty)} F_{\mathrm{eq}}^\gamma\, dA = \partial_\gamma \left[\overline{F_{\mathrm{eq}}^\gamma} \iint_{A(\gamma)\cup O(\gamma,+\infty)} dA\right]. \quad \text{(B2)}$$

Noting that, given the aspect ratio of the ocean, the surfaces bounding the considered volume from

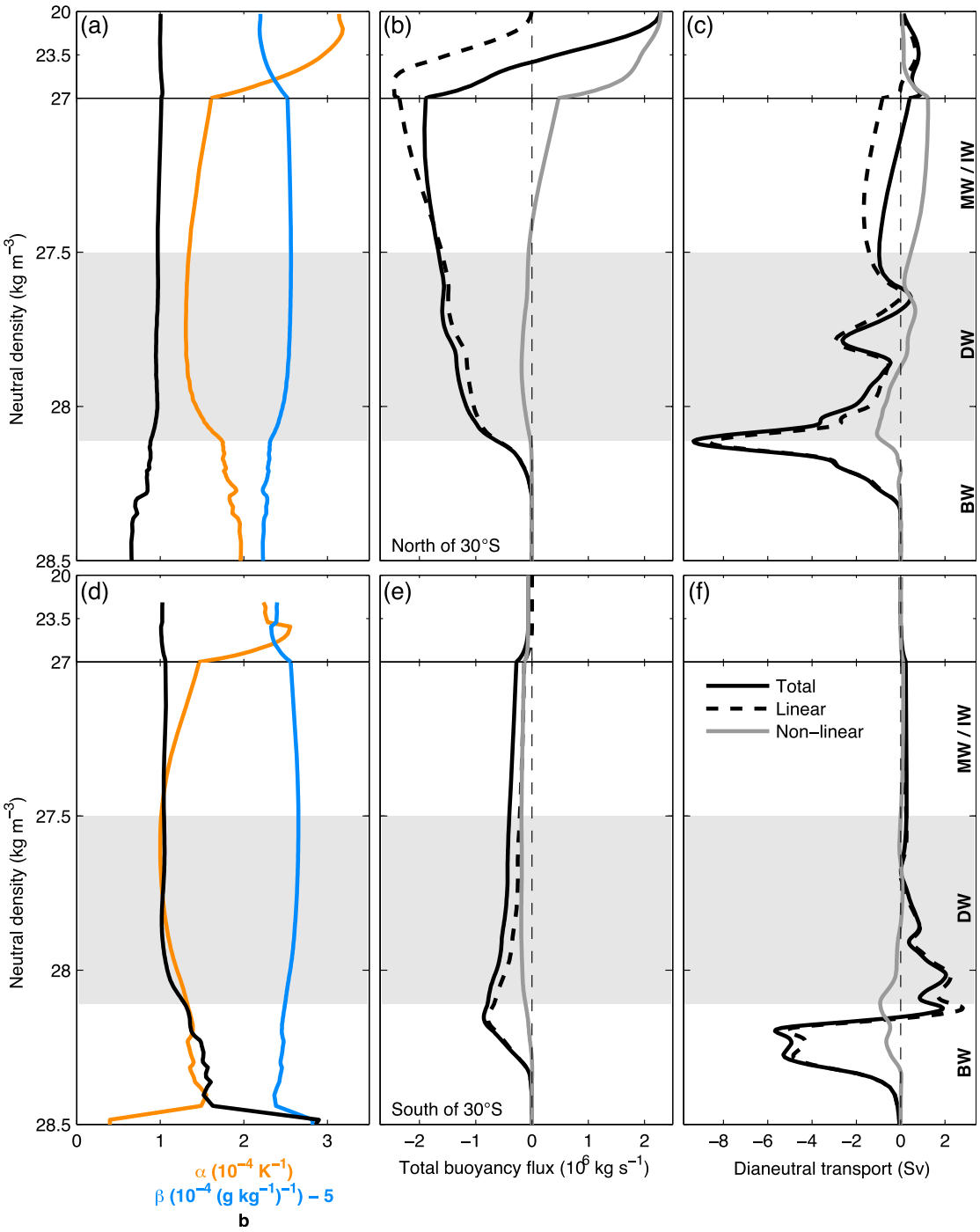

FIG. A1. Impact of the nonlinearity of the equation of state on water mass transformation by near-field mixing (top) north and (bottom) south of 30°S. (a),(d) Area-averaged thermal expansion coefficient α (orange), haline contraction coefficient β (pale blue), and b factor (black) along neutral surfaces. A value of 5×10^{-4} (g kg^{-1})$^{-1}$ is subtracted from β for display purposes. (b),(e) Total neutral density fluxes and (c),(f) dianeutral transports induced by near-field mixing including (black line) or excluding (dashed black line) the contribution of nonlinearity (gray line).

below and above have virtually equal areas $\mathcal{A}$, we can decompose T_{geo} and T_{mix} as the sum of a "mean flux term" and a "hypsometric term" as follows (Figs. B1d–f):

$$T_{\text{geo}}(\gamma) = \mathcal{A}\partial_\gamma \overline{F^\gamma_{\text{geo}}} + \overline{F^\gamma_{\text{geo}}}\partial_\gamma \mathcal{A} = \mathcal{A}\partial_\gamma \overline{F^\gamma_{\text{geo}}} + \overline{F^\gamma_{\text{geo}}}\mathcal{J}, \quad \text{and} \tag{B3}$$

$$T_{\text{mix}}(\gamma) = \mathcal{A}\partial_\gamma \overline{F^\gamma_{\text{eq}}} + \overline{F^\gamma_{\text{eq}}}\partial_\gamma \mathcal{A} = \mathcal{A}\partial_\gamma \overline{F^\gamma_{\text{eq}}} + \overline{F^\gamma_{\text{eq}}}\mathcal{J}. \tag{B4}$$

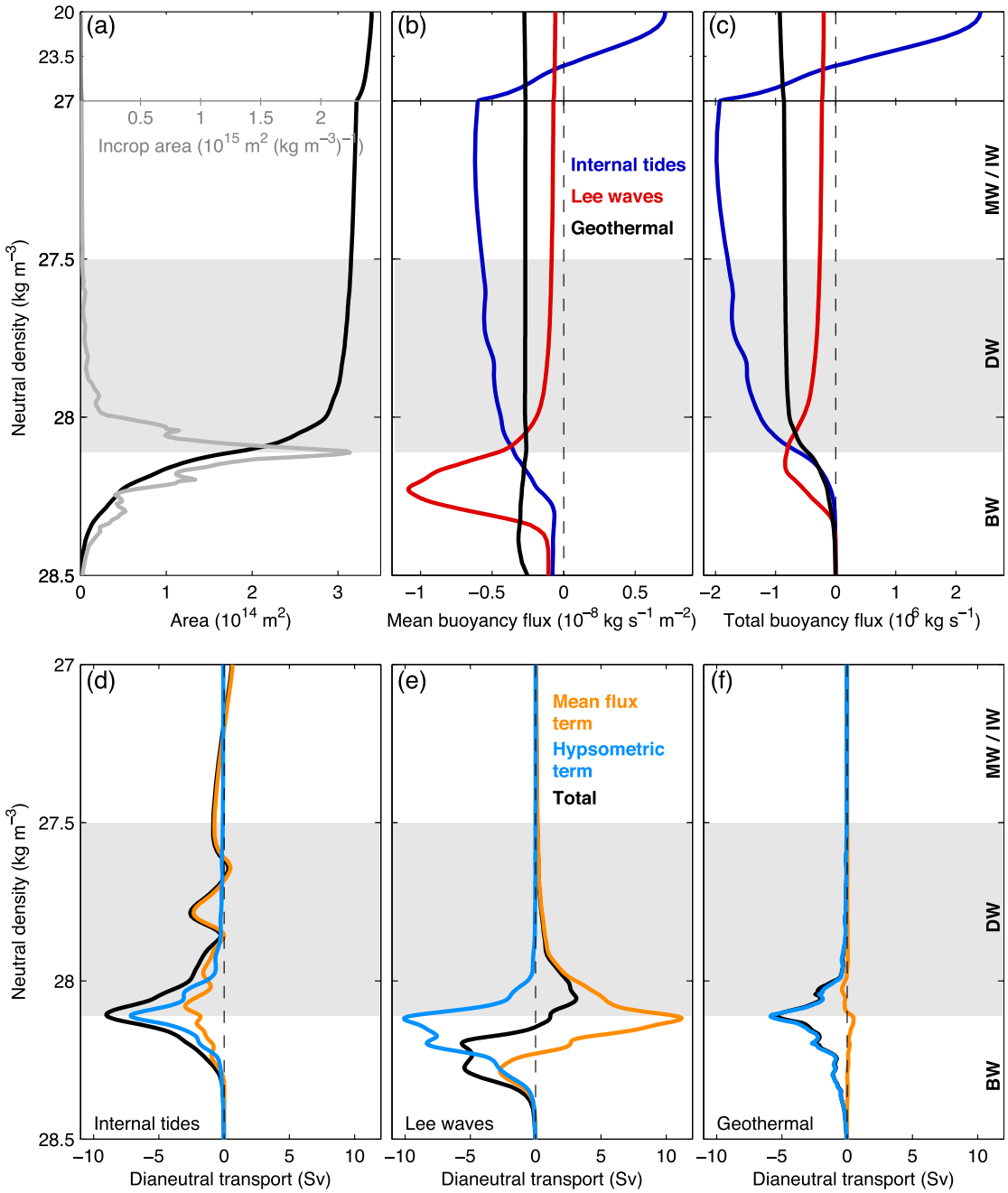

FIG. B1. Role of the incrop area on global water mass transformation by near-field mixing and geothermal heating. (a) Neutral density profile of $\mathcal{A}$ (black) and its γ derivative $\mathcal{J}$ (gray). (b) Area-averaged and (c) total neutral density fluxes induced by geothermal heating (black), near-field tidal mixing (blue), and lee-wave-driven mixing (red). Decomposition of global water mass transformation (black) by (d) near-field tidal mixing, (e) breaking lee waves, and (f) geothermal heating into mean flux (black) and hypsometric (pale blue) terms.

The second term, referred to as the hypsometric term, includes the factor $\partial_\gamma \mathcal{A} = \mathcal{J}$, which measures the reduction of the horizontal cross-sectional area of water volumes $V(\gamma, +\infty)$ as one moves to higher γ or equivalently the incrop area of neutral density layers $\mathcal{J}(\gamma)$. Strictly speaking, $\partial_\gamma \mathcal{A}$ reflects pseudohypsometry rather than hypsometry, in that it can be nonzero in the absence of sloping topography (e.g., in the presence of sloping isopycnals on a flat bottom).

The mean geothermal buoyancy flux is almost constant throughout the ocean's neutral density range, so that the convergence of the total geothermal flux is almost exclusively controlled by the shrinking rate of the area $\mathcal{A}$ (Figs. B1a–c). Therefore, one could replace the

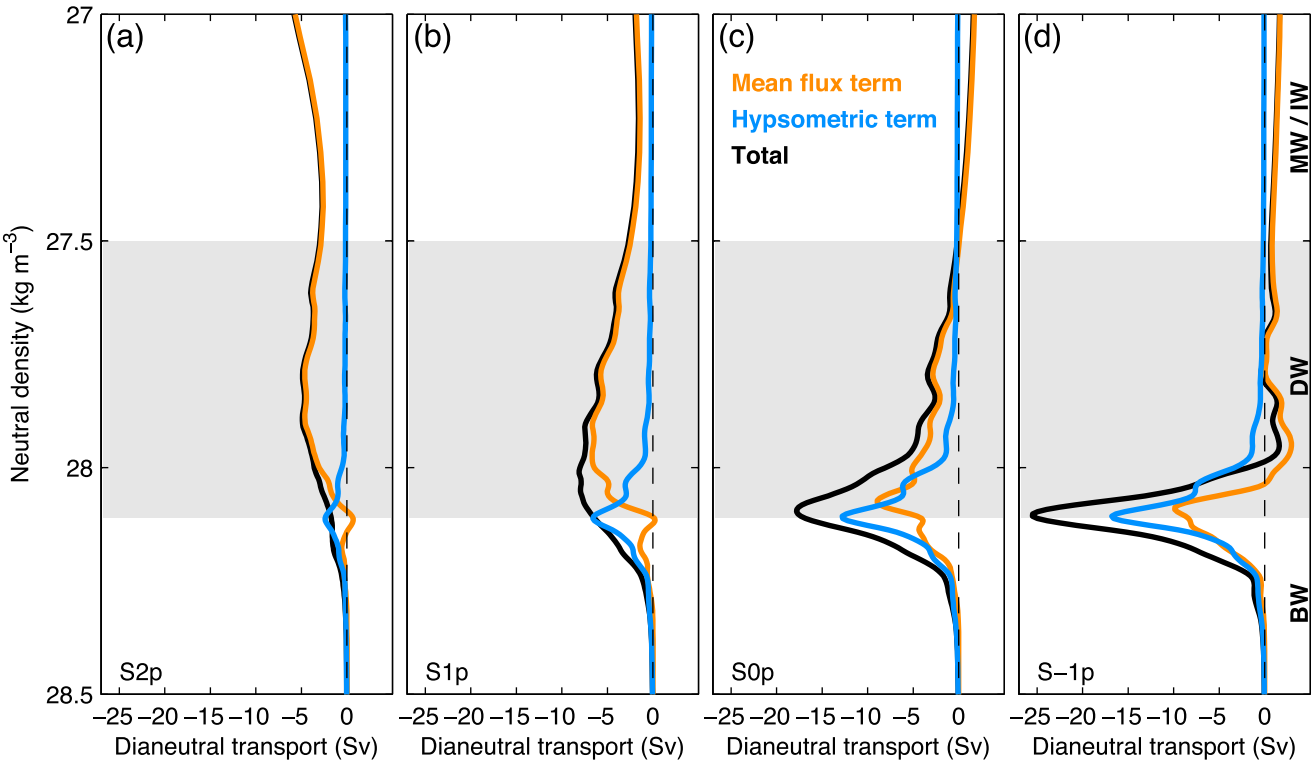

FIG. B2. Role of the incrop area on global water mass transformation by far-field tidal mixing. Decomposition of global water mass transformation by remotely dissipating internal tides (black) under scenarios (a) S2p, (b) S1p, (c) S0p, and (d) S−1p into mean flux (orange) and hypsometric (pale blue) terms.

spatially variable geothermal heat fluxes of Fig. 2c by a uniform heat flux without noticeably modifying the shape of the geothermal transformation curve; rates of geothermal upwelling are almost entirely determined by the incrop area (Fig. B1f). Near-field tidal mixing drives a mean buoyancy flux that decreases below the 27.25 kg m^{-3} neutral surface (Fig. B1b). The decrease in the mean flux adds to the sharp decrease in area $\mathcal{A}$ near 28.11 kg m^{-3} to reinforce buoyancy deposition in the light AABW density class. Yet, the peak upwelling rate forced by internal tides at $\gamma = 28.11\,\mathrm{kg\,m^{-3}}$ remains controlled by the incrop area, as shown by the dominance of the hypsometric term at abyssal densities (Fig. B1d). On the other hand, the mean buoyancy flux associated with lee-wave-driven mixing exhibits a strong peak near 28.25 kg m^{-3} (Fig. B1b) so that the increase of the mean flux counteracts the hypsometric contribution to upwelling around $\gamma = 28.11\,\mathrm{kg\,m^{-3}}$ (Fig. B1e). The maximum upwelling rate implied by breaking lee waves is reached at higher densities, when the mean flux term becomes weaker but when the mean flux multiplying $\mathcal{J}(\gamma)$ in the hypsometric term is still large.

The same decomposition between hypsometric and mean flux terms can be applied to transformation by far-field mixing (Fig. B2). Given the strong qualitative similarity between horizontal distributions Su and Sp, we choose to show only Sp scenarios. In the AABW density range, the hypsometric term systematically dominates over the mean flux term, whereas the reverse is true for neutral densities lower than 28 kg m^{-3}. This concurs with the strongest values of the incrop area being found within the 28–28.3 kg m^{-3} density range. Though the contribution of the mean flux term to upwelling at 28.11 kg m^{-3} reaches 5 Sv in scenario S0p and 9 Sv in scenario S−1p, most of the increase in AABW consumption going through scenarios S2 to S−1 can be explained by an increase in the mean buoyancy flux across the 28.11 kg m^{-3} neutral surface. Indeed, the strength of the buoyancy flux at $\gamma = 28.11\,\mathrm{kg\,m^{-3}}$ determines the actual efficiency of the hypsometry effect at the peak incrop area. But here, as in the case of near-field mixing and geothermal heating, the incrop area remains a dominant control on the structure of water mass transformation at abyssal densities, with waters of densities close to 28.11 kg m^{-3} being ideally placed to undergo rapid diabatic upwelling.

REFERENCES

Adcroft, A., J. R. Scott, and J. Marotzke, 2001: Impact of geothermal heating on the global ocean circulation. *Geophys. Res. Lett.*, **28**, 1735–1738, doi:10.1029/2000GL012182.

Bryden, H. L., and A. J. G. Nurser, 2003: Effects of strait mixing on ocean stratification. *J. Phys. Oceanogr.*, **33**, 1870–1872, doi:10.1175/1520-0485(2003)033<1870:EOSMOO>2.0.CO;2.

Cummins, P. F., G. Holloway, and A. E. Gargett, 1990: Sensitivity of the GFDL ocean general circulation model to a parameterization of vertical diffusion. *J. Phys. Oceanogr.*, **20**, 817–830, doi:10.1175/1520-0485(1990)020<0817:SOTGOG>2.0.CO;2.

Dewar, W. K., P. Berloff, and A. M. Hogg, 2011: Submesoscale generation by boundaries. *J. Mar. Res.*, **69**, 501–522, doi:10.1357/002224011799849345.

Egbert, G. D., and R. D. Ray, 2000: Significant dissipation of tidal energy in the deep ocean inferred from satellite altimeter data. *Nature*, **405**, 775–778, doi:10.1038/35015531.

Emile-Geay, J., and G. Madec, 2009: Geothermal heating, diapycnal mixing and the abyssal circulation. *Ocean Sci.*, **5**, 203–217, doi:10.5194/os-5-203-2009.

Falahat, S., J. Nycander, F. Roquet, and M. Zarroug, 2014: Global calculation of tidal energy conversion into vertical normal modes. *J. Phys. Oceanogr.*, **44**, 3225–3244, doi:10.1175/JPO-D-14-0002.1.

Ferrari, R., M. F. Jansen, J. F. Adkins, A. Burke, A. L. Stewart, and A. F. Thompson, 2014: Antarctic sea ice control on ocean circulation in present and glacial climates. *Proc. Natl. Acad. Sci. USA*, **111**, 8753–8758, doi:10.1073/pnas.1323922111.

Ganachaud, A., and C. Wunsch, 2000: Improved estimates of global ocean circulation, heat transport and mixing from hydrographic data. *Nature*, **408**, 453–457, doi:10.1038/35044048.

Gargett, A. E., 1984: Vertical eddy diffusivity in the ocean interior. *J. Mar. Res.*, **42**, 359–393, doi:10.1357/002224084788502756.

Garrett, C., and W. Munk, 1972: Space-time scales of internal waves. *Geophys. Astrophys. Fluid Dyn.*, **3**, 225–264, doi:10.1080/03091927208236082.

——, and ——, 1979: Internal waves in the ocean. *Annu. Rev. Fluid Mech.*, **11**, 339–369, doi:10.1146/annurev.fl.11.010179.002011.

——, and L. C. St. Laurent, 2002: Aspects of deep ocean mixing. *J. Oceanogr.*, **58**, 11–24, doi:10.1023/A:1015816515476.

Gouretski, V. V., and K. P. Koltermann, 2004: WOCE global hydrographic climatology: A technical report. Berichte des Bundesamtes für Seeschifffahrt und Hydrographie 35/2004, 52 pp.

Goutorbe, B., J. Poort, F. Lucazeau, and S. Raillard, 2011: Global heat flow trends resolved from multiple geological and geophysical proxies. *Geophys. J. Int.*, **187**, 1405–1419, doi:10.1111/j.1365-246X.2011.05228.x.

Heywood, K. J., A. C. Naveira Garabato, and D. P. Stevens, 2002: High mixing rates in the abyssal Southern Ocean. *Nature*, **415**, 1011–1014, doi:10.1038/4151011a.

Hofmann, M., and M. A. Morales Maqueda, 2009: Geothermal heat flux and its influence on the oceanic abyssal circulation and radiocarbon distribution. *Geophys. Res. Lett.*, **36**, L03603, doi:10.1029/2008GL036078.

Huang, R. X., 1999: Mixing and energetics of the oceanic thermohaline circulation. *J. Phys. Oceanogr.*, **29**, 727–746, doi:10.1175/1520-0485(1999)029<0727:MAEOTO>2.0.CO;2.

Huussen, T. N., A. C. Naveira-Garabato, H. L. Bryden, and E. L. McDonagh, 2012: Is the deep Indian Ocean MOC sustained by breaking internal waves? *J. Geophys. Res.*, **117**, C08024, doi:10.1029/2012JC008236.

Ito, T., and J. Marshall, 2008: Control of lower-limb overturning circulation in the Southern Ocean by diapycnal mixing and mesoscale eddy transfer. *J. Phys. Oceanogr.*, **38**, 2832–2845, doi:10.1175/2008JPO3878.1.

Iudicone, D., G. Madec, B. Blanke, and S. Speich, 2008a: The role of Southern Ocean surface forcings and mixing in the global conveyor. *J. Phys. Oceanogr.*, **38**, 1377–1400, doi:10.1175/2008JPO3519.1.

——, ——, and T. J. McDougall, 2008b: Water-mass transformations in a neutral density framework and the key role of light penetration. *J. Phys. Oceanogr.*, **38**, 1357–1376, doi:10.1175/2007JPO3464.1.

Jackett, D. R., and T. J. McDougall, 1997: A neutral density variable for the world's oceans. *J. Phys. Oceanogr.*, **27**, 237–263, doi:10.1175/1520-0485(1997)027<0237:ANDVFT>2.0.CO;2.

Jayne, S. R., 2009: The impact of abyssal mixing parameterizations in an ocean general circulation model. *J. Phys. Oceanogr.*, **39**, 1756–1775, doi:10.1175/2009JPO4085.1.

Johnson, G. C., 2008: Quantifying Antarctic Bottom Water and North Atlantic Deep Water volumes. *J. Geophys. Res.*, **113**, C05027, doi:10.1029/2007JC004477.

Kelly, S. M., N. L. Jones, J. D. Nash, and A. F. Waterhouse, 2013: The geography of semidiurnal mode-1 internal-tide energy loss. *Geophys. Res. Lett.*, **40**, 4689–4693, doi:10.1002/grl.50872.

Killworth, P. D., 1977: Mixing on the Weddell Sea continental slope. *Deep-Sea Res.*, **24**, 427–448, doi:10.1016/0146-6291(77)90482-9.

Klocker, A., and T. J. McDougall, 2010: Influence of the nonlinear equation of state on global estimates of dianeutral advection and diffusion. *J. Phys. Oceanogr.*, **40**, 1690–1709, doi:10.1175/2010JPO4303.1.

Koch-Larrouy, A., G. Madec, P. Bouruet-Aubertot, T. Gerkema, L. Bessières, and R. Molcard, 2007: On the transformation of Pacific Water into Indonesian Throughflow Water by internal tidal mixing. *Geophys. Res. Lett.*, **34**, L04604, doi:10.1029/2006GL028405.

Kunze, E., and T. B. Sanford, 1996: Abyssal mixing: Where it is not. *J. Phys. Oceanogr.*, **26**, 2286–2296, doi:10.1175/1520-0485(1996)026<2286:AMWIIN>2.0.CO;2.

——, E. Firing, J. M. Hummon, T. K. Chereskin, and A. M. Thurnherr, 2006: Global abyssal mixing inferred from lowered ADCP shear and CTD strain profiles. *J. Phys. Oceanogr.*, **36**, 1553–1576, doi:10.1175/JPO2926.1.

Ledwell, J. R., E. T. Montgomery, K. L. Polzin, L. C. St. Laurent, R. W. Schmitt, and J. M. Toole, 2000: Evidence for enhanced mixing over rough topography in the abyssal ocean. *Nature*, **403**, 179–182, doi:10.1038/35003164.

Lumpkin, R., and K. Speer, 2007: Global ocean meridional overturning. *J. Phys. Oceanogr.*, **37**, 2550–2562, doi:10.1175/JPO3130.1.

Marshall, J., D. Jamous, and J. Nilsson, 1999: Reconciling thermodynamic and dynamic methods of computation of water-mass transformation rates. *Deep-Sea Res.*, **46**, 545–572, doi:10.1016/S0967-0637(98)00082-X.

Martini, K. I., M. H. Alford, E. Kunze, S. M. Kelly, and J. D. Nash, 2011: Observations of internal tides on the Oregon continental slope. *J. Phys. Oceanogr.*, **41**, 1772–1794, doi:10.1175/2011JPO4581.1.

McDougall, T. J., 1984: The relative roles of diapycnal and isopycnal mixing on subsurface water mass conversion. *J. Phys. Oceanogr.*, **14**, 1577–1589, doi:10.1175/1520-0485(1984)014<1577:TRRODA>2.0.CO;2.

——, and P. M. Barker, 2011: Getting started with TEOS-10 and the Gibbs Seawater (GSW) oceanographic toolbox. SCOR/IAPSO WG127, 28 pp. [Available online at www.teos-10.org/pubs/Getting_Started.pdf.]

McPhee, M. G., 2003: Is thermobaricity a major factor in Southern Ocean ventilation? *Antarct. Sci.*, **15**, 153–160, doi:10.1017/S0954102003001159.

Melet, A., R. Hallberg, S. Legg, and K. Polzin, 2013a: Sensitivity of the ocean state to the vertical distribution of internal-tide-driven mixing. *J. Phys. Oceanogr.*, **43**, 602–615, doi:10.1175/JPO-D-12-055.1.

——, M. Nikurashin, C. Muller, S. Falahat, J. Nycander, P. G. Timko, B. K. Arbic, and J. A. Goff, 2013b: Internal tide generation by abyssal hills using analytical theory. *J. Geophys. Res.*, **118**, 6303–6318, doi:10.1002/2013JC009212.

——, R. Hallberg, S. Legg, and M. Nikurashin, 2014: Sensitivity of the ocean state to lee wave–driven mixing. *J. Phys. Oceanogr.*, **44**, 900–921, doi:10.1175/JPO-D-13-072.1.

Molemaker, M. J., J. C. McWilliams, and X. Capet, 2010: Balanced and unbalanced routes to dissipation in an equilibrated Eady flow. *J. Fluid Mech.*, **654**, 35–63, doi:10.1017/S0022112009993272.

Müller, P., G. Holloway, F. Henyey, and N. Pomphrey, 1986: Nonlinear interactions among internal gravity waves. *Rev. Geophys.*, **24**, 493–536, doi:10.1029/RG024i003p00493.

Munk, W., and C. Wunsch, 1998: Abyssal recipes II: Energetics of tidal and wind mixing. *Deep-Sea Res.*, **45**, 1977–2010, doi:10.1016/S0967-0637(98)00070-3.

Nash, J. D., E. Kunze, J. M. Toole, and R. W. Schmitt, 2004: Internal tide reflection and turbulent mixing on the continental slope. *J. Phys. Oceanogr.*, **34**, 1117–1134, doi:10.1175/1520-0485(2004)034<1117:ITRATM>2.0.CO;2.

Naveira Garabato, A. C., K. L. Polzin, B. A. King, K. J. Heywood, and M. Visbeck, 2004: Widespread intense turbulent mixing in the Southern Ocean. *Science*, **303**, 210–213, doi:10.1126/science.1090929.

——, D. P. Stevens, A. J. Watson, and W. Roether, 2007: Short-circuiting of the overturning circulation in the Antarctic Circumpolar Current. *Nature*, **447**, 194–197, doi:10.1038/nature05832.

Nikurashin, M., and R. Ferrari, 2010a: Radiation and dissipation of internal waves generated by geostrophic motions impinging on small-scale topography: Theory. *J. Phys. Oceanogr.*, **40**, 1055–1074, doi:10.1175/2009JPO4199.1.

——, and ——, 2010b: Radiation and dissipation of internal waves generated by geostrophic motions impinging on small-scale topography: Application to the Southern Ocean. *J. Phys. Oceanogr.*, **40**, 2025–2042, doi:10.1175/2010JPO4315.1.

——, and ——, 2011: Global energy conversion rate from geostrophic flows into internal lee waves in the deep ocean. *Geophys. Res. Lett.*, **38**, L08610, doi:10.1029/2011GL046576.

——, and S. Legg, 2011: A mechanism for local dissipation of internal tides generated at rough topography. *J. Phys. Oceanogr.*, **41**, 378–395, doi:10.1175/2010JPO4522.1.

——, and R. Ferrari, 2013: Overturning circulation driven by breaking internal waves in the deep ocean. *Geophys. Res. Lett.*, **40**, 3133–3137, doi:10.1002/grl.50542.

——, ——, N. Grisouard, and K. L. Polzin, 2014: The impact of finite-amplitude bottom topography on internal wave generation in the Southern Ocean. *J. Phys. Oceanogr.*, **44**, 2938–2950, doi:10.1175/JPO-D-13-0201.1.

Niwa, Y., and T. Hibiya, 2011: Estimation of baroclinic tide energy available for deep ocean mixing based on three-dimensional global numerical simulations. *J. Oceanogr.*, **67**, 493–502, doi:10.1007/s10872-011-0052-1.

Nurser, A. J. G., R. Marsh, and R. G. Williams, 1999: Diagnosing water mass formation from air–sea fluxes and surface mixing. *J. Phys. Oceanogr.*, **29**, 1468–1487, doi:10.1175/1520-0485(1999)029<1468:DWMFFA>2.0.CO;2.

Nycander, J., 2005: Generation of internal waves in the deep ocean by tides. *J. Geophys. Res.*, **110**, C10028, doi:10.1029/2004JC002487.

——, J. Nilsson, K. Döös, and G. Broström, 2007: Thermodynamic analysis of ocean circulation. *J. Phys. Oceanogr.*, **37**, 2038–2052, doi:10.1175/JPO3113.1.

Oka, A., and Y. Niwa, 2013: Pacific deep circulation and ventilation controlled by tidal mixing away from the sea bottom. *Nat. Commun.*, **4**, 2419, doi:10.1038/ncomms3419.

Olbers, D., and M. Wenzel, 1989: Determining diffusivities from hydrographic data by inverse methods with applications to the circumpolar current. *Oceanic Circulation Models: Combining Data and Dynamics*, D. L. T. Anderson and J. Willebrand, Eds., NATO Science Series C, Vol. 284, Springer, 95–139.

Orsi, A. H., G. C. Johnson, and J. L. Bullister, 1999: Circulation, mixing, and production of Antarctic Bottom Water. *Prog. Oceanogr.*, **43**, 55–109, doi:10.1016/S0079-6611(99)00004-X.

——, W. M. Smethie Jr., and J. L. Bullister, 2002: On the total input of Antarctic waters to the deep ocean: A preliminary estimate from chlorofluorocarbon measurements. *J. Geophys. Res.*, **107**, doi:10.1029/2001JC000976.

Osborn, T. R., 1980: Estimates of the local rate of vertical diffusion from dissipation measurements. *J. Phys. Oceanogr.*, **10**, 83–89, doi:10.1175/1520-0485(1980)010<0083:EOTLRO>2.0.CO;2.

Palter, J. B., S. M. Griffies, B. L. Samuels, E. D. Galbraith, A. Gnanadesikan, and A. Klocker, 2014: The deep ocean buoyancy budget and its temporal variability. *J. Climate*, **27**, 551–573, doi:10.1175/JCLI-D-13-00016.1.

Pollack, H. N., S. J. Hurter, and J. R. Johnson, 1993: Heat flow from the Earth's interior: Analysis of the global data set. *Rev. Geophys.*, **31**, 267–280, doi:10.1029/93RG01249.

Polzin, K. L., 2009: An abyssal recipe. *Ocean Modell.*, **30**, 298–309, doi:10.1016/j.ocemod.2009.07.006.

——, K. G. Speer, J. M. Toole, and R. W. Schmitt, 1996: Intense mixing of Antarctic Bottom Water in the equatorial Atlantic Ocean. *Nature*, **380**, 54–57, doi:10.1038/380054a0.

——, J. M. Toole, J. R. Ledwell, and R. W. Schmitt, 1997: Spatial variability of turbulent mixing in the abyssal ocean. *Science*, **276**, 93–96, doi:10.1126/science.276.5309.93.

Saenko, O. A., and W. J. Merryfield, 2005: On the effect of topographically enhanced mixing on the global ocean circulation. *J. Phys. Oceanogr.*, **35**, 826–834, doi:10.1175/JPO2722.1.

——, X. Zhai, W. J. Merryfield, and W. G. Lee, 2012: The combined effect of tidally and eddy-driven diapycnal mixing on the large-scale ocean circulation. *J. Phys. Oceanogr.*, **42**, 526–538, doi:10.1175/JPO-D-11-0122.1.

Schanze, J. J., and R. W. Schmitt, 2013: Estimates of cabbeling in the global ocean. *J. Phys. Oceanogr.*, **43**, 698–705, doi:10.1175/JPO-D-12-0119.1.

Scott, R. B., J. A. Goff, A. C. Naveira Garabato, and A. J. G. Nurser, 2011: Global rate and spectral characteristics of internal gravity wave generation by geostrophic flow over topography. *J. Geophys. Res.*, **116**, C09029, doi:10.1029/2011JC007005.

Sheen, K. L., and Coauthors, 2013: Rates and mechanisms of turbulent dissipation and mixing in the Southern Ocean: Results from the Diapycnal and Isopycnal Mixing Experiment in the Southern Ocean (DIMES). *J. Geophys. Res. Oceans*, **118**, 2774–2792, doi:10.1002/jgrc.20217.

Simmons, H. L., S. R. Jayne, L. C. St. Laurent, and A. J. Weaver, 2004: Tidally driven mixing in a numerical model of the ocean

general circulation. *Ocean Modell.*, **6**, 245–263, doi:10.1016/S1463-5003(03)00011-8.

Sloyan, B. M., 2005: Spatial variability of mixing in the Southern Ocean. *Geophys. Res. Lett.*, **32**, L18603, doi:10.1029/2005GL023568.

Stein, C. A., and S. Stein, 1992: A model for the global variation in oceanic depth and heat flow with lithospheric age. *Nature*, **359**, 123–129, doi:10.1038/359123a0.

St. Laurent, L. C., and C. Garrett, 2002: The role of internal tides in mixing the deep ocean. *J. Phys. Oceanogr.*, **32**, 2882–2899, doi:10.1175/1520-0485(2002)032<2882:TROITI>2.0.CO;2.

——, and J. D. Nash, 2004: An examination of the radiative and dissipative properties of deep ocean internal tides. *Deep-Sea Res.*, **51**, 3029–3042, doi:10.1016/j.dsr2.2004.09.008.

——, J. M. Toole, and R. W. Schmitt, 2001: Buoyancy forcing by turbulence above rough topography in the abyssal Brazil basin. *J. Phys. Oceanogr.*, **31**, 3476–3495, doi:10.1175/1520-0485(2001)031<3476:BFBTAR>2.0.CO;2.

——, H. L. Simmons, and S. R. Jayne, 2002: Estimating tidally driven mixing in the deep ocean. *Geophys. Res. Lett.*, **29**, 2106, doi:10.1029/2002GL015633.

Talley, L. D., 2008: Freshwater transport estimates and the global overturning circulation: Shallow, deep and throughflow components. *Prog. Oceanogr.*, **78**, 257–303, doi:10.1016/j.pocean.2008.05.001.

——, 2013: Closure of the global overturning circulation through the Indian, Pacific, and Southern Oceans: Schematics and transports. *Oceanography*, **26**, 80–97, doi:10.5670/oceanog.2013.07.

——, J. L. Reid, and P. E. Robbins, 2003: Data-based meridional overturning streamfunctions for the global ocean. *J. Climate*, **16**, 3213–3226, doi:10.1175/1520-0442(2003)016<3213:DMOSFT>2.0.CO;2.

Thurnherr, A. M., and K. G. Speer, 2003: Boundary mixing and topographic blocking on the mid-Atlantic ridge in the South Atlantic. *J. Phys. Oceanogr.*, **33**, 848–862, doi:10.1175/1520-0485(2003)33<848:BMATBO>2.0.CO;2.

——, L. C. St. Laurent, K. G. Speer, J. M. Toole, and J. R. Ledwell, 2005: Mixing associated with sills in a canyon on the midocean ridge flank. *J. Phys. Oceanogr.*, **35**, 1370–1381, doi:10.1175/JPO2773.1.

Toggweiler, J. R., and B. Samuels, 1995: Effect of Drake Passage on the global thermohaline circulation. *Deep-Sea Res.*, **42**, 477–500, doi:10.1016/0967-0637(95)00012-U.

Toole, J. M., R. W. Schmitt, and K. L. Polzin, 1994: Estimates of diapycnal mixing in the abyssal ocean. *Science*, **264**, 1120–1123, doi:10.1126/science.264.5162.1120.

Walin, G., 1982: On the relation between sea-surface heat flow and thermal circulation in the ocean. *Tellus*, **34A**, 187–195, doi:10.1111/j.2153-3490.1982.tb01806.x.

Waterhouse, A. F., and Coauthors, 2014: Global patterns of diapycnal mixing from measurements of the turbulent dissipation rate. *J. Phys. Oceanogr.*, **44**, 1854–1872, doi:10.1175/JPO-D-13-0104.1.

Waterman, S., A. C. Naveira Garabato, and K. L. Polzin, 2013: Internal waves and turbulence in the Antarctic Circumpolar Current. *J. Phys. Oceanogr.*, **43**, 259–282, doi:10.1175/JPO-D-11-0194.1.

——, K. L. Polzin, A. C. Naveira Garabato, K. L. Sheen, and A. Forryan, 2014: Suppression of internal wave breaking in the Antarctic Circumpolar Current near topography. *J. Phys. Oceanogr.*, **44**, 1466–1492, doi:10.1175/JPO-D-12-0154.1.

Wright, C. J., R. B. Scott, P. Ailliot, and D. Furnival, 2014: Lee wave generation rates in the deep ocean. *Geophys. Res. Lett.*, **41**, 2434–2440, doi:10.1002/2013GL059087.

Wunsch, C., and R. Ferrari, 2004: Vertical mixing, energy, and the general circulation of the oceans. *Annu. Rev. Fluid Mech.*, **36**, 281–314, doi:10.1146/annurev.fluid.36.050802.122121.

Zhai, X., H. L. Johnson, and D. P. Marshall, 2010: Significant sink of ocean-eddy energy near western boundaries. *Nat. Geosci.*, **3**, 608–612, doi:10.1038/ngeo943.

References

Adcroft, A., Scott, J. R., and Marotzke, J. (2001). Impact of geothermal heating on the global ocean circulation. *Geophysical Research Letters*, 28(9):1735–1738.

Emile-Geay, J. and Madec, G. (2009). Geothermal heating, diapycnal mixing and the abyssal circulation. *Ocean Science*, 5(2):203–217.

Ganachaud, A. and Wunsch, C. (2000). Improved estimates of global ocean circulation, heat transport and mixing from hydrographic data. *Nature*, 408(6811):453–457.

Iudicone, D., Madec, G., Blanke, B., and Speich, S. (2008a). The role of Southern Ocean surface forcings and mixing in the global conveyor. *Journal of Physical Oceanography*, 38(7):1377–1400.

Iudicone, D., Madec, G., and McDougall, T. J. (2008b). Water-mass transformations in a neutral density framework and the key role of light penetration. *Journal of Physical Oceanography*, 38(7):1357–1376.

Klocker, A. and McDougall, T. J. (2010). Influence of the nonlinear equation of state on global estimates of dianeutral advection and diffusion. *Journal of Physical Oceanography*, 40(8):1690–1709.

Lumpkin, R. and Speer, K. (2007). Global ocean meridional overturning. *Journal of Physical Oceanography*, 37(10):2550–2562.

Melet, A., Hallberg, R., Legg, S., and Nikurashin, M. (2014). Sensitivity of the ocean state to lee wave–driven mixing. *Journal of Physical Oceanography*, 44(3):900–921.

Melet, A., Legg, S., and Hallberg, R. (2016). Climatic impacts of parameterized local and remote tidal mixing. *Journal of Climate*, 29(10):3473–3500.

Naveira Garabato, A. C., Williams, A. P., and Bacon, S. (2014). The three-dimensional overturning circulation of the Southern Ocean during the WOCE era. *Progress in Oceanography*, 120:41–78.

Nikurashin, M. and Ferrari, R. (2013). Overturning circulation driven by breaking internal waves in the deep ocean. *Geophysical Research Letters*, 40(12):3133–3137.

Oka, A. and Niwa, Y. (2013). Pacific deep circulation and ventilation controlled by tidal mixing away from the sea bottom. *Nature Communications*, 4.

Saenko, O. A. and Merryfield, W. J. (2005). On the effect of topographically enhanced mixing on the global ocean circulation. *Journal of Physical Oceanography*, 35(5).

Simmons, H. L., Jayne, S. R., Laurent, L. C., and Weaver, A. J. (2004). Tidally driven mixing in a numerical model of the ocean general circulation. *Ocean Modelling*, 6(3-4):245–263.

Talley, L. (2013). Closure of the global overturning circulation through the Indian, Pacific, and Southern Oceans: Schematics and transports. *Oceanography*, 26(1):80–97.

Talley, L. D., Reid, J. L., and Robbins, P. E. (2003). Data-based meridional overturning streamfunctions for the global ocean. *Journal of Climate*, 16(19):3213–3226.

CHAPTER

II

The impact of a variable mixing efficiency on the abyssal overturning

In Chapter I, we followed previous authors by assuming a fixed mixing efficiency of one-sixth – that is, by assuming that one-sixth of the energy flux into turbulence contributes to drive a buoyancy flux, the remaining being lost through friction (Osborn 1980). However, through the enforcement of the no-flux bottom boundary condition on the mixing-driven buoyancy flux, we *de facto* let the mixing efficiency decrease to zero in the bottom grid cells of the calculation. The near-bottom collapse of the efficiency of mixing is a natural consequence of the near-bottom collapse of stratification. But the reduction of mixing efficiency need not be confined to the bottom-most cells of a gridded ocean climatology or of a gridded ocean model. Instead, mixing efficiency R_f must be a continuous function of stratification N that satisfies

$$R_f \underset{N \to 0}{\longrightarrow} 0 \, . \tag{II.1}$$

But how fast does mixing efficiency decrease with decreasing stratification? This question is not anecdotal, because the stratification-dependence of mixing efficiency determines how mixing-induced buoyancy gains and losses are distributed in the vertical. In particular, given a bottom-intensified power input to turbulence, the variation of mixing efficiency will determine the thickness and intensity of the near-bottom buoyancy deposition (Fig. 0), and the related strength of the interior downwelling and near-bottom upwelling flows.

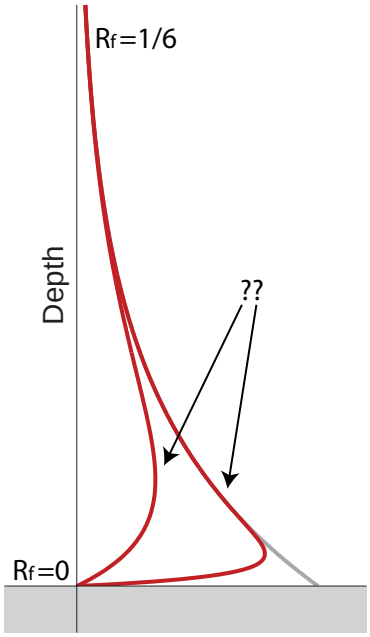

Figure 0: Schematic profiles of the diffusive density flux (red) associated with bottom intensified dissipation (gray) under two mixing efficiency scenarios. One scenario has a mixing efficiency transitioning from its maximum interior level to its zero boundary value within a thin bottom layer. The other scenario has a mixing efficiency that starts to decrease further away from the bottom.

Until now, it has been common to use ad hoc upper and lower bounds on the diapycnal diffusivity and stratification, respectively, when deducing diffusivities $K_\perp$ from the energy flux into turbulence ε_T (Simmons et al. 2004; Saenko and Merryfield 2005; Oka and Niwa 2013, among others), e.g.:

$$K_\perp = \min\Big(\frac{\varepsilon_T \,/\, 6}{\max(N^2, 10^{-8}\,\mathrm{s}^{-2})}, 10^{-2}\,\mathrm{m}^2\mathrm{s}^{-1}\Big) \tag{II.2}$$

These arbitrary bounds effectively allow for some decrease of the mixing efficiency in high energy or low stratification regions, but the approach is clearly unsatisfactory. To allow a continuous decrease of the buoyancy flux towards its zero bottom value, Melet et al. (2013) used

$$R_f = 0.2\frac{N^2}{N^2 + \Omega^2} \tag{II.3}$$

where Ω is the Earth rotation rate. Although this formulation ensures that the essential property (II.1) is satisfied, the implied reduction rate of the efficiency with decreasing stratification is not grounded in observations or theory. Moreover, confusion between the turbulent production rate ε_T and the viscous dissipation rate ε_ν has led to differing choices for the maximum mixing efficiency (e.g., set to one-sixth in (II.2) but to one-fifth in (II.3)).

Fortunately, some guidance is available to move beyond arbitrary formulations (II.2) or (II.3). In 2005, on the basis of direct numerical simulations and earlier laboratory experiments (Barry et al. 2001), Shih et al. proposed that the mixing efficiency may be expressed as a function of a buoyancy Reynolds number or turbulence intensity parameter $Re_b = \varepsilon_\nu/(\nu N^2)$, where ν is the molecular viscosity of seawater. They argued that a constant mixing efficiency of one-sixth is valid only within a certain range of Re_b,

$$K_\perp = 0.2\nu Re_b \Longleftrightarrow R_f = 1/6 \quad (Re_b \leq 100) \tag{II.4}$$

beyond which the diffusivity can be parameterized as

$$K_\perp = 2\nu\sqrt{Re_b} \Longleftrightarrow R_f = \frac{1}{1 + 0.5\sqrt{Re_b}} \quad (Re_b \geq 100)\ . \tag{II.5}$$

Equation (II.5) implies in particular that the mixing efficiency vanishes for $N \to 0$ ($Re_b \to \infty$).

Criticism of the Shih et al. (2005) numerical results persists in the oceanographic community, so that their parameterization has not generally been adopted. It is argued (Gregg et al. 2012; Kunze et al. 2012 that the limited size of their computational domain prevented resolution of the outer scales of the turbulence at high Re_b, biasing low the inferred mixing efficiency in this regime. However, a number of recent field studies (e.g., Lozovatsky and Fernando 2012; Bouffard and Boegman 2013; Bluteau et al. 2013) confirmed the decrease of mixing efficiency at high buoyancy Reynolds numbers, consistent with the theoretical requirement (II.1). These studies nonetheless reported varying regime bounds or decrease rates, suggesting that Re_b is not the only parameter controlling diffusivities (Lozovatsky and Fernando 2012; Mater and Venayagamoorthy 2014). Bouffard and Boegman (2013) recently synthesized the available

laboratory, numerical and field data, extended the parameterization of Shih et al. (2005) and showed broad agreement between their formulation and oceanic mixing efficiencies deduced from combined microstructure measurements and tracer release experiments (Ledwell et al. 1993, 2000).

In this chapter, we use the parameterization of Bouffard and Boegman (2013) to explore the impact of mixing efficiency variations on the consumption of Antarctic Bottom Water. We show that accounting for reduced mixing efficiencies in weakly-stratified, actively-mixing abyssal waters significantly damps upwelling rates forced by bottom-intensified internal wave-driven turbulence. As a result, maximum diabatic transports induced by parameterized local internal wave breaking do not exceed those maintained by geothermal heat fluxes.

The Impact of a Variable Mixing Efficiency on the Abyssal Overturning

CASIMIR DE LAVERGNE

Sorbonne Universités (UPMC, Univ. Paris 06)-CNRS-IRD-MNHN, LOCEAN Laboratory, Paris, France

GURVAN MADEC

Sorbonne Universités (UPMC, Univ. Paris 06)-CNRS-IRD-MNHN, LOCEAN Laboratory, Paris, France, and National Oceanography Centre, Southampton, United Kingdom

JULIEN LE SOMMER

CNRS-Université Grenoble Alpes, Laboratoire de Glaciologie et Géophysique de l'Environnement, Grenoble, France

A. J. GEORGE NURSER

National Oceanography Centre, Southampton, United Kingdom

ALBERTO C. NAVEIRA GARABATO

University of Southampton, National Oceanography Centre, Southampton, United Kingdom

(Manuscript received 19 December 2014, in final form 22 May 2015)

ABSTRACT

In studies of ocean mixing, it is generally assumed that small-scale turbulent overturns lose 15%–20% of their energy in eroding the background stratification. Accumulating evidence that this energy fraction, or mixing efficiency R_f, significantly varies depending on flow properties challenges this assumption, however. Here, the authors examine the implications of a varying mixing efficiency for ocean energetics and deep-water mass transformation. Combining current parameterizations of internal wave-driven mixing with a recent model expressing R_f as a function of a turbulence intensity parameter $\mathrm{Re}_b = \varepsilon_\nu/\nu N^2$, the ratio of dissipation ε_ν to stratification N^2 and molecular viscosity ν, it is shown that accounting for reduced mixing efficiencies in regions of weak stratification or energetic turbulence (high Re_b) strongly limits the ability of breaking internal waves to supply oceanic potential energy and drive abyssal upwelling. Moving from a fixed $R_f = 1/6$ to a variable efficiency $R_f(\mathrm{Re}_b)$ causes Antarctic Bottom Water upwelling induced by locally dissipating internal tides and lee waves to fall from 9 to 4 Sverdrups (Sv; 1 Sv $\equiv 10^6\,\mathrm{m^3\,s^{-1}}$) and the corresponding potential energy source to plunge from 97 to 44 GW. When adding the contribution of remotely dissipating internal tides under idealized distributions of energy dissipation, the total rate of Antarctic Bottom Water upwelling is reduced by about a factor of 2, reaching 5–15 Sv, compared to 10–33 Sv for a fixed efficiency. The results suggest that distributed mixing, overflow-related boundary processes, and geothermal heating are more effective in consuming abyssal waters than topographically enhanced mixing by breaking internal waves. These calculations also point to the importance of accurately constraining $R_f(\mathrm{Re}_b)$ and including the effect in ocean models.

1. Introduction

Away from its boundaries, where heat and freshwater exchanges with the atmosphere, cryosphere, and solid earth form and destroy water masses, buoyancy forcing of the ocean occurs almost exclusively via mixing. Though mixing along density surfaces was shown to drive significant net densification and attendant downwelling through the cabbeling and thermobaric effects (Iudicone et al. 2008a; Klocker and McDougall 2010), mixing across isopycnals is thought to be responsible for most of the interior water mass transformation (Munk and Wunsch 1998). A key process controlling the diabatic component of the meridional overturning

Corresponding author address: Casimir de Lavergne, LOCEAN Laboratory, 4 Place Jussieu, F-75005 Paris, France.
E-mail: casimir.delavergne@gmail.com

DOI: 10.1175/JPO-D-14-0259.1

circulation, diapycnal mixing thus exerts a major influence on the global distribution of temperature, salinity, and biogeochemical tracers. Observed ocean properties and transport budgets at the basin scale suggest diapycnal eddy diffusivities averaging about $10^{-4}\,m^2\,s^{-1}$ below 1000-m depth (Munk 1966; Munk and Wunsch 1998; Ganachaud and Wunsch 2000; Lumpkin and Speer 2007; Talley 2013). Yet this value masks strongly inhomogeneous mixing rates, with background values about one order of magnitude lower and localized enhanced rates up to two orders of magnitude higher (Toole et al. 1994; Munk and Wunsch 1998; Wunsch and Ferrari 2004; Waterhouse et al. 2014).

The strong spatial and temporal heterogeneity of turbulent mixing constitutes a challenge both for the representativeness of direct measurements of mixing rates and for its realistic representation in ocean models. Though ad hoc prescription of vertical diffusivities has long prevailed in numerical ocean modeling (e.g., Bryan and Lewis 1979), progress has been achieved with the development of energetically constrained parameterizations that compute diffusivities from specified dissipation rates of internal wave energy (Huang 1999; St. Laurent et al. 2002; Polzin 2009; Olbers and Eden 2013). However, in converting dissipation rates into a diapycnal diffusivity, such parameterizations rely on the knowledge of the mixing efficiency: that is, the fraction of the energy of breaking waves that actually serves to irreversibly mix the fluid.

It is commonly assumed that about one-sixth of the energy flux into turbulence contributes to diapycnal mixing, the remainder being lost as heat via viscous friction. Cross-validated estimates of diapycnal diffusivity from open ocean observations often support mixing efficiencies of 15%–25% (Toole et al. 1994; Ledwell et al. 1998, 2000), although an overall broader range of about 0%–40% has been reported (e.g., Ruddick et al. 1997; St. Laurent and Schmitt 1999). In contrast, basin-scale inferences (Stigebrandt 1976; de Young and Pond 1989; Stigebrandt and Aure 1989; Arneborg and Liljebladh 2001) and in situ observations at strongly mixing sites (Inall 2009; Bouffard and Boegman 2013; Bluteau et al. 2013) have consistently shown lower efficiencies to prevail. Recently, drawing on a large body of numerical and laboratory results, as well as field measurements, a turbulent diffusivity model that accounts for observed variability in mixing efficiency has been designed for studies of stratified turbulence (Shih et al. 2005; Bouffard and Boegman 2013). Here, we combine this new model with current parameterizations of mixing induced by breaking internal waves to investigate the implications of a varying mixing efficiency for ocean energetics and deep-water mass transformation. A description of the variable efficiency model follows (section 2). In section 3, we apply the variable R_f model to mixing driven by breaking internal tides and lee waves and revise former estimates of water mass transformation by internal wave-driven mixing (de Lavergne et al. 2015, manuscript submitted to *J. Phys. Oceanogr.*, hereinafter LMSNG). We discuss implications for the maintenance of the abyssal overturning circulation in section 4 and provide conclusions in section 5.

2. The turbulent diffusivity model

Current parameterizations of ocean mixing (St. Laurent et al. 2002; Polzin 2009; Olbers and Eden 2013) assume that the turbulent kinetic energy produced by the breaking of internal waves (ε_T) contributes in fixed proportions to a downward buoyancy flux ($K_\rho N^2$) and frictional heat production (ε_ν):

$$\varepsilon_T = \varepsilon_\nu + K_\rho N^2, \tag{1}$$

with

$$K_\rho N^2 = R_f \varepsilon_T, \quad \varepsilon_\nu = (1 - R_f)\varepsilon_T, \tag{2}$$

where K_ρ is the eddy diffusivity of density, N^2 is the buoyancy frequency, and R_f is the mixing efficiency, usually taken to be one-sixth. The latter choice means that turbulent overturns lose about 17% of their energy in raising dense water parcels over lighter ones, thus eroding the local stratification and fluxing buoyancy downward. Although frictional heating consumes most of the turbulent kinetic energy, it is generally ignored, for it represents a quasi-negligible buoyancy source in the ocean interior (LMSNG). This simple mixing model derives from the pioneering work of Osborn (1980), who argued that, given a steady-state balance between turbulent kinetic energy production, viscous dissipation, and vertical buoyancy exchange, the mixing sink term $K_\rho N^2$ should not exceed 15%–20% of the shear production ε_T. Because of difficulty in accurately estimating mixing efficiency from field measurements and for lack of deeper knowledge of its variability, this maximum value of the mixing efficiency has since served as a reference for field and modeling studies of shear-induced turbulent mixing.

However, it was soon recognized that the buoyancy flux should be proportionately less in weakly stratified waters (Osborn 1980). Indeed, in the limit of a homogenous fluid, turbulent stirring cannot drive buoyancy exchange nor modify the potential energy of the system, and all of the turbulent kinetic energy must dissipate through friction. More generally, as the restoring gravity force becomes weak compared to stirring forces, turbulent

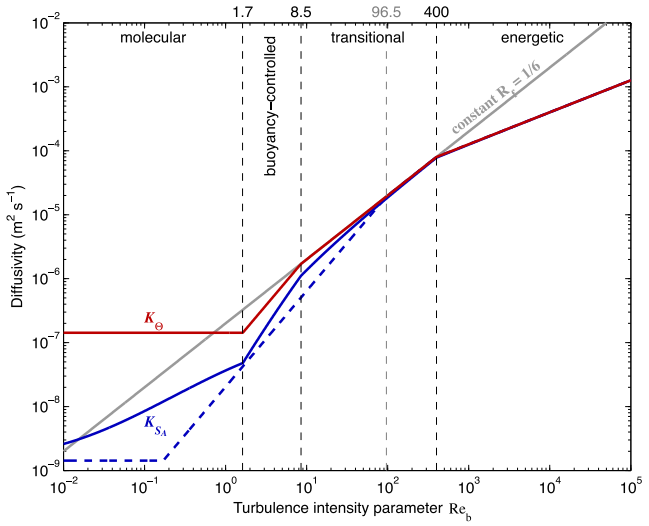

FIG. 1. Turbulent diffusivity model based on Bouffard and Boegman (2013) and Jackson and Rehmann (2014). Shown is the diapycnal diffusivity ($m^2\,s^{-1}$) of heat (red) and salt (blue) as a function of the turbulence intensity parameter. The dashed blue curve corresponds to the salt diffusivity parameterized by Bouffard and Boegman (2013), whereas the solid blue curve is deduced from the heat diffusivity (red), using the diffusivity ratio parameterization of Jackson and Rehmann (2014). Indicated regimes at the top only refer to the heat diffusivity. The thick gray line shows the Re_b dependence of diffusivities assuming a constant mixing efficiency of one-sixth. Solid red and blue curves will be referred to as the variable R_f model in subsequent calculations.

overturns become less susceptible to perform work against gravity and more susceptible to viscous damping. Thus, as stratification decreases to very low levels, it is required that R_f also approaches zero. Consistent with these theoretical expectations, the past two decades have seen a growing number of studies, based on direct numerical simulations, laboratory experiments, or field work, documenting reduced mixing efficiencies in actively mixing or weakly stratified waters (Gloor et al. 2000; Barry et al. 2001; Jackson and Rehmann 2003; Rehmann and Koseff 2004; Shih et al. 2005; Inall 2009; Davis and Monismith 2011; Hult et al. 2011; Dunckley et al. 2012; Bouffard and Boegman 2013; Bluteau et al. 2013).

In attempts to synthesize the vast spectrum of available data, several such studies have proposed that eddy diffusivities can be expressed as a function of a turbulence intensity parameter, $Re_b = \varepsilon_\nu/\nu N^2$, with ν the molecular kinematic viscosity of seawater, according to different Re_b regimes (Barry et al. 2001; Shih et al. 2005; Bouffard and Boegman 2013). Here, we adopt the most recent, field-validated parameterization of Bouffard and Boegman (2013), with a refinement offered by the parameterization of differential diffusion by Jackson and Rehmann (2014) (Fig. 1). The turbulence intensity parameter may be seen as the ratio of the destabilizing force of turbulence to the stabilizing forces of stratification and viscosity (Barry et al. 2001). Since the oceanic range of molecular viscosity is roughly 1–2 $\times$ $10^{-6}\,m^2\,s^{-1}$, with almost uniform values in the deep ocean, Re_b essentially measures the competing roles of turbulent stirring and stratification damping. At high Re_b, inertial forces overwhelm buoyancy forces, and turbulence becomes largely unaffected by stratification.

The Re_b dependence of heat and salt diffusivities proposed by Bouffard and Boegman (2013) is plotted in Fig. 1 (red and dashed blue). For $Re_b \geq 96.5$, both diffusivities are equal, and $K_\rho = K_\Theta = K_{S_A}$, where Θ denotes conservative temperature and S_A denotes absolute salinity. Within the range $96.5 \leq Re_b \leq 400$,

$$K_\rho = 0.2\nu\,Re_b, \tag{3}$$

which is equivalent to (2) with $R_f = 1/6$. Hence, the typical mixing efficiency of one-sixth is valid only for these moderate Re_b values (transitional regime), corresponding to $K_\rho = 1.9\text{–}8 \times 10^{-5}\,m^2\,s^{-1}$. In the higher Re_b range (energetic regime), mixing efficiency is reduced compared to the high-end value:

$$K_\rho = 4\nu\sqrt{Re_b}, \quad R_f = 1/(1 + 0.25\sqrt{Re_b}). \tag{4}$$

According to (4), increasingly strong turbulence intensities (as measured by Re_b) lead to increasingly small mixing efficiencies. In other words, as turbulence grows uninhibited by stratification, the energy input to small-scale turbulence becomes increasingly inefficient at driving a buoyancy flux, consistent with physical arguments. In particular, the buoyancy flux vanishes together with the stratification:

$$K_\rho N^2 = 4\sqrt{\nu\varepsilon_\nu}N \underset{N\to 0}{\longrightarrow} 0, \tag{5}$$

thus satisfying the necessary property mentioned above. We also note that the predicted $K_\rho = 4\sqrt{\varepsilon_\nu\nu}N^{-1}$ in the energetic regime is analogous to the dependence of K_ρ on stratification suggested by the field data compilation of Gargett (1984), assuming a constant $\varepsilon_\nu \sim 10^{-9}\,W\,kg^{-1}$.

At lower Re_b, turbulent mixing becomes increasingly controlled by buoyancy effects. Incomplete mixing can then favor upgradient fluxes, implying reduced mixing efficiencies relative to the transitional regime (Holt et al. 1992; Merryfield 2005; Bouffard and Boegman 2013). Because molecular diffusion of salt is two orders of magnitude slower than that of heat, reversible mixing of salt can occur at larger turbulence intensities, explaining the narrower validity of the transitional regime for K_{S_A} than for K_Θ. We use a recently proposed Re_b-dependent

parameterization of the diffusivity ratio K_{S_A}/K_Θ (Jackson and Rehmann 2014; see appendix) to deduce an alternative form of K_{S_A} from K_Θ (Fig. 1, solid blue). Both parameterizations show reasonable qualitative agreement, with weak differential diffusion for $\mathrm{Re}_b \geq 50$ and increasingly small diffusivity ratio toward the molecular regimes. In the following, we use the form of K_{S_A} deduced from the Jackson and Rehmann (2014) diffusivity ratio, as it offers a well-constrained, slightly improved parameterization of differential diffusion. Nevertheless, we find that differential diffusion and the reduced R_f in the buoyancy-controlled regime have almost negligible impact on large-scale water mass transformation by breaking internal waves. This follows from the fact that most of the wave-breaking energy falls within the transitional and energetic regimes: the bulk of buoyancy fluxes is driven by relatively energetic turbulence, with $\mathrm{Re}_b \sim O(10^2$–$10^5)$. Therefore, the discussion will henceforth be focused on the role of reduced mixing efficiencies in high-diffusivity regions.

3. Application to internal wave-driven mixing

a. Methods

The saturation of diapycnal mixing for low stratification or high mixing energy has strong implications for ocean energetics and the abyssal ocean circulation. Indeed, wave breaking and mixing occur primarily along topographically complex ocean boundaries (e.g., Waterhouse et al. 2014), in localized mixing hot spots, so most of the turbulent activity takes place where mixing efficiency is expected to be reduced. To quantify the impact of variable efficiencies on the overturning circulation, we apply the Re_b-dependent mixing model to constructed climatologies of stratification and internal wave energy dissipation.

Significantly, underlying the application to gridded mean fields of dissipation and stratification is the assumption that the $K_\rho(\mathrm{Re}_b)$ model is robust to a leap in scale from localized, time-varying turbulence to large-scale, time-mean environmental conditions. Developed from laboratory-scale experiments and direct numerical simulations as well as field microstructure measurements, the Bouffard and Boegman (2013) parameterization was primarily designed for field studies inferring diffusivities from instantaneous profile measurements of the viscous dissipation of turbulent kinetic energy. Because of the nonlinearity of $K_\rho(\mathrm{Re}_b)$ in the energetic regime, the direct applicability of the model to annual, large-scale means of N^2 and ε_ν may thus be questioned. In particular, wave-breaking events are known to be both localized and episodic so that transient Re_b levels within turbulent patches may substantially exceed larger-scale, annual average turbulence intensities. Consequently, cumulative, large-scale mixing efficiencies reflecting the net irreversible mixing achieved by an ensemble of breaking events could be lower than efficiencies inferred from a global climatology of Re_b:

$$\overline{R_f(\mathrm{Re}_b)}^{\Delta x,\Delta y,t} < R_f(\overline{\mathrm{Re}_b}^{\Delta x,\Delta y,t}), \tag{6}$$

where the overbar denotes averaging over the resolved scales of the climatology. This suggests that our methodology is likely to underestimate the effect of reduced mixing efficiencies at high Re_b. On the other hand, local density gradients, including the deep stratification, could be underestimated in some places by a coarsely resolved hydrographic climatology, possibly biasing high the computed turbulence intensities. Clearly, further research is required to assess the scale dependence of mixing efficiency (see, e.g., Arneborg 2002; Ivey et al. 2008) and to finely calibrate the Re_b-dependent model for large-scale modeling applications. Nevertheless, the fact that the Bouffard and Boegman (2013) parameterization applied to multiple microstructure profiles yields diffusivities in broad agreement with larger-scale mixing rates inferred from tracer release experiments (e.g., Watson and Ledwell 2000) suggests that its use in a global climatological setting is not unreasonable. Moreover, the physical grounds that underpin the general behavior of the parameterized $R_f(\mathrm{Re}_b)$ also hold at larger spatial and temporal scales. Thus, application of the turbulent diffusivity model described in section 2 to global climatologies of stratification and wave-breaking energy should yield a sensible first estimate of the sensitivity of deep internal wave-driven mixing to the assumed Re_b dependence of R_f.

Using published estimates of barotropic-to-baroclinic tidal conversion (Nycander 2005; Melet et al. 2013b) and lee-wave radiation (Scott et al. 2011), we first produce three-dimensional maps of locally dissipating internal tide and lee-wave energy (Figs. 2a,b). The power density distribution $\varepsilon_T(x, y, z)$ is determined by assuming that one-third of the wave energy dissipates where it is generated, spreading in the vertical according to an exponential decay from the seabed with a 500-m e-folding length (St. Laurent et al. 2002). The relatively well-constrained spatial structure of internal wave generation relative to wave dissipation motivates these partly arbitrary though widely used choices. Because we focus on sensitivity to mixing efficiency on a global scale, significant regional deviations of the inferred distribution of energy sinks from actual oceanic conditions should not undermine the present conclusions.

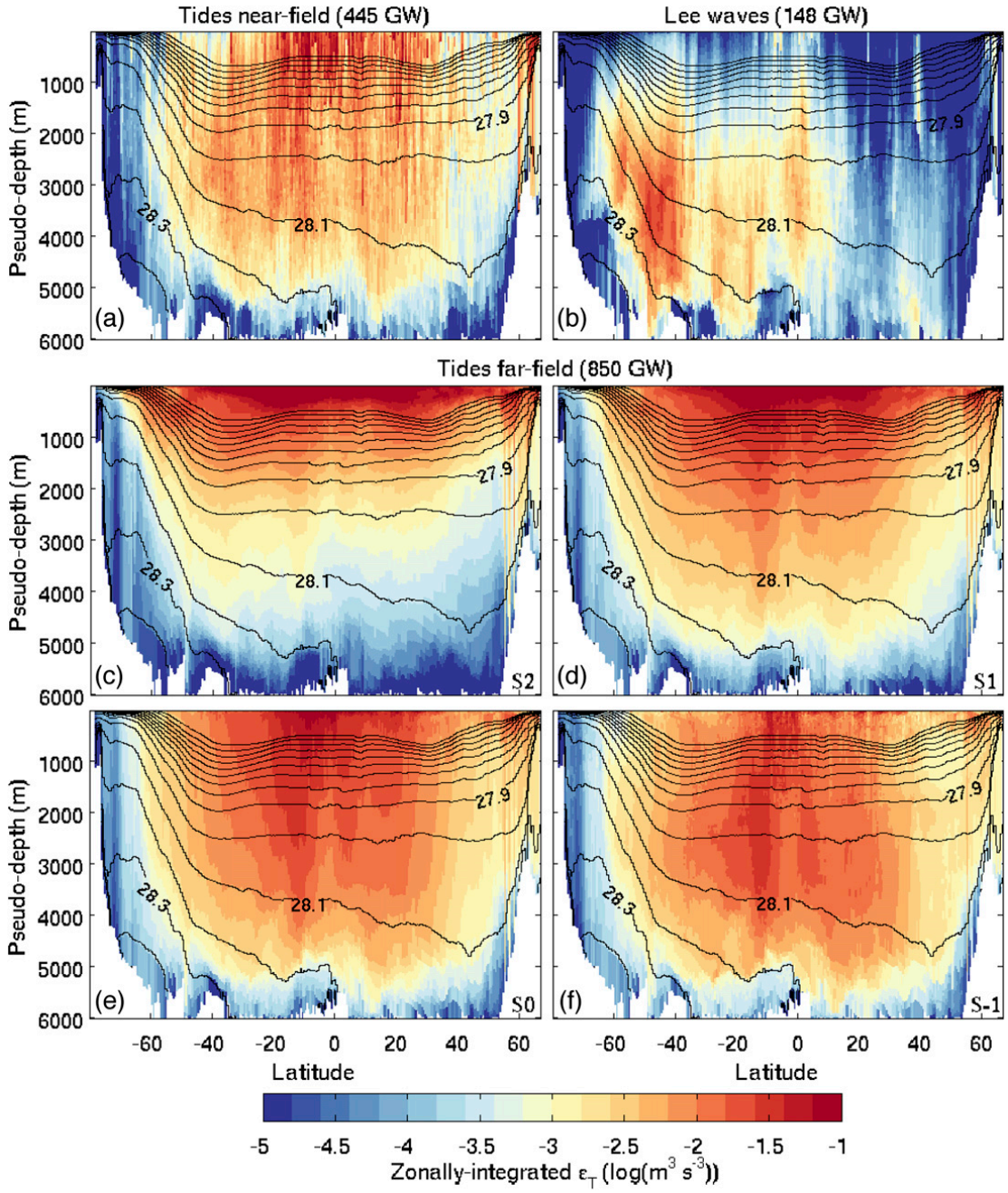

FIG. 2. Along-isopycnal zonal sum of wave-breaking energy ε_T [log(m^3 s^{-3})] from locally dissipating (a) internal tides and (b) lee waves and from (c)–(f) remotely dissipating internal tides. The vertical structure of remote tidal dissipation is specified according to scenario (c) S2, (d) S1, (e) S0, or (f) S−1. Note that the density-binned values of zonally integrated ε_T are reprojected to pseudodepth for visual purposes. The remapping procedure involves a simple bottom-up filling of each latitude band with ocean grid cells ordered from dense to light. Neutral density surfaces within 27–28.5 kg m^{-3} are contoured every 0.1 kg m^{-3}.

Following LMSNG, we assume mixing to be suppressed for the remaining two-thirds of the lee-wave energy flux. This is justified by recent observational and modeling results revealing weaker dissipation rates than would be predicted from the presently used theoretical estimate (Sheen et al. 2013; Waterman et al. 2013, 2014; Nikurashin et al. 2014). However, because the energy carried by low-mode internal tides that propagate away from generation sites could have an important role for the abyssal buoyancy budget (Oka and Niwa 2013; LMSNG), we construct idealized distributions of remote tidal dissipation as an attempt to explore the sensitivity of far-field tidal mixing to mixing efficiency (Figs. 2c–f). Guided by

published maps of column-integrated baroclinic tide dissipation (Niwa and Hibiya 2011), we specify the horizontal distribution of far-field dissipation by uniformly redistributing the remaining two-thirds of internal tide energy within a radius of 1000 km of generation sites. Admittedly, this procedure only grossly mimics the spreading of low-mode wave energy and oversimplifies a reality that should reflect specific pathways of the energy cascade, such as wave–wave interactions and topographic scattering (e.g., MacKinnon et al. 2013; Kelly et al. 2013; Eden and Olbers 2014). Nevertheless, earlier work showed that basin-scale water mass transformation is relatively insensitive to different plausible choices of the horizontal energy distribution over the open ocean (LMSNG). Much stronger sensitivity to the vertical distribution of far-field dissipation motivates the use of various scenarios for the vertical structure of wave-breaking energy (LMSNG): (S2) $\varepsilon_T \propto N^2$; (S1) $\varepsilon_T \propto N$; (S0) $\varepsilon_T \propto 1$; and (S−1) $\varepsilon_T \propto N^{-1}$. The numbering of the scenarios corresponds to exponents of N in the assumed dependence of dissipation to stratification. This choice of scenarios spans a fairly large range of possible structures (Figs. 2c–f), from pycnocline-intensified dissipation (S2 and S1) to preferential wave breaking in the abyss (S−1), thus providing probable bounds of transformation rates by far-field tidal mixing.

Next, we calculate the climatological buoyancy frequency from the World Ocean Circulation Experiment hydrographic atlas (Gouretski and Koltermann 2004), which provides annual mean fields at a resolution of 0.5° × 0.5° in the horizontal and 10–250 m in the vertical. Computing diapycnal diffusivities and mixing efficiencies from the constructed N^2 and ε_T fields now only requires rewriting the Re_b-dependent model equations in terms of ε_T rather than ε_ν (appendix). In the following, we use these constructed climatologies to contrast the traditional fixed R_f model (Fig. 1, gray) with the variable $R_f(\mathrm{Re}_b)$ parameterization (Fig. 1, red and blue) for a range of metrics relevant to the large-scale circulation.

b. Buoyancy fluxes and potential energy

The diapycnal diffusivity and mixing efficiency associated with near-field mixing alone according to the fixed and variable efficiency models are depicted in Fig. 3. The density diffusivity is shown as a zonal mean ($\iint_\gamma K_\rho\, dS/\iint_\gamma dS$; Figs. 3a,b) or as a stratification-weighted zonal mean ($\iint_\gamma K_\rho N^2\, dS/\iint_\gamma N^2\, dS$; Figs. 3c,d) along surfaces of constant neutral density γ (Jackett and McDougall 1997). In contrast to the zonal average K_ρ, the stratification-weighted mean K_ρ is directly related to the buoyancy flux and will be referred to as an effective diffusivity. Effective diffusivities tend to be smaller than mean diffusivities because of the correlation between strong mixing and weak stratification (Figs. 3a–d). Also conspicuous is the order of magnitude decrease in diffusivities over much of the ocean interior when moving from the constant to the variable R_f model. For instance, abyssal effective diffusivities do not exceed a few centimeters squared per second in the variable case, whereas $O(10)\,\mathrm{cm^2\,s^{-1}}$ values are common under a fixed efficiency. This implies that using the Re_b-dependent model causes a sharp, widespread reduction in mixing-induced buoyancy fluxes. Indeed, effective mixing efficiencies, calculated as $\iint_\gamma K_\rho N^2\, dS/\iint_\gamma \varepsilon_T\, dS$, are strongly reduced in waters hosting significant energy dissipation (Figs. 2a,b, 3e,f), resulting in a global effective efficiency of only 7.3% for near-field mixing alone (Table 1).

The potential energy supplied by diapycnal mixing to the global ocean volume V may be calculated as follows:

$$\begin{aligned}\partial_t E_p &= g\iiint_V \partial_t \rho z\, dV\\ &= g\iiint_V [\partial_\Theta \rho \partial_z (K_\Theta \partial_z \Theta) + \partial_{S_\mathrm{A}} \rho \partial_z (K_{S_\mathrm{A}} \partial_z S_\mathrm{A})] z\, dV,\end{aligned} \tag{7}$$

where E_p denotes potential energy, ρ is the locally referenced potential density, and height z increases upward and has its origin at the surface. Concurrent with the reduction in mixing efficiency, the global potential energy supply by near-field mixing drops by 55% from fixed to variable R_f, resulting in a global input of only 44 GW (Table 1). This potential energy source is comparable to the ~35 GW supplied by geothermal heating (LMSNG), suggesting that geothermal heat fluxes are as important as bottom-intensified mixing by breaking internal waves to the maintenance of the abyssal stratification.

The constant R_f model also gives mixing efficiencies below one-sixth in a few places (Fig. 3e): this stems from the upper bound imposed on diapycnal diffusivities, chosen as $100\,\mathrm{cm^2\,s^{-1}}$, required to avoid unrealistically large diffusivities at $\mathrm{Re}_b > 5 \times 10^4$. This cap is also imposed on diffusivities predicted by the Bouffard and Boegman (2013) parameterization, but concerns many fewer grid cells, since such a high diffusivity is only reached at $\mathrm{Re}_b = 6 \times 10^6$. Indeed, in contrast to the fixed R_f model, the variable R_f parameterization offers a smooth transition from the high-end mixing efficiency to fully saturated mixing, effectively pushing back the critical level at which additional energy can no longer increase buoyancy fluxes (Fig. 1).

The variable R_f model has a global mean mixing efficiency, $V^{-1}\iiint [(K_\rho N^2)/\varepsilon_T]\, dV$, that is much higher than the global effective efficiency, $\iiint K_\rho N^2\, dV/\iiint \varepsilon_T\, dV$ (Table 1). Indeed, in the presence of near-field mixing

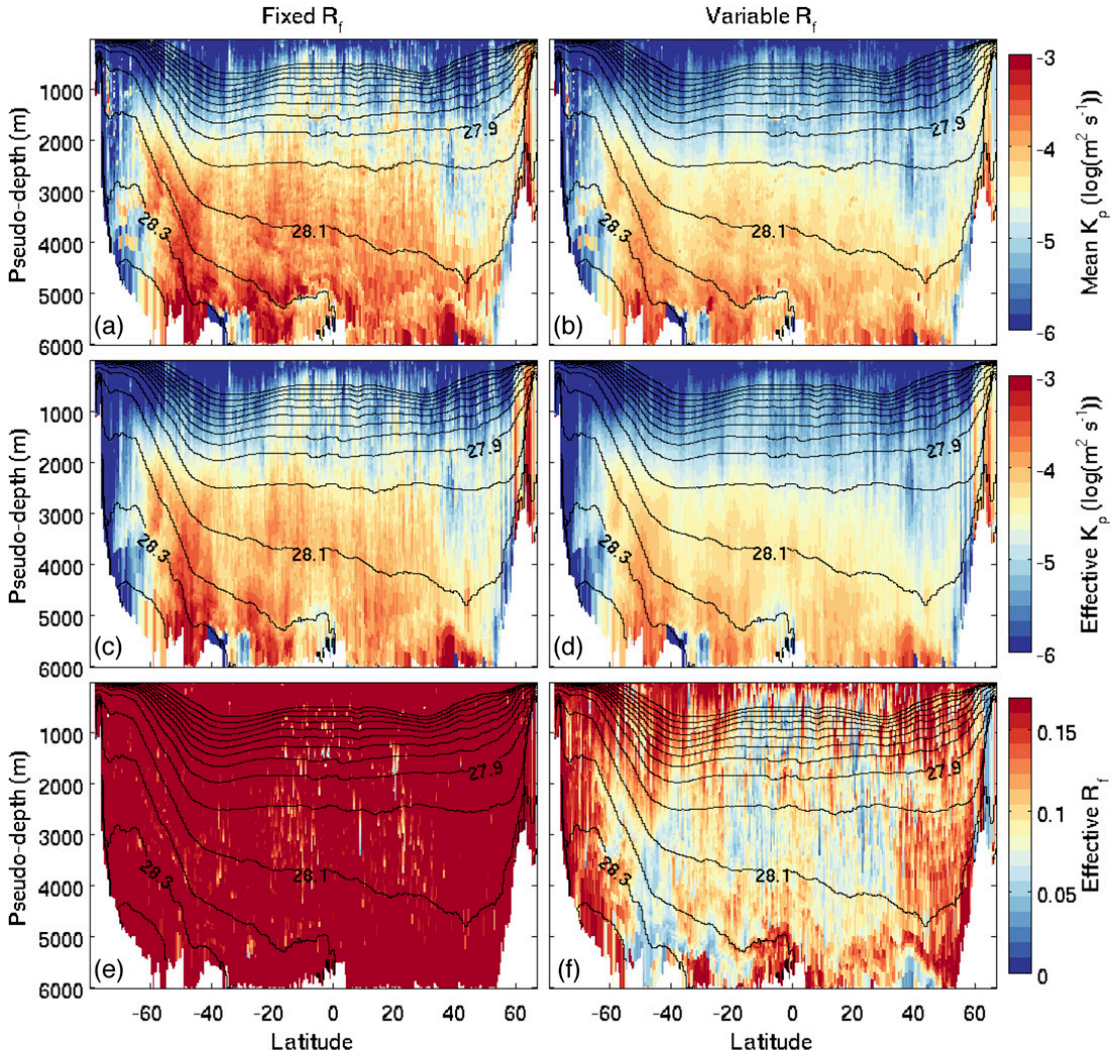

FIG. 3. Diffusivity [$\log(m^2\,s^{-1})$] and mixing efficiency resulting from near-field mixing alone, according to (left) fixed and (right) variable efficiency models. Shown are along-isopycnal (a),(b) zonal mean diffusivity $\iint_\gamma K_\rho\,dS/\iint_\gamma dS$; (c),(d) stratification-weighted zonal mean diffusivity $\iint_\gamma K_\rho N^2\,dS/\iint_\gamma N^2\,dS$; and (e),(f) effective mixing efficiency $\iint_\gamma K_\rho N^2\,dS/\iint_\gamma \varepsilon_T\,dS$, where the density-binned values are reprojected to pseudodepth for visual purposes. Neutral density surfaces within 27–28.5 kg m^{-3} are contoured every 0.1 kg m^{-3}.

only, most of the ocean volume is characterized by moderate turbulence intensities belonging to the transitional regime, but those regions that fall within the energetic regime represent the bulk of internal wave energy dissipation, implying a strong overall reduction in power contributing to mixing. The discrepancy is somewhat reduced when remote tidal dissipation is included (Table 1), as more energy dissipation occurs away

TABLE 1. Key characteristics of internal wave-driven mixing according to the fixed and variable mixing efficiency models. Values corresponding to the variable R_f parameterization are in parentheses.

	Global potential energy supply (GW)	Global effective R_f(%)	Global mean R_f(%)	AABW upwelling (30°S–67°N) (Sv)
Near-field only	97 (44)	15.8 (7.3)	16.6 (14.5)	9 (4)
Near- and far-field				
S2	161 (107)	16.3 (12.2)	16.6 (14.9)	10 (5)
S1	192 (129)	16.3 (11.7)	16.6 (14.9)	15 (8)
S0	224 (134)	16.1 (10.1)	16.6 (14.2)	25 (13)
S−1	231 (119)	15.6 (8.3)	16.5 (13.6)	33 (15)

from the weakly stratified near-bottom waters (Figs. 2, 4). Yet, even under the pycnocline-intensified wave breaking of scenarios S2 and S1, the addition of far-field energy dissipation does not always cause a commensurate increase in buoyancy fluxes, as would be expected from the assumption of a constant mixing efficiency.

Depending on the chosen scenario, the added contribution of remotely dissipating internal waves raises the global effective mixing efficiency to 8.3%–12.2% and the global potential energy supply to 107–134 GW (Table 1). The latter range can be compared to the 161–231 GW supplied by internal wave-driven mixing under a fixed efficiency and to the 240 GW that one would infer from the global energy input and assumptions of a constant $R_f = 1/6$ and a linear equation of state.[1] Though scenario S2 exhibits the largest effective mixing efficiencies, it has the lowest potential energy supply globally, a consequence of nonlinearity in the equation of state. Indeed, thermocline-intensified mixing causes significant net densification by transferring heat toward colder waters, which are less prone to thermal expansion. On the other hand, by enhancing dissipation away from the pycnocline, as assumed in scenario S−1, a similarly strong reduction in potential energy input results from saturating mixing in high Re_b waters. Thus, the combination of upper-ocean nonlinear effects and reduced efficiencies in the weakly stratified abyss appears to limit the overall potential energy source that may be derived from internal wave-driven mixing.

The lowest global effective efficiency is obtained for scenario S−1, which has the strongest energy dissipation in the deep ocean (Fig. 2), where the relatively weak stratification is unable to sustain proportionately strong buoyancy fluxes. Figure 4 illustrates the saturation of deep ocean mixing as more and more energy dissipation is placed at depth: whereas abyssal mixing levels markedly increase through scenarios S2 to S−1 under a fixed mixing efficiency (Figs. 4a,c,e,g), abyssal diffusivities show a much weaker enhancement when accounting for reduced mixing efficiencies at large Re_b (Figs. 4b,d,f,h). Hence, the impact of reduced mixing efficiencies is strongest in the abyssal ocean, with important implications for the consumption of Antarctic Bottom Water (AABW).

c. Water mass transformation

We calculate mixing-driven neutral density fluxes F^{γ}_{eq} and dianeutral transports T across neutral surfaces as follows (LMSNG):

$$F^{\gamma}_{\mathrm{eq}} = -\iiint_{\gamma' \geq \gamma} [b\partial_{\Theta}\rho\partial_z(K_{\Theta}\partial_z\Theta) + b\partial_{S_A}\rho\partial_z(K_{S_A}\partial_z S_A)]\, dV \quad \text{and} \tag{8}$$

$$T = \partial_{\gamma} F^{\gamma}_{\mathrm{eq}}, \tag{9}$$

where b is the ratio of the spatial gradients of neutral density and locally referenced potential density (Iudicone et al. 2008b). An equivalent diffusive flux of neutral density across a given neutral surface, resulting from temperature and salinity mixing below that surface is represented by F^{γ}_{eq} (de Lavergne et al. 2015).

Fluxes and transports associated with near-field mixing alone are shown in Fig. 5. North of 30°S, energy dissipation is dominated by internal tides (Fig. 2), and mixing drives a divergent neutral density flux over most of the interior density range, forcing net upward motion across neutral surfaces deeper than 27.2 kg m^{-3} (27.0 kg m^{-3}) under fixed (variable) R_f (Figs. 5a,b). The variable efficiency $R_f(\mathrm{Re}_b)$ acts to moderate neutral density fluxes and dianeutral transports, reducing peak fluxes and transports by ~60%. In particular, the maximum rate of upwelling at the deep-/bottom water boundary ($\gamma = 28.11$ kg m^{-3}) drops from 9 to 4 Sverdrups (Sv; 1 Sv $\equiv 10^6$ m^3 s^{-1}), implying that locally dissipating internal tides and lee waves may be unable to balance more than 4 Sv of northward bottom water flow out of the Southern Ocean.

In the Antarctic Circumpolar Current region, mixing is dominated by breaking lee waves (Fig. 2). Most energetic along the 28.15 kg m^{-3} neutral surface, lee waves drive a divergent density flux below that level and a convergent density flux above (Figs. 5c,d). Under the variable R_f model, buoyancy transfer from lighter ($\gamma \leq 28.15$ kg m^{-3}) to denser ($\gamma \geq 28.15$ kg m^{-3}) waters is damped, inducing both weaker upwelling of dense AABW and weaker downwelling of the overlying Circumpolar Deep Water. The net input to the bottom water layer south of 30°S is reduced from 2 Sv to less than 1 Sv. At lighter densities, the variable R_f formulation predicts even smaller transformation rates both north and south of 30°S, suggesting a weak overall influence of near-field mixing on the consumption of southward-flowing deep waters.

By accounting for the Re_b dependence of mixing efficiency, we show that focused near-bottom mixing as commonly parameterized for locally dissipating internal waves (St. Laurent et al. 2002) is only a minor contributor to the diabatic return of AABW. Nonetheless, if more widely distributed, as hypothesized in the present idealized scenarios, mixing driven by remotely breaking internal tides could be a more efficient driver of AABW

[1] Because of nonlinearities in the equation of state, the rate of change of potential energy given by (7) differs from $\iiint_V \rho K_\rho N^2\, dV = \iiint_V \rho R_f \varepsilon_T\, dV$.

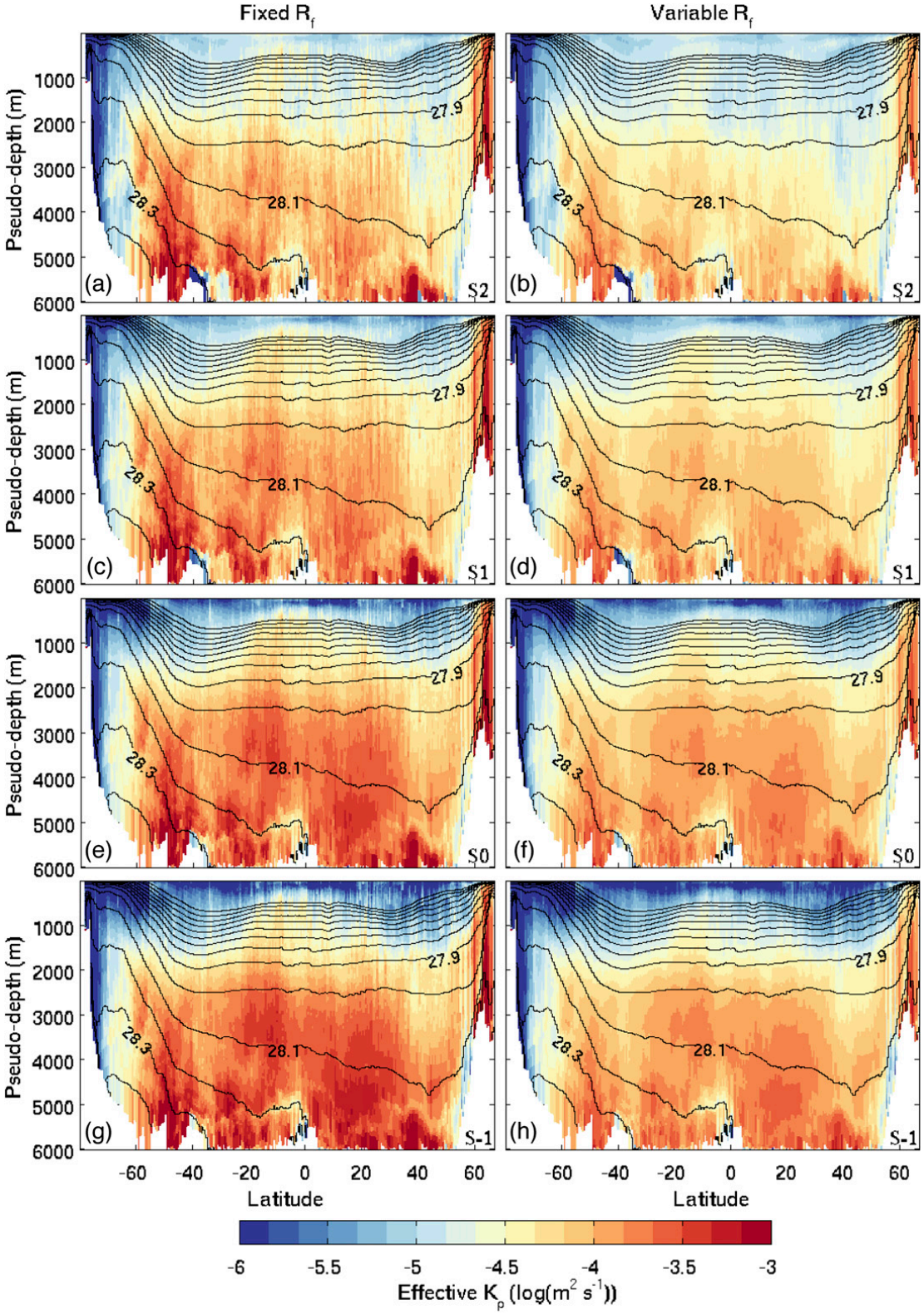

FIG. 4. Effective diffusivity [log(m^2 s^{-1})] resulting from near-field and far-field mixing combined, according to (left) fixed and (right) variable efficiency models. Effective diffusivities are calculated as a stratification-weighted mean along isopycnals ($\iint_\gamma K_\rho N^2\, dS / \iint_\gamma N^2\, dS$). The vertical structure of remote tidal dissipation is specified according to scenario (a),(b) S2; (c),(d) S1; (e),(f) S0; or (g),(h) S−1. Density-binned values are reprojected to pseudodepth for visual purposes. Neutral density surfaces within 27–28.5 kg m^{-3} are contoured every 0.1 kg m^{-3}.

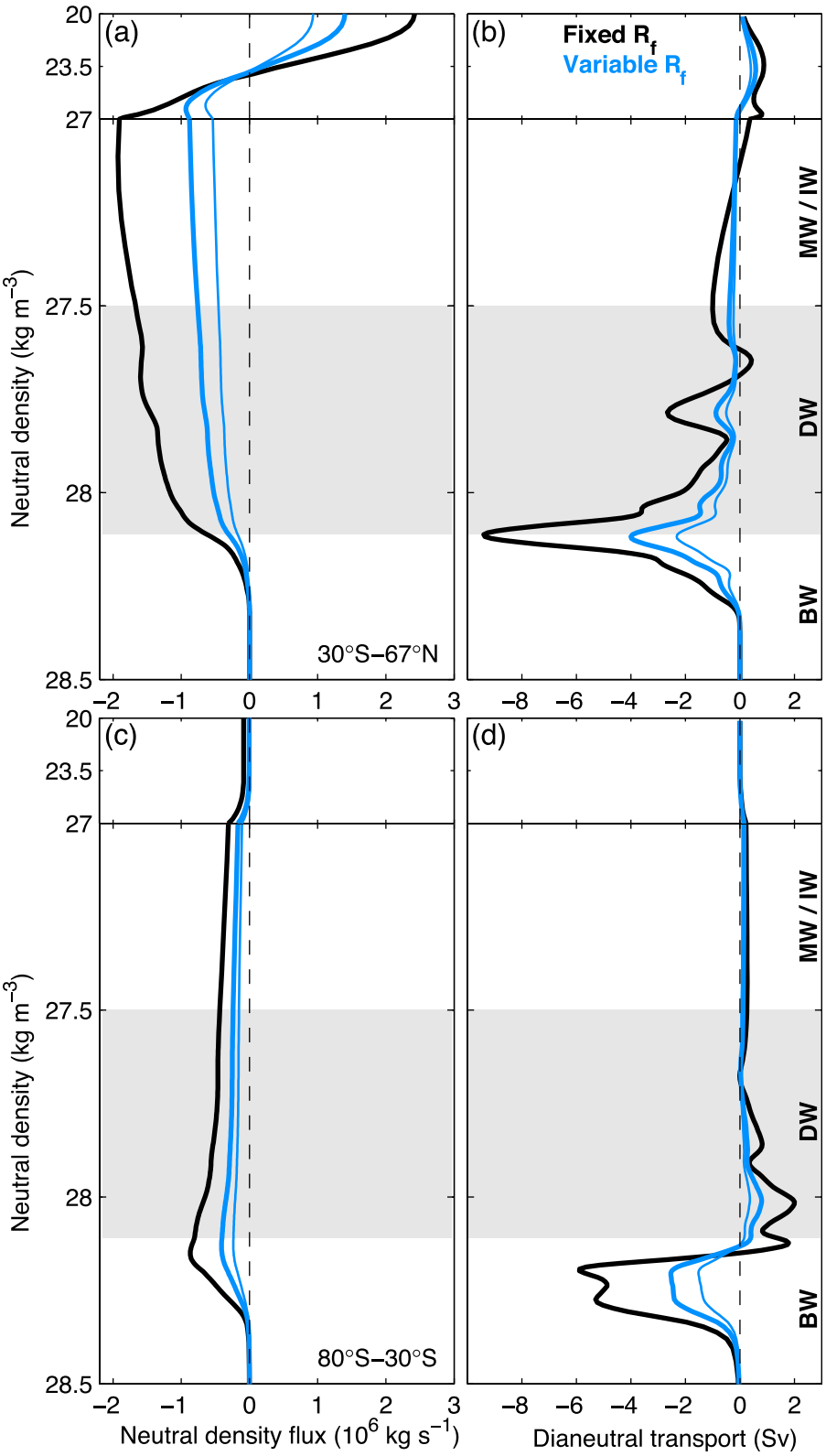

FIG. 5. Water mass transformation by near-field diapycnal mixing for the regions (a),(b) north and (c),(d) south of 30°S. (a),(c) Neutral density fluxes (10^6 kg s^{-1}) and (b),(d) dianeutral transports (Sv) induced by near-field mixing alone under fixed (thick black) and variable (thick blue) R_f. Negative dianeutral transports correspond to upwelling. The thin blue line shows results from an alternative variable R_f formulation, where the lower limit of the energetic regime is set to $\mathrm{Re}_b = 100$ instead of $\mathrm{Re}_b = 400$. Note the different vertical scale above and below $\gamma = 27$ kg m^{-3}. Neutral density ranges of bottom (BW), deep (DW), and mode/intermediate (MW/IW) waters are indicated by the light gray shading and the right-end labels.

flow. This is not the case for scenario S2, however, where the added mixing has almost no influence on abyssal waters (Fig. 6 and Table 1). With the addition of remote tidal dissipation under scenario S1 and variable R_f, AABW upwelling north of 30°S is doubled from 4 to 8 Sv, compared to an increase from 9 to 15 Sv assuming a fixed efficiency. Stronger AABW consumption rates of 13 and 15 Sv are achieved with the inclusion of far-field mixing with vertically uniform (S0) or depth-increasing (S−1) dissipation, respectively. Yet these rates remain much weaker than the corresponding 25 and 33 Sv of AABW upwelling that one would infer from a fixed mixing efficiency of one-sixth. These results suggest that internal tides and lee waves generated by tidal and geostrophic flows impinging on rough topography are unlikely to be able to sustain alone the estimated 20–30 Sv of northward bottom water inflow to the Atlantic and Indo-Pacific basins (Ganachaud and Wunsch 2000; Lumpkin and Speer 2007; Talley et al. 2003; Talley 2008, 2013; Naveira Garabato et al. 2014).

Reduced mixing efficiencies at high Re_b also have implications for the local structure of abyssal flows (Fig. 7). Because mixing-induced buoyancy fluxes must vanish at the seafloor to meet a no-flux bottom boundary condition, mixing efficiency must be zero at the seabed. (We note that the downward heat flux actually vanishes very near the seafloor before reversing sign to meet the bottom geothermal flux—a fact ignored here, for it does not affect the present discussion.) Under the assumption of a fixed efficiency, the transition from $R_f = 1/6$ to $R_f = 0$ occurs de facto within the bottom-most grid cell through the enforcement of the no-flux boundary condition for diffusive heat and salt fluxes. In the case of increasing energy dissipation with depth, as parameterized for near-field mixing, this implies that the downward buoyancy flux is divergent throughout the water column except in the deepest grid cell, where all the buoyancy deposition is concentrated. As a result, strong upwelling (defined here as dianeutral transport toward lower densities) at the lowest level contrasts with downwelling in overlying waters (LMSNG). This behavior can be observed in Fig. 7c, where large downward transports near the neutral surface incrop adjoin strong upward transports at the grounding grid cells. In contrast, the $R_f(\mathrm{Re}_b)$ model allows a natural transition toward the no-flux bottom boundary condition, with $R_f \to 0$ as $N^2 \to 0$. Consequently, the peak buoyancy flux induced by near-field mixing is generally weaker and situated higher up in the water column, and the resulting bottom buoyancy gain is both smaller and distributed over a thicker layer above the seafloor. Upwelling then occurs through weaker velocities over a thicker bottom layer, and the downward transports above that layer are significantly damped (Figs. 7a–d).

d. *Sensitivity to regime limits*

Water mass transformation estimates were found to be insensitive to the inclusion of differential diffusion and reduced efficiencies in the buoyancy-controlled regime (not shown): differences between the fixed and variable R_f models presented in Figs. 3–7 are almost entirely attributable to differing mixing efficiencies in the energetic regime. In contrast, sensitivity to the precise formulation of the energetic regime may be expected to be significant. In particular, there remains uncertainty in the validity ranges of the transitional and energetic regimes: whereas field measurements suggest a transition between these regimes close to $\mathrm{Re}_b = 400$, numerical work suggested an earlier transition near $\mathrm{Re}_b = 100$ (Shih et al. 2005; Bouffard and Boegman 2013).

To examine the sensitivity to this critical level, we repeated the analysis using the more stringent $\mathrm{Re}_b = 100$ transition. The energetic regime diffusivity and efficiency are then given by

$$K_\rho = 2\nu\sqrt{\mathrm{Re}_b}, \quad R_f = 1/(1 + 0.5\sqrt{\mathrm{Re}_b}). \qquad (10)$$

Further reduction of buoyancy fluxes and dianeutral transports was obtained (Figs. 5 and 6, thin blue), with as little as 3–8 Sv of AABW upwelling induced by near-field and far-field mixing combined. Using this formulation, locally dissipating internal waves alone sustain ~2 Sv of AABW flow and supply 26 GW of oceanic potential energy globally. This is about 40% less than the rates inferred from our reference variable R_f formulation, which was shown to be in closer agreement with available field observations (Bouffard and Boegman 2013). Although further observational constraints are thus required to narrow down the uncertainty associated with regime transitions, the sensitivity to the lower limit of the energetic regime is relatively modest compared to the difference between constant and variable efficiency models (Figs. 5 and 6).

4. Implications for the closure of the abyssal overturning

The present water mass transformation estimates show that topographically enhanced mixing driven by breaking of locally generated internal waves is unlikely to sustain more than 5 Sv of Antarctic Bottom Water flow at 30°S, providing for only about a fifth of the estimated strength of the abyssal circulation (Ganachaud and Wunsch 2000; Lumpkin and Speer 2007; Talley et al.

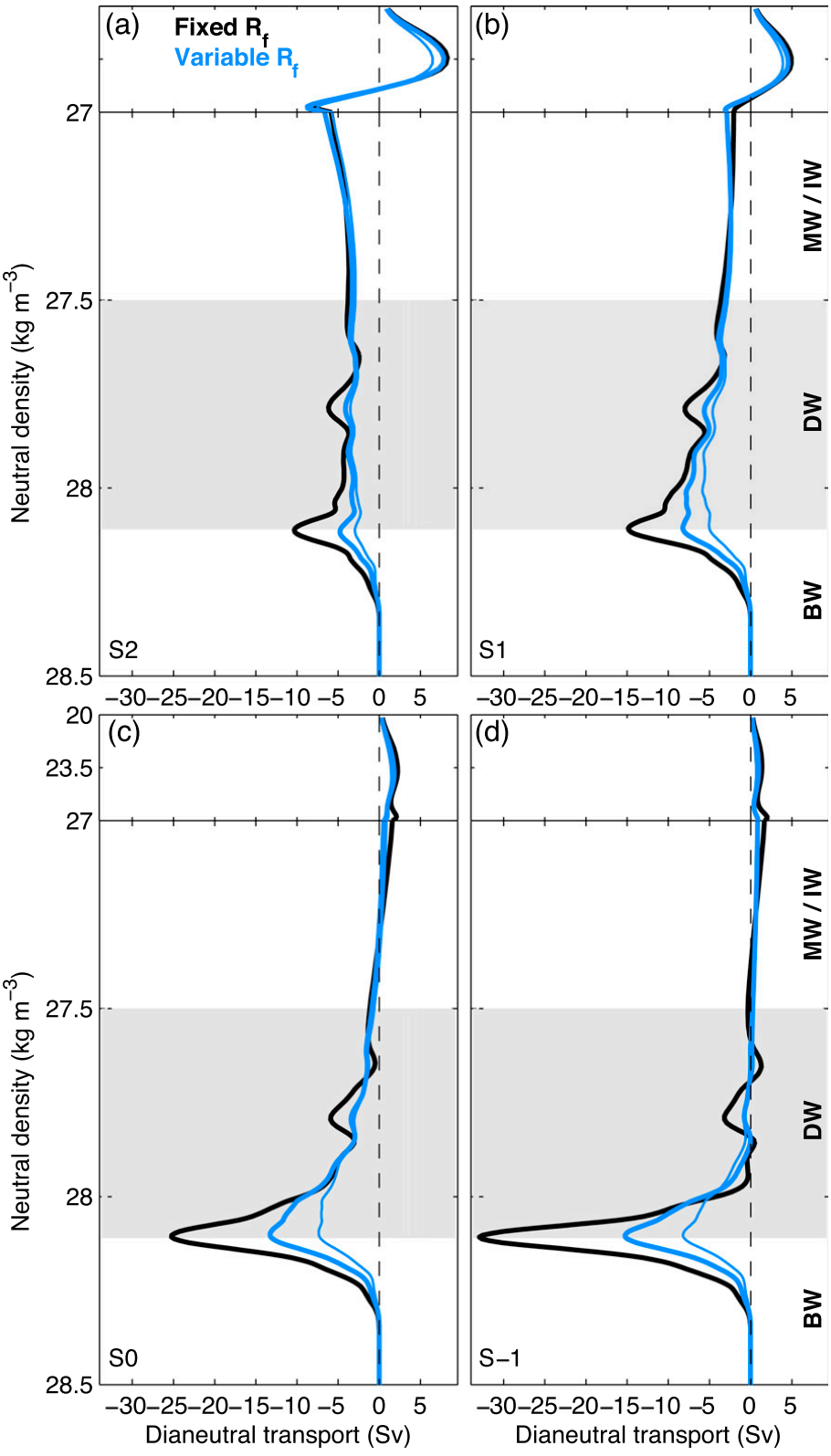

FIG. 6. Dianeutral transports (Sv) induced by near-field and far-field mixing combined within the 30°S–67°N ocean domain, under fixed (thick black) and variable (thick blue) R_f. The vertical structure of remote energy dissipation scales either as (a) N^2, (b) N, (c) 1, or (d) N^{-1}. The thin blue line shows results from an alternative variable R_f formulation where the lower limit of the energetic regime occurs at $\mathrm{Re}_b = 100$ instead of $\mathrm{Re}_b = 400$. Note the different vertical scale above and below $\gamma = 27\,\mathrm{kg\,m^{-3}}$. Neutral density ranges of bottom, deep, and mode/intermediate waters are indicated by the light gray shading and the right-end labels.

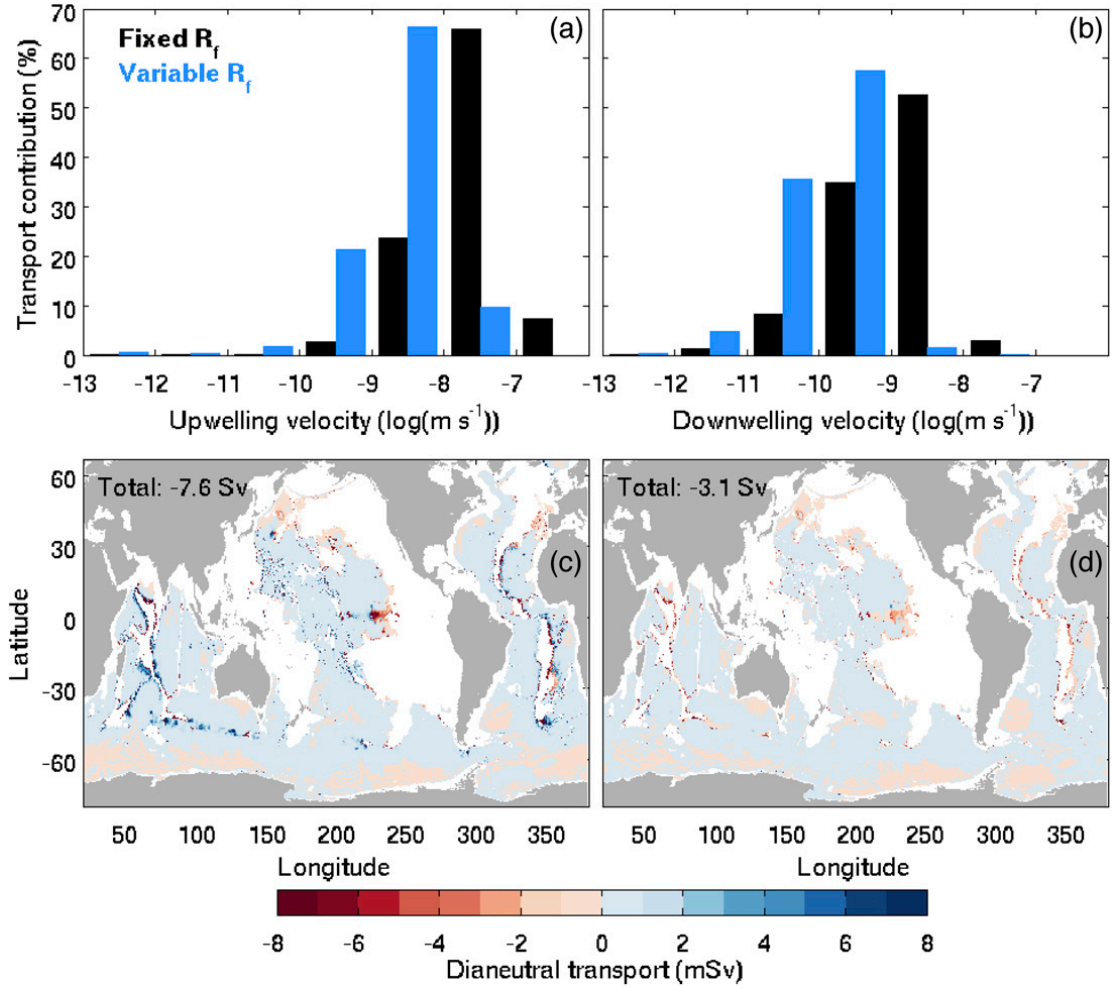

FIG. 7. Impact of mixing efficiency variability on the local structure of dianeutral transports. (a),(b) Contribution of given ranges of dianeutral velocity [log(m s^{-1})] to overall (a) upward and (b) downward transports under fixed (black) and variable (blue) R_f. (c),(d) Maps of local dianeutral transports (mSv) induced by near-field mixing across the 28.11 kg m^{-3} neutral surface according to (c) fixed and (d) variable R_f models.

2003; Talley 2008, 2013; Naveira Garabato et al. 2014). Radiation of low-mode internal tides, by redistributing internal wave energy over large ocean volumes and powering the background internal wave field, could be a more efficient driver of the abyssal overturning (Oka and Niwa 2013). Indeed, a fairly spread distribution of remote tidal dissipation would allow a larger fraction of the available energy to actually contribute to buoyancy exchange. Yet the amount of buoyancy transferred to abyssal waters is strongly dependent on the vertical structure of far-field dissipation, and little to no impact on the AABW layer is possible if the resultant mixing is mostly confined to the upper ocean. An important portion of the available energy may also be lost at continental margins without contributing to thermocline or deep-water mass transformation (Kelly et al. 2013; Waterhouse et al. 2014). Moreover, even in the highly favorable cases of vertically homogeneous or depth-increasing energy dissipation, far-field tidal mixing was estimated to contribute no more than 9–11 Sv of additional AABW upwelling.

Hence, taking current best estimates of the strength of the abyssal overturning at face value, we posit that additional sources of buoyancy or mixing are responsible for significant AABW consumption. However, nonlinearity of the Re_b-dependent model implies that additional power inputs to the internal wave field will be increasingly inefficient at causing additional mixing, especially if placed in the weakly stratified abyss. In contrast, the weak stratification of relatively light bottom waters ($\gamma \approx 28.11\,\mathrm{kg\,m^{-3}}$) plays in favor of their consumption by geothermal heating because it enhances the incrop area and thereby the overall heat gain of these neutral density layers (LMSNG). Thus, whereas mixing is more efficient at homogenizing well-stratified water masses, a direct buoyancy supply is more apt at

ultimately consuming well-homogenized waters. Nevertheless, the geothermal circulation, estimated to peak at about 5 Sv across $\gamma \approx 28.11\,\mathrm{kg\,m^{-3}}$ (Emile-Geay and Madec 2009; LMSNG), is likely insufficient to close the abyssal overturning. Another substantial contribution could be provided by mixing in constricted flows across deep sills, where strong shear, hydraulic jumps, and entrainment in descending plumes can cause much more intense mixing than the turbulence driven by instability of the internal wave field. Indeed, overflow-related mixing in major interbasin passages (Polzin et al. 1996; Bryden and Nurser 2003) or in small but widespread canyons cutting across ridge flanks and shelf slopes (Thurnherr and Speer 2003; Thurnherr et al. 2005) has been suggested to be an important actor of AABW transformation. In such deep overflows, concentrated yet highly efficient mixing is tenable because the swift, continuous inflow of dense waters maintains large density gradients.

We note that geothermal heating and internal wave breaking, by forcing upwelling along the bottom topography (St. Laurent et al. 2001; LMSNG), could contribute to drive the up-valley canyon flows suspected to trigger significant mixing downstream of canyon sills (Thurnherr et al. 2005). Nonetheless, the energy required to sustain passage flows and the associated mixing likely originates to a large extent in the surface, large-scale wind and buoyancy forcing of the general circulation (Hughes and Griffiths 2006; Hughes et al. 2009; Saenz et al. 2012). Except for the relatively small fraction of the large-scale wind work dissipated by lee-wave generation (Naveira Garabato et al. 2013), these forcings are absent from our calculations, which only include the breaking of lee and tidally forced internal waves as a direct mixing source.

To illustrate the inability of energy sources considered in this study to match bulk observational estimates of deep ocean mixing levels, we compute effective neutral density diffusivities as $\iint_\gamma F^\gamma_{\mathrm{eq}}\, dS / \iint_\gamma \partial_z \gamma\, dS$, restricted to the 32°S–48°N region, and plot the corresponding profiles of effective K_γ against the analogous inverse estimate of Lumpkin and Speer (2007) (Fig. 8). Using this definition of effective K_γ and a map of geothermal heat fluxes (Goutorbe et al. 2011), the contribution of geothermal heating can be incorporated in a fashion consistent to that of diapycnal mixing (LMSNG). Because the observationally based profile should reflect all processes affecting the inversed hydrographic properties, and since geothermal heating was shown to drive significant AABW consumption, we include its contribution here. When accounting for R_f variability, the envelope of effective diffusivities associated with the four tested scenarios remains well below the

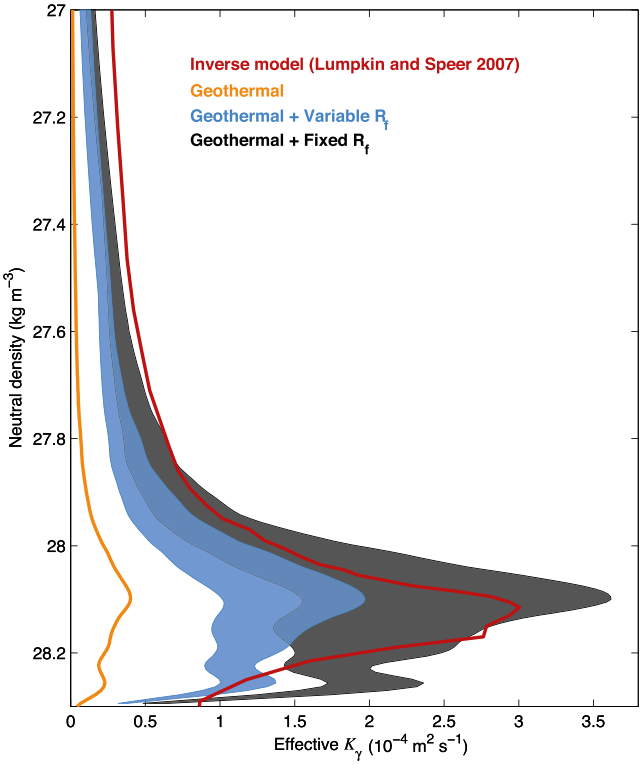

FIG. 8. Profiles of effective neutral density diffusivity ($10^{-4}\,\mathrm{m^2\,s^{-1}}$) for the 32°S–48°N region. The effective K_γ is calculated as $\iint_\gamma F^\gamma_{\mathrm{eq}}\, dS / \iint_\gamma \partial_z \gamma\, dS$. Effective diffusivities resulting from geothermal heating, near-field mixing and far-field mixing combined are shown for fixed (black) and variable (blue) R_f models, where the envelopes encompass the range of scenarios S2 to S−1. The contribution of geothermal heating alone (orange) and the inverse estimate of Lumpkin and Speer (2007) (red) are plotted. Data for the observationally based estimate obtained courtesy of R. Lumpkin.

observationally based estimate. With a fixed efficiency, effective diffusivities are significantly larger but also fall short of the inverse estimate at most levels under scenarios S2, S1, and S0. Interestingly, the mismatch is not only significant at abyssal levels but also at lighter densities throughout the range of deep, mode, and intermediate waters. The lack of mixing at these densities is suggestive of missing energy sources for the internal wave field, such as wind-generated near-inertial waves (Alford 2003; Rimac et al. 2013). Mixing in narrow passages at ridge crests could also provide for some of the missing deep-water transformation (Thurnherr 2006; St. Laurent and Thurnherr 2007). But given that AABW covers about two-thirds of the ocean floor (Johnson 2008), such boundary processes are expected to have a much more prominent role at abyssal densities.

Some clues as to which processes may supplement AABW consumption can be obtained by decomposing water mass transformation rates between the Indian, Pacific, and Atlantic basins (Table 2). Maximum

TABLE 2. Maximum abyssal upwelling rates (Sv) by basin as compared to the range of estimates from hydrographic inversions. Herein-estimated AABW upwelling rates correspond to the combined effect of near-field mixing, far-field mixing and geothermal heating. Scenarios used for the distribution of far-field dissipation are indicated in the top row. Considered observationally based estimates are referenced in the text.

	S2	S1	S0	S−1	Inverse estimates
30°S–67°N	10	13	18	20	20–30
Pacific	6	7	10	11	7–14
Atlantic	3	3	5	5	4–8
Indian	2	3	4	4	9–18

upwelling rates induced by near-field mixing, far-field mixing, and geothermal heating combined under variable R_f are indicated for all three basins, restricted to the region north of 30°S. Note that peak upwelling concurs with the peak incrop area for each basin and occurs at a slightly denser level in the Indian Ocean (28.14 kg m^{-3}) than in the other two basins (28.11 kg m^{-3}). Strikingly, the Indian Ocean also stands out when the presently estimated AABW consumption rates are compared to the approximate range of observational estimates for the strength of basin overturnings (Ganachaud and Wunsch 2000; Talley et al. 2003; Lumpkin and Speer 2007; Talley 2008, 2013). Although the Atlantic and Pacific AABW transports tend to lie on the low side of observational ranges, the discrepancy is much more pronounced in the Indian Ocean, for which all scenarios clearly fall short of the 9–18 Sv of overturning indicated by inverse estimates. Breaking internal waves in the ocean interior and geothermal heating appear unable to explain the disproportionate amount of AABW inflow to the Indian Ocean (Huussen et al. 2012; Decloedt and Luther 2012): its comparatively small area and incrop areas (not shown) would require unobserved, exceptionally strong internal wave activity or geothermal heat fluxes to sustain its strong abyssal circulation. Huussen et al. (2012) suggested that near-boundary mixing, likely concentrated in fracture zones and interbasin passages (MacKinnon et al. 2008), may instead provide for the required intense AABW transformation. Support for this hypothesis comes notably from the particularly dense network of ridges and fracture zones, the numerous subbasins (see Figs. 7c,d), and the high average abyssal hill roughness that characterize the Indian Ocean bathymetry (Goff and Arbic 2010; Huussen et al. 2012).

5. Conclusions

A recent turbulent diffusivity model that accounts for reduced mixing efficiencies in actively mixing waters was used to revise estimates of water mass transformation by breaking internal tides and lee waves. The variable R_f model led to a 50%–60% reduction of the global potential energy source and AABW upwelling rate attributable to lee-wave radiation and near-field tidal mixing taken in isolation. Indeed, mixing efficiency tends to be low in regions of enhanced internal wave breaking near rough topography, where intense turbulence rapidly erodes the near-bottom stratification, reducing its ability to sustain buoyancy fluxes. With only about 4 Sv of AABW consumption and 45 GW of global potential energy supply, the overall contribution of parameterized near-field mixing to the maintenance of the abyssal stratification is found to be comparable to that of geothermal heating.

To explore the potential importance of varying mixing efficiencies for remotely dissipating internal tides, we specified four idealized distributions of remote tidal dissipation: the available power was horizontally spread around generation sites and distributed in the vertical by assuming that energy dissipation scales with N^2, N, 1, or N^{-1}. Rather than realistic parameterizations of remote energy dissipation, these idealized scenarios are meant to achieve preliminary understanding and to provide probable bounds on water mass transformation by far-field tidal mixing. The addition of far-field energy dissipation raises the AABW consumption rate to 5–15 Sv and the potential energy supply to 107–134 GW, compared to 10–33 Sv and 161–231 GW under the traditional assumption of a fixed efficiency, where the ranges encompass the four tested vertical structures. Thus, whether low-mode internal tides tend to cause mixing in the pycnocline away from AABW or in weakly stratified abyssal waters, breaking lee waves and internal tides appear unable to sustain alone a 20–30-Sv abyssal overturning.

The important role of variability in mixing efficiency for deep-water mass transformation and ocean energetics implies that the common assumption of a constant efficiency of 17%–20% should be abandoned for more consistent formulations, such as the Re_b-dependent model employed here (Shih et al. 2005; Bouffard and Boegman 2013). In particular, the $R_f(\mathrm{Re}_b)$ model is suitable for inclusion in mixing parameterizations of ocean models that infer diapycnal diffusivities from energy dissipation rates (St. Laurent et al. 2002; Polzin 2009; Olbers and Eden 2013). Its implementation will obviate the need to impose an arbitrary minimum on stratification when deducing K_ρ from N^2 and ε_T (Simmons et al. 2004; Oka and Niwa 2013) and will strongly reduce sensitivity to the chosen upper bound on K_ρ. Moreover, it will allow the buoyancy flux to naturally satisfy the no-flux bottom boundary condition (e.g., Melet et al. 2013a).

TABLE A1. Parameterization of the diapycnal heat diffusivity. The top two rows describe the Re_b-dependent formulation of Bouffard and Boegman (2013). The bottom two rows indicate ranges and equations used in the present implementation. The indicated upper limits of the energetic regime correspond to the imposed upper-bound on K_Θ, taken as $10^{-2}\,\mathrm{m^2\,s^{-1}}$.

Regime	Molecular	Buoyancy controlled	Transitional	Energetic
Re_b (range)	[0; 1.7]	[1.7; 8.5]	[8.5; 400]	[400; 6.25×10^6]
$K_\Theta(\mathrm{Re}_b)$ ($\mathrm{m^2\,s^{-1}}$)	1.4×10^{-7}			
Re_b^T (range)	[0; 1.93]	[1.93; 10.2]	[10.2; 480]	[480; 7.50×10^7]
$K_\Theta(\mathrm{Re}_b^T)$ ($\mathrm{m^2\,s^{-1}}$)	1.4×10^{-7}			

Although this Re_b-dependent parameterization has been shown to be consistent with available numerical, experimental, and field data (Bouffard and Boegman 2013), including Brazil basin observations (Ledwell et al. 2000), significant uncertainty remains in the exact definition of the different regimes. Because decreased mixing efficiencies and differential diffusion at low turbulence intensities have a minimal impact on large-scale transformation by internal wave-driven mixing, only uncertainty at relatively high Re_b is of concern here. We tested an alternative variable R_f formulation where the shift from the transitional to the energetic regime occurs at a lower Re_b level. This formulation, which agrees more closely with numerical results (Shih et al. 2005) but less so with field measurements (Bouffard and Boegman 2013), leads to even stronger reductions of potential energy input and AABW consumption by internal wave breaking, with near-field and far-field mixing together contributing 3–8 Sv of AABW upwelling north of 30°S. The sensitivity to this critical Re_b highlights the need to reduce uncertainties associated with validity ranges of the high-diffusivity regimes. Targeted field measurements (e.g., Bluteau et al. 2013) are required to further constrain the Re_b dependence of mixing efficiency in strongly mixing waters and to critically examine the model's limitations across a range of oceanic conditions and scales.

Local oceanic mixing efficiencies likely depend on the specific flow instabilities through which energy cascades to the dissipation scale, and the time–space intermittency of turbulence implies that they must vary on short spatial and temporal scales (Smyth et al. 2001; Ivey et al. 2008; Mashayek et al. 2013; Mashayek and Peltier 2013). Ocean general circulation models do not resolve the turbulent cascade and require parameterizations that realistically incorporate the large-scale statistics of irreversible mixing (Arneborg 2002). Although the universality of the proposed Re_b regimes is debatable (e.g., Mater and Venayagamoorthy 2014), it is argued that the $R_f(\mathrm{Re}_b)$ model improves upon the constant efficiency assumption by capturing some of the statistical variability of oceanic mixing efficiency, in accord with observations and theory (Bouffard and Boegman 2013). Implementation of the Re_b-dependent parameterization, together with efforts to refine and generalize the model by factoring in the process and scale dependence of mixing efficiency, should therefore contribute to improve the representation of diapycnal mixing in ocean models.

Acknowledgments. We are grateful to F. Roquet and A. Melet for sharing the datasets of the energy flux into internal tides of Nycander (2005) and Melet et al. (2013b). We also thank R. Lumpkin for providing data from his inverse solution and J.-B. Sallée for helpful comments on the manuscript. Suggestions from two anonymous reviewers helped to substantially improve the manuscript. This work was undertaken as part of the EMBRACE project, funded by the European Union's Seventh Framework Programme under Grant Agreement 282672.

APPENDIX

Implementation of the Turbulent Diffusivity Model

The turbulent diffusivity (Shih et al. 2005; Bouffard and Boegman 2013) and diffusivity ratio (Jackson and Rehmann 2014) parameterizations considered in this study are both expressed as a function of the turbulence intensity parameter $\mathrm{Re}_b = \varepsilon_\nu/(\nu N^2)$. Although frictional dissipation ε_ν is the most readily accessible quantity from observations in the field, mixing parameterizations for ocean models are formulated upon the energy lost to the internal wave field, $\varepsilon_T = \varepsilon_\nu + K_\rho N^2$. To reframe the model equations in terms of ε_T rather than ε_ν, we first define a modified turbulence intensity parameter $\mathrm{Re}_b^T = \varepsilon_T/(\nu N^2) = \mathrm{Re}_b + (K_\rho/\nu)$. The Re_b^T-dependent formulation can then obtained by substituting $\mathrm{Re}_b^T - (K_\rho/\nu)$ for Re_b in $K_\rho(\mathrm{Re}_b)$ equations and solving for K_ρ. This is easily done for the transitional and energetic regimes:

$$\text{Transitional } (10.2 \le \mathrm{Re}_b^T \le 480)\text{: } K_\rho = \frac{1}{6}\nu\,\mathrm{Re}_b^T \quad \text{and} \tag{A1}$$

$$\text{Energetic } (480 \le \mathrm{Re}_b^T)\text{: } K_\rho = 4\nu\left(\sqrt{4 + \mathrm{Re}_b^T} - 2\right). \tag{A2}$$

No simple analytical solution can be obtained for the buoyancy-controlled regime, however. Given the inherent

degree of uncertainty in the exponents and coefficients of the Bouffard and Boegman (2013) experimental fits, we deem it justified to simplify Re_b^T-dependent equations in the buoyancy-controlled and energetic regimes by using expressions of the form $K_\rho = C\nu(\mathrm{Re}_b^T)^n$, where the exponent n is kept the same as in the original Re_b-based fits, and the nondimensional constant C is adjusted to respect both continuity and the limits of the transitional regime (Table A1). This simplification conserves the general behavior of the energetic regime, and the resulting K_ρ deviates by less than 10% from that given by (A2). Note that the difference between heat and density diffusivities at low Re_b complicates in principle the reformulation of K_Θ in the buoyancy-controlled regime, but such complications can be ignored in view of the above-mentioned uncertainty, especially in this weak diffusivity regime.

The salt diffusivity is then deduced from $K_\Theta(\mathrm{Re}_b^T)$ using the diffusivity ratio parameterized by Jackson and Rehmann (2014):

$$K_{S_A}/K_\Theta = \frac{1.01}{2} + \frac{0.99}{2}\tanh\left\{0.92\left[\log\left(\frac{5}{6}\mathrm{Re}_b^T\right) - 0.60\right]\right\}, \tag{A3}$$

where the original equation was simply modified by replacing Re_b with $(5/6)\mathrm{Re}_b^T$. This modification introduces a slight distortion of the original fit outside of the transitional regime but preserves the exact Re_b dependence within $8.5 \le \mathrm{Re}_b \le 400$. Again, this necessary adjustment is deemed well within the uncertainty of the parameterization.

REFERENCES

Alford, M. H., 2003: Improved global maps and 54-year history of wind-work on ocean inertial motions. *Geophys. Res. Lett.*, **30**, 1424, doi:10.1029/2002GL016614.

Arneborg, L., 2002: Mixing efficiencies in patchy turbulence. *J. Phys. Oceanogr.*, **32**, 1496–1506, doi:10.1175/1520-0485(2002)032<1496:MEIPT>2.0.CO;2.

——, and B. Liljebladh, 2001: The internal seiches in Gullmar Fjord. Part II: Contribution to basin water mixing. *J. Phys. Oceanogr.*, **31**, 2567–2574, doi:10.1175/1520-0485(2001)031<2567:TISIGF>2.0.CO;2.

Barry, M. E., G. N. Ivey, K. B. Winters, and J. Imberger, 2001: Measurements of diapycnal diffusivities in stratified fluids. *J. Fluid Mech.*, **442**, 267–291, doi:10.1017/S0022112001005080.

Bluteau, C. E., N. L. Jones, and G. N. Ivey, 2013: Turbulent mixing efficiency at an energetic ocean site. *J. Geophys. Res.*, **118**, 4662–4672, doi:10.1002/jgrc.20292.

Bouffard, D., and L. Boegman, 2013: A diapycnal diffusivity model for stratified environmental flows. *Dyn. Atmos. Oceans*, **61–62**, 14–34, doi:10.1016/j.dynatmoce.2013.02.002.

Bryan, K., and L. J. Lewis, 1979: A water mass model of the World Ocean. *J. Geophys. Res.*, **84**, 2503–2517, doi:10.1029/JC084iC05p02503.

Bryden, H. L., and A. J. G. Nurser, 2003: Effects of strait mixing on ocean stratification. *J. Phys. Oceanogr.*, **33**, 1870–1872, doi:10.1175/1520-0485(2003)033<1870:EOSMOO>2.0.CO;2.

Davis, K. A., and S. G. Monismith, 2011: The modification of bottom boundary layer turbulence and mixing by internal waves shoaling on a barrier reef. *J. Phys. Oceanogr.*, **41**, 2223–2241, doi:10.1175/2011JPO4344.1.

de Lavergne, C., G. Madec, J. Le Sommer, A. J. G. Nurser, and A. C. Naveira Garabato, 2015: On the consumption of Antarctic Bottom Water in the abyssal ocean. *J. Phys. Oceanogr.*, **46**, 635–651, doi:10.1175/JPO-D-14-0201.1.

de Young, B., and S. Pond, 1989: Partition of energy loss from the barotropic tide in fjords. *J. Phys. Oceanogr.*, **19**, 246–252, doi:10.1175/1520-0485(1989)019<0246:POELFT>2.0.CO;2.

Decloedt, T., and D. S. Luther, 2012: Spatially heterogeneous diapycnal mixing in the abyssal ocean: A comparison of two parameterizations to observations. *J. Geophys. Res.*, **117**, C11025, doi:10.1029/2012JC008304.

Dunckley, J. F., J. R. Koseff, J. V. Steinbuck, S. G. Monismith, and A. Genin, 2012: Comparison of mixing efficiency and vertical diffusivity models from temperature microstructure. *J. Geophys. Res.*, **117**, C10008, doi:10.1029/2012JC007967.

Eden, C., and D. Olbers, 2014: An energy compartment model for propagation, nonlinear interaction, and dissipation of internal gravity waves. *J. Phys. Oceanogr.*, **44**, 2093–2106, doi:10.1175/JPO-D-13-0224.1.

Emile-Geay, J., and G. Madec, 2009: Geothermal heating, diapycnal mixing and the abyssal circulation. *Ocean Sci.*, **5**, 203–217, doi:10.5194/os-5-203-2009.

Ganachaud, A., and C. Wunsch, 2000: Improved estimates of global ocean circulation, heat transport and mixing from hydrographic data. *Nature*, **408**, 453–457, doi:10.1038/35044048.

Gargett, A. E., 1984: Vertical eddy diffusivity in the ocean interior. *J. Mar. Res.*, **42**, 359–393, doi:10.1357/002224084788502756.

Gloor, M., A. Wüest, and D. M. Imboden, 2000: Dynamics of mixed bottom boundary layers and its implications for diapycnal transport in a stratified, natural water basin. *J. Geophys. Res.*, **105**, 8629–8646, doi:10.1029/1999JC900303.

Goff, J. A., and B. K. Arbic, 2010: Global prediction of abyssal hill roughness statistics for use in ocean models from digital maps of paleo-spreading rate, paleo-ridge orientation, and sediment thickness. *Ocean Modell.*, **32**, 36–43, doi:10.1016/j.ocemod.2009.10.001.

Gouretski, V. V., and K. P. Koltermann, 2004: WOCE global hydrographic climatology. Bundesamt für Seeschifffahrt und Hydrographie Tech. Rep. 35, 52 pp. [Available online at http://odv.awi.de/fileadmin/user_upload/odv/data/Gouretski-Koltermann-2004/BSH35_report_final.pdf.]

Goutorbe, B., J. Poort, F. Lucazeau, and S. Raillard, 2011: Global heat flow trends resolved from multiple geological and geophysical proxies. *Geophys. J. Int.*, **187**, 1405–1419, doi:10.1111/j.1365-246X.2011.05228.x.

Holt, S. E., J. R. Koseff, and J. H. Ferziger, 1992: A numerical study of the evolution and structure of homogenous stably stratified sheared turbulence. *J. Fluid Mech.*, **237**, 499–539, doi:10.1017/S0022112092003513.

Huang, R. X., 1999: Mixing and energetics of the oceanic thermohaline circulation. *J. Phys. Oceanogr.*, **29**, 727–746, doi:10.1175/1520-0485(1999)029<0727:MAEOTO>2.0.CO;2.

Hughes, G. O., and R. W. Griffiths, 2006: A simple convective model of the global overturning circulation, including effects

of entrainment into sinking regions. *Ocean Modell.*, **12**, 46–79, doi:10.1016/j.ocemod.2005.04.001.

——, A. M. Hogg, and R. W. Griffiths, 2009: Available potential energy and irreversible mixing in the meridional overturning circulation. *J. Phys. Oceanogr.*, **39**, 3130–3146, doi:10.1175/2009JPO4162.1.

Hult, E. L., C. D. Troy, and J. R. Koseff, 2011: The mixing efficiency of interfacial waves breaking at a ridge: 1. Overall mixing efficiency. *J. Geophys. Res.*, **116**, C02003, doi:10.1029/2010JC006485.

Huussen, T. N., A. C. Naveira Garabato, H. L. Bryden, and E. L. McDonagh, 2012: Is the deep Indian Ocean MOC sustained by breaking internal waves? *J. Geophys. Res.*, **117**, C08024, doi:10.1029/2012JC008236.

Inall, M. E., 2009: Internal wave induced dispersion and mixing on a sloping boundary. *Geophys. Res. Lett.*, **36**, L05604, doi:10.1029/2008GL036849.

Iudicone, D., G. Madec, B. Blanke, and S. Speich, 2008a: The role of Southern Ocean surface forcings and mixing in the global conveyor. *J. Phys. Oceanogr.*, **38**, 1377–1400, doi:10.1175/2008JPO3519.1.

——, ——, and T. J. McDougall, 2008b: Water-mass transformations in a neutral density framework and the key role of light penetration. *J. Phys. Oceanogr.*, **38**, 1357–1376, doi:10.1175/2007JPO3464.1.

Ivey, G. N., K. B. Winters, and J. R. Koseff, 2008: Density stratification, turbulence, but how much mixing? *Annu. Rev. Fluid Mech.*, **40**, 169–184, doi:10.1146/annurev.fluid.39.050905.110314.

Jackett, D. R., and T. J. McDougall, 1997: A neutral density variable for the world's oceans. *J. Phys. Oceanogr.*, **27**, 237–263, doi:10.1175/1520-0485(1997)027<0237:ANDVFT>2.0.CO;2.

Jackson, P. R., and C. R. Rehmann, 2003: Laboratory measurements of differential diffusion in a diffusively stable, turbulent flow. *J. Phys. Oceanogr.*, **33**, 1592–1603, doi:10.1175/2405.1.

——, and ——, 2014: Experiments on differential scalar mixing in turbulence in a sheared, stratified flow. *J. Phys. Oceanogr.*, **44**, 2661–2680, doi:10.1175/JPO-D-14-0027.1.

Johnson, G. C., 2008: Quantifying Antarctic Bottom Water and North Atlantic Deep Water volumes. *J. Geophys. Res.*, **113**, C05027, doi:10.1029/2007JC004477.

Kelly, S. M., N. L. Jones, J. D. Nash, and A. F. Waterhouse, 2013: The geography of semidiurnal mode-1 internal-tide energy loss. *Geophys. Res. Lett.*, **40**, 4689–4693, doi:10.1002/grl.50872.

Klocker, A., and T. J. McDougall, 2010: Influence of the nonlinear equation of state on global estimates of dianeutral advection and diffusion. *J. Phys. Oceanogr.*, **40**, 1690–1709, doi:10.1175/2010JPO4303.1.

Ledwell, J. R., A. J. Watson, and C. S. Law, 1998: Mixing of a tracer in the pycnocline. *J. Geophys. Res.*, **103**, 21 499–21 529, doi:10.1029/98JC01738.

——, E. T. Montgomery, K. L. Polzin, L. C. St. Laurent, R. W. Schmitt, and J. M. Toole, 2000: Evidence for enhanced mixing over rough topography in the abyssal ocean. *Nature*, **403**, 179–182, doi:10.1038/35003164.

Lumpkin, R., and K. Speer, 2007: Global ocean meridional overturning. *J. Phys. Oceanogr.*, **37**, 2550–2562, doi:10.1175/JPO3130.1.

MacKinnon, J. A., T. M. S. Johnston, and R. Pinkel, 2008: Strong transport and mixing of deep water through the Southwest Indian Ridge. *Nat. Geosci.*, **1**, 755–758, doi:10.1038/ngeo340.

——, M. H. Alford, R. Pinkel, J. Klymak, and Z. Zhao, 2013: The latitudinal dependence of shear and mixing in the Pacific transiting the critical latitude for PSI. *J. Phys. Oceanogr.*, **43**, 3–16, doi:10.1175/JPO-D-11-0107.1.

Mashayek, A., and W. R. Peltier, 2013: Shear-induced mixing in geophysical flows: Does the route to turbulence matter to its efficiency? *J. Fluid Mech.*, **725**, 216–261, doi:10.1017/jfm.2013.176.

——, C. P. Caulfield, and W. R. Peltier, 2013: Time-dependent, non-monotonic mixing in stratified turbulent shear flows: implications for oceanographic estimates of buoyancy flux. *J. Fluid Mech.*, **736**, 570–593, doi:10.1017/jfm.2013.551.

Mater, B. D., and S. K. Venayagamoorthy, 2014: The quest for an unambiguous parameterization of mixing efficiency in stably stratified geophysical flows. *Geophys. Res. Lett.*, **41**, 4646–4653, doi:10.1002/2014GL060571.

Melet, A., R. Hallberg, S. Legg, and K. L. Polzin, 2013a: Sensitivity of the ocean state to the vertical distribution of internal tide-driven mixing. *J. Phys. Oceanogr.*, **43**, 602–615, doi:10.1175/JPO-D-12-055.1.

——, M. Nikurashin, C. Muller, S. Falahat, J. Nycander, P. G. Timko, B. K. Arbic, and J. A. Goff, 2013b: Internal tide generation by abyssal hills using analytical theory. *J. Geophys. Res.*, **118**, 6303–6318, doi:10.1002/2013JC009212.

Merryfield, W. J., 2005: Dependence of differential mixing on N and R_ρ. *J. Phys. Oceanogr.*, **35**, 991–1003, doi:10.1175/JPO2747.1.

Munk, W. H., 1966: Abyssal recipes. *Deep-Sea Res. Oceanogr. Abstr.*, **13**, 707–730, doi:10.1016/0011-7471(66)90602-4.

——, and C. Wunsch, 1998: Abyssal recipes II: Energetics of tidal and wind mixing. *Deep-Sea Res.*, **45**, 1977–2010, doi:10.1016/S0967-0637(98)00070-3.

Naveira Garabato, A. C., A. J. G. Nurser, R. B. Scott, and J. A. Goff, 2013: The impact of small-scale topography on the dynamical balance of the ocean. *J. Phys. Oceanogr.*, **43**, 647–668, doi:10.1175/JPO-D-12-056.1.

——, A. P. Williams, and S. Bacon, 2014: The three-dimensional overturning circulation of the Southern Ocean during the WOCE era. *Prog. Oceanogr.*, **120**, 41–78, doi:10.1016/j.pocean.2013.07.018.

Nikurashin, M., R. Ferrari, N. Grisouard, and K. L. Polzin, 2014: The impact of finite-amplitude bottom topography on internal wave generation in the Southern Ocean. *J. Phys. Oceanogr.*, **44**, 2938–2950, doi:10.1175/JPO-D-13-0201.1.

Niwa, Y., and T. Hibiya, 2011: Estimation of baroclinic tide energy available for deep ocean mixing based on three-dimensional global numerical simulations. *J. Oceanogr.*, **67**, 493–502, doi:10.1007/s10872-011-0052-1.

Nycander, J., 2005: Generation of internal waves in the deep ocean by tides. *J. Geophys. Res.*, **110**, C10028, doi:10.1029/2004JC002487.

Oka, A., and Y. Niwa, 2013: Pacific deep circulation and ventilation controlled by tidal mixing away from the sea bottom. *Nat. Commun.*, **4**, 2419, doi:10.1038/ncomms3419.

Olbers, D., and C. Eden, 2013: A global model for the diapycnal diffusivity induced by internal gravity waves. *J. Phys. Oceanogr.*, **43**, 1759–1779, doi:10.1175/JPO-D-12-0207.1.

Osborn, T. R., 1980: Estimates of the local rate of vertical diffusion from dissipation measurements. *J. Phys. Oceanogr.*, **10**, 83–89, doi:10.1175/1520-0485(1980)010<0083:EOTLRO>2.0.CO;2.

Polzin, K. L., 2009: An abyssal recipe. *Ocean Modell.*, **30**, 298–309, doi:10.1016/j.ocemod.2009.07.006.

——, K. G. Speer, J. M. Toole, and R. W. Schmitt, 1996: Intense mixing of Antarctic Bottom Water in the equatorial Atlantic Ocean. *Nature*, **380**, 54–57, doi:10.1038/380054a0.

Rehmann, C. R., and J. R. Koseff, 2004: Mean potential energy change in stratified grid turbulence. *Dyn. Atmos. Oceans*, **37**, 271–294, doi:10.1016/j.dynatmoce.2003.09.001.

Rimac, A., J.-S. von Storch, C. Eden, and H. Haak, 2013: The influence of high-resolution wind stress field on the power input to near-inertial motions in the ocean. *Geophys. Res. Lett.*, **40**, 4882–4886, doi:10.1002/grl.50929.

Ruddick, B., D. Walsh, and N. Oakey, 1997: Variations in apparent mixing efficiency in the North Atlantic Central Water. *J. Phys. Oceanogr.*, **27**, 2589–2605, doi:10.1175/1520-0485(1997)027<2589:VIAMEI>2.0.CO;2.

Saenz, J. A., A. M. Hogg, G. O. Hughes, and R. W. Griffiths, 2012: Mechanical power input from buoyancy and wind to the circulation in an ocean model. *Geophys. Res. Lett.*, **38**, L13605, doi:10.1029/2012GL052035.

Scott, R. B., J. A. Goff, A. C. Naveira Garabato, and A. J. G. Nurser, 2011: Global rate and spectral characteristics of internal gravity wave generation by geostrophic flow over topography. *J. Geophys. Res.*, **116**, C09029, doi:10.1029/2011JC007005.

Sheen, K. L., and Coauthors, 2013: Rates and mechanisms of turbulent dissipation and mixing in the Southern Ocean: Results from the Diapycnal and Isopycnal Mixing Experiment in the Southern Ocean (DIMES). *J. Geophys. Res.*, **118**, 2774–2792, doi:10.1002/jgrc.20217.

Shih, L. H., J. R. Koseff, G. N. Ivey, and J. H. Ferziger, 2005: Parameterization of turbulent fluxes and scales using homogeneous sheared stably stratified turbulence simulations. *J. Fluid Mech.*, **525**, 193–214, doi:10.1017/S0022112004002587.

Simmons, H. L., S. R. Jayne, L. C. St. Laurent, and A. J. Weaver, 2004: Tidally driven mixing in a numerical model of the ocean general circulation. *Ocean Modell.*, **6**, 245–263, doi:10.1016/S1463-5003(03)00011-8.

Smyth, W. D., J. N. Moum, and D. R. Caldwell, 2001: The efficiency of mixing in turbulent patches: Inferences from direct simulations and microstructure observations. *J. Phys. Oceanogr.*, **31**, 1969–1992, doi:10.1175/1520-0485(2001)031<1969:TEOMIT>2.0.CO;2.

St. Laurent, L. C., and R. W. Schmitt, 1999: The contribution of salt fingers to vertical mixing in the North Atlantic Tracer Release Experiment. *J. Phys. Oceanogr.*, **29**, 1404–1424, doi:10.1175/1520-0485(1999)029<1404:TCOSFT>2.0.CO;2.

——, and A. M. Thurnherr, 2007: Intense mixing of lower thermocline water on the crest of the Mid-Atlantic Ridge. *Nature*, **448**, 680–683, doi:10.1038/nature06043.

——, J. R. Toole, and R. W. Schmitt, 2001: Buoyancy forcing by turbulence above rough topography in the abyssal Brazil basin. *J. Phys. Oceanogr.*, **31**, 3476–3495, doi:10.1175/1520-0485(2001)031<3476:BFBTAR>2.0.CO;2.

——, H. L. Simmons, and S. R. Jayne, 2002: Estimating tidally driven mixing in the deep ocean. *Geophys. Res. Lett.*, **29**, 21-1–21-4, doi:10.1029/2002GL015633.

Stigebrandt, A., 1976: Vertical diffusion driven by internal waves in a sill fjord. *J. Phys. Oceanogr.*, **6**, 486–495, doi:10.1175/1520-0485(1976)006<0486:VDDBIW>2.0.CO;2.

——, and J. Aure, 1989: Vertical mixing in basin waters of fjords. *J. Phys. Oceanogr.*, **19**, 917–926, doi:10.1175/1520-0485(1989)019<0917:VMIBWO>2.0.CO;2.

Talley, L. D., 2008: Freshwater transport estimates and the global overturning circulation: Shallow, deep and throughflow components. *Prog. Oceanogr.*, **78**, 257–303, doi:10.1016/j.pocean.2008.05.001.

——, 2013: Closure of the global overturning circulation through the Indian, Pacific and Southern Oceans: Schematics and transports. *Oceanography*, **26**, 80–97, doi:10.5670/oceanog.2013.07.

——, J. L. Reid, and P. E. Robbins, 2003: Data-based meridional overturning streamfunctions for the global ocean. *J. Climate*, **16**, 3213–3226, doi:10.1175/1520-0442(2003)016<3213:DMOSFT>2.0.CO;2.

Thurnherr, A. M., 2006: Diapycnal mixing associated with an overflow in a deep submarine canyon. *Deep-Sea Res.*, **53**, 194–206, doi:10.1016/j.dsr2.2005.10.020.

——, and K. G. Speer, 2003: Boundary mixing and topographic blocking on the Mid-Atlantic Ridge in the South Atlantic. *J. Phys. Oceanogr.*, **33**, 848–862, doi:10.1175/1520-0485(2003)33<848:BMATBO>2.0.CO;2.

——, L. C. St. Laurent, K. G. Speer, J. M. Toole, and J. R. Ledwell, 2005: Mixing associated with sills in a canyon on the midocean ridge flank. *J. Phys. Oceanogr.*, **35**, 1370–1381, doi:10.1175/JPO2773.1.

Toole, J. M., R. W. Schmitt, and K. L. Polzin, 1994: Estimates of diapycnal mixing in the abyssal ocean. *Science*, **264**, 1120–1123, doi:10.1126/science.264.5162.1120.

Waterhouse, A. F., and Coauthors, 2014: Global patterns of diapycnal mixing from measurements of the turbulent dissipation rate. *J. Phys. Oceanogr.*, **44**, 1854–1872, doi:10.1175/JPO-D-13-0104.1.

Waterman, S., A. C. Naveira Garabato, and K. L. Polzin, 2013: Internal waves and turbulence in the Antarctic Circumpolar Current. *J. Phys. Oceanogr.*, **43**, 259–282, doi:10.1175/JPO-D-11-0194.1.

——, K. L. Polzin, A. C. Naveira Garabato, K. L. Sheen, and A. Forryan, 2014: Suppression of internal wave breaking in the Antarctic Circumpolar Current near topography. *J. Phys. Oceanogr.*, **44**, 1466–1492, doi:10.1175/JPO-D-12-0154.1.

Watson, A. J., and J. R. Ledwell, 2000: Oceanographic tracer release experiments using sulphur hexafluoride. *J. Geophys. Res.*, **105**, 14 325–14 337, doi:10.1029/1999JC900272.

Wunsch, C., and R. Ferrari, 2004: Vertical mixing, energy, and the general circulation of the oceans. *Annu. Rev. Fluid Mech.*, **36**, 281–314, doi:10.1146/annurev.fluid.36.050802.122121.

References

Barry, M. E., Ivey, G. N., Winters, K. B., and Imberger, J. (2001). Measurements of diapycnal diffusivities in stratified fluids. *Journal of Fluid Mechanics*, 442:267–291.

Bluteau, C. E., Jones, N. L., and Ivey, G. N. (2013). Turbulent mixing efficiency at an energetic ocean site. *Journal of Geophysical Research*, 118(9):4662–4672.

Bouffard, D. and Boegman, L. (2013). A diapycnal diffusivity model for stratified environmental flows. *Dynamics of Atmospheres and Oceans*, 61-62:14–34.

Gregg, M., Alford, M., Kontoyiannis, H., Zervakis, V., and Winkel, D. (2012). Mixing over the steep side of the Cycladic Plateau in the Aegean Sea. *Journal of Marine Systems*, 89(1):30–47.

Kunze, E., MacKay, C., McPhee-Shaw, E. E., Morrice, K., Girton, J. B., and Terker, S. R. (2012). Turbulent mixing and exchange with interior waters on sloping boundaries. *Journal of Physical Oceanography*, 42(6):910–927.

Ledwell, J. R., Montgomery, E. T., Polzin, K. L., Laurent, L. C. S., Schmitt, R. W., and Toole, J. M. (2000). Evidence for enhanced mixing over rough topography in the abyssal ocean. *Nature*, 403(6766):179–182.

Ledwell, J. R., Watson, A. J., and Law, C. S. (1993). Evidence for slow mixing across the pycnocline from an open-ocean tracer-release experiment. *Nature*, 364(6439):701–703.

Lozovatsky, I. D. and Fernando, H. J. S. (2012). Mixing efficiency in natural flows. *Philosophical Transactions of the Royal Society*, 371(1982):20120213–20120213.

Mater, B. D. and Venayagamoorthy, S. K. (2014). The quest for an unambiguous parameterization of mixing efficiency in stably stratified geophysical flows. *Geophysical Research Letters*, 41(13):4646–4653.

Melet, A., Hallberg, R., Legg, S., and Polzin, K. (2013). Sensitivity of the ocean state to the vertical distribution of internal-tide-driven mixing. *Journal of Physical Oceanography*, 43(3):602–615.

Oka, A. and Niwa, Y. (2013). Pacific deep circulation and ventilation controlled by tidal mixing away from the sea bottom. *Nature Communications*, 4.

Osborn, T. R. (1980). Estimates of the local rate of vertical diffusion from dissipation measurements. *Journal of Physical Oceanography*, 10(1):83–89.

Saenko, O. A. and Merryfield, W. J. (2005). On the effect of topographically enhanced mixing on the global ocean circulation. *Journal of Physical Oceanography*, 35(5).

Shih, L. H., Koseff, J. R., Ivey, G. N., and Ferziger, J. H. (2005). Parameterization of turbulent fluxes and scales using homogeneous sheared stably stratified turbulence simulations. *Journal of Fluid Mechanics*, 525:193–214.

Simmons, H. L., Jayne, S. R., Laurent, L. C., and Weaver, A. J. (2004). Tidally driven mixing in a numerical model of the ocean general circulation. *Ocean Modelling*, 6(3-4):245–263.

CHAPTER

III

Geometric controls of the meridional overturning

Estimates of abyssal water mass transformation presented in chapters I and II revealed a robust feature: upwelling rates tend to peak within the neutral density layer which has the largest seafloor coverage. This feature is mainly caused by the following factor: the bottom boundary condition on the diffusive density flux favours the destruction of near-bottom waters. It is amplified by two additional factors: turbulence tends to be concentrated along boundaries, so that interior density fluxes tend to be strongest near the bottom boundary; the global incrop area profile exhibits a sharp peak, so that a narrow density range monopolizes a sizeable fraction of the ocean floor.

The climatological neutral density field thus contains much information about the structure of the abyssal overturning. Through the peak incrop area, it determines the neutral surface of peak upwelling and the boundary between southward-flowing deep waters and northward-flowing bottom waters. Through the narrow density range of significant incrop areas, it constrains the overall vertical range of strong diabatic transports. By revealing that Antarctic Bottom Water (AABW) monopolizes access to the seafloor, it corroborates the picture of an overturning characterized by a diabatic, northward abyssal branch contrasting with a predominantly adiabatic, deep southward branch.

That the observed density field tells much about the abyssal overturning is perhaps not surprising given that it is largely shaped by that circulation. Indeed, because the AABW circulation is essentially diabatic, abyssal flows and density gradients are tightly coupled. Nonetheless, since it is specifically the *seabed coverage* of density layers that controls the structure

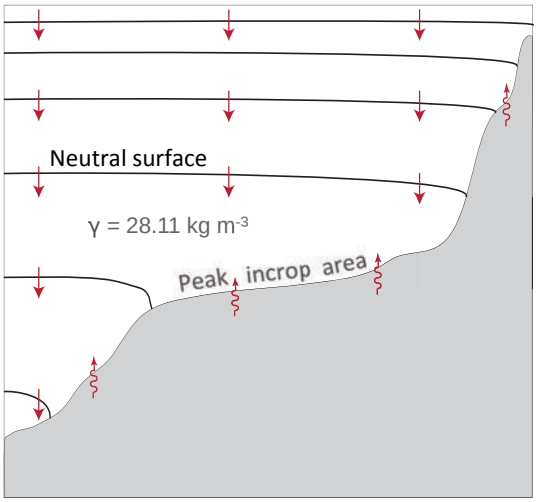

Figure 0: Schematic showing a set of neutral density layers (delimited by black lines) intersecting the seafloor (gray). The thickness of density layers increases with depth in accord with a depth-decreasing stratification. A combination of weak stratification and weakly sloping floor gives the layer centred around neutral density $\gamma = 28.11$ kg m^{-3} the largest seafloor coverage. The no-flux bottom boundary condition on the downward mixing-driven buoyancy flux (straight red arrows) and the presence of a bottom geothermal buoyancy source (red wiggly arrows) mean that this layer is likely to receive more buoyancy than its neighbours.

of diabatic upwelling, the mere distribution of ocean floor may already contain significant information about the abyssal overturning. Large incrop areas result from the combination of weak stratification and weakly sloping floor (Fig. 0). The freedom the ocean has to establish the level of peak upwelling and the structure of the abyssal overturning should thus depend on the balance between stratification and topography controls on large incrop areas.

In this chapter, we show that the depth distribution of ocean floor is a major determinant of AABW's itinerary across the deep Pacific, Indian and Atlantic basins, thereby limiting the degrees of freedom of the abyssal ocean to adjust to new boundary conditions.

Abstract:

The deep ocean is broadly characterized by northward flow of densest waters in the abyss and southward flow of lighter waters at mid-depths. Understanding what controls the strength and structure of these inter-hemispheric flows, referred to as the meridional overturning, is key to quantifying the deep ocean's ability to store carbon and heat. Here we show that the geometry of ocean basins, by shaping the diffusive density flux descending into the abyss, sets the divide between northward and southward limbs of the overturning and the vertical extent of abyssal upwelling. The analysis suggests that changes in basin area with depth, together with constrictive passages regulating sub-basin exchanges, place strong external constraints on present and past deep ventilation rates and pathways.

Dense waters originating from the surface high latitudes make up the overwhelming majority of the ocean volume. Formed through intense heat loss and salinification, gravitation allows them to sink and spread along the ocean floor, carrying surface information into the slow-paced abyss and contributing to the long memory of the ocean. But the memory time and buffering effect of the deep ocean ultimately depend upon the rate at which these dense waters are removed from deep seas and returned to the surface. Physical controls on the volume and return pathways of dense waters are therefore key to the ocean's carbon and heat storage capacity and its role in centennial to multi-millennial climate variability (Sigman et al. 2010; Ferrari et al. 2014).

The cycle of formation, transformation and destruction of dense water masses is often conceptualized as a meridional overturning circulation composed of two dynamically distinct limbs (Fig. 1; Nikurashin and Vallis 2012): an abyssal, northward limb that carries the densest Antarctic-sourced waters (Antarctic Bottom Water, abbreviated as AABW) until they upwell into lighter waters of the Indian, Pacific and Atlantic basins ; and a deep, southward limb that carries these lighter deep waters to the Southern Ocean. Because it involves a gradual decrease in the density of AABW, the abyssal branch is considered as a diabatic circulation. In contrast,

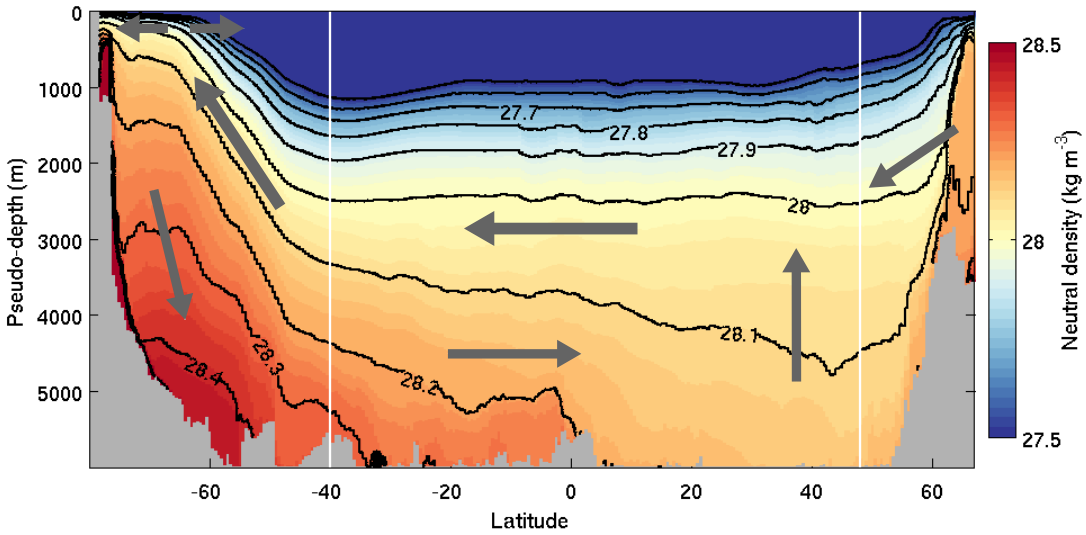

Figure 1: Climatological density field and schematic overturning transports. Neutral density is shown as a function of latitude and pseudo-depth, where the pseudo-depth of density surfaces is found by filling each latitude band from the bottom up with ocean grid cells ordered from dense to light. Gray arrows give a simplified view of overturning transports. Arrows oriented along density surfaces correspond to adiabatic flows, those crossing density surfaces correspond to diabatic flows.

the southward flow of overlying deep waters is thought to be predominantly adiabatic, that is, density-preserving. This dynamical divide is consistent with the two regimes apparent in the present deep ocean density distribution (Fig. 1): north of the Antarctic Circumpolar Current and away from polar sinking, flat density surfaces above 3,000 m depth appear compatible with an adiabatic arrangement of water masses, whereas the northward descent of deeper density surfaces signals transformation of abyssal waters as they travel meridionally. However, what sets the boundary between northward abyssal flow and southward deep flow and the transition between diabatic and adiabatic regimes remains largely unclear. Here, we show that these transitions are intimately linked to the shape of ocean basins.

The deep ocean communicates with the surface in two high-latitude regions (Fig. 1): the North Atlantic, where deep waters are formed and exported southward to ventilate the $\sim$ 27.72-28.14 kg m^{-3} density range (Ganachaud and Wunsch 2000; Lumpkin and Speer 2007), and the Southern Ocean, where rising density surfaces allow deep waters to upwell primarily adiabatically (Toggweiler and Samuels 1993; Marshall 1997; Marshall and Speer 2012), the densest of which are ultimately converted into sinking AABW through near-surface

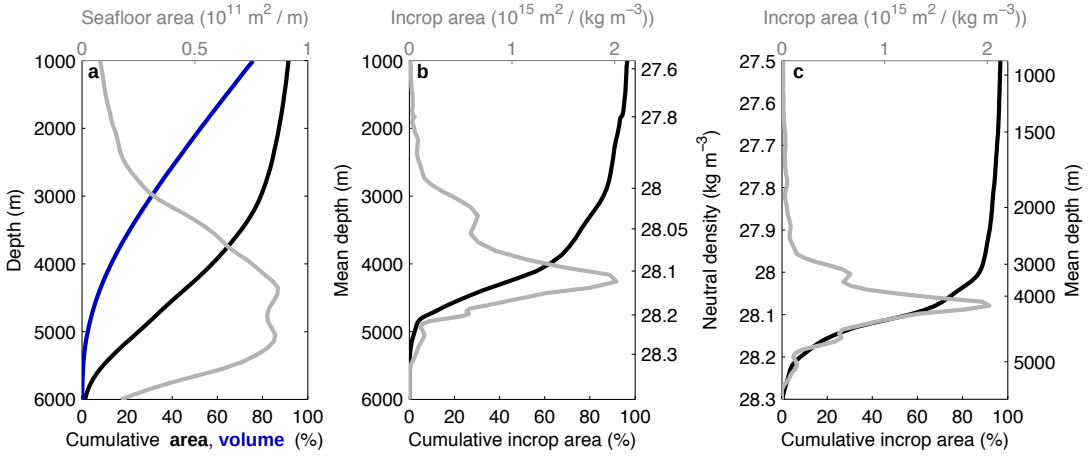

Figure 2: Depth distributions of ocean floor, water volume and incrop areas for the 40°S-48°N ocean domain. (**a**) Cumulative (black) seafloor area and (blue) ocean volume from the bottom upwards and (gray) seafloor area per unit depth. (**b**) Incrop area (seafloor area per unit density, gray) and its bottom-up cumulative sum (black) shown as a function of neutral density (right axis) and incrop area-weighted depth (left axis). (**c**) Same as (**b**), with a linear neutral density axis on the left. The ocean bathymetry used is the 1/30-degree resolution 'etopo2v2' product (Smith and Sandwell 1997).

densification (Talley 2013). Note that we use neutral density, denoted γ, as a globally consistent density variable (Jackett and McDougall 1997), and subtract 1,000 kg m^{-3} to all density values for concision. Away from these regions, dense waters are isolated from surface forcing, so that their density transformation and upwelling rely on interior, diabatic processes. We henceforth focus on these interior processes and restrict the analysis to ocean waters situated below 1,000 m depth and between 40°S and 48°N.

Between 300 and 3,000 m depth, ocean topography is dominated by relatively steep continental slopes, occupying no more than 20 % of the seabed (Figs. 2a and 3). At larger depths, flatter abyssal plains and spreading ridges dominate and account for almost 80 % of the ocean's area. Ocean layers therefore have unequal access to the seafloor: 1/4 of the water volume, below 3,500 m, occupies 3/4 of the seabed, with a peak coverage in the 4,300-5,300 m depth range. This inequality is reinforced when considering the seafloor coverage of density layers – that is, layers defined by a fixed density interval –, because their thickness generally increases with depth in the deep ocean (Figs. 2b,c and 4). By analogy with surface outcrop areas, the bottom area intersected by density layers is termed incrop area, with units of m^2/(kg m^{-3}). Fig. 2c shows that the relatively narrow 28-28.25 kg m^{-3} density

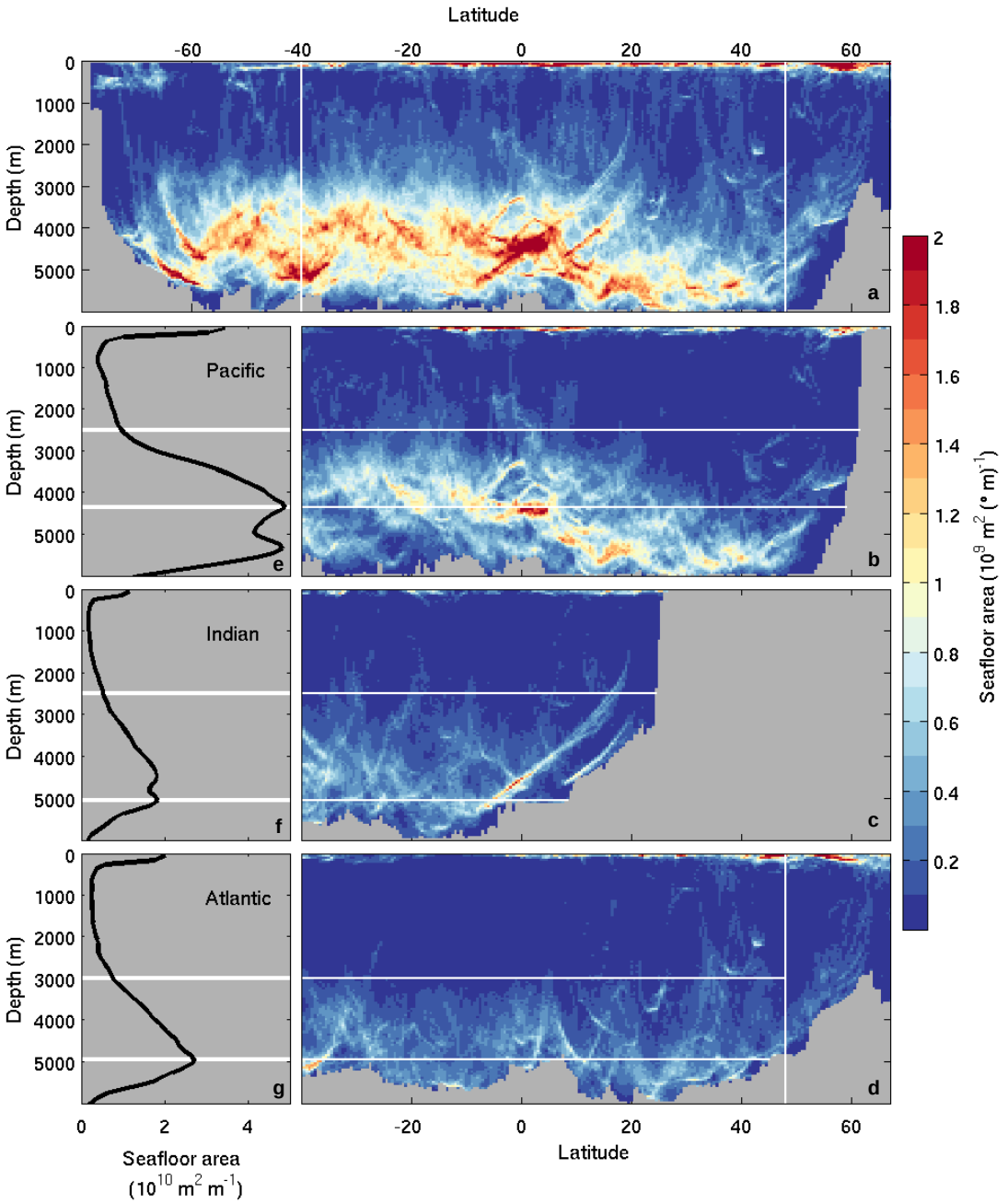

Figure 3: Depth-latitude distributions of seafloor area. (**a-d**) Zonal sum of seafloor area for the (**a**) global, (**b**) Pacific, (**c**) Indian and (**d**) Atlantic oceans. (**e-g**) Zonal and latitudinal sum of seafloor area shown as a depth profile for the (**e**) Pacific, (**f**) Indian and (**g**) Atlantic oceans. White lines indicate the depth of peak seafloor coverage as well as the approximate depth marking the transition between diabatic and adiabatic regimes.

range takes up over 80 % of the ocean floor between 40°S and 48°N, the lion's share going to $\sim$ 28.11 kg m^{-3} waters. Because the thickness of abyssal density layers varies smoothly in the vertical, and because the large-scale slopes of deep density surfaces remain modest at temperate latitudes, the depth distribution and maxima of incrop areas correlate strongly with those of the seafloor area both on global (Fig. 2) and local scales (Figs. 3 and 4). This implies that the incrop area distribution is largely controlled by overall basin geometries, or, more precisely, by the reduction rate of basin areas with depth. The gradual northward weakening of the abyssal stratification and associated expansion of incrop areas further imply that northern parts of the three major ocean basins exert the strongest control on total incrop areas.

These simple geometric considerations have strong implications for the destruction rate and upwelling pathways of dense waters. Deep ocean sources of density transformation have long been recognized to be concentrated near the seabed (Polzin et al. 1996, 1997; Munk and Wunsch 1998; Adcroft et al. 2001), where boundary-catalyzed turbulence and geothermal heating combine to erode the near-bottom stratification and progressively lighten the bottom-most waters of the ocean. The resulting near-bottom confinement of density loss suggests that deep water masses benefiting from a large seafloor coverage are likely to be more efficiently destroyed than those isolated from the bottom. Consistent with a preferential lightening of bottom boundary waters, the latitudinal distribution of incrop areas shows that they tend to increase along the northward path of AABW and to slowly migrate towards smaller densities, indicative of a successive removal of incropping density layers (Fig. 4). The coincidence between the regime of sloping density surfaces and the presence of significant incrop areas, below about 3,000 m depth, is further suggestion of the dominant role of boundary transformation. Hence, the concentration of seafloor area around the 4,300-5,300 m and 28.11 kg m^{-3} peaks may be expected to strongly influence the strength and structure of dense water upwelling across density surfaces and the associated meridional flows.

To formally relate overturning flows to incrop areas, we first set out the link between cross-density transport and the vertical structure of diffusive density fluxes. Within the 40°S-48°N deep ocean domain, the steady-state density budget reduces to a vertical

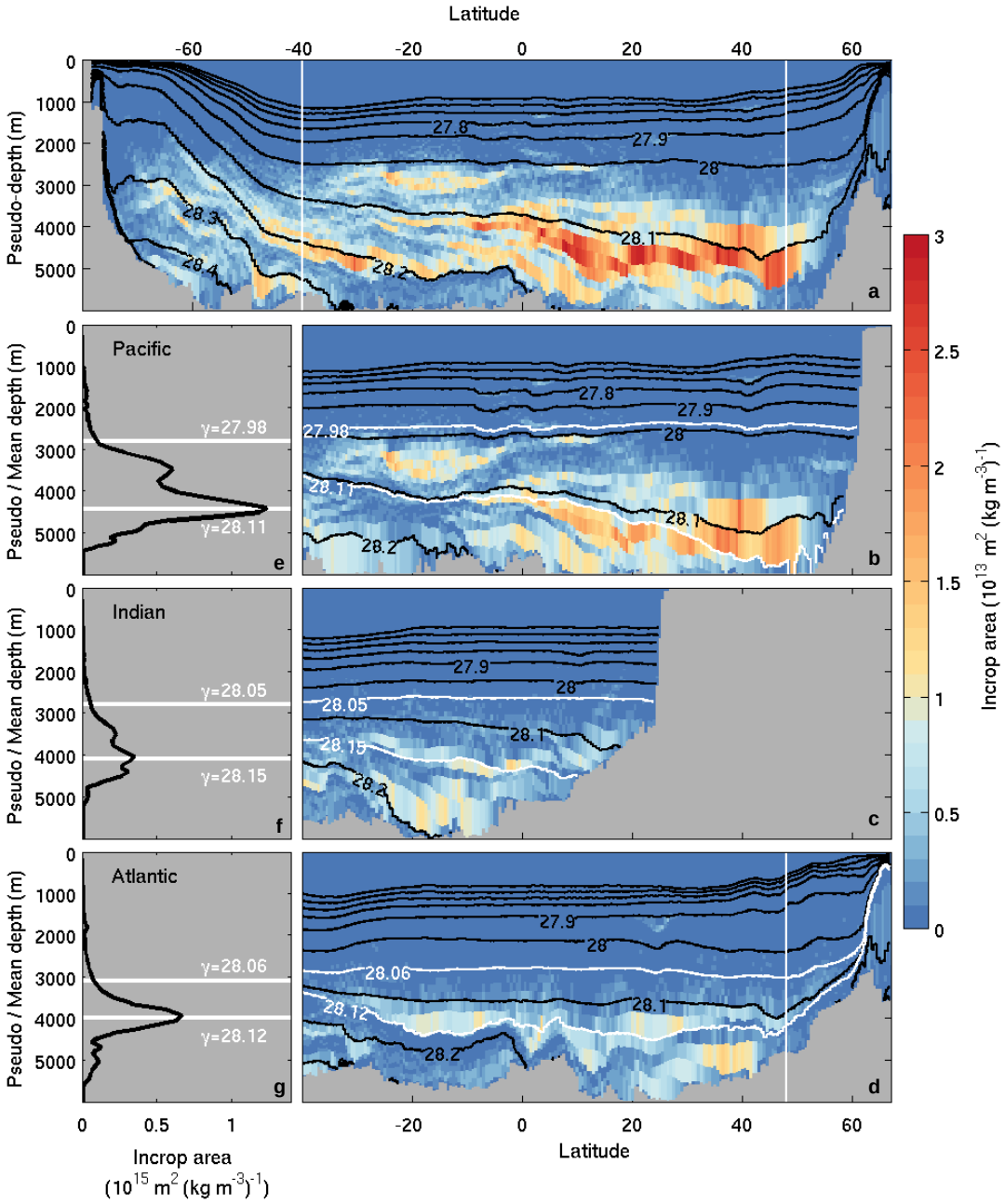

Figure 4: Depth-latitude distributions of incrop area. (**a-d**) Zonal sum of incrop area for the (**a**) global, (**b**) Pacific, (**c**) Indian and (**d**) Atlantic oceans shown as function of pseudo-depth and latitude. The pseudo-depth of density surfaces is found by filling global or basin latitude bands with water grid cells ordered from dense to light. (**e-g**) Zonal and latitudinal sum of incrop area shown as a function of incrop area-weighted depth for the (**e**) Pacific, (**f**) Indian and (**g**) Atlantic oceans. White contours indicate surfaces of peak seafloor coverage as well as the approximate surface marking the transition between diabatic and adiabatic regimes.

advective-diffusive balance (Palter et al. 2014):

$$\omega\,\partial_z\gamma = \partial_z(K_\perp\partial_z\gamma)\ . \tag{III.1}$$

In (III.1), z is depth and ω and $K_\perp$ stand respectively for the velocity and turbulent diffusivity in the direction perpendicular to density surfaces, referred to as the dianeutral direction. For simplicity, we have assumed a linear equation of state, an assumption that will be relaxed below. Noting that density can be used as a vertical coordinate, we can rewrite the dianeutral velocity simply as the density-derivative of the diffusive density flux:

$$\omega = \partial_\gamma(K_\perp\partial_z\gamma)\ . \tag{III.2}$$

Equations (III.1)-(III.2) state that cross-density advection equates the divergence of mixing-driven density fluxes: a convergent, depth-decreasing flux causes lightening, balanced by upwelling ($\omega < 0$, directed to lower density), whereas a depth-increasing density flux implies densification and downwelling ($\omega > 0$). Integrating ω over a density surface $A(\gamma)$, we obtain the total dianeutral transport

$$T = \iint_{A(\gamma)} \omega\,dA = \iint_{A(\gamma)} \partial_\gamma(K_\perp\partial_z\gamma)\,dA\ . \tag{III.3}$$

Using the no-flux bottom boundary condition, the constraint that turbulent mixing cannot flux density across the seafloor, and defining $F = \iint_{A(\gamma)} K_\perp\partial_z\gamma\,dA$ as the total diffusive density flux crossing the neutral surface $A(\gamma)$, (III.3) reduces to

$$T = \partial_\gamma \iint_{A(\gamma)} K_\perp\partial_z\gamma\,dA = \partial_\gamma F\ , \tag{III.4}$$

the large-scale advective-diffusive balance that mirrors the local balance (III.2). Derived here for turbulent mixing acting upon neutral density gradients, (III.4) generalizes to a non-linear equation of state and the presence of bottom geothermal heat fluxes by defining $F(\gamma)$ as an equivalent density flux crossing $A(\gamma)$ (de Lavergne et al. 2016b). Geothermal density fluxes are then represented by a vertically-uniform but bottom-vanishing density flux, generating the same bottom density extraction.

Equation (III.4) implies that dianeutral upwelling is controlled by $F(\gamma)$, the density profile of the downward diffusive buoyancy flux that penetrates in the ocean. In turn, we can relate basin-scale dianeutral transports to meridional, along-density flows by realizing that T must equate the net meridional mass flux into the volume underlying $A(\gamma)$. In the Indian and Pacific oceans, where deep density layers only connect with the Southern Ocean (Fig. 4b,c), the net southward transport across a latitudinal section $y = y_s$ and below a given density surface, denoted $\psi(y_s, \gamma)$, is simply equal to $T(y \geq y_s, \gamma)$. This entails in particular that the surface of peak upwelling T north of 40°S defines the boundary between northward and southward flow at 40°S. In the deep Atlantic ocean, which is fed both from the Arctic and the Antarctic Circumpolar Current (Fig. 4d), we have

$$\psi(y_s, \gamma) - \psi(y_n, \gamma) = T(y_s \leq y \leq y_n, \gamma) \tag{III.5}$$

where y_s and y_n define respectively the southern and northern bounding latitudes of the domain. Depending on the densest water influx at 48°N, the transition between northward and southward Atlantic transport at 40°S may therefore occur at a somewhat denser level than the maximum upwelling rate.

Fig. 5 shows the profile of the total and mean density flux F as well as the associated 40°S-48°N dianeutral transports under four different scenarios: (S1) vertically and horizontally uniform density flux; (S2) bottom-enhanced density flux, with uniform bottom magnitude; (S3) effective diffusivity profile inferred from an inverse estimate of ocean transports (Lumpkin and Speer 2007); and (S4) constant upwelling of 30×10^6 m^3 s^{-1} from 4,000 to 1,000 m depth, following assumptions of the *Abyssal Recipes II* calculation (Munk and Wunsch 1998). In scenarios (S1) and (S2), the flux magnitude is chosen so that the peak upwelling rate matches that of (S3). The bottom-intensification of (S2) density fluxes is specified as an exponential decay from the seafloor with a 500 m e-folding scale, a structure representative of turbulence observations in the abyssal Brazil Basin (St. Laurent et al. 2002).

Scenario (S1) corresponds to a diabatic bottom boundary overlain by an adiabatic ocean

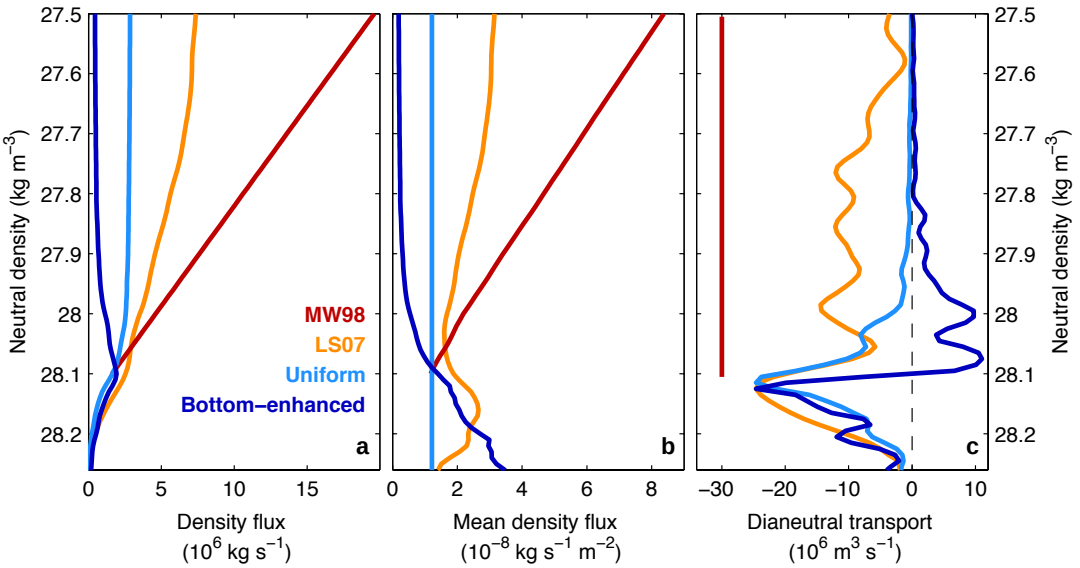

Figure 5: Density fluxes and associated dianeutral transports for the 40°S-48°N ocean domain. Shown are (**a**) the total density flux F, (**b**) the mean density flux and (**c**) total dianeutral transports for four different scenarios (see text): (pale blue) uniform local density flux, (blue) bottom-enhanced local density flux, (orange) density flux implied by the effective diffusivity profile obtained by Lumpkin and Speer (2007), and (red) constant dianeutral upwelling of 30×10^6 m^3 s^{-1} from 4,000 to 1,000 m depth, following assumptions of Munk and Wunsch (1998).

interior: convergence of local density fluxes occurs only in the unstratified bottom boundary layer, where the density flux decreases to match the no-flux boundary condition. Though a drastic simplification, this idealization has grounding in the observational and theoretical evidence that lightening of deep and abyssal waters mostly occurs along the bottom boundary (Wunsch and Ferrari 2004; Emile-Geay and Madec 2009; Huussen et al. 2012; Polzin et al. 2014; de Lavergne et al. 2016b). The scenario results in diabatic upwelling peaking at $\gamma = 28.11\,\mathrm{kg\,m^{-3}}$ and mostly confined to below the $\gamma = 28\,\mathrm{kg\,m^{-3}}$ density surface (Fig. 5c), matching the incrop area distribution (Fig. 2c). This behaviour can be understood by noting that the total density flux follows the area of density surfaces, $\mathcal{A}(\gamma) = \iint_{A(\gamma)} dA$, whose shrinking rate $-\partial_\gamma \mathcal{A}$ is equal to the incrop area. Because a uniform density flux homogeneously lightens waters covering the ocean floor, scenario (S1) implies that density layers upwell in proportion to their access to the seafloor. Consequently, diabatic upwelling is then restricted to the depth and density range of significant incrop areas, and the boundary between northward and southward meridional transport coincides with the peak basin incrops (Fig. 6) – except for a potential, small downward displacement in the Atlantic.

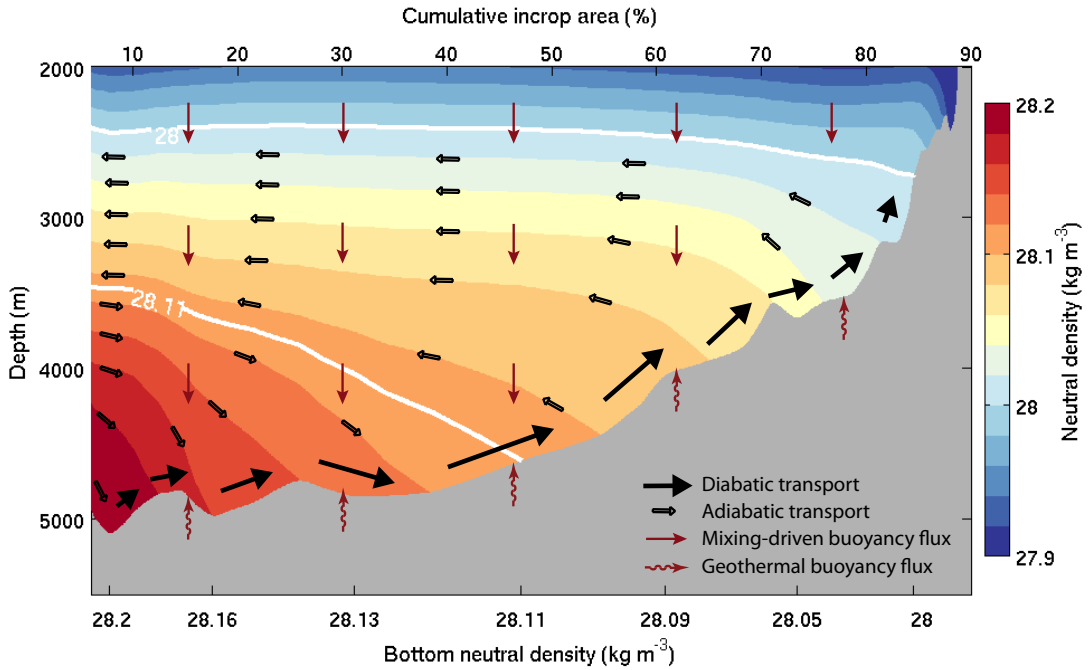

Figure 6: Schematic abyssal overturning circulation north of 40°S. The average depth of density surfaces is shown as function of (lower axis) bottom neutral density (see Fig. 7) and (upper axis) cumulative incrop area going from dense to light bottom density. The surface of maximum incrop area ($\gamma = 28.11\,\mathrm{kg\,m^{-3}}$), corresponding to meridional flow reversal, and the surface marking the approximate transition between diabatic and adiabatic flow regimes ($\gamma = 28\,\mathrm{kg\,m^{-3}}$), are contoured in white. Density loss and diabatic upwelling are confined to near-bottom waters, which climb across density surfaces and along ridge flanks at a rate roughly commensurate with the incrop area. Through mass conservation, this cross-density, along-bottom circulation maintains an along-density, interior circulation which supplies (returns) dense waters from (to) the Antarctic Circumpolar Current. (In the Atlantic ocean, these along-density flows may have an additional supply component from the subpolar North Atlantic.)

In particular, most of Antarctic-sourced abyssal waters must flow back to the Antarctic Circumpolar Current below 2,500 m depth (Fig. 4), concurring with a pivotal role of the Southern Ocean in their ultimate surface return (Toggweiler and Samuels 1993; Marshall 1997; Marshall and Speer 2012) but contrasting with the low-latitude upwelling scenario (S4).

Whether incrop areas control the actual structure of deep ocean upwelling depends on the degree to which the uniform-flux scenario captures gross properties of abyssal water mass transformation. Because geothermal heat fluxes exhibit relatively weak spatial variations away from ridge crests (Goutorbe et al. 2011) and contribute net bottom density losses, they are well described by the uniform-flux assumption. In contrast, deep ocean mixing is

observed to be dominated by patchy, topographically-enhanced turbulence (e.g., Polzin et al. 1996, 1997; Bryden and Nurser 2003; Thurnherr et al. 2005; Huussen et al. 2012; Waterhouse et al. 2014). Such turbulence is generally associated with a bottom-enhanced density flux, whereby lightening of densest waters occurs at the expense of densification immediately above. Scenario (S2) explores the impact of an idealized, geographically homogeneous bottom-intensification of density fluxes. Under this scenario, density loss (gain) generally dominates for density layers that have a larger (smaller) incrop area than their underlying neighbour. Upwelling is consequently found within waters denser than 28.11 kg m^{-3}, peaking just under this level, whereas density gain and downwelling characterize lighter waters, for which the total density flux F is divergent. Hence, scenario (S2) leads to broadly similar upwelling as implied by (S1) but confined to below the 28.11 kg m^{-3} density surface.

In reality, rather than equally distributed along the bottom, energetic abyssal turbulence is thought to be largely restricted to regions of strong internal wave generation by flow over topography (Kunze and Sanford 1996; Polzin et al. 1997; Garrett and Laurent 2002; Nikurashin and Ferrari 2010) and to a relatively small number of inter-basin passages (Polzin et al. 1996; Bryden and Nurser 2003). Because internal wave generation is heavily weighted toward shallower, strongly-stratified regions (Nycander 2005), the associated bottom-intensified turbulence tends to drive a convergent density flux across the deep Atlantic and Indo-Pacific basins, with an estimated upwelling structure broadly matching that of incrop areas (de Lavergne et al. 2016a,b). Such a match cannot be expected for the mixing occurring within main circulation chokepoints, where intense, extremely localized density fluxes efficiently consume the densest flowing waters (Bryden and Nurser 2003). The leading role of restrictive passages connecting Indian and Atlantic sub-basins in transforming northward-flowing AABW is clearly demonstrated by the bottom density field (Fig. 7). Indeed, because it is essentially confined to the near-bottom, the cross-density circulation can largely be tracked from the bottom density distribution. Whereas the Pacific has few topographic restrictions and relatively smooth bottom density gradients, density transformation appears to be concentrated at flow constrictions in the Indian and Atlantic oceans. There, access to constrictive passages may therefore be as strong a determinant of diabatic upwelling rates as is the access to large seafloor areas.

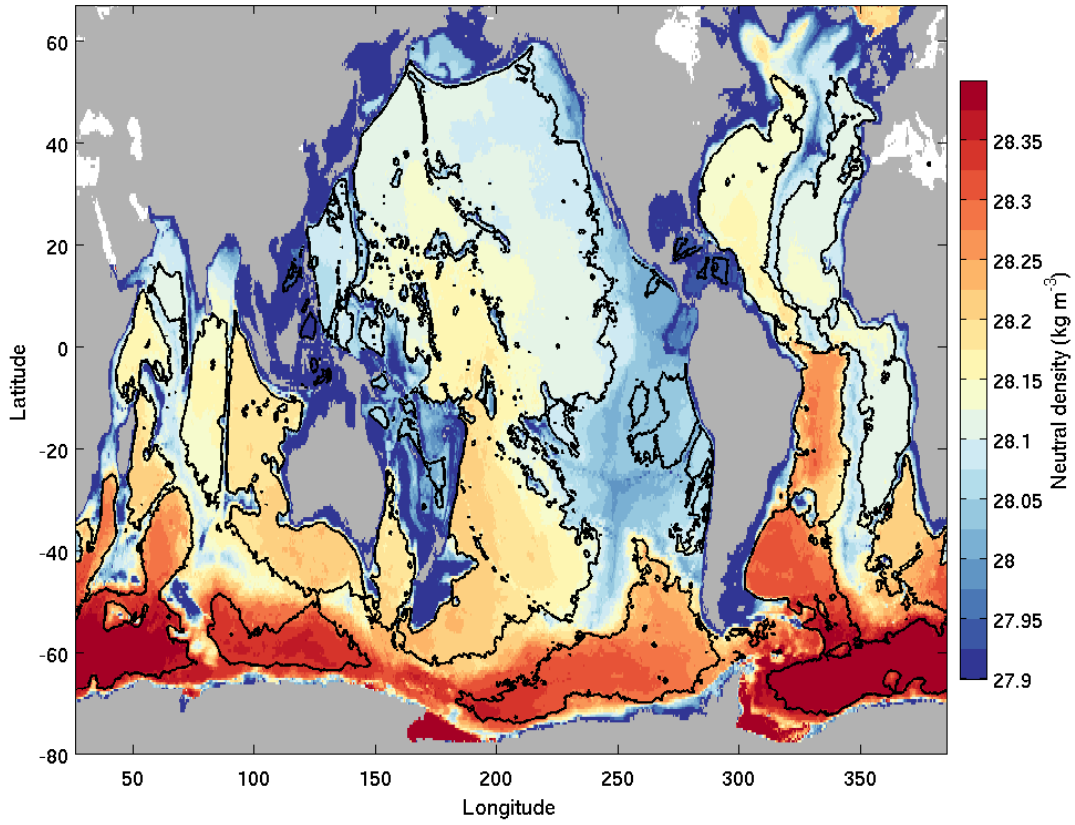

Figure 7: Bottom neutral density field (shading) and 4,000 m bathymetric contour (black).

Nevertheless, simple reasoning suggests that mixing at deep straits and sills acts to reinforce rather than supplant the influence of incrop areas on the overall overturning structure. First, by eroding the stratification of through- and over-flowing waters, such mixing increases the thickness of bottom density layers, augmenting their incrop area further downstream and thus contributing to the density concentration of incrops. Second, major passages are crossed along the northward path of AABW, indicating that they do not host the peak diabatic transports that define the meridional flow reversal. In other words, though they considerably transform the densest categories of AABW, deep inter-basin through-flows do not account for the pivot upwelling of the lighter, end-basin waters. Instead, they contribute to the progressive homogenization of AABW that allows the lighter categories to spread along the ocean floor and undergo strongest upwelling.

Consistent with these arguments, an estimate of the density flux grounded in an inversion of hydrographic observations (scenario (S3)), together with an independent inverse solution (Ganachaud and Wunsch 2000), place the peak upwelling rate and associated flow transition at the 28.11 kg m^{-3} level. Further, scenario (S3), in agreement with (S1), results in dianeutral upwelling decreasing to 25 % of its maximum value at $\gamma = 28.05\,\mathrm{kg\,m^{-3}}$, suggesting that the bulk of upwelling waters retains densities larger than 28.05 kg m^{-3} and enters the Antarctic Circumpolar Current within the approximate 2,500-3,500 m depth range (Figs. 4 and 6). Thus, the result anticipated from (S1) that diabatic upwelling peaks within the density layer that has the largest seafloor coverage, and decreases rapidly for lighter densities, appears to be robust. The robustness of this structure owes to two principal facts: boundary mixing and geothermal heating restrict density loss to the bottom boundary; density layers have strongly unequal access to the seafloor. The ensuing picture of the overturning's functioning is summarized in Fig. 6. It has wide ranging implications.

First, estimates of the mixing energy required to maintain cross-density upwelling at temperate latitudes (Munk and Wunsch 1998) must account for its restricted vertical extent. Despite their recognition that density transformation is concentrated along the boundaries, Munk and Wunsch (1998) neglected the role of basin geometry, which dictates that upwelling is largely limited to weakly sloping abyssal floor (Fig. 5). A fixed ratio of 1/5 between the density flux (times gravity) and the associated power yields values of respectively 0.38, 0.19, 0.64 and 0.96 TW for scenarios (S1) to (S4) and densities comprised between 28.11 and 27.5 kg m^{-3}. Note that the larger 2.1 TW number obtained by Munk and Wunsch (1998) stems from their use of a different stratification field and of the total ocean area, rather than that of their 40°S-48°N domain, in the final estimate. Next, the abyssal stratification and overturning are indivisible from the ocean bathymetry and its depth distribution. Theories (Nikurashin and Vallis 2011, 2012) aiming to quantitatively predict the strength and structure of the abyssal circulation must therefore account for geometric controls of the basin-scale diffusive density flux. Our analysis suggests that the depth-varying area of ridges largely sets the peak level and vertical extent of abyssal upwelling. The presence of sub-basins and bathymetric constrictions is an additional strong determinant of the north-south AABW density range, and may be thought of as an effective enlarger of basin areas.

Third, the abyssal overturning may be more vertically confined than commonly thought (Talley 2013; Ferrari et al. 2014). The present analysis suggests that diabatic dense water upwelling north of 40°S is largely limited to depths greater than 2,500 m and densities greater than $28\,\mathrm{kg\,m^{-3}}$ (Fig. 6). Therefore, only a minor fraction of Antarctic-sourced waters may be able to diffuse up to the shallower cores of Indian and Pacific Deep Water, whose implied isolation concurs with their characteristic low oxygen concentrations and radiocarbon activities. The bulk of Antarctic-origin waters may instead return to the Antarctic Circumpolar Current at sufficiently high densities to be upwelled south of the permanent sea ice line ($\gamma \approx 27.9\,\mathrm{kg\,m^{-3}}$; Ferrari et al. 2014) and recycled back into AABW, implying that the abyssal overturning functions primarily – but not strictly – as a closed loop. Further, the seafloor area distribution may be used to estimate the level at which southward-flowing North Atlantic Deep Water can be considered as largely decoupled from Antarctic-sourced bottom waters, corresponding to the transition level between diabatic and adiabatic regimes: near 3,000 m depth (Fig. 4d,g). Last, the incrop area control of the divide between northward and southward deep transport raises important questions regarding past reorganizations of deep water masses and their involvement in natural climate changes. In the absence of abrupt depth variations in the large-scale abyssal stratification, the broad coincidence between peak seafloor and incrop areas must hold. The volume of Antarctic-sourced waters participating in the slowest, northward limb of the overturning may therefore be constrained by current basin geometry to depths greater than $\sim$4,000 m, limiting the effective storage capacity of the abyssal ocean.

References

Adcroft, A., Scott, J. R., and Marotzke, J. (2001). Impact of geothermal heating on the global ocean circulation. *Geophysical Research Letters*, 28(9):1735–1738.

Bryden, H. L. and Nurser, A. J. G. (2003). Effects of strait mixing on ocean stratification. *Journal of Physical Oceanography*, 33(8):1870–1872.

de Lavergne, C., Madec, G., Le Sommer, J., Nurser, A. J. G., and Naveira Garabato, A. C. (2016a). The impact of a variable mixing efficiency on the abyssal overturning. *Journal of Physical Oceanography*, 46(2):663–681.

de Lavergne, C., Madec, G., Le Sommer, J., Nurser, A. J. G., and Naveira Garabato, A. C. (2016b). On the consumption of Antarctic Bottom Water in the abyssal ocean. *Journal of Physical Oceanography*, 46(2):635–661.

Emile-Geay, J. and Madec, G. (2009). Geothermal heating, diapycnal mixing and the abyssal circulation. *Ocean Science*, 5(2):203–217.

Ferrari, R., Jansen, M. F., Adkins, J. F., Burke, A., Stewart, A. L., and Thompson, A. F. (2014). Antarctic sea ice control on ocean circulation in present and glacial climates. *Proceedings of the National Academy of Sciences*, 111(24):8753–8758.

Ganachaud, A. and Wunsch, C. (2000). Improved estimates of global ocean circulation, heat transport and mixing from hydrographic data. *Nature*, 408(6811):453–457.

Garrett, C. and Laurent, L. S. (2002). Aspects of deep ocean mixing. *Journal of oceanography*, 58(1):11–24.

Goutorbe, B., Poort, J., Lucazeau, F., and Raillard, S. (2011). Global heat flow trends resolved from multiple geological and geophysical proxies. *Geophysical Journal International*, 187(3):1405–1419.

Huussen, T. N., Naveira-Garabato, A. C., Bryden, H. L., and McDonagh, E. L. (2012). Is the deep Indian Ocean MOC sustained by breaking internal waves? *Journal of Geophysical Research*, 117(C8):C08024.

Jackett, D. R. and McDougall, T. J. (1997). A neutral density variable for the World's oceans. *Journal of Physical Oceanography*, 27(2):237–263.

Kunze, E. and Sanford, T. B. (1996). Abyssal mixing: Where it is not. *Journal of Physical Oceanography*, 26(10):2286–2296.

Lumpkin, R. and Speer, K. (2007). Global ocean meridional overturning. *Journal of Physical Oceanography*, 37(10):2550–2562.

Marshall, D. (1997). Subduction of water masses in an eddying ocean. *Journal of Marine Research*, 55(2):201–222.

Marshall, J. and Speer, K. (2012). Closure of the meridional overturning circulation through Southern Ocean upwelling. *Nature Geoscience*, 5(3):171–180.

Munk, W. and Wunsch, C. (1998). Abyssal recipes II: Energetics of tidal and wind mixing. *Deep-Sea Research*, 45(12):1977–2010.

Nikurashin, M. and Ferrari, R. (2010). Radiation and dissipation of internal waves generated by geostrophic motions impinging on small-scale topography: Theory. *Journal of Physical Oceanography*, 40(5):1055–1074.

Nikurashin, M. and Vallis, G. (2011). A theory of deep stratification and overturning circulation in the ocean. *Journal of Physical Oceanography*, 41(3):485–502.

Nikurashin, M. and Vallis, G. (2012). A theory of the interhemispheric meridional overturning circulation and associated stratification. *Journal of Physical Oceanography*, 42(10):1652–1667.

Nycander, J. (2005). Generation of internal waves in the deep ocean by tides. *Journal of Geophysical Research*, 110(C10).

Palter, J. B., Griffies, S. M., Samuels, B. L., Galbraith, E. D., Gnanadesikan, A., and Klocker, A. (2014). The deep ocean buoyancy budget and its temporal variability. *Journal of Climate*, 27(2):551–573.

Polzin, K. L., Garabato, A. C. N., Abrahamsen, E. P., Jullion, L., and Meredith, M. P. (2014). Boundary mixing in Orkney Passage outflow. *Journal of Geophysical Research*, 119:C010099.

Polzin, K. L., Speer, K. G., Toole, J. M., and Schmitt, R. W. (1996). Intense mixing of Antarctic Bottom Water in the equatorial Atlantic Ocean. *Nature*, 380(6569):54–57.

Polzin, K. L., Toole, J. M., Ledwell, J. R., and Schmitt, R. W. (1997). Spatial variability of turbulent mixing in the abyssal ocean. *Science*, 276(5309):93–96.

Sigman, D. M., Hain, M. P., and Haug, G. H. (2010). The polar ocean and glacial cycles in atmospheric CO2 concentration. *Nature*, 466(7302):47–55.

Smith, W. H. F. and Sandwell, D. T. (1997). Global sea floor topography from satellite altimetry and ship depth soundings. *Science*, 277(5334):1956–1962.

St. Laurent, L. C., Simmons, H. L., and Jayne, S. R. (2002). Estimating tidally driven mixing in the deep ocean. *Geophysical Research Letters*, 29(23).

Talley, L. (2013). Closure of the global overturning circulation through the Indian, Pacific, and Southern Oceans: Schematics and transports. *Oceanography*, 26(1):80–97.

Thurnherr, A. M., St. Laurent, L. C., Speer, K. G., Toole, J. M., and Ledwell, J. R. (2005). Mixing associated with sills in a canyon on the midocean ridge flank. *Journal of Physical Oceanography*, 35(8):1370–1381.

Toggweiler, J. R. and Samuels, B. (1993). New radiocarbon constraints on the upwelling of abyssal water to the ocean's surface. In Heimann, M., editor, *The Global Carbon Cycle*, number 15 in NATO ASI Series, pages 333–366. Springer Berlin Heidelberg.

Waterhouse, A. F., MacKinnon, J. A., Nash, J. D., Alford, M. H., Kunze, E., Simmons, H. L., Polzin, K. L., St. Laurent, L. C., Sun, O. M., Pinkel, R., Talley, L. D., Whalen, C. B., Huussen, T. N., Carter, G. S., Fer, I., Waterman, S., Naveira Garabato, A. C., Sanford, T. B., and Lee, C. M. (2014). Global patterns of diapycnal mixing from measurements of the turbulent dissipation rate. *Journal of Physical Oceanography*, 44(7):1854–1872.

Wunsch, C. and Ferrari, R. (2004). Vertical mixing, energy, and the general circulation of the oceans. *Annual Review of Fluid Mechanics*, 36(1):281–314.

CHAPTER

IV

Observing and modelling the bottom boundary layer: challenges

In chapter I, we argued that buoyancy gain and diabatic upwelling are mainly confined to a thin bottom layer. Variations of the mixing efficiency control the thickness of this bottom layer (chapter II). In chapter III, we showed that the near-bottom concentration of buoyancy gain has important implications for the overall structure of the abyssal overturning. These studies thus emphasize the central role of the bottom boundary layer for the circulation of Antarctic Bottom Water and, more generally, for deep water mass transformation. The emerging, idealized picture is that of an adiabatic ocean interior, where water masses spread unperturbed along density surfaces, sandwiched between surface and bottom boundary layers, where the bulk of water mass transformation is accomplished. Yet the parallel between the roles of surface and bottom boundary layers contrasts vividly with their unequal representation in the oceanographic literature, observational databases and modelling practices.

Reasons to explain the difference in the attention given to top and bottom boundaries are manifold. Not least is the inherent difficulty of observing the bottom, lightless waters of the ocean, 85 % of which lie below 2,000 m depth, the maximum sampling depth of autonomous Argo floats (Roemmich et al. 2009). Current knowledge of deep ocean properties therefore relies exclusively on ship-based measurements, mostly along repeated hydrographic sections (Purkey and Johnson 2010), leaving wide swaths of the abyss unexplored. In addition, instrument cost and protection imply that microstructure profilers are generally programmed to drop their ballast about 200 m above the bottom, leaving out the bottom-most waters. As a result,

knowledge of near-bottom stratification and turbulence levels in the abyss is strongly limited. In particular, the ensuing uncertainty in the abyssal density field of gridded ocean climatologies is a major source of uncertainty for the water mass transformation calculations presented in previous chapters.

But the sparseness of near-bottom observations is not solely a limitation for estimates of abyssal cross-density flows. Interactions between currents and topography are an important route of the cascade that drains energy out of the general circulation (e.g., Dewar et al. 2011; Nikurashin et al. 2012; Naveira Garabato et al. 2013; Wright et al. 2012, 2013, 2014). Present understanding of the energy balance of the general circulation, and consequently modelling of that same circulation and its climatic role, suffers from a lack of accurate quantification of bottom boundary dissipative processes (Naveira Garabato 2012). In turn, the insufficient characterization and quantification of bottom dissipative processes can be traced in part to limited direct observations of these processes and to the coarse vertical resolution of general circulation models at abyssal depths.

In this chapter, we argue that better observing and modelling the bottom boundary layer is a research priority to improve our understanding of the ocean's role in climate.

Uncovering the ocean's hidden face

A growing body of research points to the ocean bottom boundary both as a cornerstone in the ocean's functioning and as a chokepoint in our understanding of the ocean's role in climate. Clearing the bottleneck requires concerted observational and modelling efforts to unveil the physical and biochemical phenomena that hide along the ocean floor.

In May 1959, defending a bold underwater drilling project that would help unravelling the composition of the Earth's mantle, American geophysicist Gordon Lill wrote: "The ocean's bottom is at least as important to us as the Moon's behind." (Lill and Maxwell, 1959: The Earth's mantle. *Science* 129, 1407-1410). Almost half a century later, despite the lasting exploration efforts fostered by Lill's initiative, it can be said that the ocean bottom remains as uncharted as the dark side of the Moon.

Much of this relative neglecting can be traced to historical and logistical reasons. The opacity of the ocean implies that observation of its subsurface and bed relies largely on in-situ measurements, which are particularly costly and difficult to operate at abyssal depths, besides remote from continents. The study of weather and climate has stirred extensive research on the ocean's top, where heat, freshwater and gas exchanges with the atmosphere take place, but generally left its bottom in its cold obscurity. The productive sunlit surface and continental margins of the ocean have been natural focal points for marine biology and chemistry, which thrive on satellite observations of surface ocean colour. To a large extent, logistical constraints have dictated data availability and modelling capabilities, and ultimately orientated ocean sciences away from its underside.

Nevertheless, we argue that the current paucity of knowledge about ocean bottom phenomena also stems from an underestimation of their importance for ocean physics, biogeochemistry and climate. Here, we outline some recent advances in our understanding of ocean dynamics that pinpoint the key role of bottom boundary processes for ocean circulation and ventilation, and thereby for the transport of heat, salt, nutrients, gases and sediments, on timescales of months to millennia. We also impress upon persistent blind spots and sketch priority paths to

narrow them down.

Accelerated by surface wind and thermohaline forcing, oceanic flows rely largely on interactions with the slopes and roughness of the bottom topography for their ultimate arrest (e.g., Zhai et al. 2010; Naveira Garabato et al. 2013). Though they set the energy and momentum balance of the ocean, these near-bottom, dissipative processes remain rather poorly known, some of them still lacking identification or understanding and all of them lacking accurate quantification (Naveira Garabato 2012). The lack of a reliable closure of momentum and energy budgets hampers in turn our ability to describe and model the flow of heat and other climatically important tracers across the oceans, both on the seasonal to multidecadal timescales characteristic of upper-ocean dynamics and on the longer timescales governed by deep and abyssal layers.

In particular, the concentration of energy dissipation along the bottom boundary is a key determinant of the large-scale distribution of ocean properties, and of the rate at which the atmosphere and the deep ocean heat and carbon reservoirs communicate. The dissipation of oceanic flows is synonymous to a transfer of their kinetic energy to small-scale turbulence through various instabilities – themselves a crucial and active area of research. The resulting turbulent mixing redistributes seawater properties in the interior, balancing local advective transports and, more fundamentally, global tracer fluxes through the ocean's surface and bottom boundaries (Walin 1982). The seafloor-catalysed energy dissipation is thus tied to elevated near-bottom turbulent mixing rates that largely contribute to shape tracer distributions and to set the overall ventilation rate of the deep ocean (Munk and Wunsch 1998).

Furthermore, the bottom intensification of dissipation goes hand in hand with a near-bottom confinement of the downwelling and upwelling flows that carry dense waters along the meridional overturning circulation (Fig. 1). Gravitation naturally tends to confine dense water downwelling to a thin bottom layer. Part of the kinetic energy of the downslope currents is then lost to turbulent mixing, which densifies entrained waters but lightens the descending bottom waters. At steady state, the near-bottom buoyancy gain is balanced by renewed advection of dense waters along the seafloor, and the buoyancy loss above by

sinking of overlying lighter waters. An analogous behaviour, though involving different spatial and temporal scales, characterizes dense water upwelling forced by bottom-enhanced turbulence (St. Laurent et al. 2001; de Lavergne et al. 2016b). Indeed, such turbulence drives downward buoyancy fluxes that likewise peak near the seafloor, causing buoyancy gain of densest waters but buoyancy loss of the waters above. Maintenance of the density field implies that the lightened bottom waters must then seep upwards along the seabed, while the overlying densified waters undergo sinking. The along-slope flow is reinforced by the action of geothermal heating, which supplies additional buoyancy to the bottom-most waters, with global significance (Adcroft et al. 2001; de Lavergne et al. 2016b).

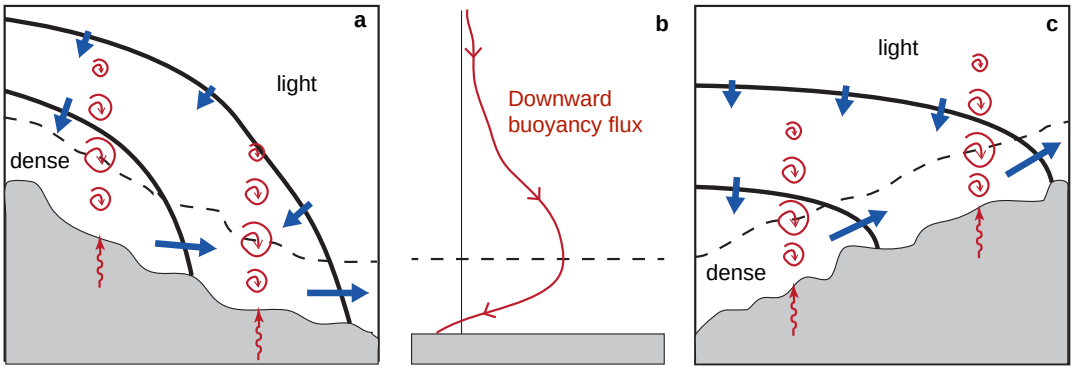

Figure 1: Downslope (**a**) and upslope (**c**) currents controlled by near-bottom diffusive buoyancy fluxes (**b**). Boundary-catalysed turbulence (red spirals) and geothermal heat fluxes (red wiggly arrows) drive a convergent buoyancy flux within a thin bottom layer (dashed line) and a divergent buoyancy flux above it. The bottom buoyancy gain is balanced by along-slope flow, whereas the buoyancy loss above is balanced by sinking of interior waters (blue arrows). Thick black lines represent density surfaces.

Thus, in addition to hosting key boundary processes and exchanges, the bottom boundary layer stands out as a bottleneck for the ventilation of the ocean's abyss. Yet a host of unknowns makes the bottom boundary layer an equally strong bottleneck for our quantitative description and modelling of the meridional overturning. Basic knowledge of the thickness of the well-mixed bottom layer, of the near-bottom levels of stratification and turbulent dissipation and of their distribution across the world ocean is lacking. The precise magnitude of geothermal heat fluxes and the dynamics associated with their absorption by bottom waters remain largely elusive. The efficiency through which abyssal turbulence mixes stratified fluid constitutes an additional key uncertainty (de Lavergne et al. 2016a). As a result, the shape and

magnitude of near-bottom diffusive buoyancy fluxes, which control the strength and structure of the upslope and downslope flows that maintain the overturning, remain poorly constrained.

The disproportionate significance of bottom boundary processes poses numerous observational and modelling challenges. Lowering ship-based instruments to abyssal depths is time-consuming and costly, and their protection often prohibits sampling of the very bottom waters. Indeed, the prominence of bottom processes for water property modification has generally been inferred from a mismatch between basin-scale budgets and interior observations, rather than directly observed (Huussen et al. 2012; Polzin et al. 2014). The lack of direct evidence impedes dynamical understanding, and therefore modelling, of the involved processes. The sparseness of abyssal observations further hinders the description and quantification of dense water flows and properties and their temporal variability. Perhaps even more challenging is an accurate representation of bottom processes in global ocean models, whose vertical resolution is coarsest close to the bottom and whose coordinate systems generally disallow a faithful simulation of along-slope dynamics. An emblematic example is the long-standing difficulty of ocean climate models to simulate the export of dense waters along downslope currents, through straits or over sills (Snow et al. 2015).

The gap to be bridged is well illustrated by the opposition between depth-distributions of seafloor area and model resolution or observational coverage (Fig. 2). Most of the ocean's bed lies at depths between 3,000 and 6,000 m, well below the current synoptic temperature and salinity sampling by automated Argo probes (Riser et al. 2016), which dive to only about 2,000 m. At depths greater than 3,000 m, the vertical grid spacing of global ocean models and hydrographic climatologies is typically about 200 m, compared to 1-10 m near the surface, preventing resolution of the bottom boundary layer. It is thus long before sampling and modelling of the bottom boundary layer may rival that of its surface counterpart.

Nevertheless, some progress may be at hand. Generalized coordinate systems allowing for the combined use of depth and terrain-following or density-following vertical levels have been shown to improve model representations of bottom boundary layer dynamics without demanding unaffordable horizontal and vertical resolution increases (Griffies et al.

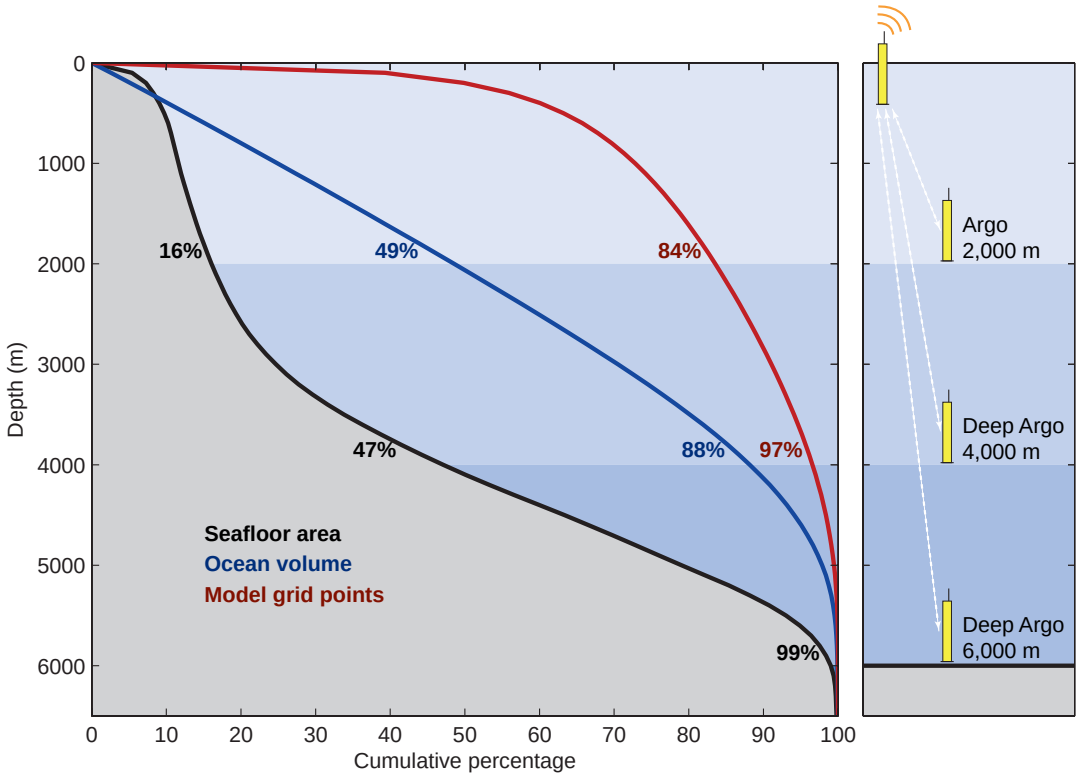

Figure 2: Contrasting depth-distributions of seafloor area (black), ocean volume (blue) and number of model grid points (red). The depth-distributions are shown as a cumulative percentage from the surface downward. The overwhelming majority of hydrographic observations is concentrated in the upper 2,000 m, the depth range covered by current Argo floats. New robotic probes, termed Deep Argo floats, are being developed to sample deeper waters (Riser et al. 2016). Among present Deep Argo prototypes, some can dive to 4,000 m and others are able to reach 6,000 m depth. Floats profiling to 4,000 m cover 88 % of the ocean volume but only 47 % of the ocean floor. The state-of-the-art model grid taken as example is a 73-level, nominally 1°x1° global ORCA mesh.

2000; Ezer and Mellor 2004). Improved process understanding may be achieved with high resolution idealized or regional model studies focusing on flow-topography interactions, boundary instabilities and mixing (e.g., Nikurashin et al. 2012). But headway will remain slow unless new observations can bring into focus leading processes and provide ground-truth context to modelling work. The Deep Argo programme (Riser et al. 2016), which aims for a global array of deep-diving floats allowing full-depth closure of heat and freshwater budgets, offers the perspective of a spatial and temporal scale change in abyssal hydrographic sampling. We suggest that seafloor area coverage should be considered alongside volume coverage in the programme's design, implying encouraged development of floats able to reach 6,000 m depth (Fig. 2). More ongoing instrumental developments, including deep-sea gliders

or terrain-following floats together with biochemical sensors, have the potential to further improve property mapping and process understanding of the bottom ocean. In general, we believe that wider recognition of the need to bring the ocean's hidden face to light will stir new observational endeavours, yield scientific surprises and catalyse progress in a range of geoscience disciplines.

References

Adcroft, A., Scott, J. R., and Marotzke, J. (2001). Impact of geothermal heating on the global ocean circulation. *Geophysical Research Letters*, 28(9):1735–1738.

de Lavergne, C., Madec, G., Le Sommer, J., Nurser, A. J. G., and Naveira Garabato, A. C. (2016a). The impact of a variable mixing efficiency on the abyssal overturning. *Journal of Physical Oceanography*, 46(2):663–681.

de Lavergne, C., Madec, G., Le Sommer, J., Nurser, A. J. G., and Naveira Garabato, A. C. (2016b). On the consumption of Antarctic Bottom Water in the abyssal ocean. *Journal of Physical Oceanography*, 46(2):635–661.

Dewar, W. K., Berloff, P., and Hogg, A. M. (2011). Submesoscale generation by boundaries. *Journal of Marine Research*, 69(4-6):501–522.

Ezer, T. and Mellor, G. L. (2004). A generalized coordinate ocean model and a comparison of the bottom boundary layer dynamics in terrain-following and in z-level grids. *Ocean Modelling*, 6(3–4):379–403.

Griffies, S. M., Böning, C., Bryan, F. O., Chassignet, E. P., Gerdes, R., Hasumi, H., Hirst, A., Treguier, A.-M., and Webb, D. (2000). Developments in ocean climate modelling. *Ocean Modelling*, 2(3–4):123–192.

Huussen, T. N., Naveira-Garabato, A. C., Bryden, H. L., and McDonagh, E. L. (2012). Is the deep Indian Ocean MOC sustained by breaking internal waves? *Journal of Geophysical Research*, 117(C8):C08024.

Lill, G. G. and Maxwell, A. E. (1959). The Earth's mantle. *Science*, 129:1407–1410.

Munk, W. and Wunsch, C. (1998). Abyssal recipes II: Energetics of tidal and wind mixing. *Deep-Sea Research*, 45(12):1977–2010.

Naveira Garabato, A. C. (2012). A perspective on the future of physical oceanography. *Philosophical Transactions of the Royal Society of London*, 370(1980):5480–5511.

Naveira Garabato, A. C., Nurser, A. J. G., Scott, R. B., and Goff, J. A. (2013). The impact of small-scale topography on the dynamical balance of the ocean. *Journal of Physical Oceanography*, 43(3):647–668.

Nikurashin, M., Vallis, G. K., and Adcroft, A. (2012). Routes to energy dissipation for geostrophic flows in the Southern Ocean. *Nature Geoscience*, 6(1):48–51.

Polzin, K. L., Garabato, A. C. N., Abrahamsen, E. P., Jullion, L., and Meredith, M. P. (2014). Boundary mixing in Orkney Passage outflow. *Journal of Geophysical Research*, 119:C010099.

Purkey, S. G. and Johnson, G. C. (2010). Warming of global abyssal and deep Southern Ocean waters between the 1990s and 2000s: Contributions to global heat and sea level rise budgets. *Journal of Climate*, 23(23):6336–6351.

Riser, S. C., Freeland, H. J., Roemmich, D., Wijffels, S., Troisi, A., Belbéoch, M., Gilbert, D., Xu, J., Pouliquen, S., Thresher, A., Le Traon, P.-Y., Maze, G., Klein, B., Ravichandran, M., Grant, F., Poulain, P.-M., Suga, T., Lim, B., Sterl, A., Sutton, P., Mork, K.-A., Vélez-Belchí, P. J., Ansorge, I., King, B., Turton, J., Baringer, M., and Jayne, S. R. (2016). Fifteen years of ocean observations with the global Argo array. *Nature Climate Change*, 6(2):145–153.

Roemmich, D., Johnson, G., Riser, S., Davis, R., Gilson, J., Owens, W. B., Garzoli, S., Schmid, C., and Ignaszewski, M. (2009). The Argo Program: Observing the global oceans with profiling floats. *Oceanography*, 22(2):34–43.

Snow, K., Hogg, A. M., Downes, S. M., Sloyan, B. M., Bates, M. L., and Griffies, S. M. (2015). Sensitivity of abyssal water masses to overflow parameterisations. *Ocean Modelling*, 89:84–103.

St. Laurent, L. C., Toole, J. M., and Schmitt, R. W. (2001). Buoyancy forcing by turbulence above rough topography in the abyssal Brazil Basin. *Journal of Physical Oceanography*, 31(12):3476–3495.

Walin, G. (1982). On the relation between sea-surface heat flow and thermal circulation in the ocean. *Tellus*, 34(2):187–195.

Wright, C. J., Scott, R. B., Ailliot, P., and Furnival, D. (2014). Lee wave generation rates in the deep ocean. *Geophysical Research Letters*, 41(7):2434–2440.

Wright, C. J., Scott, R. B., Arbic, B. K., and Furnival, D. F. (2012). Bottom dissipation of subinertial currents at the Atlantic zonal boundaries. *Journal of Geophysical Research*, 117(C3):C03049.

Wright, C. J., Scott, R. B., Furnival, D., Ailliot, P., and Vermet, F. (2013). Global observations of ocean-bottom subinertial current dissipation. *Journal of Physical Oceanography*, 43(2):402–417.

Zhai, X., Johnson, H. L., and Marshall, D. P. (2010). Significant sink of ocean-eddy energy near western boundaries. *Nature Geoscience*, 3(9):608–612.

CHAPTER

V

Towards a parameterization of internal wave-driven mixing

In chapters I and II, we explored the role of locally or remotely breaking bottom-generated internal waves for deep water mass transformation. The specified distributions of the wave-breaking energy used to infer diapycnal diffusivities relied on several gross simplifications, including:

(1) One-third of the estimated energy flux into internal tides and lee waves dissipates locally according to a fixed exponential decay with height above bottom.

(2) The remaining internal tide energy dissipation is proportional to water depth or uniformly spread within 1,000 km of sources, with a vertical distribution that depends on an integer power of the buoyancy frequency N.

Simplification (1) is commonly adopted to parameterize bottom-enhanced tidal mixing in global ocean models (e.g., Simmons et al. 2004b; Jayne 2009; Melet et al. 2014). Assumptions (2) are strongly idealized scenarios which aimed at exploring the sensitivity to key choices.

To narrow down uncertainties in the contributions of internal tides and lee waves to the consumption of Antarctic Bottom Water (AABW), and to improve model representations of internal wave-driven mixing, it is necessary to construct more accurate three-dimensional maps of internal tide and lee wave energy sinks. This entails relaxing assumptions of a fixed fraction and fixed vertical structure of local dissipation, and estimating where the energy of the propagating, lower-mode internal tides cascades down to the dissipation scale. In particular, the

analysis of chapter I showed that the vertical structure of the dissipation should receive special attention. Because we expect this vertical structure to depend upon the process causing internal waves to dissipate (e.g., Nikurashin and Legg 2011; Legg 2014; Melet et al. 2016), we must aim to distinguish different process contributions to the dissipation of internal waves.

In this chapter, building on recent advances in our understanding of how and where internal tides dissipate (e.g., Bühler and Holmes-Cerfon 2011; Klymak et al. 2011, 2013; MacKinnon et al. 2013b; Kelly et al. 2012, 2013; Legg 2014; Eden and Olbers 2014; Lefauve et al. 2015; Melet et al. 2016; Zhao et al. 2016), we present a framework for estimating internal tide energy sinks and parameterizing internal tide- and lee wave-driven mixing in ocean climate models. The proposed mixing scheme has been implemented in the NEMO ocean model, and is currently employed in the ocean component of the IPSL climate model participating to phase six of the Coupled Model Intercomparison Project. Nonetheless, despite its advanced development, the parameterization remains a work in progress as the comparison of mapped dissipation rates against available turbulence observations (Waterhouse et al. 2014) has not been completed.

The rationale of the mixing parameterization is the following. First, we estimate the horizontal distribution of internal wave energy dissipation as a function of the process transferring energy to small dissipative scales (section V.1). Second, we convert two-dimensional maps of available power into three-dimensional energy fields by applying a vertical structure of dissipation appropriate to each dissipative process (section V.2). Last, we deduce a three-dimensional diffusivity field from total dissipation rates using a variable mixing efficiency (chapter II).

V.1 Two-dimensional mapping of internal tide energy sinks

Context

The interaction of barotropic tidal currents with topography generates internal tides of various vertical scales (Garrett and Kunze 2007). Waves of small vertical scale are more prone to instability than larger-scale waves, which can propagate over longer distances and dissipate far from their generation site (e.g., St. Laurent and Garrett 2002). To characterize the vertical scales of internal tides, it is customary to describe their vertical wavenumber spectrum by a discrete set of vertical normal modes or "equivalent" modes. Whereas the first few modes have been observed to travel over up to several thousands of kilometres (Ray and Mitchum 1996; Zhao et al. 2016), higher modes are thought to break into small-scale turbulence within a relatively small radius of their emission. The breaking of high mode internal tides is thus generally mapped using the assumptions that high modes represent a uniform fraction of the energy source and feed local dissipation (St. Laurent et al. 2002). Where and how the energy of lower modes is lost to turbulence remains a subject of active research (MacKinnon et al. 2013b; Melet et al. 2016; Pinkel et al. 2016).

Niwa and Hibiya (2011) recently constructed a map of low-mode tidal dissipation using global three-dimensional numerical experiments that include tidal forcing and a 30-day linear damping of baroclinic perturbations. But though these global simulations allow a representation of the generation and propagation of low-mode internal tides (Simmons et al. 2004a; Niwa and Hibiya 2011; Waterhouse et al. 2014), they do not resolve the downscale energy transfer through which internal tides dissipate. As a result, the inferred low-mode dissipation is dependent on model numerics (Nugroho et al. 2015) and/or artificial damping terms (Niwa and Hibiya 2011). Process-based attenuation of the simulated internal tide would have to be parameterized in order to faithfully diagnose the full distribution of remote tidal dissipation.

An alternative approach to map low-mode tidal dissipation consists in resolving an evolution equation for a given mode's column-integrated energy E, a function of time t,

geographical position $\vec{x} = (x, y)$ and angle of energy propagation ϕ (Eden and Olbers 2014):

$$\partial_t E + \mathrm{div}_{\vec{x},\phi}\, \vec{F} = S - D \tag{V.1}$$

where $\vec{F} = \vec{c_g} E$ is the horizontal energy transport by the modal group velocity $\vec{c_g}$, D encapsulates energy sinks and S is the angle- and position-dependent generation rate of the considered mode. Note that the divergence of $\vec{F}$ includes both position (propagation) and angle (refraction or reflection) terms. Eden and Olbers (2014) solved equation (V.1) for the M2 tidal constituent using the WOCE hydrographic climatology (Gouretski and Koltermann 2004) and the following principal choices:

- The first few modes can be grouped into one evolution equation. Because mode 1 is expected to dominate, the group speed and estimated dissipation rates of mode 1 are used.
- The energy source S is taken as one-half the internal tide generation rate estimated by Nycander (2005), and uniformly distributed in angle.
- Dissipation is parameterized by three terms reflecting three (groups of) processes: (1) a non-linear term representing interaction with, and energy transfer to, higher-mode internal waves, evaluated via a transfer integral describing resonantly interacting waves; (2) an attenuation term for the scattering of the internal tide off abyssal hills, based on Müller and Xu (1992); (3) a fixed e-folding attenuation time of 7 days within 300 km of coastlines, representing dissipation at continental slopes and shelves.

They find that triadic wave instabilities (also referred to as parametric subharmonic instability) equatorward of 28.8° latitudes and scattering through reflection against rough ocean floor are the dominant sinks of low mode energy, attenuating the M2 internal tide over $\mathcal{O}(1\,\mathrm{day})$ timescales. As a result, they obtain weak sensitivity to the slower, spatially more restricted coastal attenuation. Nonetheless, the estimated rates of open-ocean attenuation contrast with in-situ (Alford et al. 2007; MacKinnon et al. 2013b) and satellite (Zhao and Alford 2009; Zhao et al. 2016) observations of long-range propagation of the first-mode internal tide, whose typical decay time appears to exceed 10 days even in the latitude zone where parametric subharmonic instability is active.

Strategy

Here, we construct climatological maps of column-integrated internal tide energy dissipation representing distinct breaking mechanisms. Combined with a vertical structure appropriate to each breaking pathway, these maps may be employed to diagnose tidal water mass transformation and parameterize internal tide-driven mixing in ocean models. We follow the approach of Eden and Olbers (2014) but incorporate the following extensions and modifications:

- The three main tidal constituents are considered: M2, S2 and K1.
- Equation (V.1) is solved separately for each of the first five vertical modes of each constituent. Higher modes are assumed to dissipate where they are generated, consistent with the calculated weak residence time (≈ 4 days) and mean propagation distance (≈ 100 km) of mode 5. Hence we do not assume a fixed ratio of local dissipation.
- The energy source for each constituent and each mode is taken from the mode-decomposed internal tide generation estimates of Falahat et al. (2014), with uniform angle distribution and an ad hoc correction for negative local rates. Internal tide generation at abyssal hill topography, estimated by Melet et al. (2013) but absent from the Falahat et al. (2014) estimates, is assumed to contribute modes higher than 5 only.
- Four dissipative processes are included: (1) wave-wave interactions, crudely represented by a latitude- and mode-dependent attenuation time compatible with available observations (Alford et al. 2007; MacKinnon et al. 2013b,a) and theory (Olbers 1983; Young et al. 2008; Hazewinkel and Winters 2011; MacKinnon et al. 2013b) ; (2) scattering by small-scale roughness, based on Bühler and Holmes-Cerfon (2011) and abyssal hill topography parameters of Goff (2010); (3) scattering at critical slopes, estimated from wave slopes and the 1/30-degree resolution 'etopo2v2' bathymetry (Smith and Sandwell 1997) using geometric arguments; (4) shoaling at subcritical slopes, parameterized based on results of Legg (2014).
- Energy exchanges between the first five modes are neglected: dissipative processes are assumed to transfer energy directly to small-scale turbulence.

- Angle redistribution of the energy flux due to refraction but also to reflection at supercritical slopes is included.

- Because we are only interested in the steady-state solution, we set the term $\partial_t E$ to zero and propagate the energy flux $\vec{F}$ using a simple Eulerian scheme. Since this scheme induces a significant degree of diffusion, a concern if the assumed isotropic emission of the internal tide is to be replaced by a more concentrated, beam-like emission, we plan to adopt a Lagrangian approach in the future.

Preliminary results

Fig. 1 shows the calculated modal dissipation fields for the semi-diurnal M2 tidal constituent. Low modes are dominated by mode 1, whose energy source of about 0.3 TW is comparable to the total power input to modes 2-5. The generation of modes greater than 5 is dominated by the 0.1 TW contribution of abyssal hill topography (Fig. 1d). Wave-wave interactions are relatively inefficient at attenuating the first-mode internal tide (Olbers 1983; MacKinnon et al. 2013b; Zhao et al. 2016), so that mode 1 waves are able to propagate across ocean basins and lose a large fraction of their energy through interaction with bathymetric slopes ($\sim 40\,\%$) and roughness ($\sim 30\,\%$). In contrast, wave-wave interactions are found to be the dominant dissipative mechanism of higher modes.

In order to parameterize internal tide-driven mixing, we need maps of the total energy flux into turbulence from each type of wave instability. Fig. 2 shows the estimated process-dependent dissipation rates summed over the principal eight tidal constituents. This sum D_{all} is obtained by assuming that the geographies of M2, S2 and K1 dissipation respectively approximate those of N2, K2 and the next three diurnal constituents (Egbert and Ray 2003), so that, using appropriate power ratios: $D_{all} = 1.05\,D_{M2} + 1.09\,D_{S2} + 1.70\,D_{K1}$. The total dissipation amounts to 1.04 TW, composed of five contributions: low-mode dissipation via wave-wave interactions (41 %); low-mode scattering by small-scale seafloor roughness (16 %); low-mode scattering at critical slopes (16 %); low-mode breaking through shoaling

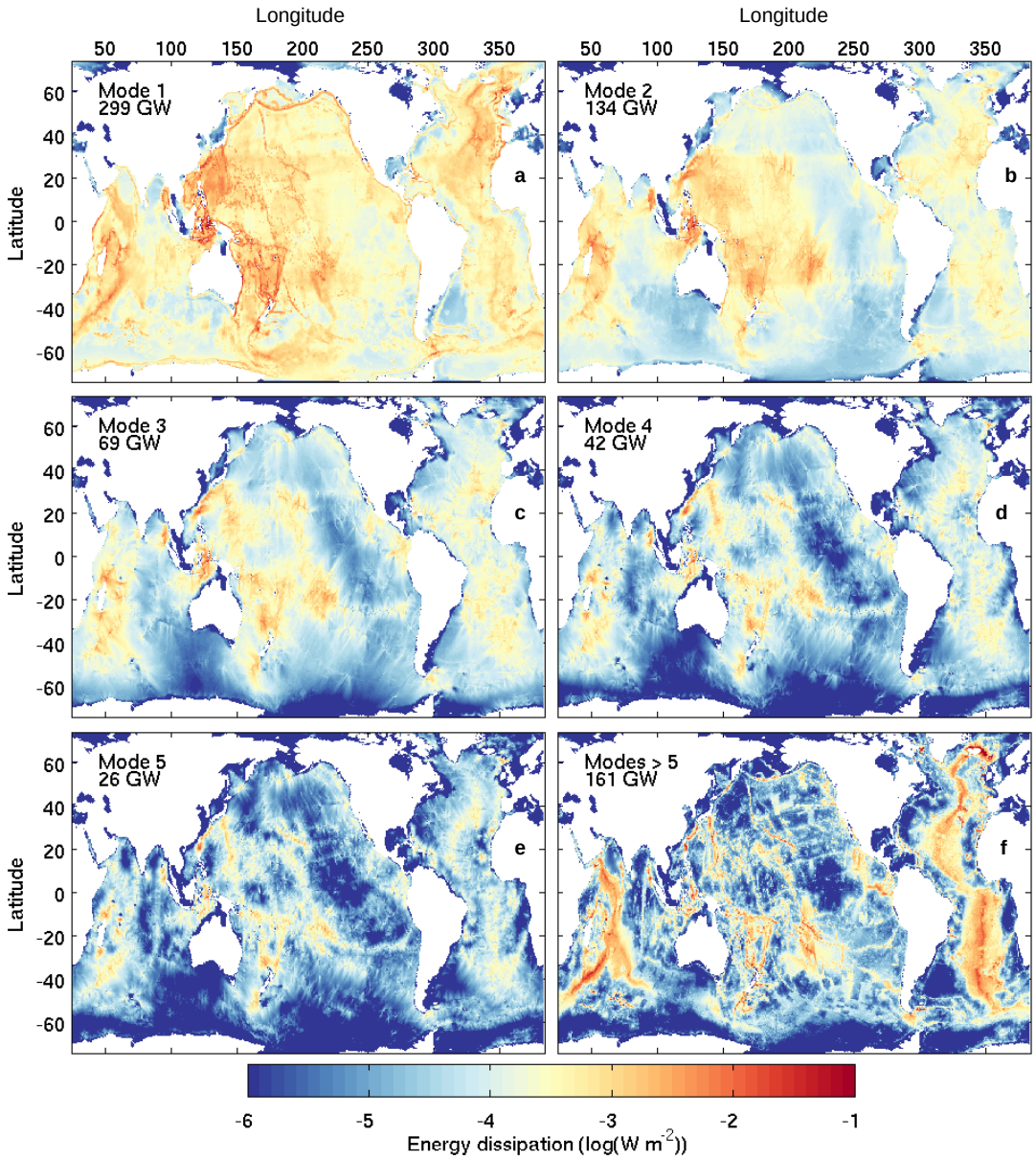

Figure 1: Estimated dissipation of the (**a**) mode 1, (**b**) mode 2, (**c**) mode 3, (**d**) mode 4, (**e**) mode 5 and (**f**) higher mode M2 internal tide. Modes greater than 5 are assumed to dissipate locally and include internal tides radiated from abyssal hills (Melet et al. 2013).

(11 %); high-mode, local dissipation (19 %). Despite the large uncertainties that surround the calculation, the mapped total dissipation shows fairly good agreement with a recent near-global observational map of column-integrated dissipation rates estimated from high resolution hydrographic profiles (Kunze, presentation at Ocean Sciences Meeting 2016).

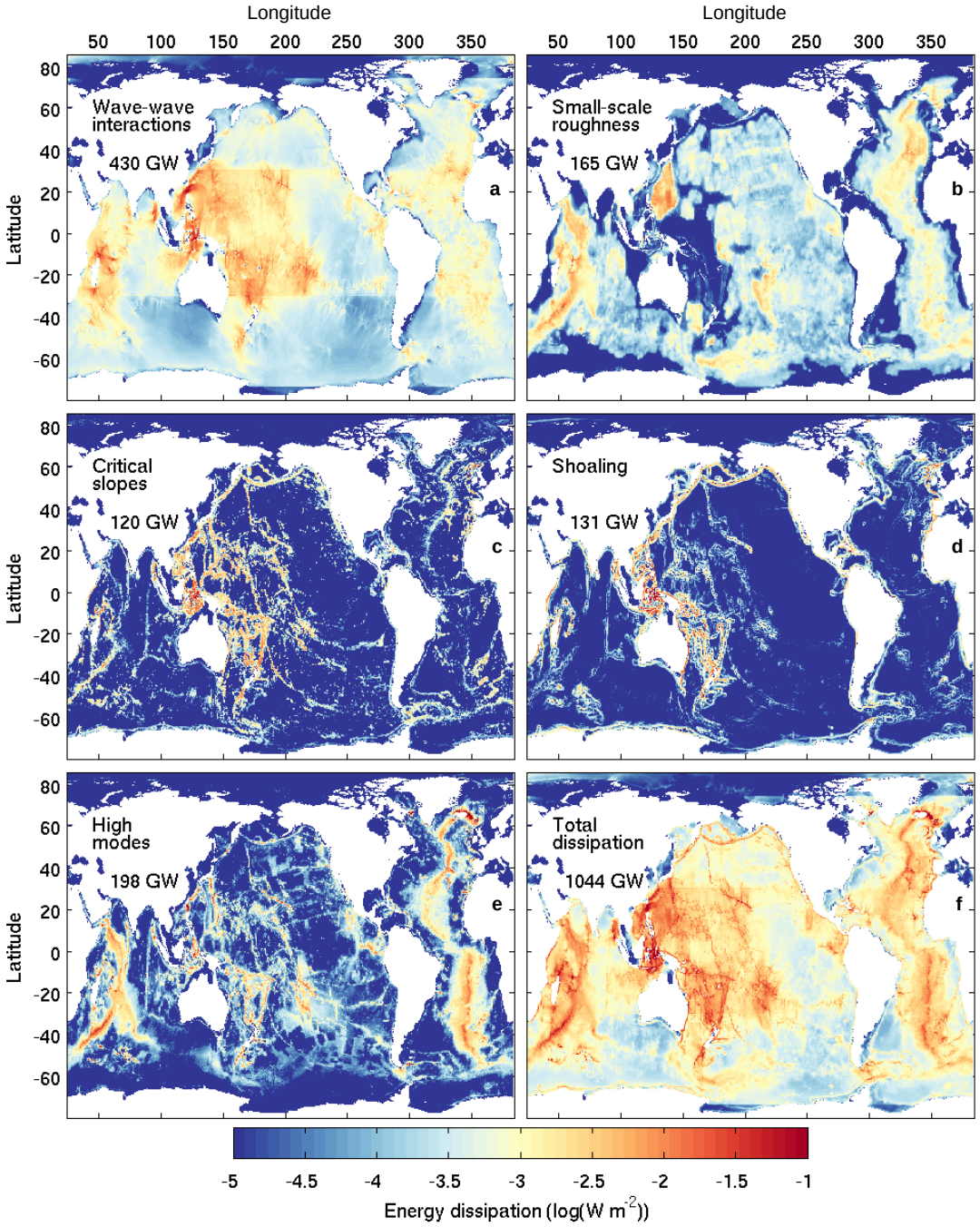

Figure 2: Internal tide energy dissipation by process. Low mode dissipation due to (**a**) wave-wave interactions, (**b**) scattering off abyssal hill topography, (**c**) scattering at critical slopes and (**d**) shoaling. (**e**) High mode, local dissipation and (**f**) total energy dissipation. The first eight tidal constituents are considered.

V.2 Parameterizing internal wave-driven mixing

Context

Mixing parameterizations of most global ocean models only explicitly incorporate the contribution of locally-dissipating high mode internal tides: they posit that one-third of the power input to internal tides contributes to local, bottom-enhanced turbulence (St. Laurent et al. 2002). The remaining two-thirds of the baroclinic tide energy source are then surmised to participate in sustaining a fixed background diffusivity of about $10^{-5}\,\mathrm{m^2 s^{-1}}$. Recently, mixing parameterizations that explicitly account for the dissipation of low mode internal tides have been developed for global ocean models (Oka and Niwa 2013; Eden and Olbers 2014; Melet et al. 2016). Oka and Niwa (2013) parameterized mixing driven by remotely-dissipating internal tides using a static two-dimensional map of baroclinic tide dissipation diagnosed from global numerical experiments (Niwa and Hibiya 2011). However, the mapped low-mode dissipation is reliant on a specified attenuation time of baroclinic wave fluctuations (Niwa and Hibiya 2011) and the assumption of vertically homogeneous dissipation rates.

Eden and Olbers (2014) developed a simple model for the propagation and dissipation of a low-mode internal wave energy compartment. Coupled to a parameterization of the dissipation of high mode internal waves through resonant wave-wave interactions (Olbers and Eden 2013), the model allows online, interactive computation of the three-dimensional distribution of internal wave-induced turbulent diffusivities. Nonetheless, the parameterized vertical structure of dissipation reflects only weak wave-wave interactions rather than specific internal wave breaking pathways. In addition, the predicted leading role of triadic instabilities for the decay of the first-mode internal tide appears at odds with the observed and simulated open-ocean attenuation rate of low-mode wave beams (Alford et al. 2007; Hazewinkel and Winters 2011; MacKinnon et al. 2013b; Zhao et al. 2016).

Melet et al. (2016) used a set of idealized scenarios for the horizontal and vertical distributions of internal tide energy dissipation to explore the sensitivity of the simulated climate

to these distributions. Consistent with water mass transformation diagnostics (chapter I), they found that the vertical structure of the open-ocean dissipation is a key ingredient of internal wave-driven mixing parameterizations. The climate simulations also reveal sensitivity of deep ocean properties to levels of mixing within formation regions of dense water masses.

Strategy

Here, we propose a comprehensive parameterization of mixing by breaking internal tides and lee waves that allows:

- energetic consistency, by obviating the need for a non-molecular (non-zero) floor on diffusivity (turbulent kinetic energy);
- the combined use of different vertical structures of wave-breaking energy, appropriate to different breaking processes;
- interactive evolution of these vertical structures in response to stratification changes;
- realistic variations of the fraction of local, high mode dissipation;
- realistic variations of the mixing efficiency (chapter II).

The parameterization uses four static maps of available power (Fig. 3) associated with four different vertical structures of dissipation, thus favouring a faithful representation of the depth distribution of turbulence to the interactivity of low-mode energy propagation with simulated, evolving ocean states.

The first map (Fig. 3a) corresponds to the dissipation of low mode internal tides due to wave-wave interactions, a process for which observations and theory suggest that turbulent production ε_T scales with the square of the buoyancy frequency N^2 (e.g., Müller et al. 1986; Gregg 1989; Polzin et al. 1995; Kunze and Sanford 1996; Kunze 2016). The second component (Fig. 3b) embodies the direct breaking of low mode internal tides through shoaling, where the dissipation structure roughly matches the energy of the wave, proportional to N (Legg 2014). The third component of the parameterization (Fig. 3c) represents the scattering of low mode internal tides at critical slopes, which generates boundary turbulence

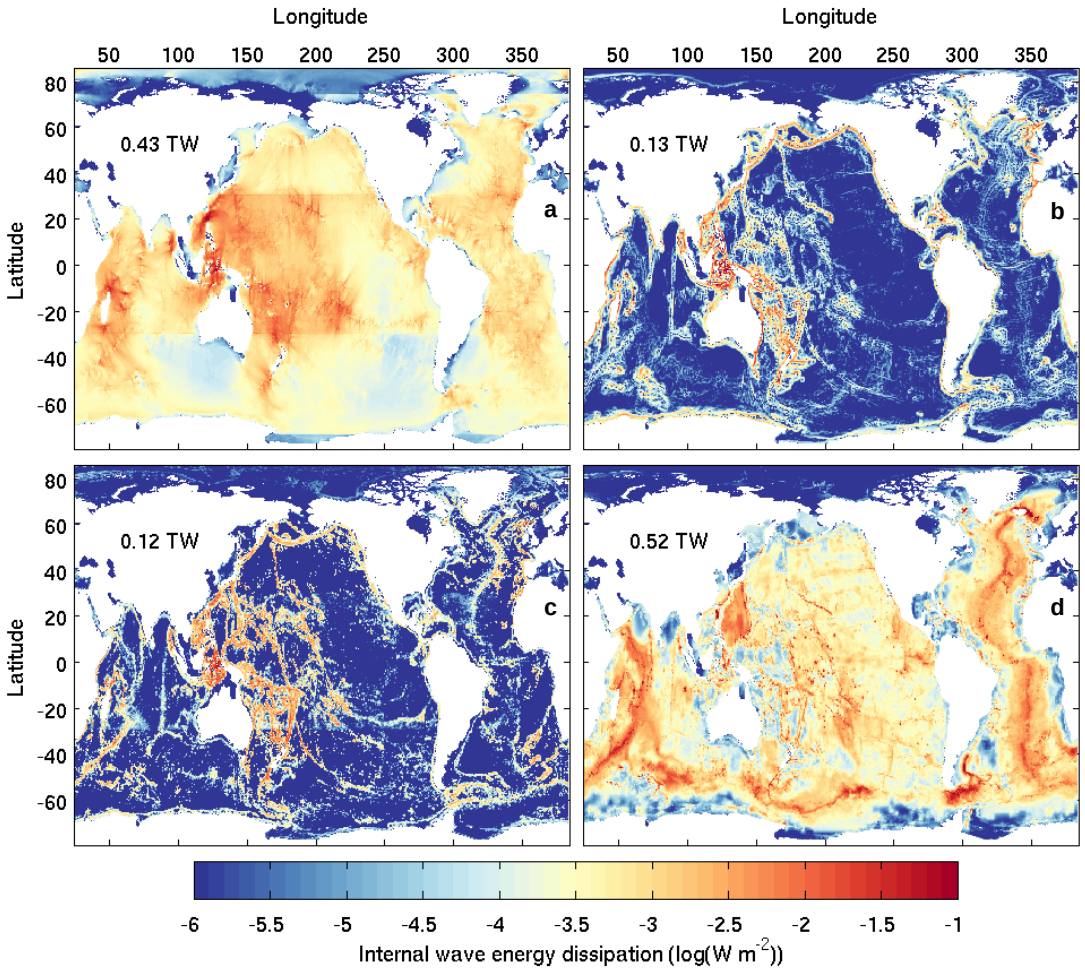

Figure 3: Power input to internal wave-driven turbulence. (**a-c**) Dissipation of low mode internal tides due to (**a**) wave-wave interactions, (**b**) shoaling and (**c**) scattering at critical slopes. (**d**) Dissipation of small-scale waves radiated from the bottom.

along the slope (e.g., Moum et al. 2002; Legg and Adcroft 2003; Nash et al. 2004). The along-slope concentration of dissipation is not easily mimicked in a coarsely-resolved ocean with step-like topography. To roughly capture the vertical extent and bottom-intensification of the dissipation, we use an exponential decay from the seafloor with an e-folding scale equal to the along-slope height difference ΔH:

$$\varepsilon_T \propto \exp[-h_{ab}(z)/\Delta H(x,y)] \tag{V.2}$$

with h_{ab} the height above bottom and z the local height.

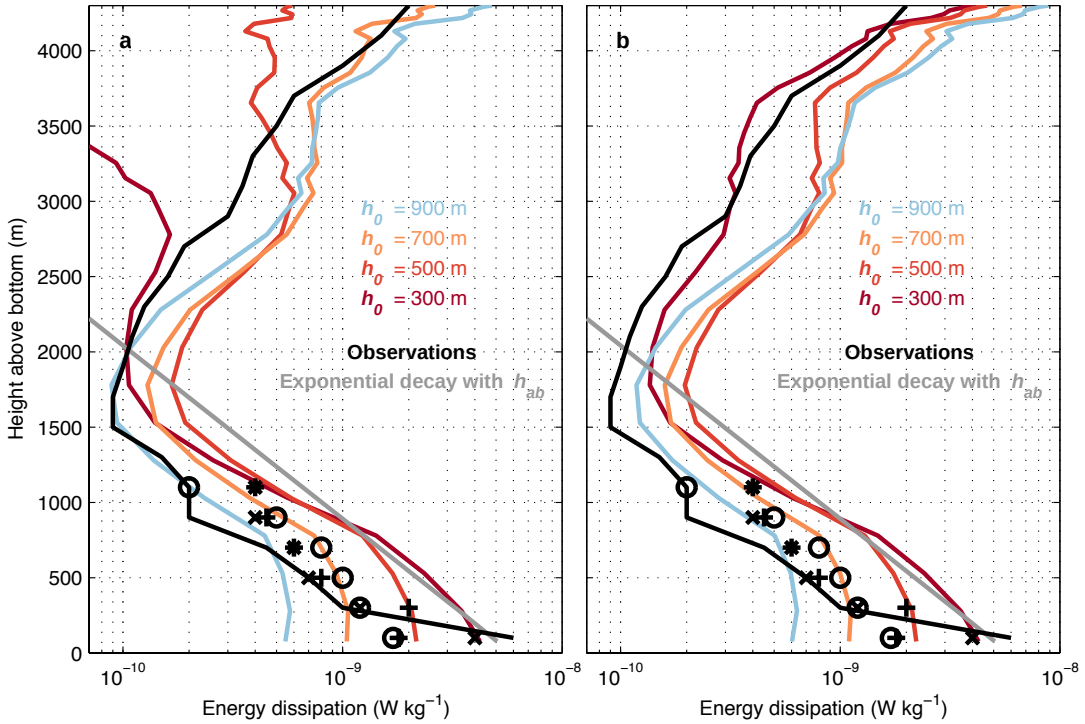

Figure 4: Comparison of the parameterized dissipation (V.3,V.4) with Brazil Basin (21.5°S, 18°W) microstructure observations. (**a**) Modelled energy dissipation rates (coloured curves) given four values of the vertical decay scale h_0 and the calculated local power input to small-scale waves $E_0 = 3\,\mathrm{mW\,m^{-2}}$. The grey line shows the parameterized dissipation assuming instead an exponential decay with h_{ab} and a 500 m e-folding scale (St. Laurent et al. 2002). Compilations of microstructure observations by (curve) Polzin (2009) and (symbols) St. Laurent et al. (2001) are shown in black. (**b**) Same as (**a**), with the parameterized low-mode dissipation due to wave-wave interactions (estimated as $1.5\,\mathrm{mW\,m^{-2}}$ and vertically distributed as proportional to N^2) added to coloured curves. Low-mode dissipation due to shoaling or critical slope scattering is negligible at this location.

The fourth map (Fig. 3d) estimates the dissipation of small-scale waves emitted from the ocean bottom, grouping three components of similar global power contribution: locally generated high mode internal tides; lower mode internal tides scattered off small-scale topography; and lee waves radiated by geostrophic flows impinging on small-scale topography (Nikurashin et al. 2014). Local dissipation of these small-scale waves is set as proportional to N^2 times an exponential decay with WKB-stretched height above bottom (Lefauve et al. 2015):

$$\varepsilon_T \propto N^2 \exp[-h_{wkb}(z)/h_0(x,y)] \tag{V.3}$$

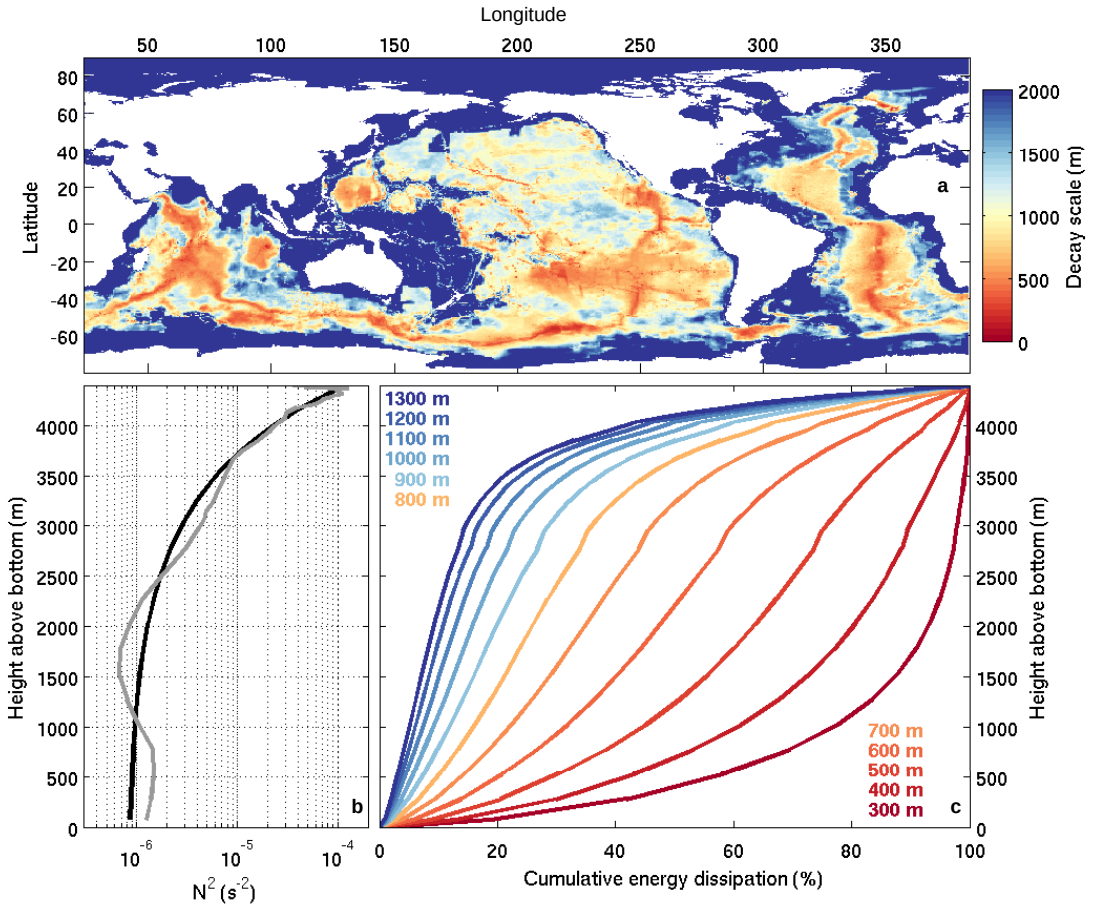

Figure 5: Parameterized decay scale h_0 and implications for the vertical distribution of energy dissipation. (**a**) Map of h_0 deduced from (V.5). (**b**) Analytical fit (black) to the observed (grey) Brazil Basin stratification profile. (**c**) Bottom-up cumulative distribution of energy dissipation predicted by (V.3) for the black stratification profile shown in (**a**) and various values (colors) of the e-folding height h_0.

where h_0 is the e-folding height and

$$h_{wkb}(z) = H \, \frac{\int_{-H}^{z} N \, dz}{\int_{-H}^{0} N \, dz} \, . \tag{V.4}$$

This empirical vertical distribution was shown to capture well the dissipation structure of internal tides radiated from abyssal hills, given a spatially varying decay scale that depends on the bottom root-mean-square wave amplitude (Lefauve et al. 2015). This root-mean-square amplitude can be related to the bottom energy flux E_0 and the mean horizontal wavelength of

abyssal hills κ, yielding the parameterized decay scale:

$$h_0(x,y) = h_0(x_B,y_B)\left[\frac{E_0(x_B,y_B)\,\kappa(x_B,y_B)^3}{E_0(x,y)\,\kappa(x,y)^3}\right]^{1/4} \tag{V.5}$$

where x_B, y_B mark the Brazil Basin location used for calibration against microstructure observations (Fig. 4). We choose $h_0(x_B,y_B) = 600\,\mathrm{m}$ as the best match to the observed fraction of energy contained in separate 1,000 m thick layers. The resulting map of the decay scale h_0 (Fig. 5) predicts that only the combined presence of small-horizontal-scale topographic features and energetic internal wave radiation allows a strong near-bottom concentration of wave breaking, consistent with observations and theory (Polzin et al. 1997; Kunze and Llewellyn Smith 2004; Muller and Bühler 2009). Elsewhere, a sizeable fraction of the energy of small-scale waves transfers to turbulence only when it reaches the higher stratification of the mid- to upper-ocean (Kunze et al. 2006; Nikurashin and Legg 2011; Wu et al. 2011; Whalen et al. 2012; Meyer et al. 2015; Lefauve et al. 2015).

Preliminary results

To document energy and diffusivity distributions implied by the parameterization, we first apply it to the WOCE global hydrographic climatology (Gouretski and Koltermann 2004). The zonal sum of the total energy flux into turbulence, indicative of the net downward buoyancy flux that penetrates in the ocean, is shown in Fig. 6b. Clearly apparent is the concentration of internal wave energy dissipation in the upper 2,000 m of the ocean, expected from the stratification dependence of three of the four vertical structures. The predicted tendency of internal waves to break in strongly-stratified regions is a consequence of the reduction of their vertical scale as stratification increases, and of the vertical structure of internal tide energy, which scales as N (e.g., Müller et al. 1986; Legg 2014; Lefauve et al. 2015). As a result, only about 20 % (10 %) of internal wave energy dissipates deeper than 2,000 m (3,000 m) depth under the present parameterization (Fig. 6a). The associated effective diffusivities, or stratification-weighted mean diffusivities, show a general but modest enhancement with depth (Fig. 6c,d). At the global scale, the effective diffusivity increases quasi-linearly from $1.8\times10^{-5}\,\mathrm{m^2\,s^{-1}}$ at 1,000 m to $4.5\times10^{-5}\,\mathrm{m^2 s^{-1}}$ at 4,000 m depth. Consistent with observations (e.g., Gregg 1989; Ffield and Gordon 1992; Ledwell et al. 1993; Gregg et al. 2003;

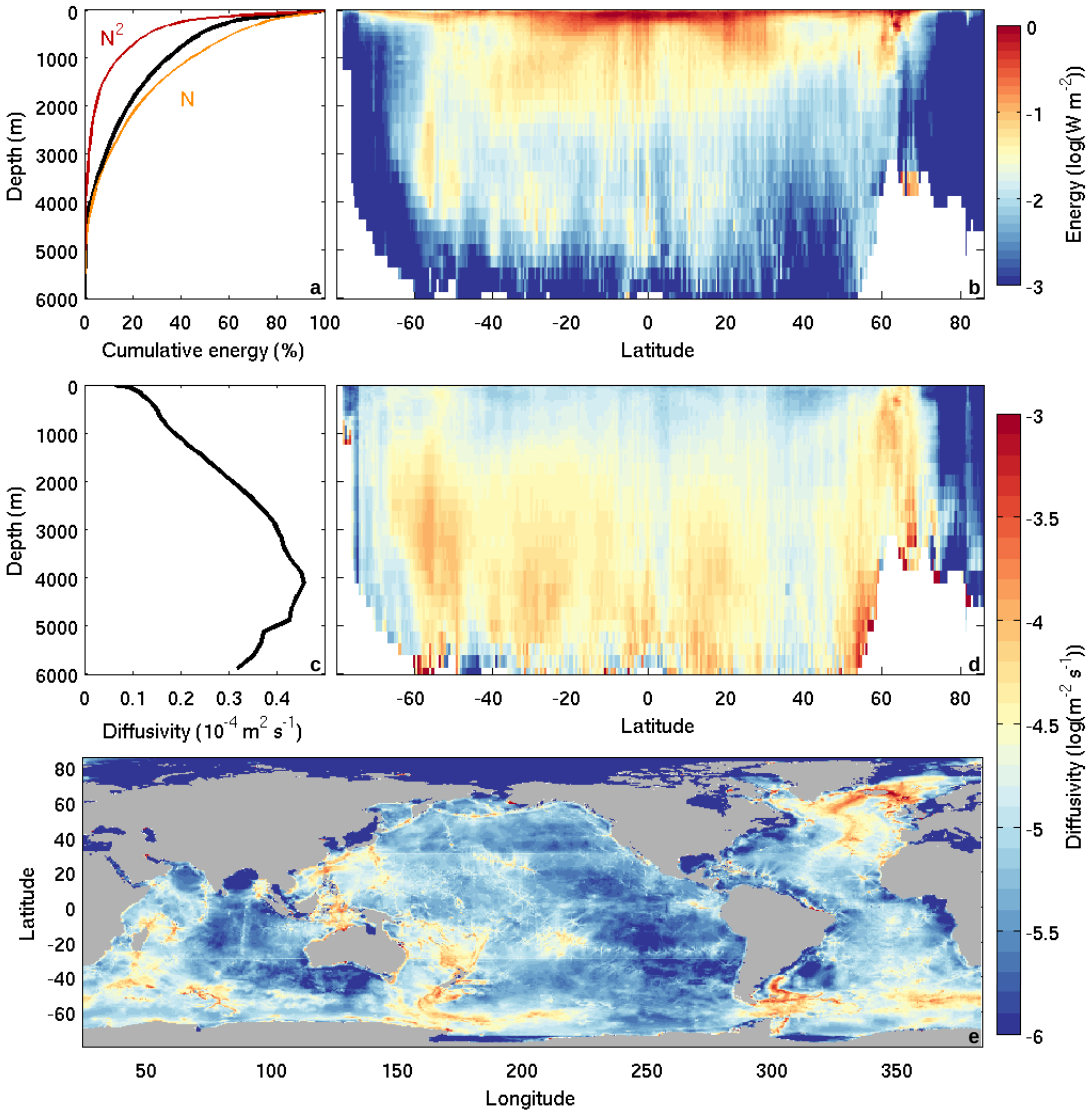

Figure 6: Parameterized internal wave energy dissipation and induced diffusivity. (**a**) Bottom-up cumulative sum and (**b**) zonal sum of energy dissipation. Red and orange profiles in (**a**) correspond to fictitious cumulative distributions obtained by setting dissipation globally proportional to N^2 and to N, respectively. (**c**) Stratification-weighted mean diffusivity as a function of (**c**) depth and (**d**) depth and latitude. (**e**) Diffusivity at the depth of maximum local stratification. A variable mixing efficiency according to the reference formulation of chapter II was used to infer diffusivities from dissipation.

Rainville and Winsor 2008; Fer 2009; Whalen et al. 2012; Watson et al. 2013; Waterhouse et al. 2014), upper-ocean diffusivities average about 10^{-5} m^2 s^{-1} in the main pycnocline, with higher values in regions of strong internal wave generation, such as the Indonesian Seas or the Scotia Sea, and lower values in the eastern Pacific, eastern Indian and Arctic oceans (Fig. 6d,e).

To explore implications of the parameterization for deep water mass transformation, we integrate mixing-driven buoyancy fluxes over neutral surfaces, following methods outlined in chapter I. North of 30°S, the total downward buoyancy flux is convergent throughout the deep ocean density range (Fig. 7a, black), driving net upwelling of dense waters (Fig. 7b, black). Upwelling rates remain relatively modest however, peaking just over 6 Sv near the 27.9 kg m^{-3} neutral density level, and amounting to only 3 Sv within the weakly-stratified layer that defines the boundary between bottom and deep waters (28.11 kg m^{-3}). In particular, the vertical structure (V.3) adopted for the dissipation of small-scale waves radiated from the bottom leads to very different water mass transformation than the commonly-employed exponential decay with height above bottom (Fig. 7a,b, pale blue versus grey). Indeed, (V.3) implies that small-scale internal waves feed turbulence not only within the near-bottom waters but also in the more stratified overlying waters. As a result, convergence of the total buoyancy flux and induced upwelling north of 30°S are maximal above rather than within the thick, homogeneous water mass of density $\approx$ 28.11 kg m^{-3} that occupies much of the abyssal floor. South of 30°S (Fig. 7c,d), deep transformation is also dominated by small-scale waves emitted at the bottom, as expected from the dominance of lee wave radiation in the Antarctic Circumpolar Current (Melet et al. 2014). In contrast to the uniform exponential decay employed in chapters I and II, the stratification-dependent vertical structure (V.3) entails net (but modest) consumption and upwelling of AABW in the Southern Ocean. Nevertheless, both vertical structures conduce to homogenization of AABW, with net volume gain of 28.11-28.2 kg m^{-3} waters and net volume loss of denser waters.

Inclusion of the mixing parameterization in a global ocean model allows investigation of its impact in a self-consistent, interactive context where stratification and rates of dense water formation may adjust to interior mixing[1]. We performed two 500-year simulations with the 2°-resolution configuration of the NEMO ocean model forced by normal year air-sea fluxes (CORE.2; Griffies et al. 2012). The first simulation uses the model's standard mixing schemes: a second-order turbulent kinetic energy closure for near-surface mixing (Blanke and Delecluse 1993; Madec 2015), with a floor on turbulent kinetic energy inducing moderate, dis-

[1]Implementation in a global *climate* model would be desirable to obtain complete self-consistency and freedom of adjustment. We plan to perform coupled ocean-atmosphere experiments in the near future.

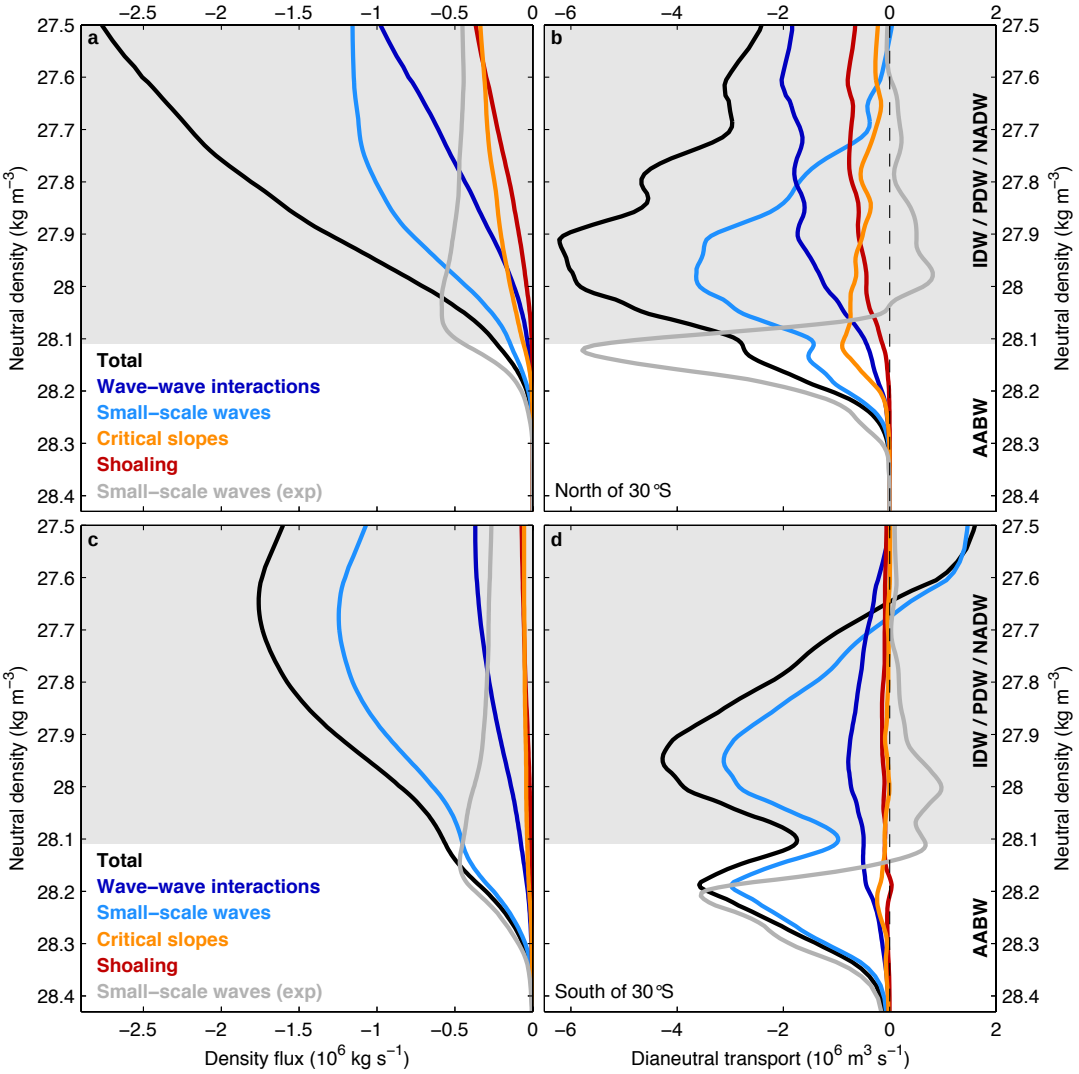

Figure 7: Deep water mass transformation by parameterized internal wave-driven mixing (**a**,**b**) north and (**c**,**d**) south of 30°S. (**a**,**c**) Neutral density flux across neutral surfaces and (**b**,**d**) implied dianeutral transport for (colors) each component of the parameterization taken in isolation and (black) the full parameterization. For comparison, we show in grey the density flux and transports induced by small-scale waves radiated from the bottom when replacing the present vertical structure by an exponential decay with h_{ab} and a 500 m e-folding scale. Negative (positive) dianeutral transport corresponds to upwelling (downwelling). The density range of bottom (AABW) and deep (IDW / PDW / NADW) waters is indicated by the grey shading and the right-side labels.

tributed deep mixing; a fixed background diffusivity of $10^{-5}\,\mathrm{m^2\,s^{-1}}$; and a parameterization of local, bottom-enhanced tidal mixing (St. Laurent et al. 2002). The second simulation uses the same mixed layer physics but incorporates the present parameterization as a replacement for the background diffusivity and turbulent kinetic energy and for the former tidal mixing scheme. Fig. 8 shows the Atlantic and Indo-Pacific meridional streamfunctions averaged over

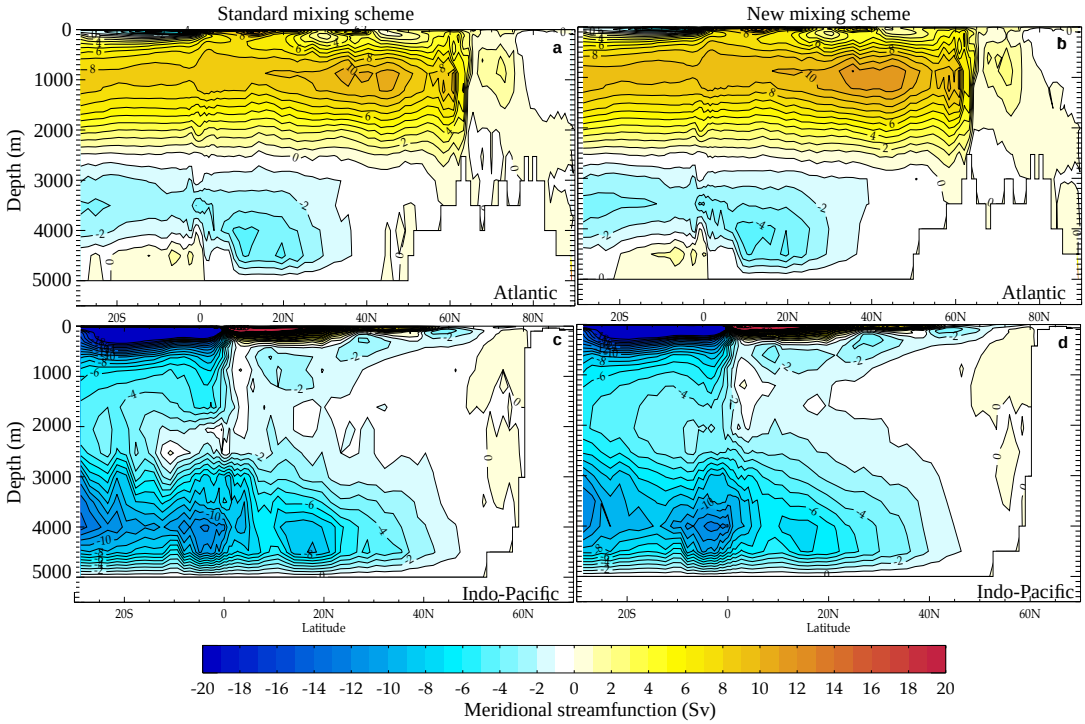

Figure 8: Impact of the parameterization on the meridional overturning in a 2°-resolution configuration of the NEMO ocean model. Mean (**a**,**b**) Atlantic and (**c**,**d**) Indo-Pacific meridional overturning streamfunction [Sv] simulated under (**a**,**c**) standard and (**b**,**d**) present internal wave-driven mixing parameterizations. The streamfunction has been averaged over the last 50 years of a 500-year ocean-only experiment forced with CORE.2 normal year air-sea fluxes (Griffies et al. 2012).

the last 50 years of each experiment. Changes in the strength and structure of AABW and North Atlantic Deep Water (NADW) circulations brought on by the new parameterization are modest, consistent with the relatively low deep ocean transformation rates documented in Fig. 7. Two positive impacts can nonetheless be noted: a slight enhancement of the NADW circulation, likely attributable to changes in the intensity and distribution of mixing in the upper 1,000 m; and a somewhat smoother abyssal overturning structure, attributable to the more distributed internal tide dissipation predicted by the new scheme.

Discussion

In order to fully validate the parameterization, we need to examine the sensitivity of low-mode dissipation maps to the energy propagation scheme and wave-wave interaction decay times, and to compare modelled vertical structures with microstructure observations from regions other than the Brazil Basin (Waterhouse et al. 2014). Completion of this key validation phase

will help to reduce uncertainties in the contributions of internal tides and lee waves to the consumption of AABW. In particular, whether the vertical structure (V.3,V.4) combined to the recent lee wave generation estimate of Nikurashin et al. (2014) adequately captures the distribution of lee wave breaking remains to be assessed. Preliminary estimates of water mass transformation presented in Fig. 7 thus have largest uncertainties in the Southern Ocean. Inclusion of additional internal wave energy sinks and sources, such as surface generation of near-inertial waves (Alford 2003; Jochum et al. 2013) and interactions between internal waves and mesoscale eddies (Brown and Owens 1981; Polzin 2008, 2010; Dunphy and Lamb 2014; Jouanno et al. 2016), will also contribute to improve the parameterization and the quantification of internal wave-driven density transformation.

In spite of these limitations, the result that breaking internal tides are not a leading contributor to the destruction and upwelling of AABW is expected to be robust. Indeed, the predicted upper-ocean concentration of internal tide dissipation (Fig. 6a), with over 65 % taking place above 1,000 m depth and less than 10 % below 3,000 m, is largely independent of inaccuracies of the parameterization and is corroborated by observational syntheses (Kunze et al. 2006; Huussen et al. 2012; Kunze 2016). Several lines of reasoning support the conclusion that only a minor fraction of internal tide dissipation is available to abyssal mixing:

- Estimates of internal tide generation (Nycander 2005; Melet et al. 2013) indicate that less than 20 % of the conversion occurs below 3,000 m, so that most of the local dissipation affects mid- to upper-ocean waters.

- Even in regions of strong internal wave generation over rough topography, observations (Kunze et al. 2006; Polzin 2009; Waterhouse et al. 2014; Meyer et al. 2015) and numerical studies (Nikurashin and Legg 2011; Olbers and Eden 2013; Lefauve et al. 2015) suggest that a sizeable or even dominant proportion of the dissipation occurs in the pycnocline.

- A large body of theoretical (Müller et al. 1986; Polzin et al. 1995; Hazewinkel and Winters 2011; Lefauve et al. 2015) and observational (Gregg 1989; Kunze and Sanford 1996; Kunze 2016) evidence points to an N^2 scaling of internal wave dissipation away from sources, which implies that the upper 1,000 m of the ocean should concentrate ~ 85 % of the non-local, open-ocean dissipation (Fig. 6a).

- Remote dissipation of internal tides at continental slopes and shelves contributes mostly upper-ocean mixing.

As a result, breaking internal tides could contribute no more than ~ 3 Sv of upwelling across the (most probable) boundary between northward-flowing AABW and southward-flowing deep waters, but drive somewhat higher upwelling rates within the deep water density range (Fig. 7b).

Such a weak role of internal tides for abyssal upwelling contrasts with the larger transformation obtained under the hypotheses of chapter I and with the important or even dominant role attributed to tides by the recent literature (e.g., Wunsch and Ferrari 2004; Niwa and Hibiya 2011; Nikurashin and Ferrari 2013; Waterhouse et al. 2014; Ferrari 2014). We argue that tidally-forced dense water upwelling has been overestimated for several reasons. First, bulk energy considerations overlooked the sensitivity of abyssal water mass transformation to the precise depth distribution of turbulence (chapter I). Second, the assumption of a constant mixing efficiency has led to overestimation of the impact of concentrated, bottom-enhanced turbulence (chapter II), or to omission of the no-flux bottom boundary condition and misinterpretations (Nikurashin and Ferrari 2013; see chapter I). Third, the use of a parameterization based on Brazil Basin observations (St. Laurent et al. 2002) has led to magnify the global proportion of abyssal dissipation. Indeed, this area of the Mid-Atlantic Ridge is characterized by strong small-scale topographic roughness (Goff 2010), which contributes a substantial fraction of the local tidal conversion (Nikurashin and Legg 2011; Melet et al. 2013) and favours near-bottom dissipation (Kunze and Llewellyn Smith 2004; Muller and Bühler 2009). Evidence from these studies thus shows that the Brazil Basin near-bottom dissipation is largely controlled by the presence of abyssal hills. Global application of a one-third fraction of local dissipation to internal tide generation estimates (e.g., Nycander 2005) that exclude the

contribution of abyssal hills, and of an exponential decay that reflects particular topographic (and hydrographic) conditions, is therefore hazardous. Use of the present parameterization reduces the global amount of dissipation within 500 m of the bottom by almost a factor of 4.

In short, the estimated distributions of internal wave energy dissipation suggest that breaking internal tides and lee waves power much of the background turbulence of the ocean interior but are not dominant drivers of the diabatic abyssal circulation. Other sources of boundary mixing, aided by geothermal heating, are therefore required to close the abyssal overturning. Preliminary results also emphasize that water mass transformation estimates relying on the simple assumptions of the commonly-used tidal mixing parameterization (St. Laurent et al. 2002), such as those presented in chapters I and II, should be taken with caution: they must be regarded as the transformation implied by the assumptions entering the parameterization.

References

Alford, M. H. (2003). Improved global maps and 54-year history of wind-work on ocean inertial motions. *Geophysical Research Letters*, 30(8):1424.

Alford, M. H., MacKinnon, J. A., Zhao, Z., Pinkel, R., Klymak, J., and Peacock, T. (2007). Internal waves across the Pacific. *Geophysical Research Letters*, 34(24):L24601.

Blanke, B. and Delecluse, P. (1993). Variability of the tropical Atlantic Ocean simulated by a general circulation model with two different mixed-layer physics. *Journal of Physical Oceanography*, 23(7):1363–1388.

Brown, E. D. and Owens, W. B. (1981). Observations of the horizontal interactions between the internal wave field and the mesoscale flow. *Journal of Physical Oceanography*, 11(11):1474–1480.

Bühler, O. and Holmes-Cerfon, M. (2011). Decay of an internal tide due to random topography in the ocean. *Journal of Fluid Mechanics*, 678:271–293.

Dunphy, M. and Lamb, K. G. (2014). Focusing and vertical mode scattering of the first mode internal tide by mesoscale eddy interaction. *Journal of Geophysical Research*, 119(1):523–536.

Eden, C. and Olbers, D. (2014). An energy compartment model for propagation, nonlinear interaction, and dissipation of internal gravity waves. *Journal of Physical Oceanography*, 44(8):2093–2106.

Egbert, G. D. and Ray, R. D. (2003). Semi-diurnal and diurnal tidal dissipation from TOPEX/Poseidon altimetry. *Geophysical Research Letters*, 30(17):1907.

Falahat, S., Nycander, J., Roquet, F., and Zarroug, M. (2014). Global calculation of tidal energy conversion into vertical normal modes. *Journal of Physical Oceanography*, 44(12):3225–3244.

Fer, I. (2009). Weak vertical diffusion allows maintenance of cold halocline in the central Arctic. *Atmospheric and Oceanic Science Letters*, 2(3):148–152.

Ferrari, R. (2014). Oceanography: What goes down must come up. *Nature*, 513(7517):179–180.

Ffield, A. and Gordon, A. L. (1992). Vertical mixing in the Indonesian thermocline. *Journal of Physical Oceanography*, 22(2):184–195.

Garrett, C. and Kunze, E. (2007). Internal tide generation in the deep ocean. *Annual Review of Fluid Mechanics*, 39(1):57–87.

Goff, J. A. (2010). Global prediction of abyssal hill root-mean-square heights from small-scale altimetric gravity variability. *Journal of Geophysical Research*, 115(B12):B12104.

Gouretski, V. and Koltermann, K. P. (2004). Woce global hydrographic climatology. Technical Report 35, Berichte des Bundesamtes für Seeschiffahrt und Hydrographie.

Gregg, M. C. (1989). Scaling turbulent dissipation in the thermocline. *Journal of Geophysical Research*, 94(C7):9686–9698.

Gregg, M. C., Sanford, T. B., and Winkel, D. P. (2003). Reduced mixing from the breaking of internal waves in equatorial waters. *Nature*, 422(6931):513–515.

Griffies, S., Danabasoglu, G., Yeager, S., Marsland, S., Drange, H., and Bentsen, M. (2012). Datasets and protocol for the CLIVAR WGOMD coordinated ocean-sea ice reference experiments (COREs). Technical Report 21, World Research Climate Programme.

Hazewinkel, J. and Winters, K. B. (2011). PSI of the internal tide on a beta-plane: Flux divergence and near-inertial wave propagation. *Journal of Physical Oceanography*, 41(9):1673–1682.

Huussen, T. N., Naveira-Garabato, A. C., Bryden, H. L., and McDonagh, E. L. (2012). Is the deep Indian Ocean MOC sustained by breaking internal waves? *Journal of Geophysical Research*, 117(C8):C08024.

Jayne, S. R. (2009). The impact of abyssal mixing parameterizations in an ocean general circulation model. *Journal of Physical Oceanography*, 39(7):1756–1775.

Jochum, M., Briegleb, B. P., Danabasoglu, G., Large, W. G., Norton, N. J., Jayne, S. R., Alford, M. H., and Bryan, F. O. (2013). The impact of oceanic near-inertial waves on climate. *Journal of Climate*, 26(9):2833–2844.

Jouanno, J., Capet, X., Madec, G., Roullet, G., Klein, P., and Masson, S. (2016). Dissipation of the energy imparted by mid-latitude storms in the Southern Ocean. *Ocean Science Discussions*, pages 1–49.

Kelly, S. M., Jones, N. L., Nash, J. D., and Waterhouse, A. F. (2013). The geography of semidiurnal mode-1 internal-tide energy loss. *Geophysical Research Letters*, 40(17):4689–4693.

Kelly, S. M., Nash, J. D., Martini, K. I., Alford, M. H., and Kunze, E. (2012). The cascade of tidal energy from low to high modes on a continental slope. *Journal of Physical Oceanography*, 42(7):1217–1232.

Klymak, J. M., Alford, M. H., Pinkel, R., Lien, R.-C., Yang, Y. J., and Tang, T.-Y. (2011). The breaking and scattering of the internal tide on a continental slope. *Journal of Physical Oceanography*, 41(5):926–945.

Klymak, J. M., Buijsman, M., Legg, S., and Pinkel, R. (2013). Parameterizing surface and internal tide scattering and breaking on supercritical topography: The one- and two-ridge cases. *Journal of Physical Oceanography*, 43(7):1380–1397.

Kunze, E. (2016). Internal-wave-driven turbulence and the meridional overturning circulation. In *2016 Ocean Sciences Meeting*.

Kunze, E., Firing, E., Hummon, J. M., Chereskin, T. K., and Thurnherr, A. M. (2006). Global abyssal mixing inferred from lowered ADCP shear and CTD strain profiles. *Journal of Physical Oceanography*, 36(8).

Kunze, E. and Llewellyn Smith, S. G. (2004). The role of small-scale topography in turbulent mixing of the global ocean. *Oceanography*, 17(1):55–64.

Kunze, E. and Sanford, T. B. (1996). Abyssal mixing: Where it is not. *Journal of Physical Oceanography*, 26(10):2286–2296.

Ledwell, J. R., Watson, A. J., and Law, C. S. (1993). Evidence for slow mixing across the pycnocline from an open-ocean tracer-release experiment. *Nature*, 364(6439):701–703.

Lefauve, A., Muller, C., and Melet, A. (2015). A three-dimensional map of tidal dissipation over abyssal hills. *Journal of Geophysical Research*, 120(7):4760–4777.

Legg, S. (2014). Scattering of low-mode internal waves at finite isolated topography. *Journal of Physical Oceanography*, 44(1):359–383.

Legg, S. and Adcroft, A. (2003). Internal wave breaking at concave and convex continental slopes. *Journal of Physical Oceanography*, 33(11):2224–2246.

MacKinnon, J. A., Alford, M. H., Pinkel, R., Klymak, J., and Zhao, Z. (2013a). The latitudinal dependence of shear and mixing in the Pacific transiting the critical latitude for PSI. *Journal of Physical Oceanography*, 43(1):3–16.

MacKinnon, J. A., Alford, M. H., Sun, O., Pinkel, R., Zhao, Z., and Klymak, J. (2013b). Parametric subharmonic instability of the internal tide at 29n. *Journal of Physical Oceanography*, 43(1):17–28.

Madec, G. (2015). Nemo ocean engine. Technical Report 27, Institut Pierre-Simon Laplace.

Melet, A., Hallberg, R., Legg, S., and Nikurashin, M. (2014). Sensitivity of the ocean state to lee wave–driven mixing. *Journal of Physical Oceanography*, 44(3):900–921.

Melet, A., Legg, S., and Hallberg, R. (2016). Climatic impacts of parameterized local and remote tidal mixing. *Journal of Climate*, 29(10):3473–3500.

Melet, A., Nikurashin, M., Muller, C., Falahat, S., Nycander, J., Timko, P. G., Arbic, B. K., and Goff, J. A. (2013). Internal tide generation by abyssal hills using analytical theory. *Journal of Geophysical Research*, 118(11):6303–6318.

Meyer, A., Sloyan, B. M., Polzin, K. L., Phillips, H. E., and Bindoff, N. L. (2015). Mixing variability in the Southern Ocean. *Journal of Physical Oceanography*, page 150109122722005.

Moum, J. N., Caldwell, D. R., Nash, J. D., and Gunderson, G. D. (2002). Observations of boundary mixing over the continental slope. *Journal of Physical Oceanography*, 32(7):2113–2130.

Muller, C. J. and Bühler, O. (2009). Saturation of the internal tides and induced mixing in the abyssal ocean. *Journal of Physical Oceanography*, 39(9):2077–2096.

Müller, P., Holloway, G., Henyey, F., and Pomphrey, N. (1986). Nonlinear interactions among internal gravity waves. *Reviews of Geophysics*, 24(3):493–536.

Müller, P. and Xu, N. (1992). Scattering of oceanic internal gravity waves off random bottom topography. *Journal of Physical Oceanography*, 22(5):474–488.

Nash, J. D., Kunze, E., Toole, J. M., and Schmitt, R. W. (2004). Internal tide reflection and turbulent mixing on the continental slope. *Journal of Physical Oceanography*, 34(5):1117–1134.

Nikurashin, M. and Ferrari, R. (2013). Overturning circulation driven by breaking internal waves in the deep ocean. *Geophysical Research Letters*, 40(12):3133–3137.

Nikurashin, M., Ferrari, R., Grisouard, N., and Polzin, K. (2014). The impact of finite-amplitude bottom topography on internal wave generation in the Southern Ocean. *Journal of Physical Oceanography*, 44(11):2938–2950.

Nikurashin, M. and Legg, S. (2011). A mechanism for local dissipation of internal tides generated at rough topography. *Journal of Physical Oceanography*, 41(2):378–395.

Niwa, Y. and Hibiya, T. (2011). Estimation of baroclinic tide energy available for deep ocean mixing based on three-dimensional global numerical simulations. *Journal of Oceanography*, 67(4):493–502.

Nugroho, D., Koch-larrouy, A., Tranchant, B., Reffray, G., Gaspar, P., and Madec, G. (2015). Mixing and energy produced by explicit internal tides in the Indonesian seas using a realistic OGCM. In *EGU General Assembly Conference Abstracts*, volume 17, page 11191.

Nycander, J. (2005). Generation of internal waves in the deep ocean by tides. *Journal of Geophysical Research*, 110(C10).

Oka, A. and Niwa, Y. (2013). Pacific deep circulation and ventilation controlled by tidal mixing away from the sea bottom. *Nature Communications*, 4.

Olbers, D. and Eden, C. (2013). A global model for the diapycnal diffusivity induced by internal gravity waves. *Journal of Physical Oceanography*, 43(8):1759–1779.

Olbers, D. J. (1983). Models of the oceanic internal wave field. *Reviews of Geophysics*, 21(7):1567–1606.

Pinkel, R., Alford, M., Lucas, A. J., Johnston, S., MacKinnon, J., Waterhouse, A., Jones, N., Kelly, S., Klymak, J., Nash, J., Rainville, L., Zhao, Z., Simmons, H., and Strutton, P. (2016). Breaking internal tides keep the ocean in balance. *Eos*, 96.

Polzin, K. L. (2008). Mesoscale eddy–internal wave coupling. Part I: Symmetry, wave capture, and results from the Mid-Ocean Dynamics Experiment. *Journal of Physical Oceanography*, 38(11):2556–2574.

Polzin, K. L. (2009). An abyssal recipe. *Ocean Modelling*, 30(4):298–309.

Polzin, K. L. (2010). Mesoscale eddy–internal wave coupling. Part II: Energetics and results from PolyMode. *Journal of Physical Oceanography*, 40(4):789–801.

Polzin, K. L., Toole, J. M., Ledwell, J. R., and Schmitt, R. W. (1997). Spatial variability of turbulent mixing in the abyssal ocean. *Science*, 276(5309):93–96.

Polzin, K. L., Toole, J. M., and Schmitt, R. W. (1995). Finescale parameterizations of turbulent dissipation. *Journal of Physical Oceanography*, 25(3):306–328.

Rainville, L. and Winsor, P. (2008). Mixing across the Arctic Ocean: Microstructure observations during the Beringia 2005 expedition. *Geophysical Research Letters*, 35(8):L08606.

Ray, R. D. and Mitchum, G. T. (1996). Surface manifestation of internal tides generated near Hawaii. *Geophysical Research Letters*, 23(16):2101–2104.

Simmons, H. L., Hallberg, R. W., and Arbic, B. K. (2004a). Internal wave generation in a global baroclinic tide model. *Deep Sea Research*, 51(25-26):3043–3068.

Simmons, H. L., Jayne, S. R., Laurent, L. C., and Weaver, A. J. (2004b). Tidally driven mixing in a numerical model of the ocean general circulation. *Ocean Modelling*, 6(3-4):245–263.

Smith, W. H. F. and Sandwell, D. T. (1997). Global sea floor topography from satellite altimetry and ship depth soundings. *Science*, 277(5334):1956–1962.

St. Laurent, L. and Garrett, C. (2002). The role of internal tides in mixing the deep ocean. *Journal of Physical Oceanography*, 32(10):2882–2899.

St. Laurent, L. C., Simmons, H. L., and Jayne, S. R. (2002). Estimating tidally driven mixing in the deep ocean. *Geophysical Research Letters*, 29(23).

St. Laurent, L. C., Toole, J. M., and Schmitt, R. W. (2001). Buoyancy forcing by turbulence above rough topography in the abyssal Brazil Basin. *Journal of Physical Oceanography*, 31(12):3476–3495.

Waterhouse, A. F., MacKinnon, J. A., Nash, J. D., Alford, M. H., Kunze, E., Simmons, H. L., Polzin, K. L., St. Laurent, L. C., Sun, O. M., Pinkel, R., Talley, L. D., Whalen, C. B., Huussen, T. N., Carter, G. S., Fer, I., Waterman, S., Naveira Garabato, A. C., Sanford, T. B., and Lee, C. M. (2014). Global patterns of diapycnal mixing from measurements of the turbulent dissipation rate. *Journal of Physical Oceanography*, 44(7):1854–1872.

Watson, A. J., Ledwell, J. R., Messias, M.-J., King, B. A., Mackay, N., Meredith, M. P., Mills, B., and Naveira Garabato, A. C. (2013). Rapid cross-density ocean mixing at mid-depths in the Drake Passage measured by tracer release. *Nature*, 501(7467):408–411.

Whalen, C. B., Talley, L. D., and MacKinnon, J. A. (2012). Spatial and temporal variability of global ocean mixing inferred from Argo profiles. *Geophysical Research Letters*, 39(18):n/a–n/a.

Wu, L., Jing, Z., Riser, S., and Visbeck, M. (2011). Seasonal and spatial variations of Southern Ocean diapycnal mixing from Argo profiling floats. *Nature Geoscience*, 4(6):363–366.

Wunsch, C. and Ferrari, R. (2004). Vertical mixing, energy, and the general circulation of the oceans. *Annual Review of Fluid Mechanics*, 36(1):281–314.

Young, W. R., Tsang, Y.-K., and Balmforth, N. J. (2008). Near-inertial parametric subharmonic instability. *Journal of Fluid Mechanics*, 607.

Zhao, Z. and Alford, M. H. (2009). New altimetric estimates of mode-1 M2 internal tides in the central North Pacific ocean. *Journal of Physical Oceanography*, 39(7):1669–1684.

Zhao, Z., Alford, M. H., Girton, J. B., Rainville, L., and Simmons, H. L. (2016). Global observations of open-ocean mode-1 M2 internal tides. *Journal of Physical Oceanography*.

Conclusions and perspectives

1 Conclusions

Using a global hydrographic climatology, estimates of mixing-driven and geothermal buoyancy fluxes, and simple but powerful diagnostics based on the density balance of deep waters, we explored the roles of geothermal heating and mixing by breaking internal waves for the abyssal circulation. Because they rely on imperfect maps of internal wave generation rates and geothermal heat fluxes as well as simplifying assumptions about the three-dimensional distribution of internal wave energy dissipation, the estimated rates of abyssal upwelling carry large uncertainties. Nevertheless, several robust results and new insights emerged from the calculations.

1.1 Drivers of Antarctic Bottom Water consumption

Geothermal heating is a significant player of the abyssal overturning, accounting for about 5 Sv of upwelling across the density layer with the largest seafloor coverage. The role of geothermal heating has often been dismissed on the basis that the $\mathcal{O}(0.1\,\mathrm{W\,m^{-2}})$ bottom heat fluxes are negligible compared to the $\mathcal{O}(100\,\mathrm{W\,m^{-2}})$ air-sea fluxes, or that the ~ 0.05 TW geothermal potential energy source is small compared to the ~ 2 TW mechanical energy input by winds and tides (Munk and Wunsch 1998; Wunsch and Ferrari 2004). But the first argument overlooks the fact that bottom density gradients tend to be much smaller than surface

density gradients, so that a given buoyancy gain causes stronger cross-density flow along the bottom boundary relative to the surface boundary. In other words, because maximum incrop areas are orders of magnitude larger than maximum outcrop areas (chapter I, Fig. 4), relatively small (but always of the same sign) bottom boundary fluxes are able to drive significant abyssal upwelling rates. The second, energy comparison argument muddles up different quantities and regions: of the ~ 2 TW of wind and tidal energy input, only a fraction (dependent on the mixing efficiency and the non-linearity of the equation of state) is converted into potential energy via mixing, and an even smaller fraction raises the potential energy of the abyss. The net abyssal potential energy supply by tidal and wind-powered mixing may therefore be comparable to the geothermal supply (chapters I and II).

In fact, the role of geothermal heating appears to be very complementary to that of abyssal mixing: geothermal buoyancy fluxes contribute mostly to the upwelling of unstratified waters that drape relatively smooth abyssal plains, where sources of mixing energy are scarce and the efficiency of mixing is small. Conversely, abyssal mixing tends to reduce the stratification of Antarctic Bottom Water (AABW) as it flows northward, contributing to the weak bottom density gradients or large incrop areas that accentuate the strength of the geothermal circulation.

Breaking internal tides are unlikely to be a leading contributor to AABW upwelling. When accounting for reduced mixing efficiencies in high diffusivity regions, abyssal upwelling rates induced by local, bottom-enhanced internal tide breaking do not exceed a few Sv (chapter II). The more distributed remote tidal dissipation could be a stronger driver of AABW upwelling if sufficiently spread across the water column (chapters I and II), but observational and theoretical evidence indicates that most of the remote dissipation actually takes place in the strongly-stratified upper ocean (chapter V). As a result, tidally-forced turbulence may contribute no more than ~ 3 Sv (~ 7 Sv) of diabatic upwelling within the bottom (deep) water density range (chapter V).

A preliminary estimate of the full three-dimensional distribution of internal tide dissipation (chapter V) suggests that over 90 % of the dissipation takes place at depths shallower than 3,000 m, leaving only ~ 0.1 TW to drive diabatic upwelling in the underlying abyss. Using a mixing efficiency of one-sixth yields an (upper-bound) potential energy supply of ~ 0.02 TW

under 3,000 m, less than the geothermal input. Munk and Wunsch (1998) suggested that ~ 1 TW of barotropic-to-baroclinic tidal conversion contributes to diabatic upwelling of dense waters across the 4,000-1,000 m depth range. We find that the majority of this energy source actually contributes to mixing above 1,000 m, and that only a minor fraction contributes to mixing below 3,000 m depth, where the bulk of diabatic upwelling is presumed to occur (chapter III; Marshall and Speer 2012).

Breaking lee waves homogenize AABW in the Antarctic Circumpolar Current, but are unlikely to drive substantial AABW upwelling further north. In contrast to internal tides, estimates of lee wave radiation (Scott et al. 2011; Nikurashin et al. 2014) indicate that over 80 % of the energy source is placed at depths greater than 3,000 m. But most of the lee wave generation is located in the Antarctic Circumpolar Current (ACC), where deep-reaching geostrophic flows lose energy to lee waves at an estimated circumpolar rate of 0.08 TW (Nikurashin et al. 2014). The fraction of lee waves dissipating near the bottom of the ACC may contribute significant homogenization of abyssal waters, and could slightly augment the northward volume transport of AABW (chapters I, II and V). Nonetheless, because of the strong abyssal stratification of the Southern Ocean and the weak lee wave radiation in northern basins, basin-scale dianeutral transports induced by lee wave-driven mixing do not surpass a few Sv. Besides, the vertical structure of lee wave breaking, the pathways through which their energy is dissipated (Waterman et al. 2013, 2014), and the overall magnitude of their generation (Nikurashin et al. 2014; Wright et al. 2014), are still poorly constrained. As a result, whether breaking lee waves contribute net formation or consumption of AABW across the ACC, and whether or not they significantly alter the global abyssal stratification, remain open questions.

A dominant role for overflow-related boundary processes? According to present water mass transformation estimates, geothermal heating, breaking internal tides and breaking lee waves do not balance more than ~ 10 Sv of northward AABW flow out of the Southern Ocean. Inverse models suggest that the strength of the northward abyssal limb of the overturning most likely lies within the 20-30 Sv range (Ganachaud and Wunsch 2000; Lumpkin and Speer 2007; Talley 2013; Naveira Garabato et al. 2014). How to explain the

discrepancy? Inverse solutions of ocean transports are known to carry large uncertainties (e.g., Naveira Garabato et al. 2014), and might overestimate the strength of the AABW circulation. Yet direct observations of transports in circulation chokepoints (e.g., Mercier and Speer 1998; McDonagh et al. 2002; MacKinnon et al. 2008; Voet et al. 2015), independent inversions of multiple-tracer observations (e.g., Schmitz 1996; Ganachaud and Wunsch 2000; Talley et al. 2003; Lumpkin and Speer 2007; McDonagh et al. 2008; Talley 2013) and assimilation experiments (e.g., Ferron and Marotzke 2003) seem to converge towards values of $\sim$10 Sv for each of the Pacific and Indian basins and $\sim$ 5 Sv for the Atlantic basin.

On the other hand, it is possible that limitations of our methodology and/or inaccuracies in the constructed climatologies of buoyancy fluxes bias low the transformation estimates. Nonetheless, prescription of similar buoyancy fluxes in global ocean models shows a comparably modest response to parameterized internal wave-driven mixing and geothermal heating (chapters I and V). In addition, bulk diffusivities implied by these buoyancy fluxes systematically fall short of their equivalent obtained from inverse solutions, irrespective of parameterization choices (chapter II; Decloedt and Luther 2012). This is particularly true for the Indian Ocean, where the mismatch between parameterized or observed levels of internal wave activity and overturning transports most clearly points to an additional, near-bottom source of density transformation (Huussen et al. 2012). In general, the recurring discrepancy between measured levels of dissipation in the interior and larger-scale tracer-release or budget inferences of mixing levels calls for additional bottom boundary mixing (Huussen et al. 2012; Watson et al. 2013; Polzin et al. 2014).

Mixing in narrow passages connecting sub-basins is one major candidate for such boundary transformation (chapters II and III; Bryden and Nurser 2003). Density jumps across sub-basins clearly demonstrate the significance of transformation at deep straits and sills. A leading role of mixing within inter-basin passages and cascading plumes for AABW lightening would imply that surface buoyancy forcing – coupled to wind forcing – actively contributes to power the abyssal overturning (chapter II; Hughes et al. 2009; Saenz et al. 2012). Together with the significant geothermal potential energy supply, this suggests that thermodynamic forcing has a non-negligible part in the energy flows that maintain the overturning, alongside the important part played by winds and tides.

1.2 Local pathways and global structure of abyssal upwelling

The influential *Abyssal Recipes* (Munk 1966; Munk and Wunsch 1998) have led to the widespread view that mixing always drives upwelling of deep waters. Indeed, the assumption of a uniform diffusivity (Munk 1966), the need for sinking dense waters to rise back to the surface (Munk and Wunsch 1998), and the intuitive understanding that diffusion transfers buoyancy from the light upper-ocean down to the dense abyss (Stommel 1958), all point to a net buoyancy gain of deep waters. Yet mixing cannot be only a source of buoyancy: rather, it is a transfer of buoyancy. If buoyancy is supplied to deep waters, where is it extracted? What determines the distribution of sources and sinks of buoyancy is the vertical profile of the mixing-driven buoyancy flux, and the associated depth ranges of divergence (buoyancy loss) and convergence (buoyancy gain). In the *Abyssal Recipes*, the downward buoyancy flux decreases with depth, so that deep buoyancy gain is implicitly balanced by buoyancy loss in the upper ocean. Yet – as recognized by Munk and Wunsch (1998) – abyssal turbulence and mixing tend to be intensified along the bottom boundary. Such deep boundary mixing cannot transfer buoyancy from the upper-ocean to the abyss: rather, it lightens the bottom-most waters and densifies waters immediately above. This corresponds to a buoyancy flux that increases toward the bottom, but declines within the lightened bottom layer to match the no-flux bottom boundary condition (Fig. 1a). This simple realization has a number of consequences.

1. Lightening, and therefore upwelling, of abyssal waters is focused along the bottom boundary. Boundary mixing lightens bottom-most waters. To maintain a stable density distribution, this buoyancy gain is balanced by lateral inflow of denser waters along the bottom, and the buoyancy loss above by diabatic sinking (Fig. 1a,b). Geothermal heating reinforces this behaviour by supplying additional buoyancy to the bottom ocean. In fact, even in the case of a depth-decreasing buoyancy flux, the bottom boundary condition on the buoyancy flux implies that waters lying along the bottom are likely to receive more buoyancy than the adjacent, interior waters (Fig. 1c,d). The pattern of interior downwelling and boundary upwelling had been documented from Brazil Basin observations (Ledwell et al. 2000; St. Laurent et al. 2001) and idealized numerical simulations (Marotzke 1997), but gone

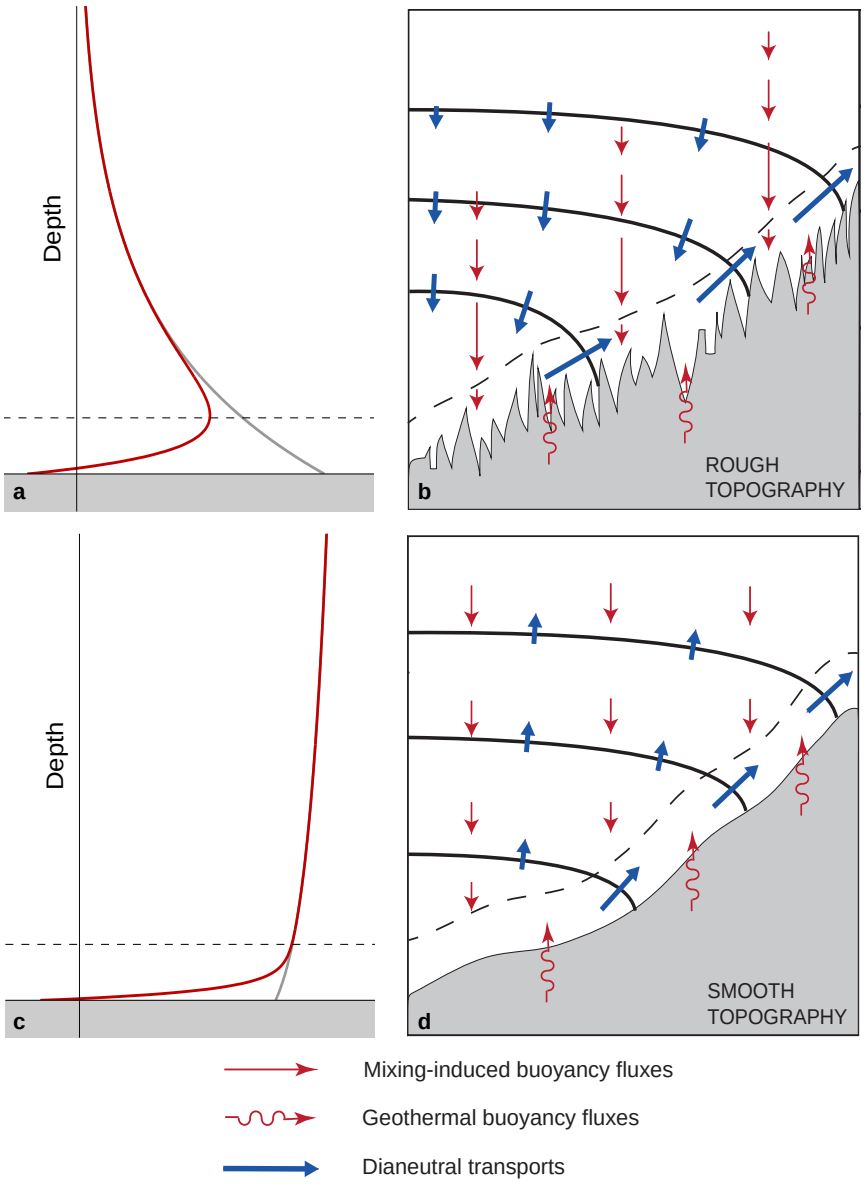

Figure 1: Schematic buoyancy fluxes and dianeutral transports under (**a**,**b**) depth-increasing or (**c**,**d**) depth-decreasing dissipation. (**a**,**c**) Profiles of (red) downward buoyancy fluxes roughly follow those of (grey) turbulent kinetic energy production above the (dashed line) unstratified bottom boundary layer where the buoyancy flux decreases to zero and changes sign to match the upward geothermal buoyancy flux. (**b**,**d**) Convergence of (red arrows) buoyancy fluxes is strongest near the bottom, where buoyancy gain is balanced by (blue arrows) upward advection along topography. If turbulence is bottom-enhanced (**b**), as often observed above rough topography, buoyancy loss and downwelling occur above the bottom layer. In the opposite case (**d**), typical of smooth abyssal floor, buoyancy gain and upwelling occur throughout the deep water column (with compensating buoyancy loss found only higher up).

largely unnoticed. Our work shows that the near-bottom concentration of diabatic upwelling is a global pattern (chapter I). Further recognition that AABW lightening through gravitational

sinking and entrainment, near its formation sites or downstream in abyssal overflows, occurs mostly along the bottom entails that the diabatic circulation of AABW is largely confined to an $\mathcal{O}(500\,\mathrm{m})$ thick bottom layer (chapter IV).

2. Variations of the mixing efficiency are a major uncertainty for rates of abyssal upwelling. Given bottom-enhanced turbulence production, the magnitude of the bottom buoyancy gain and the thickness over which it is spread are set by the efficiency of mixing. Theoretical arguments and experimental evidence indicate that the efficiency should decrease for high values of the ratio between viscous dissipation and stratification (chapter II; Shih et al. 2005; Bouffard and Boegman 2013). Nonetheless, the dependency of mixing efficiency on scale and other flow parameters is poorly known. As a result, patterns and strengths of diabatic downwelling and upwelling flows forced by boundary mixing remain very uncertain. More generally, the effectiveness of density transformation by boundary turbulence depends on the rate of exchange between interior and turbulent waters (Armi 1978; Kunze et al. 2012; Winters 2015). In essence, the efficiency of boundary mixing should increase with the ratio of the timescale of re-stratification by advection to that of gradient suppression by small-scale turbulence. For instance, mixing-driven buoyancy fluxes in quiescent waters over abyssal plains would be expected to saturate at a weaker level than in swift constricted flows or actively-stirred eddying regions, with important – but as yet unquantified – implications for how and where AABW is consumed. Mixing efficiency variations are also a major uncertainty for evaluations of the energy requirement of the overturning, because they imply that buoyancy fluxes depend on detailed flow properties and turbulence space-time distributions.

3. The reduction of basin areas with depth is key to abyssal upwelling. For a given ocean layer to undergo net diabatic upwelling, it must be traversed by a convergent buoyancy flux. If turbulence is bottom-intensified, local buoyancy fluxes are divergent in the ocean interior (away from a thin bottom layer). Therefore, the ocean layer will receive buoyancy only if the depth-reduction in basin area across the layer is able to overwhelm the depth-increase of local buoyancy fluxes, yielding a convergent *total* buoyancy flux. Equivalently, net diabatic upwelling is achieved if buoyancy gain at the layer incrops

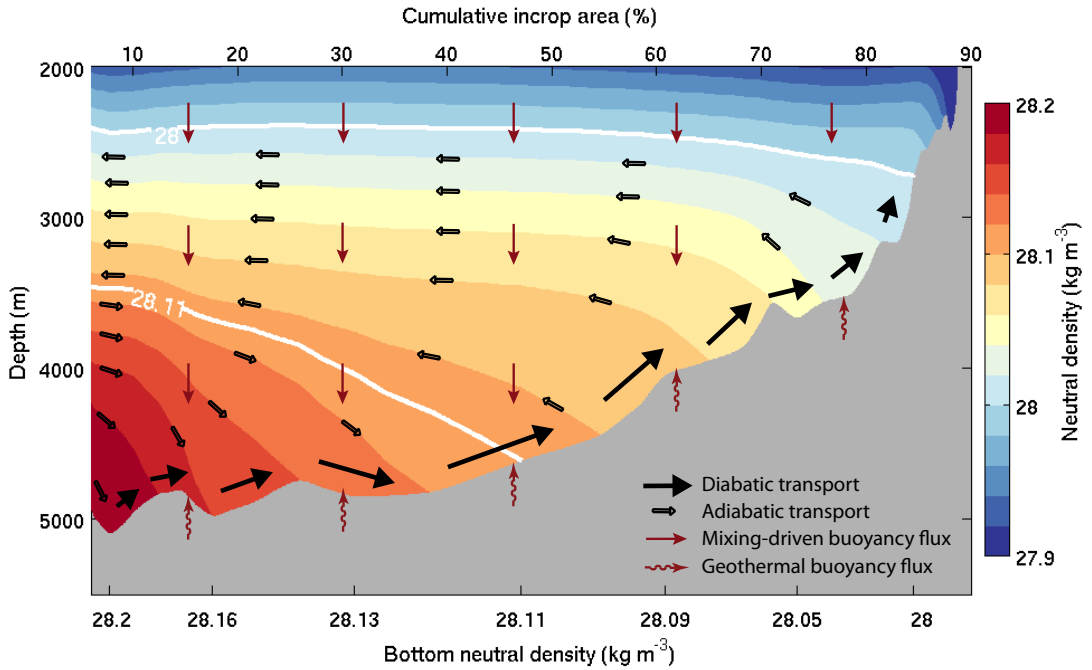

Figure 2: Idealized schematic of the abyssal overturning circulation north of 40°S. The average depth of density surfaces is shown as function of (lower axis) bottom neutral density and (upper axis) cumulative incrop area going from dense to light bottom density. The surface of maximum incrop area ($\gamma = 28.11\,\mathrm{kg\,m^{-3}}$), corresponding to meridional flow reversal, and the surface marking the approximate transition between diabatic and adiabatic flow regimes ($\gamma = 28\,\mathrm{kg\,m^{-3}}$), are contoured in white. Density loss and diabatic upwelling are confined to near-bottom waters, which climb across density surfaces and along ridge flanks at a rate roughly commensurate with the incrop area. Through mass conservation, this cross-density, along-bottom circulation maintains an along-density, interior circulation which supplies (returns) dense waters from (to) the Antarctic Circumpolar Current. See chapter III for details.

outweighs buoyancy loss in its interior. Given that abyssal mixing is thought to be dominated by bottom-enhanced turbulence, AABW upwelling is therefore reliant on the reduction of basins areas with depth, combined to the no-density-flux bottom boundary condition. But though net upwelling of AABW is required at the global scale, diabatic sinking of abyssal layers may occur on local to regional scales. For instance, boundary mixing in the ACC could drive net densification and downwelling of Lower Circumpolar Deep Water and light AABW, thus contributing additional AABW formation in the deep ocean (chapter I).

4. The reduction rate of basin areas with depth shapes the abyssal overturning. The vertical structure of basin-scale diabatic upwelling is strongly influenced by the two following effects: (i) the larger the seafloor coverage of an ocean layer, the larger its exposure

to near-bottom buoyancy deposition by boundary mixing and geothermal heating; (ii) the weaker its stratification, the larger the upwelling rate required to balance a given buoyancy gain. Because both stratification and topographic steepness tend to decrease with depth in the deep ocean, diabatic upwelling rates are expected to be strongest in the abyss, below $\sim$3,000 m depth, and weaker toward shallower depths. More precisely, we find that the upwelling rate peaks within the 4,000-5,500 m depth range, where basin areas shrink most rapidly and force a proportionate convergence of basin-scale buoyancy fluxes; and dwindles higher up to reach a small fraction of the peak value near 2,500 m depth, where topography becomes dominated by steep continental slopes (chapter III). Hence, both the peak level and vertical extent of diabatic upwelling appear constrained by basin geometry. Noting that the peak and upper levels of diabatic upwelling respectively coincide with northward/southward and adiabatic/diabatic regime transitions of the overturning, the shape of the three main ocean basins emerges as a key ingredient of the overturning's functioning (Fig. 2).

2. Perspectives

Limitations of, and questions raised by, the present PhD work offer several avenues for future work. First, I intend to complete the validation of the internal wave-driven mixing parameterization presented in chapter V. I must explore the sensitivity of constructed two-dimensional maps of internal tide dissipation to poorly constrained parameters entering modelled sink terms, and to the propagation scheme and angle distribution of energy sources. I will next extend the comparison of parameterized vertical structures of dissipation with microstructure measurements, using the global data compilation of Waterhouse et al. (2014). Finally, numerical experiments using the one-degree configuration of the NEMO ocean model, possibly coupled to an atmosphere model, will be carried to document the impact of the parameterization on the simulated property distributions and transports. In particular, the simulated response of the deep ocean circulation will be compared to water mass transformation estimates based on an observational climatology.

Inclusion of this mixing parameterization in NEMO is part of a broader strategy aiming to ensure energetic consistency of the model and to understand and improve modelled energy pathways (Eden et al. 2014). In this context, several improvements of the model mixing parameterizations are considered. First, other energy sources for mixing should be incorporated, such as the contribution of wind-generated near-inertial waves, whose power input should depend on the time-varying atmospheric forcing (Jochum et al. 2013). Second, I plan to explore the use of a second-order turbulent closure in the specification of internal wave-induced diffusivities, via unification of the currently distinct closures employed in near-surface and interior mixing modules. Third, the energy input to lee waves should be explicitly treated as a sink of modelled (resolved and parameterized) kinetic energy (Marshall and Naveira Garabato 2008). More generally, routes by which the energy of mesoscale and large-scale flows may cascade into small-scale turbulence should be quantified and parameterized – whether or not they involve the internal wave field.

Indeed, internal waves are not the only source of interior mixing, and perhaps not the main source of abyssal mixing. In particular, strait and sill mixing stands out as a major alternate source of water mass transformation that presently lacks quantification and faithful representation in ocean models. Bulk estimates of density fluxes within important straits may be obtained from observational information about the cross-basin transport and density difference (Bryden and Nurser 2003; Voet et al. 2015). However, detailed vertical profiles of inflow and upstream and downstream density would be needed to obtain a direct estimate of water mass transformation rates. Alternatively, estimates of dianeutral transports within individual sub-basins could be used to infer the missing transformation occurring within inter-basin passages. If reliable, estimates of transformation in passages may then provide guidance for improving its representation in ocean climate models, and could help to resolve the long-standing discrepancy between simulations and observational inferences of Indian Ocean overturning transports (Ferron and Marotzke 2003).

While mixing in major inter-basin passages should help to bridge the apparent shortfall of boundary transformation, it is likely that other near-bottom processes – distinct from the radiation and subsequent shear instability of internal waves – contribute significantly to the modification of AABW within sub-basins (chapter III). Such processes could involve canyons cutting across shelf and ridge slopes together with overflows (Thurnherr et al. 2005; Thurnherr

2006; St Laurent and Thurnherr 2007) and/or tidal (Arneborg and Liljebladh 2009) or wind (Hickey 1997) forcing. The magnitude of geothermal forcing and the dynamics associated with exchanges between the solid (but porous) seafloor and seawater also require attention (e.g., Lupton et al. 1985; Hofmann and Morales Maqueda 2009). But understanding and quantification of the large-scale impact of those processes would greatly benefit from better knowledge of the characteristics of the bottom boundary layer and their relation to topography scales and roughness across the global abyss (chapter IV). Detailed analysis of available ship-based hydrographic data could be a first step in this direction (e.g., Lozovatsky et al. 2008).

I also have a growing curiosity for the implications of boundary-dominated transformation for the overturning's functioning and its involvement in climate transitions, such as those associated with glacial-interglacial cycles. The role of past and present changes in the formation of AABW (Appendix) for long-term shifts in water mass configurations and climate represents a complementary and equally engaging research road.

References

Armi, L. (1978). Some evidence for boundary mixing in the deep ocean. *Journal of Geophysical Research*, 83(C4):1971–1979.

Arneborg, L. and Liljebladh, B. (2009). Overturning and dissipation caused by baroclinic tidal flow near the sill of a fjord basin. *Journal of Physical Oceanography*, 39(9):2156–2174.

Bouffard, D. and Boegman, L. (2013). A diapycnal diffusivity model for stratified environmental flows. *Dynamics of Atmospheres and Oceans*, 61-62:14–34.

Bryden, H. L. and Nurser, A. J. G. (2003). Effects of strait mixing on ocean stratification. *Journal of Physical Oceanography*, 33(8):1870–1872.

Decloedt, T. and Luther, D. S. (2012). Spatially heterogeneous diapycnal mixing in the abyssal ocean: A comparison of two parameterizations to observations. *Journal of Geophysical Research*, 117(C11):C11025.

Eden, C., Czeschel, L., and Olbers, D. (2014). Toward energetically consistent ocean models. *Journal of Physical Oceanography*, 44(12):3160–3184.

Ferron, B. and Marotzke, J. (2003). Impact of 4d-variational assimilation of WOCE hydrography on the meridional circulation of the Indian Ocean. *Deep Sea Research*, 50(12–13):2005–2021.

Ganachaud, A. and Wunsch, C. (2000). Improved estimates of global ocean circulation, heat transport and mixing from hydrographic data. *Nature*, 408(6811):453–457.

Hickey, B. M. (1997). The response of a steep-sided, narrow canyon to time-variable wind forcing. *Journal of Physical Oceanography*, 27(5):697–726.

Hofmann, M. and Morales Maqueda, M. A. (2009). Geothermal heat flux and its influence on the oceanic abyssal circulation and radiocarbon distribution. *Geophysical Research Letters*, 36(3):L03603.

Hughes, G. O., Hogg, A. M. C., and Griffiths, R. W. (2009). Available potential energy and irreversible mixing in the meridional overturning circulation. *Journal of Physical Oceanography*, 39(12):3130–3146.

Huussen, T. N., Naveira-Garabato, A. C., Bryden, H. L., and McDonagh, E. L. (2012). Is the deep Indian Ocean MOC sustained by breaking internal waves? *Journal of Geophysical Research*, 117(C8):C08024.

Jochum, M., Briegleb, B. P., Danabasoglu, G., Large, W. G., Norton, N. J., Jayne, S. R., Alford, M. H., and Bryan, F. O. (2013). The impact of oceanic near-inertial waves on climate. *Journal of Climate*, 26(9):2833–2844.

Kunze, E., MacKay, C., McPhee-Shaw, E. E., Morrice, K., Girton, J. B., and Terker, S. R. (2012). Turbulent mixing and exchange with interior waters on sloping boundaries. *Journal of Physical Oceanography*, 42(6):910–927.

Ledwell, J. R., Montgomery, E. T., Polzin, K. L., Laurent, L. C. S., Schmitt, R. W., and Toole, J. M. (2000). Evidence for enhanced mixing over rough topography in the abyssal ocean. *Nature*, 403(6766):179–182.

Lozovatsky, I., Fernando, H., and Shapovalov, S. (2008). Deep-ocean mixing on the basin scale: Inference from North Atlantic transects. *Deep Sea Research*, 55(9):1075–1089.

Lumpkin, R. and Speer, K. (2007). Global ocean meridional overturning. *Journal of Physical Oceanography*, 37(10):2550–2562.

Lupton, J. E., Delaney, J. R., Johnson, H. P., and Tivey, M. K. (1985). Entrainment and vertical transport of deep-ocean water by buoyant hydrothermal plumes. *Nature*, 316(6029):621–623.

MacKinnon, J. A., Johnston, T. M. S., and Pinkel, R. (2008). Strong transport and mixing of deep water through the Southwest Indian Ridge. *Nature Geoscience*, 1(11):755–758.

Marotzke, J. (1997). Boundary mixing and the dynamics of three-dimensional thermohaline circulations. *Journal of Physical Oceanography*, 27(8):1713–1728.

Marshall, D. P. and Naveira Garabato, A. C. (2008). A conjecture on the role of bottom-enhanced diapycnal mixing in the parameterization of geostrophic eddies. *Journal of Physical Oceanography*, 38(7):1607–1613.

Marshall, J. and Speer, K. (2012). Closure of the meridional overturning circulation through Southern Ocean upwelling. *Nature Geoscience*, 5(3):171–180.

McDonagh, E. L., Arhan, M., and Heywood, K. J. (2002). On the circulation of bottom water in the region of the Vema Channel. *Deep Sea Research*, 49(7):1119–1139.

McDonagh, E. L., Bryden, H. L., King, B. A., and Sanders, R. J. (2008). The circulation of the Indian Ocean at 32s. *Progress in Oceanography*, 79(1):20–36.

Mercier, H. and Speer, K. G. (1998). Transport of bottom water in the Romanche fracture zone and the Chain fracture zone. *Journal of Physical Oceanography*, 28(5):779–790.

Munk, W. and Wunsch, C. (1998). Abyssal recipes II: Energetics of tidal and wind mixing. *Deep-Sea Research*, 45(12):1977–2010.

Munk, W. H. (1966). Abyssal recipes. *Deep Sea Research*, 13(4):707–730.

Naveira Garabato, A. C., Williams, A. P., and Bacon, S. (2014). The three-dimensional overturning circulation of the Southern Ocean during the WOCE era. *Progress in Oceanography*, 120:41–78.

Nikurashin, M., Ferrari, R., Grisouard, N., and Polzin, K. (2014). The impact of finite-amplitude bottom topography on internal wave generation in the Southern Ocean. *Journal of Physical Oceanography*, 44(11):2938–2950.

Polzin, K. L., Garabato, A. C. N., Abrahamsen, E. P., Jullion, L., and Meredith, M. P. (2014). Boundary mixing in Orkney Passage outflow. *Journal of Geophysical Research*, 119:C010099.

Saenz, J. A., Hogg, A. M., Hughes, G. O., and Griffiths, R. W. (2012). Mechanical power input from buoyancy and wind to the circulation in an ocean model. *Geophysical Research Letters*, 39(13):L13605.

Schmitz, W. J. (1996). On the world ocean circulation. Volume II, the Pacific and Indian Oceans/a global update. Technical Report WHOI-96-08, Woods Hole Oceanographic Institution.

Scott, R. B., Goff, J. A., Naveira Garabato, A. C., and Nurser, A. J. G. (2011). Global rate and spectral characteristics of internal gravity wave generation by geostrophic flow over topography. *Journal of Geophysical Research*, 116(C9).

Shih, L. H., Koseff, J. R., Ivey, G. N., and Ferziger, J. H. (2005). Parameterization of turbulent fluxes and scales using homogeneous sheared stably stratified turbulence simulations. *Journal of Fluid Mechanics*, 525:193–214.

St Laurent, L. C. and Thurnherr, A. M. (2007). Intense mixing of lower thermocline water on the crest of the Mid-Atlantic Ridge. *Nature*, 448(7154):680–683.

St. Laurent, L. C., Toole, J. M., and Schmitt, R. W. (2001). Buoyancy forcing by turbulence above rough topography in the abyssal Brazil Basin. *Journal of Physical Oceanography*, 31(12):3476–3495.

Stommel, H. (1958). The abyssal circulation. *Deep Sea Research*, 5(1):80–82.

Talley, L. (2013). Closure of the global overturning circulation through the Indian, Pacific, and Southern Oceans: Schematics and transports. *Oceanography*, 26(1):80–97.

Talley, L. D., Reid, J. L., and Robbins, P. E. (2003). Data-based meridional overturning streamfunctions for the global ocean. *Journal of Climate*, 16(19):3213–3226.

Thurnherr, A. M. (2006). Diapycnal mixing associated with an overflow in a deep submarine canyon. *Deep Sea Research*, 53(1–2):194–206.

Thurnherr, A. M., St. Laurent, L. C., Speer, K. G., Toole, J. M., and Ledwell, J. R. (2005). Mixing associated with sills in a canyon on the midocean ridge flank. *Journal of Physical Oceanography*, 35(8):1370–1381.

Voet, G., Girton, J. B., Alford, M. H., Carter, G. S., Klymak, J. M., and Mickett, J. B. (2015). Pathways, volume transport, and mixing of abyssal water in the Samoan Passage. *Journal of Physical Oceanography*, 45(2):562–588.

Waterhouse, A. F., MacKinnon, J. A., Nash, J. D., Alford, M. H., Kunze, E., Simmons, H. L., Polzin, K. L., St. Laurent, L. C., Sun, O. M., Pinkel, R., Talley, L. D., Whalen, C. B., Huussen, T. N., Carter, G. S., Fer, I., Waterman, S., Naveira Garabato, A. C., Sanford, T. B., and Lee, C. M. (2014). Global patterns of diapycnal mixing from measurements of the turbulent dissipation rate. *Journal of Physical Oceanography*, 44(7):1854–1872.

Waterman, S., Naveira Garabato, A. C., and Polzin, K. L. (2013). Internal waves and turbulence in the Antarctic Circumpolar Current. *Journal of Physical Oceanography*, 43(2):259–282.

Waterman, S., Polzin, K. L., Naveira Garabato, A. C., Sheen, K. L., and Forryan, A. (2014). Suppression of internal wave breaking in the Antarctic Circumpolar Current near topography. *Journal of Physical Oceanography*, 44(5):1466–1492.

Watson, A. J., Ledwell, J. R., Messias, M.-J., King, B. A., Mackay, N., Meredith, M. P., Mills, B., and Naveira Garabato, A. C. (2013). Rapid cross-density ocean mixing at mid-depths in the Drake Passage measured by tracer release. *Nature*, 501(7467):408–411.

Winters, K. B. (2015). Tidally driven mixing and dissipation in the stratified boundary layer above steep submarine topography. *Geophysical Research Letters*, 42(17):7123–7130.

Wright, C. J., Scott, R. B., Ailliot, P., and Furnival, D. (2014). Lee wave generation rates in the deep ocean. *Geophysical Research Letters*, 41(7):2434–2440.

Wunsch, C. and Ferrari, R. (2004). Vertical mixing, energy, and the general circulation of the oceans. *Annual Review of Fluid Mechanics*, 36(1):281–314.

Appendix

Processes responsible for the consumption of Antarctic Bottom Water (AABW) affect the storage capacity and ventilation rate of the abyssal ocean. But ventilation of and storage by the abyss also hinge upon the surface-forced production and subsequent export of AABW. Two main types of AABW production have been observed (Fig. 1) (Killworth 1983): (i) formation within latent heat polynyas of continental margins where sustained sea ice formation and export cause a strong salt-enrichment of shelf waters, which subsequently sink and mix with surrounding waters in downslope currents; (ii) formation through deep winter convection in offshore, sensible heat polynyas, where surface heat loss drives sinking in convective plumes and upwelling of warmer deep waters, gradually mixing and cooling the whole water column. The first process is currently active in four primary coastal sites: the western Weddell Sea, the Ross Sea, off Adélie Land and off Cape Darnley (Meredith 2013). The second process was only observed in 1974-1976, when just-launched microwave-observing satellites revealed the persistence of an ice-free area about the size of Italy in the open Weddell Sea (Gordon 1978; Carsey 1980). Because of its non-recurrence since 1976, deep convection in the open Southern Ocean is now considered to be unimportant for the ventilation and cooling of the abyss, which is exclusively replenished from the shelves.

Satellite and in-situ observations of the Southern Ocean reveal several significant trends since the late 1970s, including: surface freshening of subpolar seas (Jacobs et al. 2002; Durack and Wijffels 2010; Azaneu et al. 2013; Aoki et al. 2013; de Lavergne et al. 2014; Rye et al. 2014), possibly owing to increased precipitation (Durack et al. 2012; Fyfe et al. 2012) and/or

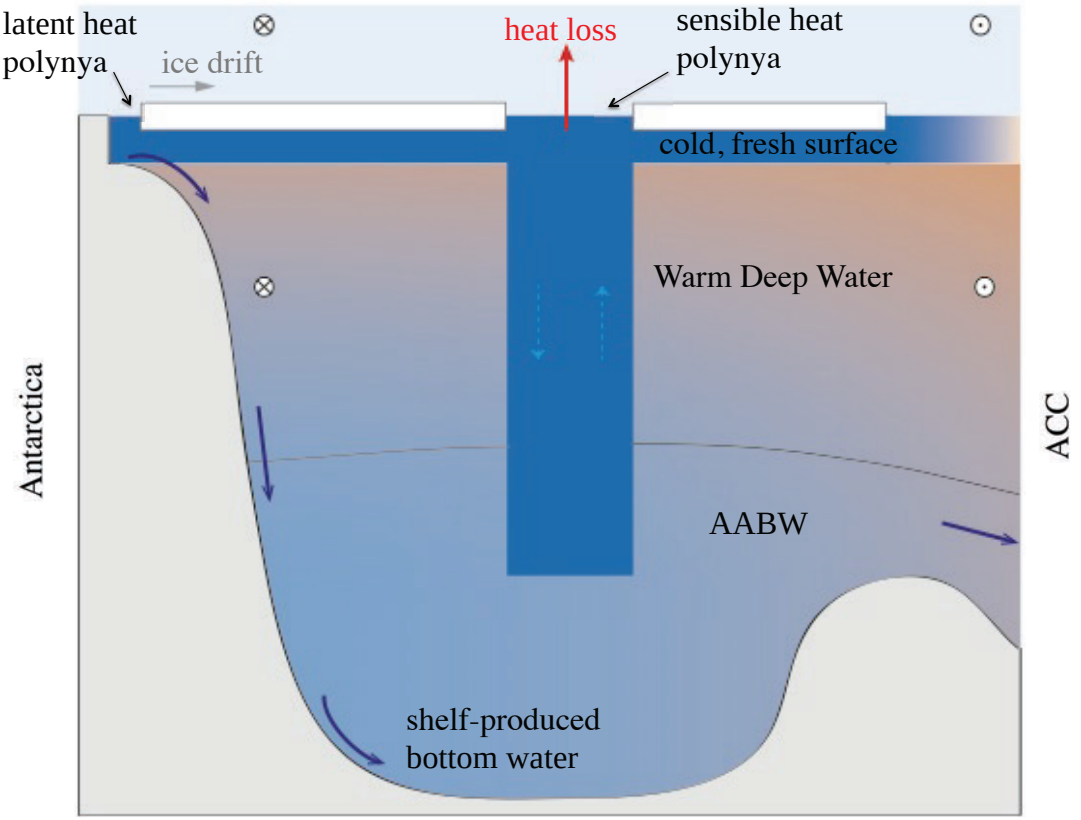

Figure 1: Schematic illustrating the shelf and open-ocean pathways of AABW production.

glacier mass loss (Rignot et al. 2013); subsurface warming across much of the Southern Ocean (Gille 2008; Schmidtko et al. 2014); warming of abyssal waters (Purkey and Johnson 2010; Fahrbach et al. 2011; Azaneu et al. 2013), extending to northern basins (Purkey and Johnson 2010; Kouketsu et al. 2011); and ageing of Weddell Sea deep and bottom waters (Huhn et al. 2013). Because of the brevity of the instrumental record and the strong multidecadal variability and model biases in this region, it is not clear whether (or which of) these recent trends are part of a long-term climate shift and whether they have a significant anthropogenic component (Hobbs et al. 2014; Bothe et al. 2015). Nonetheless, the spatial coherence and distribution of abyssal warming (Fig. 2), the detected freshening trend around Antarctica extending back to the 1960s (Jacobs et al. 2002; Azaneu et al. 2013; de Lavergne et al. 2014) and the long memory of the abyssal ocean are together suggestive of a 20th-century decline in AABW production (Purkey and Johnson 2012).

Given the sensitivity of vertical stability and dense water formation to changes in freshwater fluxes in the subpolar Southern Ocean (Martinson 1991; Jullion et al. 2013; de Lavergne et al. 2014; Naveira Garabato et al. 2016; Snow et al. 2016), it is conceivable that AABW formation has slowed in response to long-term surface freshening, leading to AABW shrinking and, thereby, to widespread abyssal warming. In turn, it is conceivable that slowed ventilation results not only from reduced shelf production but also, or even primarily, from the loss of open ocean convection as a significant mode of AABW production. This previously overlooked scenario is proposed in the following article (de Lavergne et al., 2014: Cessation of deep convection in the open Southern Ocean under anthropogenic climate change, *Nature Climate Change* 4, 278-282). A second manuscript (Jones et al., 2016: Assessing recent trends in Southern Hemisphere high latitude surface climate, *Nature Climate Change*, in press) presents a thorough assessment of recent Antarctic surface trends in the context of longer proxy records and climate simulations, highlighting the substantial multidecadal variability of southern high latitude climate and the need for extended/improved observational records to identify and attribute long-term trends in this region.

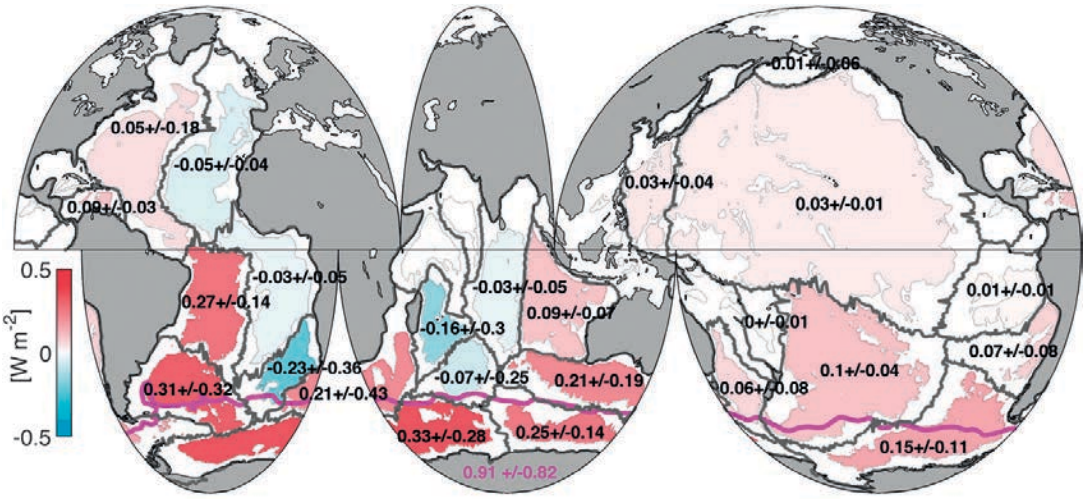

Figure 2: Heat gain below 4,000 m depth from the 1990s to the 2000s expressed as a mean heat flux within each sampled basin. Numbers and 95 % confidence intervals are indicated for each basin. From Purkey and Johnson (2010).

References

Aoki, S., Kitade, Y., Shimada, K., Ohshima, K. I., Tamura, T., Bajish, C. C., Moteki, M., and Rintoul, S. R. (2013). Widespread freshening in the seasonal ice zone near 140E off the Adélie Land coast, Antarctica, from 1994 to 2012. *Journal of Geophysical Research*, 118(11):6046–6063.

Azaneu, M., Kerr, R., Mata, M. M., and Garcia, C. A. E. (2013). Trends in the deep Southern Ocean (1958-2010): Implications for Antarctic Bottom Water properties and volume export. *Journal of Geophysical Research*, 118(9):4213–4227.

Bothe, O., Evans, M., Donado, L., Bustamante, E., Gergis, J., Gonzalez-Rouco, J., Goosse, H., Hegerl, G., Hind, A., Jungclaus, J. H., Kaufman, D., Lehner, F., McKay, N., Moberg, A., Raible, C., Schurer, A., Shi, F., Smerdon, J., Von Gunten, L., Wagner, S., Warren, E., Widmann, M., Yiou, P., and Zorita, E. (2015). Continental-scale temperature variability in PMIP3 simulations and PAGES 2k regional temperature reconstructions over the past millennium. *Climate of the Past*, 11:1673–1699.

Carsey, F. D. (1980). Microwave observation of the Weddell Polynya. *Monthly Weather Review*, 108(12):2032–2044.

de Lavergne, C., Palter, J. B., Galbraith, E. D., Bernardello, R., and Marinov, I. (2014). Cessation of deep convection in the open Southern Ocean under anthropogenic climate change. *Nature Climate Change*, 4:278–282.

Durack, P. J. and Wijffels, S. E. (2010). Fifty-year trends in global ocean salinities and their relationship to broad-scale warming. *Journal of Climate*, 23(16):4342–4362.

Durack, P. J., Wijffels, S. E., and Matear, R. J. (2012). Ocean salinities reveal strong global water cycle intensification during 1950 to 2000. *Science*, 336(6080):455–458.

Fahrbach, E., Hoppema, M., Rohardt, G., Boebel, O., Klatt, O., and Wisotzki, A. (2011). Warming of deep and abyssal water masses along the Greenwich meridian on decadal time scales: The Weddell gyre as a heat buffer. *Deep Sea Research*, 58(25-26):2509–2523.

Fyfe, J. C., Gillett, N. P., and Marshall, G. J. (2012). Human influence on extratropical Southern Hemisphere summer precipitation. *Geophysical Research Letters*, 39(23):n/a–n/a.

Gille, S. T. (2008). Decadal-scale temperature trends in the Southern Hemisphere ocean. *Journal of Climate*, 21(18):4749–4765.

Gordon, A. L. (1978). Deep Antarctic convection west of Maud Rise. *Journal of Physical Oceanography*, 8(4):600–612.

Hobbs, W. R., Bindoff, N. L., and Raphael, M. N. (2014). New perspectives on observed and simulated Antarctic sea ice extent trends using optimal fingerprinting techniques. *Journal of Climate*, 28(4):1543–1560.

Huhn, O., Rhein, M., Hoppema, M., and van Heuven, S. (2013). Decline of deep and bottom water ventilation and slowing down of anthropogenic carbon storage in the Weddell Sea, 1984–2011. *Deep Sea Research*, 76:66–84.

Jacobs, S. S., Giuvili, C. F., and Mele, P. A. (2002). Freshening of the Ross Sea during the late 20th century. *Science*, 297(5580):386–389.

Jones, J. M., Gille, S. T., Goosse, H., Abram, N. J., Canziani, P. O., Charman, D. J., Clem, K. R., Crosta, X., de Lavergne, C., Eisenman, I., England, M. H., Fogt, R. L., Frankcombe, L. M., Marshall, G. J., Masson-Delmotte, V., Morrison, A. K., Orsi, A. J., Raphael, M. N., Renwick, J. A., Schneider, D. P., Simpkins, G. R., Steig, E. J., Stenni, B., Swingedouw, D., and Vance, T. R. (2016). Assessing recent trends in high latitude Southern Hemisphere surface climate. *Nature Climate Change*, in press.

Jullion, L., Naveira Garabato, A. C., Meredith, M. P., Holland, P. R., Courtois, P., and King, B. A. (2013). Decadal freshening of the Antarctic Bottom Water exported from the Weddell Sea. *Journal of Climate*, 26(20):8111–8125.

Killworth, P. D. (1983). Deep convection in the world ocean. *Reviews of Geophysics*, 21(1):1–26.

Kouketsu, S., Doi, T., Kawano, T., Masuda, S., Sugiura, N., Sasaki, Y., Toyoda, T., Igarashi, H., Kawai, Y., Katsumata, K., Uchida, H., Fukasawa, M., and Awaji, T. (2011). Deep ocean heat content changes estimated from observation and reanalysis product and their influence on sea level change. *Journal of Geophysical Research*, 116(C3):C03012.

Martinson, D. G. (1991). Open ocean convection in the Southern Ocean. *Elsevier Oceanography Series*, 57:37–52.

Meredith, M. P. (2013). Oceanography: Replenishing the abyss. *Nature Geoscience*, 6(3):166–167.

Naveira Garabato, A. C., Zika, J. D., Jullion, L., Brown, P. J., Holland, P. R., Meredith, M. P., and Bacon, S. (2016). The thermodynamic balance of the Weddell Gyre. *Geophysical Research Letters*, 43(1):317–325.

Purkey, S. G. and Johnson, G. C. (2010). Warming of global abyssal and deep Southern Ocean waters between the 1990s and 2000s: Contributions to global heat and sea level rise budgets. *Journal of Climate*, 23(23):6336–6351.

Purkey, S. G. and Johnson, G. C. (2012). Global contraction of Antarctic Bottom Water between the 1980s and 2000s. *Journal of Climate*, 25(17):5830–5844.

Rignot, E., Jacobs, S., Mouginot, J., and Scheuchl, B. (2013). Ice-shelf melting around Antarctica. *Science*, 341(6143):266–270.

Rye, C. D., Naveira Garabato, A. C., Holland, P. R., Meredith, M. P., George Nurser, A. J., Hughes, C. W., Coward, A. C., and Webb, D. J. (2014). Rapid sea-level rise along the Antarctic margins in response to increased glacial discharge. *Nature Geoscience*, 7(10):732–735.

Schmidtko, S., Heywood, K. J., Thompson, A. F., and Aoki, S. (2014). Multidecadal warming of Antarctic waters. *Science*, 346(6214):1227–1231.

Snow, K., Hogg, A. M., Sloyan, B. M., and Downes, S. M. (2016). Sensitivity of Antarctic Bottom Water to changes in surface buoyancy fluxes. *Journal of Climate*, 29(1):313–330.

LETTERS
PUBLISHED ONLINE: 2 MARCH 2014 | DOI: 10.1038/NCLIMATE2132
nature climate change

Cessation of deep convection in the open Southern Ocean under anthropogenic climate change

Casimir de Lavergne[1]*, Jaime B. Palter[1], Eric D. Galbraith[2], Raffaele Bernardello[3] and Irina Marinov[3]

In 1974, newly available satellite observations unveiled the presence of a giant ice-free area, or polynya, within the Antarctic ice pack of the Weddell Sea, which persisted during the two following winters[1]. Subsequent research showed that deep convective overturning had opened a conduit between the surface and the abyssal ocean, and had maintained the polynya through the massive release of heat from the deep sea[2,3]. Although the polynya has aroused continued interest[1–9], the presence of a fresh surface layer has prevented the recurrence of deep convection there since 1976[8], and it is now largely viewed as a naturally rare event[10]. Here, we present a new analysis of historical observations and model simulations that suggest deep convection in the Weddell Sea was more active in the past, and has been weakened by anthropogenic forcing. The observations show that surface freshening of the southern polar ocean since the 1950s has considerably enhanced the salinity stratification. Meanwhile, among the present generation of global climate models, deep convection is common in the Southern Ocean under pre-industrial conditions, but weakens and ceases under a climate change scenario owing to surface freshening. A decline of open-ocean convection would reduce the production rate of Antarctic Bottom Waters, with important implications for ocean heat and carbon storage, and may have played a role in recent Antarctic climate change.

Antarctic Bottom Water (AABW) is the coldest, densest and most voluminous[11] water mass of the world ocean and its shrinking in recent decades[12,13] has been linked to deep ocean heat uptake[12,14]. Produced at present on Antarctic continental shelves, AABW is exported northwards to fill the deepest layers of the three oceanic basins and feed the deep branch of the meridional overturning circulation[11,15]. In 1928, on the basis of early hydrographic observations, it was suggested[16] that open-ocean convection also contributes to the production of AABW, as it does to North Atlantic Deep Water in the Labrador Sea. It was argued that deep convection occurred within the Weddell Gyre, but because of difficulty monitoring the Weddell Sea during austral winter, this contention went unverified until the mid-1970s[6].

Microwave observing satellites were first launched in December 1972, providing global observations of sea ice, and soon thereafter revealed the presence of a 250,000-km^2 ice-free area within the seasonally ice-covered Weddell Sea[1] (Fig. 1a). The huge polynya, located near Maud Rise (65° S, 0°), reappeared during the winters of 1974 to 1976, slowly drifting westward with the background flow[1]. The polynya was maintained by vigorous convective mixing, whereby the upward flux of relatively warm deep waters supplied enough heat to prevent sea ice formation[1–3]. Heat loss at the surface drove cooling to depths of about 3,000 m, producing new deep waters[3] that could have fed the observed surge in Southern Ocean AABW volume during the following decade[13]. Together with the inference from hydrographic data of a Weddell convective event circa 1960[3], these observations confirm that deep convection in the open Weddell Sea has been a significant mode of AABW ventilation[5,6]. However, following 1976, no similar polynya has been observed. The continuing quiescence over the past 37 of 41 available years of satellite observation makes it tempting to assume that deep convection in the open Southern Ocean occurs rarely, with little global consequence. Here we propose, instead, that deep convection was more common in the pre-industrial state, but that the hydrological changes associated with global warming[17–19] are now suppressing this convective activity.

The high-latitude Southern Ocean is weakly stratified, with a cold, fresh surface layer overlying a warmer, saltier interior of nearly identical density[6,20]. Weddell Sea convection is thought to occur when the weak stratification is overcome by low-frequency variability in precipitative–evaporative fluxes[8,21], brine rejection during sea ice formation[2], or circulation–topography interactions[7,20]. Wind variability may participate in polynya initiation through spin-up of the cyclonic gyre, enhancing Ekman upwelling at the gyre centre and uplift at Maud Rise[20], or by dynamically[9] and thermodynamically[4] weakening the ice pack. Thermobaric effects, which cause the cold surface waters to become relatively denser as they sink, abruptly extend the depth of convective overturning once it begins[22]. Deep convective mixing may continue until an excessive surface freshwater supply[2,23] or the exhaustion of the deep heat reservoir[23] allows column re-stratification.

It has been suggested that a persistent positive phase in the Southern Annular Mode, brought on by stratospheric ozone depletion and rising CO_2 concentrations, may be delaying the return of the Weddell Polynya by inhibiting the re-establishment of the dry atmospheric conditions and associated high surface salinities favourable for destabilizing the winter halocline[8]. However, given that increasing inputs of fresh water to the southern high-latitude ocean over the past 50 years are well documented[17–19], a long-term, large-scale upper-ocean stratification trend could be expected to be superimposed on interannual and decadal variability. To evaluate

[1]Department of Atmospheric and Oceanic Sciences, Burnside Hall, McGill University, 805 Sherbrooke Street West, Montreal, Quebec H3A 0B9, Canada, [2]Department of Earth and Planetary Sciences, McGill University, 3450 University Street, Montreal, Quebec H3A 0E8, Canada, [3]Department of Earth and Environmental Science, Hayden Hall, University of Pennsylvania, 240 S. 33rd Street, Philadelphia, Pennsylvania 19104-6316, USA.
*e-mail: casimir.delavergne@gmail.com

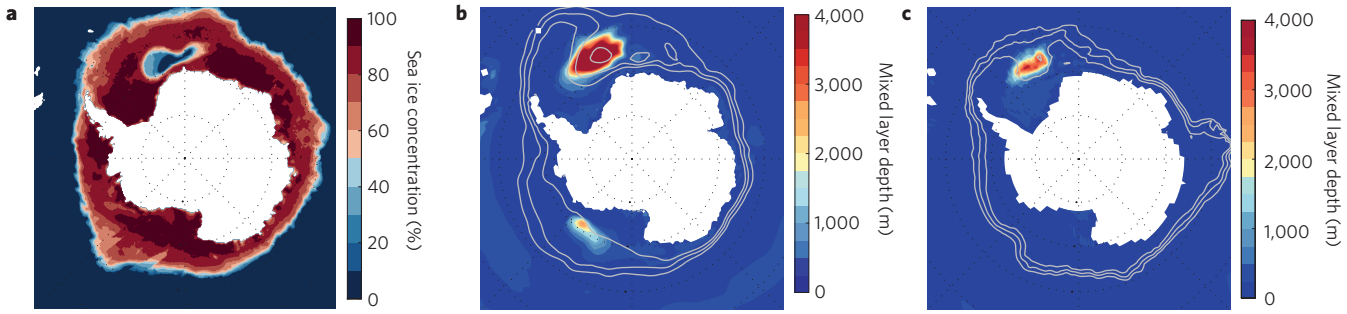

Figure 1 | Spatial pattern of Southern Ocean deep convection in observations and models. a, Observed 1974–1976 mean September sea ice concentration (%) from Nimbus-5 ESMR Polar Gridded Sea Ice Concentrations[30] delineating the Weddell Polynya extent. **b**, September mixed layer depth (shading) and 25%, 50% and 75% September sea ice concentration contours (grey lines) in the MPI-ESM-LR model, averaged over pre-industrial control years during which the convection area exceeds half of its overall maximum. **c**, The same as in **b**, but for the HadGEM2-ES model. Deep mixed layers, coinciding with anomalously low sea ice concentrations, are found over an area of comparable size to the Weddell Polynya and in a similar location. The spatial pattern of deep convection in all convective models is presented in Supplementary Fig. 1.

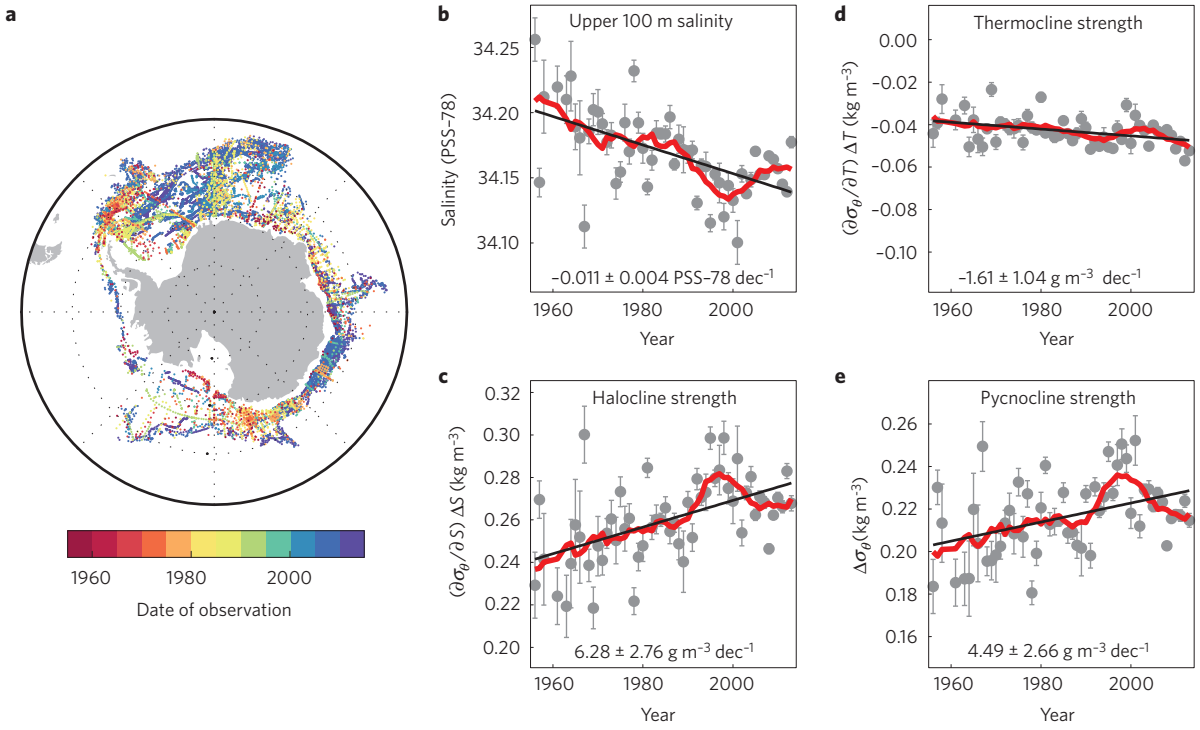

Figure 2 | Southern polar ocean freshening and stratification. a, Spatial distribution (dots) and year of observation (colour) of the 20,613 profiles included in this study. Excluding years with observations in fewer than 20 half-degree grid squares results in quasi-continuous coverage from 1956 onwards (Methods). Data from the BLUELink Ocean Archive[28]. **b**–**e**, Annual mean (± one standard error, grey), 10-year running mean (red) and linear trend (black) of 0–100 m salinity (**b**), halocline strength (**c**), thermocline strength (**d**) and pycnocline strength (**e**). The density stratification (**e**; $\Delta\sigma_\theta$) and its salinity (**c**; $(\partial\sigma_\theta/\partial S)\Delta S$) and temperature (**d**; $(\partial\sigma_\theta/\partial T)\Delta T$) components are calculated as differences between 100–200 m and 0–100 m, and presented with equal vertical range for comparison. Decadal trends with their 95% confidence intervals are indicated at the bottom.

this possibility, we examined 20,000 profiles of salinity and temperature selected to lie within the southern polar ocean, south of the Antarctic Circumpolar Current, but excluding the Antarctic continental shelf (Methods; Fig. 2a). Despite the historically sparse data coverage, significant circumpolar, area-averaged surface freshening over the past 60 years is detected (Fig. 2b). As the surface layer has become more buoyant, both vertical salinity and temperature gradients have intensified (Fig. 2c,d). As a result of the strong salinity control on density at the prevailing near-freezing temperatures, the salinity contribution to the density stratification dominates, resulting in increased stability (Fig. 2e). This long-term freshening of southern polar surface waters is consistent with changes in the precipitation–evaporation balance related to global water cycle amplification[17] and the positive Southern Annular Mode trend[8,18], and with accelerating melting and calving of Antarctic glaciers[19].

To explore the potential sensitivity of open-ocean deep convection to Southern Ocean freshening under anthropogenic climate change, we examined 36 models of the most recent Coupled Model Intercomparison Project (CMIP5; ref. 24). Although these models lack fully interactive land ice and cannot simulate increased glacial melt in response to ocean warming (Supplementary Information), they simulate changes in precipitation, evaporation, winds, sea ice and ocean circulation. Twenty-five models were found

to exhibit significant deep (>2,000 m) open-ocean convection between 90° S and 55° S under pre-industrial conditions (Methods). We stress here the caveat that these global climate models are too coarse to capture the export of dense shelf waters along the continental slope, and therefore miss this important source of deep ocean ventilation[10]. The lack of downslope currents could cause the Southern Ocean to be too weakly stratified, making it more prone to convective activity. Consequently, the simulated convection may be unrealistically strong in some cases, with reduced sensitivity to freshwater loading. On the other hand, the fact that convective chimneys have been clearly observed in the Weddell Sea[3,5,6] implies that the non-convecting models are missing a real mode of Southern Ocean ventilation. Indeed, models with no convective activity more often have overly strong vertical stratification, excessive summer ice coverage, or both[10] (Supplementary Fig. 3).

The areal extent of convection averages 930,000 km^2 over pre-industrial control years across the 25 convecting models. The Weddell and Ross gyres generally host most of the deep convection, but some models also place convective chimneys in the Indian and eastern Pacific sectors (Supplementary Fig. 1). Figure 1b,c shows the spatial pattern of convection simulated by two models, chosen for their accurate simulations of AABW properties[10] and extended climate change experiments (continuing to 2300), that provide among the best qualitative representations of the Weddell Polynya in size, location and intensity of the deep convection. The frequency of convective events is variable across models (Supplementary Table 1 and Fig. 2), reflecting the sensitivity of convection to features of ocean circulation, air–sea fluxes, sea ice[23] and model resolution[25]. Eleven of the models simulate convection almost every winter, whereas multiple decades can separate convective events in some weakly convecting models. By averaging over the 25-model ensemble, we find that 63% of all model years exhibit deep convection in the Southern Ocean, with a mean spacing between convective events of 10 years.

When subjected to increasing CO_2 concentrations following historical and Representative Concentration Pathway 8.5 (RCP8.5) forcings (Methods), all convecting models show a decrease in the strength of deep convection over the course of years 1900 to 2100 (Fig. 3 and Supplementary Table 2), with seven models exhibiting a complete cessation before 2030 (Supplementary Table 1). Simulations continued to year 2300 show no return of deep convection over this period. The fact that the slowing of Southern Ocean ventilation is so common across models suggests that a shared process is hampering the development of deep convective chimneys under warming conditions.

To explore the mechanisms driving the shutdown of convection under RCP8.5, we performed additional climate change experiments with a model (CM2Mc) featuring strong, episodic Weddell Sea ventilation events[21]. In a three-member ensemble using this model (Supplementary Information), the final convection events ended in years 1952, 1987 and 2005, highlighting the intrinsic variability and sensitivity to initial conditions of the convection cycles. Enhanced freshwater input south of 45° S, driven by increased precipitation and decreased evaporation (Supplementary Fig. 4), contributes to strengthening the halocline, building an efficient barrier to convective mixing. To test the role of the surface freshwater balance versus that of wind stress changes on ocean circulation, we made two additional sets of simulations with CM2Mc: one three-member ensemble in which we applied only the precipitation–evaporation changes over 90° S–40° S and another in which only global wind stress changes were applied (Supplementary Fig. 5). With the application of the wind stress perturbation alone, convection shifted from the Weddell Sea to the Ross Sea, but there was no significant decrease in overall deep Southern Ocean ventilation (Supplementary Fig. 6). In contrast, the precipitation–evaporation perturbation south of 40° S alone was

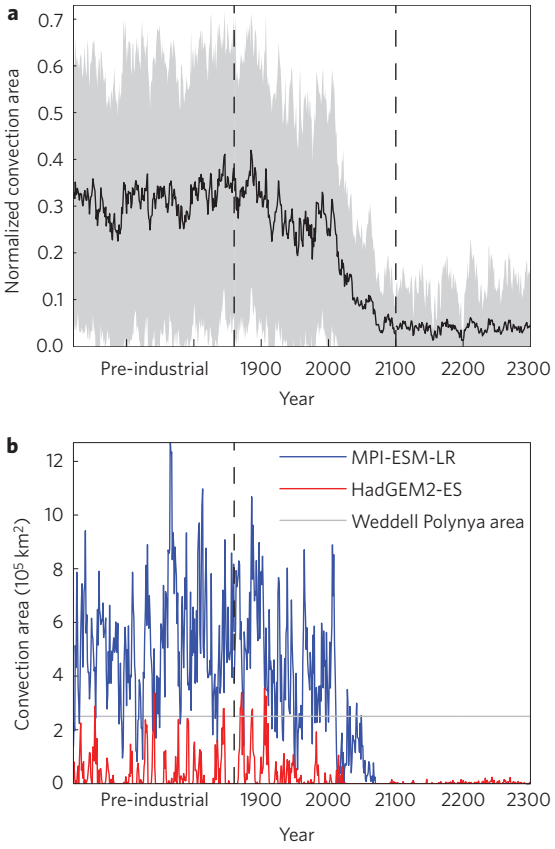

Figure 3 | Southern Ocean (55° S–90° S) convection area. a, Ensemble mean (black line) and multi-model standard deviation (grey shading) of normalized convection areas in the 25 CMIP5 convecting models. For each model, the area is normalized by the maximum areal extent of convection recorded in the entire simulation. Shown are the last 240 years of pre-industrial control runs followed by historical (1860–2005) and RCP8.5 (2006–2300) simulations. Only eight models were run beyond year 2100. **b**, Convection area in the MPI-ESM-LR (blue) and HadGEM2-ES (red) models. The 1974–1976 Weddell Polynya area[1] is indicated by the light grey line for comparison.

sufficient to stop the deep convection, with the latest convection events ending in years 1977, 1989 and 2021 for each ensemble member. We conclude that the decrease in ventilation of Southern Ocean deep and intermediate waters simulated under RCP8.5 can be explained by altered surface freshwater fluxes at southern high latitudes (Supplementary Fig. 6).

As in CM2Mc and the observational record (Fig. 2), surface freshening of the southern polar ocean is observed in 34 of the 36 CMIP5 models and significantly exceeds unforced multidecadal variability in all but two of these models (Fig. 4a and Supplementary Fig. 7). The resulting increase of salinity stratification causes the model pycnoclines to strengthen (Fig. 4b). On average, the stratification strengthens later and more slowly in convecting models than in non-convecting models, owing in part to the disruption of freshwater build-up at the surface by convective exchange with saltier deep waters. Therefore, any tendency of convective models to overestimate convection probably delays their response to a perturbed freshwater balance in comparison with the real ocean: models with more extensive convection areas generally convect further into the twenty-first century (Supplementary Fig. 8). In addition, as CMIP5 models do not include the additional freshwater input from increased glacial melt, they probably underestimate the rate of freshening under climate

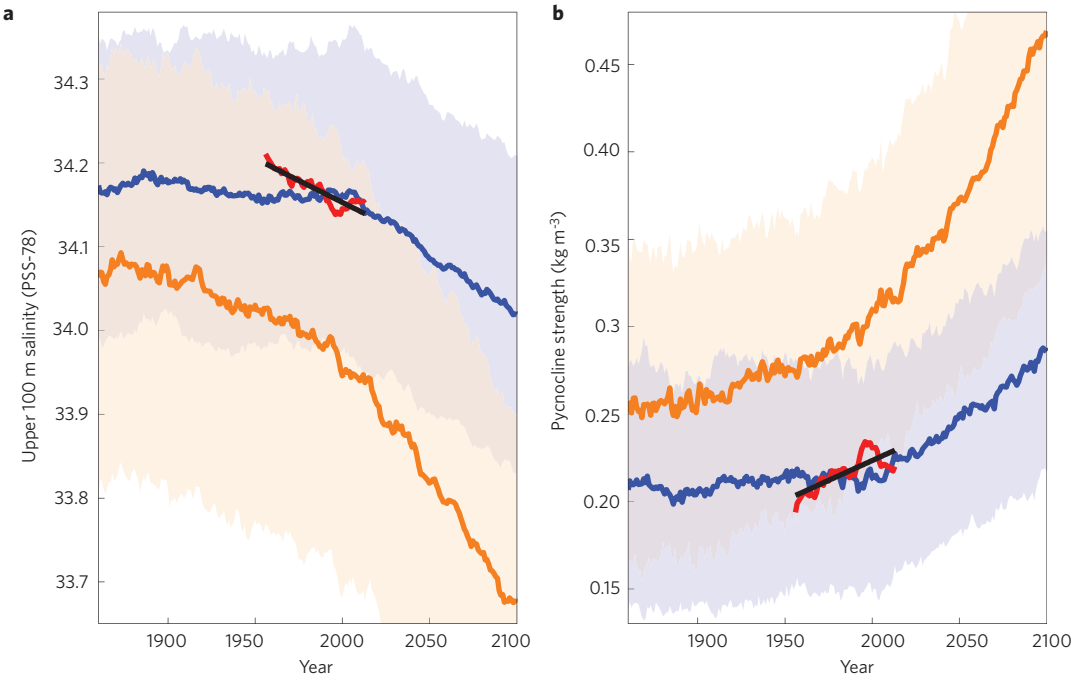

Figure 4 | Southern polar ocean freshening and stratification in CMIP5 models. a,**b**, Ensemble mean 0–100 m salinity (**a**) and pycnocline strength (**b**) of 25 convecting (blue) and 11 non-convecting (orange) CMIP5 models run over the twenty-first century with the RCP8.5 scenario. Both are annual means averaged over the area situated south of the Antarctic Circumpolar Current (where the surface dynamic height relative to 1500 m is less than its minimum within Drake Passage), excluding shelf waters. Shadings correspond to one multi-model standard deviation. The 10-year running mean (red) and linear trend (black) from the corresponding observations shown in Fig. 2 are repeated here for comparison.

warming. Indeed, freshening and stratification rates equivalent to those observed over 1956–2013 are not simulated by the ensemble of convecting models until the first half of the twenty-first century (Fig. 4), the period when the modelled convection strength undergoes its sharpest decrease (Fig. 3). In short, the CMIP5 model ensemble is consistent with a weakening of deep Southern Ocean convection under anthropogenic change, due to approximately the same degree of surface freshening and stratification as we find in the observational record.

The estimated 2–3 Sv of near-freezing surface waters that ventilated the upper AABW layer of the Weddell Sea during the three observed polynya years[3] represent a significant addition to the 5.4 ± 1.7 Sv of shelf water input to the bottom layer of the Southern Ocean[15]. Hence, a decreased frequency of deep convection would be expected to have slowed AABW production[3], and could have affected the denser shelf-produced AABW by altering the properties of deep waters involved in its formation and subsequent mixing[3,13]. The recent absence of Weddell Sea convection could thus be contributing to the observed widespread warming and volume loss of AABW[12,13].

A regime shift in Southern Ocean deep ventilation would also have had impacts on the air–sea exchange of heat and carbon. The heat release from the Weddell Polynya over 1974–1976 was estimated to be 0.4×10^{21} J yr^{-1} (ref. 3), nearly 10% of the average annual rise in ocean heat content over the 1972–2008 period[26]. Hence, stratification in the Weddell Sea may have increased ocean heat storage and attendant thermosteric sea level rise, and slowed warming of the atmosphere. Indeed, it has been suggested that decelerations of global warming are related to increased deep ocean heat storage, with a role for reduced AABW formation[14]. The recent absence of deep open-ocean convection could be contributing to contemporary trends in Southern Hemisphere climate, including slowed surface warming, subsurface ocean warming, sea ice expansion and poleward-intensifying surface westerlies[25]. In addition, by exchanging with the vast deep ocean carbon pool, Weddell convective events would have modified atmospheric pCO_2. It is possible that Southern Ocean deep convection also varied significantly during past, natural climate changes, such as on centennial timescales of recent millennia[25] and during the last deglaciation, when proxies suggest marked ventilation changes in the deep South Atlantic[27]. Further proxy studies from the Weddell Sea may be able to shed light on these possibilities.

Methods

Observational record. All profiles were taken from the latest version of the BLUELink Ocean Archive[28]. We also used salinity and temperature monthly climatologies from the CSIRO (Commonwealth Scientific and Industrial Research Organisation) Atlas of Regional Seas[28] (CARS 2009), which is built from the same database. We first selected profiles with sufficient depth coverage for which the 0–1,500 m dynamic height is less than the CARS monthly minimum within Drake Passage (5.1–5.7 dyn dm). This dynamic height criterion allows a focus on profiles south of the Antarctic Circumpolar Current. To optimize the use of the relatively sparse data, an equivalent 0–500 m dynamic height threshold (2.2–2.6 dyn dm) was determined using the strong relationship between 0–1,500 m and 0–500 m dynamic heights, as obtained from a simple linear regression. This enabled us to include additional profiles covering only the 0–500 m depth range.

Salinity, *in situ* temperature and surface-referenced potential density were averaged over 0–100 m and 100–200 m for every profile. The derivatives of potential density with respect to salinity and temperature are also calculated and averaged over 0–200 m to obtain the individual contributions of salinity and temperature to the vertical density gradient. To avoid the aliasing of spatial and seasonal variability, we subtract the appropriate monthly gridded (0.5° × 0.5°) CARS atlas values from the 0–100 m and 100–200 m profile means. Yearly anomalies are then constructed as area-weighted averages over the sampled monthly, 0.5° × 0.5° bins. We finally add the CARS climatological annual mean to the yearly anomalies to obtain the annual mean time series of Fig. 2. Standard errors are obtained from the standard deviation across sampled bins within each year (July to June), scaled by the square root of their number. Note that years with less than 20 sampled bins were discarded, resulting in quasi-continuous coverage from 1956 onwards.

CMIP5 archive. We analysed all CMIP5 models for which 'piControl', 'historical' and 'rcp85' experiments with potential temperature, salinity and sea ice concentration monthly fields were available. Model outputs were downloaded from the Program for Climate Model Diagnosis and Intercomparison data portal[24] at http://pcmdi9.llnl.gov/esgf-web-fe/. A list of all analysed models along with details on their numerical treatment of oceanic convection is given in Supplementary Table 3.

Pre-industrial control runs use fixed boundary conditions, held at the 1860 level. Historical experiments include the full range of natural and anthropogenic forcings, consistent with observations. RCP8.5 corresponds to a high-emissions scenario that includes time-varying greenhouse gas, stratospheric ozone, anthropogenic aerosols, and solar forcings. Under RCP8.5, the radiative forcing relative to pre-industrial conditions rises continuously to reach about 8.5 W m^{-2} in 2100, and increases for another 150 years in the 22–23 century extension before stabilizing at approximately 12 W m^{-2}.

Only one run (r1i1p1) per model and per experiment was considered. Available pre-industrial control simulations had lengths ranging between 240 and 1,000 years. Historical (1860–2005) and RCP8.5 (2006–2100 or 2006–2300) outputs were concatenated to obtain the climate change time series. Nine models had extended RCP8.5 integrations (2006–2300).

CMIP5 model output analysis. From monthly salinity and temperature fields, we determined mixed layer depths as the depth z at which $\sigma_\theta(z) - \sigma_\theta(10\,\mathrm{m}) = 0.03\,\mathrm{kg\,m^{-3}}$, where σ_θ is the potential density referenced to the surface[29]. This criterion was found to provide a robust diagnostic of modelled mixed layers in the southern polar regions as deep mixed layers were observed to coincide closely with positive sea surface temperature and sea surface salinity anomalies, as well as low sea ice concentration anomalies, signalling the strong vertical flux of heat and salt. Convection area is defined as the total surface area south of 55° S with a September mixed layer depth exceeding 2,000 m. This depth criterion ensures that only deep convection in the open ocean is taken into account. Convection areas are relatively insensitive to the chosen depth threshold because deep convective overturning was generally observed to extend over most of the water column. September was chosen because maximum convection depths and areas are commonly found at the end of austral winter.

Convective years are defined as years during which the convection area is larger than 100,000 km^2 (about a third of the observed 1970s Weddell Polynya area). The 11 models featuring no significant open ocean convection are those that do not simulate any convection area above this threshold (with the exception of MIROC-ESM, which convects during the last 100 years of its 630-year-long control run as a result of drifting deep Southern Ocean densities, but exhibits no convective activity during the historical period; see Supplementary Table 2).

Received 2 September 2013; accepted 13 January 2014; published online 2 March 2014

References

1. Carsey, F. D. Microwave observation of the Weddell Polynya. *Mon. Weath. Rev.* **108,** 2032–2044 (1980).
2. Martinson, D. G., Killworth, P. D. & Gordon, A. L. A convective model for the Weddell Polynya. *J. Phys. Oceanogr.* **11,** 466–488 (1981).
3. Gordon, A. L. Weddell deep water variability. *J. Mar. Res.* **40,** 199–217 (1982).
4. Parkinson, C. L. On the development and cause of the Weddell Polynya in a sea ice simulation. *J. Phys. Oceanogr.* **13,** 501–511 (1983).
5. Killworth, P. D. Deep convection in the world ocean. *Rev. Geophys.* **21,** 1–26 (1983).
6. Martinson, D. G. in *Deep Convection and Deep Water Formation in the Oceans* (eds Chu, P. C. & Gascard, J. C.) 37–52 (Elsevier Oceanography Series, 1991).
7. Holland, D. M. Explaining the Weddell Polynya—a large ocean eddy shed at Maud Rise. *Science* **292,** 1697–1700 (2001).
8. Gordon, A. L., Visbeck, M. & Comiso, J. C. A possible link between the Weddell Polynya and the Southern Annular Mode. *J. Clim.* **20,** 2558–2571 (2007).
9. Hirabara, M., Tsujino, H., Nakano, H. & Yamanaka, G. Formation mechanism of the Weddell Sea Polynya and the impact on the global abyssal ocean. *J. Oceanogr.* **68,** 771–796 (2012).
10. Heuzé, C., Heywood, K. J., Stevens, D. P. & Ridley, J. K. Southern Ocean bottom water characteristics in CMIP5 models. *Geophys. Res. Lett.* **40,** 1409–1414 (2013).
11. Johnson, G. C. Quantifying Antarctic Bottom Water and North Atlantic Deep Water volumes. *J. Geophys. Res.* **113,** C05027 (2008).
12. Purkey, S. G. & Johnson, G. C. Global contraction of Antarctic Bottom Water between the 1980s and 2000s. *J. Clim.* **25,** 5830–5844 (2012).
13. Azaneu, M., Kerr, R., Mata, M. M. & Garcia, C. A. E. Trends in the deep Southern Ocean (1958–2010): implications for Antarctic Bottom Water properties and volume export. *J. Geophys. Res.* **118,** 4213–4227 (2013).
14. Meehl, G. A., Hu, A., Arblaster, J. M., Fasullo, J. T. & Trenberth, K. E. Externally forced and internally generated decadal climate variability associated with the Interdecadal Pacific Oscillation. *J. Clim.* **26,** 7298–7310 (2013).
15. Orsi, A. H., Smethie, W. M. Jr & Bullister, J. L. On the total input of Antarctic waters to the deep ocean: a preliminary estimate from chlorofluorocarbon measurements. *J. Geophys. Res.* **107,** 3122–3135 (2002).
16. Wüst, G. Der Ursprung der Atlantischen Tiefenwasser. *Gesellsch. f. Erdk. Zeits.* 409–509 (1928).
17. Durack, P. J., Wijffels, S. E. & Matear, R. J. Ocean salinities reveal strong global water cycle intensification during 1950 to 2000. *Science* **336,** 455–458 (2012).
18. Fyfe, J. C., Gillett, N. P. & Marshall, G. J. Human influence on extratropical Southern Hemisphere summer precipitation. *Geophys. Res. Lett.* **39,** L23711 (2012).
19. Rignot, E., Jacobs, S., Mouginot, J. & Scheuchl, B. Ice-shelf melting around Antarctica. *Science* **341,** 266–270 (2013).
20. Gordon, A. L. & Huber, B. A. Southern Ocean winter mixed layer. *J. Geophys. Res.* **95,** 11655–11672 (1990).
21. Galbraith, E. D. *et al.* Climate variability and radiocarbon in the CM2Mc Earth System Model. *J. Clim.* **24,** 4230–4254 (2011).
22. Akitomo, K. Open-ocean deep convection due to thermobaricity: 1. Scaling argument. *J. Geophys. Res.* **104,** 5225–5234 (1999).
23. Martin, T., Park, W. & Latif, M. Multi-centennial variability controlled by Southern Ocean convection in the Kiel Climate Model. *Clim. Dynam.* **40,** 2005–2022 (2013).
24. Taylor, K. E., Stouffer, R. J. & Meehl, G. A. An overview of CMIP5 and the experiment design. *Bull. Am. Meteorol. Soc.* **93,** 485–498 (2012).
25. Latif, M., Martin, T. & Park, W. Southern Ocean sector centennial climate variability and recent decadal trends. *J. Clim.* **26,** 7767–7782 (2013).
26. Church, J. A. *et al.* Revisiting the Earth's sea-level and energy budgets from 1961 to 2008. *Geophys. Res. Lett.* **38,** L18601 (2011).
27. Burke, A. & Robinson, L. F. The Southern Ocean's role in carbon exchange during the last deglaciation. *Science* **335,** 557–561 (2012).
28. Ridgway, K. R., Dunn, J. R. & Wilkin, J. L. Ocean interpolation by four-dimensional weighted least squares—application to the waters around Australasia. *J. Atmos. Oceanic Technol.* **19,** 1357–1375 (2002).
29. de Boyer Montégut, C., Madec, G., Fischer, A. S., Lazar, A. & Iudicone, D. Mixed layer depth over the global ocean: An examination of profile data and a profile-based climatology. *J. Geophys. Res.* **109,** C12003 (2004).
30. Parkinson, C. L., Comiso, J. C. & Zwally, H. J. Nimbus-5 ESMR polar gridded sea ice concentrations. September 1974–1976 Boulder, Colorado USA: National Snow and Ice Data Center. (1999, updated 2004).

Acknowledgements

We thank D. Bianchi for his help with the analysis. This work was supported by the Stephen and Anastasia Mysak Graduate Fellowship in Atmospheric and Oceanic Sciences, by the Natural Sciences and Engineering Research Council of Canada (NSERC) Discovery programme, by the Canadian Institute for Advanced Research (CIFAR) and by computing infrastructure provided to E.D.G. by the Canadian Foundation for Innovation and Compute Canada. R.B. and I.M. were financially supported by grant NOAA-NA10OAR4310092.

Author contributions

All authors shared responsibility for writing the manuscript. C.d.L. assembled and analysed observational data and model output. J.B.P. and E.D.G. conceived and supervised the study. I.M., R.B., E.D.G. and J.B.P. designed the CM2Mc experiments. R.B. performed the CM2Mc experiments.

Additional information

Supplementary information is available in the online version of the paper. Reprints and permissions information is available online at www.nature.com/reprints. Correspondence and requests for materials should be addressed to C.d.L.

Competing financial interests

The authors declare no competing financial interests.

nature climate change

SUPPLEMENTARY INFORMATION

DOI: 10.1038/NCLIMATE2132

Cessation of deep convection in the open Southern Ocean under anthropogenic climate change

Supplementary Information for:

Cessation of deep convection in the open Southern Ocean under anthropogenic climate change

Casimir de Lavergne, Jaime B. Palter, Eric D. Galbraith, Raffaele Bernardello, Irina Marinov

This pdf file includes:

Supplementary text

Supplementary tables S1-S3

Supplementary figures S1-S8

Supplementary references

1. Additional CM2Mc experiments.

The model used for the additional simulations, CM2Mc[21], is a three-degree version of NOAA GFDL's coupled climate model, ESM2M[31], with a simpler land model (LM2) and excluding the iceberg model[32]. Subgrid-scale oceanic convection is parameterized through enhanced vertical diffusivity (see section 2 and Table S3) within the surface boundary layer scheme, which uses the K-profile parameterization[33]. As described in ref. 34, three ensemble members are run for *Climate Change, Wind stress perturbation* and *Precipitation-evaporation* (*P-E) perturbation* experiments. Each member is started from initial conditions taken 20 years apart from a 1000-year pre-industrial simulation segment performed after the end of the spin-up period.

The *Climate Change* experiments use the historical and RCP8.5 forcing data[35] recommended by the Coupled Model Intercomparison Project-CMIP5[24], so that the boundary conditions are identical to those used in 'historical' and 'rcp8.5' CMIP5 experiments. To compute the time-varying perturbation to the wind stress and to the surface freshwater flux used respectively in the *Wind stress perturbation* and *P-E perturbation* experiments, we start by running an additional *Control* simulation, where greenhouse gases are held constant at pre-industrial (1860) levels. We next compute the anomalies in vector wind stress and precipitative-evaporative flux as the differences in monthly means between the *Climate Change* and *Control* simulations. In order to remove the interannual signal caused by the main climate modes of variability, we smooth these anomalies by calculating 20-year running means, for each month, over the period 1860-2100. The smoothed anomalies are then applied at each ocean time step, restricted to the 90°S-40°S region in the case of the *P-E perturbation*. In the *Wind stress perturbation* runs, the wind stress anomalies are applied only when the momentum fluxes are passed from the atmosphere to the

ocean and do not directly interfere with any other process, including buoyancy forcing calculated with bulk formulae, as in ref. 36. In both ensembles, the atmosphere does not feel the perturbation except for any feedbacks resulting from changes in ocean circulation.

Figures S4, S5, and S6 document the response of the Southern Ocean to the full climate, wind stress only and P-E only forcings. In particular, Figure S5 shows the time evolution of the maximum Southern Ocean zonal mean westerly wind stress as well as latitudinal profiles of the zonally averaged zonal wind stress and P-E flux in all ensemble experiments for the 2070-2100 period. The difference between *Climate Change* and *Control* curves gives the wind stress or P-E anomalies applied to the ocean in the *Wind stress perturbation* and *P-E perturbation* runs. The *Wind stress perturbation* experiments exhibit no long-term change in the precipitation-evaporation balance, and neither *Wind stress perturbation* nor *P-E perturbation* simulations show significant changes in the sea level pressure field (Figure S5). On the other hand, in the *Climate Change* simulations, both the P-E and sea level pressure meridional contrasts are significantly altered (Figure S5). We note that these simulated changes under RCP8.5 are qualitatively consistent with an amplification of the global water cycle[17] and a southward shift and intensification of Southern Hemisphere extratropical storm tracks in association with the positive SAM trend[18,37].

In the *Wind stress perturbation* ensemble, though the overall ventilation rate of the deep Southern Ocean shows little change (Figure S6), all three members show a migration of the bulk of the deep convection from the Weddell Sea to the Ross Sea. In two of the three members, the last Weddell Sea convection event ends around 2010, and convection establishes almost permanently in the Ross Sea from 2020 onwards. The third member shows some deep

convection in the Weddell Sea until the end of the simulation, though Ross Sea convection predominates after 2050. The change in the location of deep ventilation arises mainly from a change in ocean circulation: the zonal and meridional wind stress perturbations, which are not zonally homogenous, result in a weakening of the Weddell Gyre's barotropic circulation, but a spin-up of the Ross Gyre. The reduced Ekman upwelling within the Weddell Gyre deepens the pycnocline and increases the stability of the water column there. The opposite is true for the Ross Gyre.

2. Representation of convective and land ice processes in CMIP5 models.

Coarse-resolution, hydrostatic CMIP5 models must employ a convective parameterization in order to remove gravitational instabilities through vertical mixing, mimicking the effect of the convective plumes that would rapidly homogenize the water column in nature. These parameterizations have proven efficient in reproducing the gross properties of convective chimneys[38]. Table S3 lists the numerical schemes used in the CMIP5 models included in this study. The most common approach is to increase the vertical diffusivity to very high values (e.g. ~ 10 $m^2.s^{-1}$) in regions of gravitational instability, also allowing for some mixing below the depth of neutral stability (i.e. penetrative convection). Alternatively, non-penetrative convective adjustment, such as the scheme of ref. 39, is also frequently used to restore neutral or stable stratification in the water column. Table S3 reveals in particular that the pre-industrial presence or absence of deep convection does not relate to the numerical choices to parameterize open ocean convective processes.

Land ice, dominated by Antarctic and Greenland ice sheets, is only crudely represented in CMIP5 models. Generally, the treatment of these land-based ice sheets will include a prognostic or prescribed albedo and a simple energy and mass balance scheme that, e.g., transports excess snow accumulating over the continent to the coast as frozen runoff, implying a stable long-term mean ice sheet mass and a closed freshwater cycle[32]. In particular, most models do not explicitly account for the effect of freshwater fed into the ocean through ice-shelf basal melting[40] and iceberg calving[32], despite its potential importance for regional freshwater budgets, sea ice cover and deep ocean ventilation[32,40-42]. Some models[31] now incorporate Lagrangian icebergs[32] that can realistically redistribute iceberg melt away from the coast. The unresolved ocean-ice shelf interactions[43] mean, however, that CMIP5 models cannot simulate the observed and projected mass loss of Antarctic ice shelves in response to ocean warming and ocean circulation changes[19,41]. Thus, none of the CMIP5 models analyzed in this study account for changing rates of glacial melt, likely underestimating the rate of freshening of Southern Ocean surface waters under anthropogenic change[43,44].

3. Assessment of model drift in CMIP5 Southern Ocean simulations.

Though reduced when averaged over a large ensemble of models, drift can be significant in individual model simulations, especially in the deep ocean, due to its long equilibration timescale[45]. Therefore, pre-industrial control simulations have been analyzed for drift in Southern Ocean surface and deep water properties. The drift is estimated as the linear trend over the full length of ‘piControl’ time series[45], and compared to the 2005-2100 RCP8.5 linear trend (Table S2). Multi-model averages of pre-industrial control and RCP8.5 trends, calculated as the

mean over statistically significant (at the 95% level) individual trends, are also given for the convecting and non-convecting model groups.

Table S2 shows that the multi-model mean drift is one to three orders of magnitude smaller than the RCP8.5 trends for all analyzed variables. The drift in convection area averages a gain of 31,000 km^2 per century across the convecting models, compared to a multi-model mean decreasing trend of –384,000 km^2 per century for the 1860-2100 period. Therefore, model drift does not contribute to the slowdown in ensemble mean deep convection documented in Figure 3. Indeed, the small positive ensemble mean drift in both convection area and normalized convection area implies that the decrease in convection strength under RCP8.5 (Figure 3) would only be reinforced if drift were accounted for.

Ensemble mean drift in southern polar ocean 0-100 m salinity and pycnocline strength is so small that the time series presented in Figure 4 are nearly identical whether linear drift is subtracted from the climate change time series or not. Though insignificant for the ensemble mean, drift can be important for the freshening and stratification of individual models. Therefore, a linear drift was subtracted from the warming-driven trends for each model when constructing Figure S7. This figure shows freshening and stratification during 1860-2100 despite the subtracted drift. The correction mostly affects the GISS-E2-H and CNRM-CM5 models, which have the largest drift-to-trend ratios in upper 100 m salinity and are the only two models simulating surface salinification of the southern polar ocean over the 21st century.

Models	Maximum convection area (10^5 km^2)	Mean convection area (10^5 km^2)	Percentage convective years (%)	Mean number of consecutive convective winters	Mean number of consecutive non-convective winters	Maximum number of consecutive non-convective winters	Latest convective year (historical-rcp85)
ACESS1.0	18.97	10.11	100.0	…	0.0	0	2053
ACCESS1.3	22.25	8.86	93.0	…	0.0	17	2068
BCC-CSM1.1*	23.08	1.87	36.2	2.5	4.3	22	*2125
BCC-CSM1.1m	32.26	8.17	66.7	7.2	3.6	45	2095
CMCC-CESM	13.59	2.51	56.3	5.2	4.0	13	2068
CMCC-CM	13.80	3.33	57.6	11.9	8.2	24	2084
CMCC-CMS	14.80	1.46	29.0	3.7	9.1	39	1993
CNRM-CM5*	16.61	1.39	26.6	11.9	31.2	91	*2027
CSIRO-Mk3.6*	2.18	0.05	1.8	2.3	98.2	161	*1862
FGOALS-g2	2.88	0.35	6.4	1.6	21.8	110	1975
FGOALS-s2	51.21	37.76	100.0	…	0.0	0	2095
GFDL-CM3	37.34	10.23	81.6	19.4	4.6	20	2066
GFDL-ESM2G	35.10	14.04	99.4	…	0.0	3	2081
GFDL-ESM2M	21.07	8.83	96.6	…	0.0	6	2084
GISS-E2-H*	40.09	29.44	100.0	…	0.0	0	*2295
GISS-E2-R*	59.03	47.55	100.0	…	0.0	0	*2300
HadGEM2-CC	7.00	0.85	30.4	2.8	6.4	17	2023
HadGEM2-ES*	4.13	0.49	19.8	2.0	8.1	49	*2015
IPSL-CM5A-LR*	10.00	0.40	11.0	2.8	22.3	231	*2097
IPSL-CM5A-MR	27.01	4.41	67.3	16.8	8.2	21	2062
IPSL-CM5B-LR	4.08	0.19	3.7	2.2	13.5	33	2011
MIROC5	17.55	8.42	99.4	…	0.0	2	2100
MPI-ESM-LR*	13.59	5.46	99.1	…	0.0	2	*2051
MPI-ESM-MR	19.52	8.02	100.0	…	0.0	0	2069
MRI-CGCM3	28.48	17.89	100.0	…	0.0	0	2100
CM2Mc	27.96	7.57	65.7	17.3	7.1	27	1981
BNU-ESM	0.28	0.00	0.0	…	…	…	…
CanESM2	0.24	0.03	0.0	…	…	…	…
CCSM4*	0.24	0.00	0.0	…	…	…	…
CESM1-BGC	0.35	0.00	0.0	…	…	…	…
CESM1-CAM5	0.00	0.00	0.0	…	…	…	…
CESM1-WACCM	0.09	0.00	0.0	…	...	…	…
INMCM4	0.00	0.00	0.0	…	…	…	…
MIROC-ESM	8.19	0.40	15.9	9.0	69.8	531	…
MIROC-ESM-CHEM	0.00	0.00	0.0	…	…	…	…
NorESM1-M	0.03	0.00	0.0	…	…	…	...
NorESM1-ME	0.00	0.00	0.0	…	…	…	…

Table S1: **Characteristics of convection in CMIP5 models and CM2Mc.**

All metrics were calculated from the full extent of pre-industrial model outputs, except for the latest convective year (last column), which pertains to climate change simulations, extending from 1860 to 2100 or from 1860 to 2300 in nine models (asterisks). The upper 25 models are

those referred to as ‘convecting’ models while the bottom 11 models are ‘non-convecting’ models. Characteristics of convection in CM2Mc are also given for comparison. Despite the significant convection displayed by MIROC-ESM at the end of its control simulation, this model was classified as non-convecting because no single convective year was found in historical and RCP8.5 experiments (see Table S2). Convective years correspond to a convection area in excess of 100,000 km^2. Two models (GISS-E2-H and GISS-E2-R) show robust convection until 2300, while seven models cease convecting before 2030.

Models	0-100 m salinity (PSS-78.cent^{-1})		Pycnocline strength (g.m^{-3}.cent^{-1})		surface density (g.m^{-3}.cent^{-1})		2000 m density (g.m^{-3}.cent^{-1})		Convection area (10^{5} km^{2}.cent^{-1})	
	piControl	rcp8.5	piControl	rcp8.5	piControl	rcp8.5	piControl	rcp8.5	piControl	hist-rcp8.5
ACCESS1.0	-0.001	**-0.158**	**1.0**	**110.9**	**-8.1**	**-346.3**	**-6.2**	**-33.1**	**0.25**	**-4.68**
ACCESS1.3	**0.007**	**-0.226**	-0.2	**117.8**	**2.1**	**-316.1**	**8.5**	**-43.9**	**-0.82**	**-3.95**
BCC-CSM1.1	**-0.008**	**-0.041**	**0.8**	**35.1**	**-5.5**	**-243.4**	**-4.7**	**-23.9**	-0.02	**-0.99**
BCC-CSM1.1m	**-0.002**	**-0.133**	**1.3**	**45.2**	**-3.2**	**-189.0**	**-4.7**	**-34.1**	0.40	**-5.99**
CMCC-CESM	**-0.005**	**-0.138**	**2.9**	**79.6**	**-6.8**	**-303.1**	**-1.5**	**-15.7**	-0.23	**-1.25**
CMCC-CM	**0.018**	**-0.096**	**-4.2**	**73.4**	**-7.8**	**-307.4**	**-4.2**	**-23.2**	**0.86**	**-2.82**
CMCC-CMS	0.000	**-0.066**	-0.7	**55.9**	0.0	**-274.4**	**-1.3**	**-16.9**	**0.17**	**-1.13**
CNRM-CM5	**-0.022**	**0.013**	**1.7**	**52.5**	**-22.4**	**-298.8**	**-11.1**	**-15.5**	0.00	**-0.86**
CSIRO-MK3.6	-0.001	**-0.267**	**1.9**	**131.3**	**-2.0**	**-354.6**	**7.6**	**-4.3**	**-0.02**	**-0.05**
FGOALS-g2	**0.027**	**-0.164**	0.1	**18.9**	**16.3**	**-284.7**	**27.5**	**-32.5**	0.01	**-0.26**
FGOALS-s2	**0.012**	**-0.456**	**0.8**	**171.1**	**15.9**	**-527.8**	**17.5**	**-53.7**	**0.35**	**-19.71**
GFDL-CM3	**0.004**	**-0.211**	0.0	**134.3**	**-12.4**	**-338.3**	**-9.5**	**-49.9**	**1.61**	**-4.53**
GFDL-ESM2G	-0.003	**-0.395**	0.8	**138.0**	-0.2	**-318.1**	**1.2**	**-18.9**	-0.03	**-6.24**
GFDL-ESM2M	**-0.002**	**-0.116**	0.0	**64.4**	**-3.2**	**-196.5**	**-2.8**	**-21.6**	0.03	**-5.02**
GISS-E2-H	**0.042**	**0.101**	**-7.0**	**-115.0**	**26.8**	**-158.1**	**12.4**	**-22.0**	**0.73**	**-2.62**
GISS-E2-R	0.001	**-0.123**	-0.1	**65.0**	-0.1	**-211.3**	**3.0**	**-50.2**	-0.50	**-13.69**
HADGEM2-CC	-0.001	**-0.293**	-0.3	**134.3**	**7.0**	**-398.2**	**-3.0**	**-45.2**	-0.02	**-0.35**
HADGEM2-ES	**-0.006**	**-0.244**	0.4	**128.7**	**-7.4**	**-424.1**	**-6.1**	**-41.9**	-0.03	**-0.44**
IPSL-CM5A-LR	**0.001**	**-0.066**	**-0.6**	**32.3**	0.2	**-235.6**	**-0.5**	**-19.0**	**0.07**	0.21
IPSL-CM5A-MR	-0.002	**-0.079**	0.2	**30.7**	**-5.6**	**-203.9**	**3.4**	**-16.1**	0.30	**-1.12**
IPSL-CM5B-LR	**0.014**	**-0.096**	**-18.3**	**93.6**	**10.6**	**-343.2**	**-10.0**	**-30.8**	**0.15**	**-0.10**
MIROC5	**0.003**	**-0.164**	**2.7**	**66.4**	**-7.0**	**-187.1**	**-8.7**	**-43.6**	**0.30**	**-2.88**
MPI-ESM-LR	0.000	**-0.111**	**-0.2**	**58.6**	0.3	**-204.8**	**-0.2**	**-28.1**	0.01	**-2.87**
MPI-ESM-MR	0.000	**-0.115**	0.0	**78.4**	**-0.6**	**-171.5**	**-0.8**	**-27.4**	**-0.08**	**-3.85**
MRI-CGCM3	**0.004**	**-0.086**	**-1.1**	**35.4**	**5.1**	**-365.3**	**-4.2**	**-29.9**	**0.46**	**-6.74**
Multimodel mean	0.005	-0.156	-1.3	73.5	-0.4	-288.1	0.1	-29.6	0.31	-3.84
CM2Mc	-0.001	**-0.137**	-1.9	**99.1**	2.8	**-242.2**	**-0.88**	**-20.9**	-0.06	**-3.42**
BNU-ESM	-0.011	**-0.085**	-7.9	**58.6**	-1.1	**-352.7**	**-18.2**	**-40.5**	…	…
CanESM2	**-0.003**	**-0.338**	**1.9**	**180.7**	**-4.8**	**-365.8**	**8.3**	**-4.9**	…	…
CCSM4	**0.007**	**-0.531**	**-1.8**	**303.6**	**2.3**	**-448.0**	**5.1**	**-24.6**	…	…
CESM1-BGC	**0.006**	**-0.411**	0.1	**276.3**	**-1.1**	**-436.4**	**8.1**	**-20.1**	…	…
CESM1-CAM5	**-0.015**	**-0.298**	**4.1**	**231.0**	**-10.9**	**-447.1**	**-4.2**	**-22.4**	…	…
CESM1-WACCM	**0.013**	**-0.387**	**12.7**	**282.8**	**-8.3**	**-467.2**	**9.6**	**-10.0**	…	…
INM-CM4	**0.003**	**-0.076**	**-4.9**	**56.2**	**-1.5**	**-216.2**	**12.4**	**2.6**	…	…
MIROC-ESM	0.002	**-0.227**	**1.7**	**157.1**	**-14.6**	**-283.1**	**-30.6**	**-48.5**	**0.32**	…
MIROC-ESM-CHEM	**-0.029**	**-0.198**	**8.7**	**154.2**	**-19.3**	**-305.1**	**-34.5**	**-51.9**	…	…
NORESM1-M	**0.005**	**-0.382**	-0.2	**75.2**	**-5.6**	**-358.0**	**-2.5**	**-31.1**	…	…
NORESM1-ME	0.008	**-0.439**	**-3.6**	**85.9**	**3.6**	**-351.3**	**-4.8**	**-25.9**	…	…
Multimodel mean	-0.002	-0.307	2.4	169.3	-6.0	-366.4	-4.7	-25.2	…	…

Table S2: Pre-industrial control and RCP8.5 Southern Ocean linear trends in CMIP5 models and CM2Mc.

Upper 100 m salinity and pycnocline strength refer to southern polar ocean annual means, as presented in Figure 4; surface and 2000 m density refer to 90°S-50°S annual mean locally-

referenced potential densities; convection area is as defined in Methods and as presented in Figure 3. Full-length pre-industrial control and 2005-2100 (1860-2100 for the convection area) RCP8.5 linear trends are compared. Statistically significant trends at the 95% level are indicated in bold. Multi-model averages, calculated as the mean over 95%-level significant trends, are also given for the convecting and non-convecting model groups. Note that differing lengths of 'piControl' time series preclude a direct assessment of the drift (and its significance) in ensemble mean properties. The multi-model mean drift is one to three orders of magnitudes smaller than RCP8.5 trends. All convecting models show a significant decrease in convection area over 1860-2100 except IPSL-CM5A-LR, which shows non-significant change over this period but ceases to convect following 2097 (Table S1). The MIROC-ESM models exhibit the strongest drift in 2000 m density: warming and freshening of Southern Ocean deep waters gradually weaken the vertical stability, eventually causing the abrupt convective onset at year 530 of the MIROC-ESM pre-industrial simulation (only 255 years are available for MIROC-ESM-CHEM).

Models	Ocean code	Mixed layer scheme	Treatment of convection
ACESS1.0	MOM4.1	K-profile parameterization (33)	enhanced vertical diffusion
ACCESS1.3	MOM4.1	K-profile parameterization (33)	enhanced vertical diffusion
BCC-CSM1.1	MOM4-L40	K-profile parameterization (33)	enhanced vertical diffusion
BCC-CSM1.1m	MOM4-L40	K-profile parameterization (33)	enhanced vertical diffusion
CMCC-CESM	NEMO(OPA8.2)	Turbulent kinetic energy closure (46,47)	enhanced vertical diffusion
CMCC-CM	NEMO(OPA8.2)	Turbulent kinetic energy closure (46,47)	enhanced vertical diffusion
CMCC-CMS	NEMO(OPA8.2)	Turbulent kinetic energy closure (46,47)	enhanced vertical diffusion
CNRM-CM5	NEMO3.2	Turbulent kinetic energy closure (46,47)	enhanced vertical diffusion
CSIRO-Mk3.6	MOM2.2	Kraus-Turner scheme (48)	convective adjustment (39)
FGOALS-g2	LICOM2	Turbulent kinetic energy closure (49,50)	convective adjustment (39)
FGOALS-s2	LICOM2	Turbulent kinetic energy closure (49,50)	convective adjustment (39)
GFDL-CM3	MOM4.1	K-profile parameterization (33)	enhanced vertical diffusion
GFDL-ESM2G	GOLD	Bulk mixed layer/Turbulent kinetic energy closure (48,51,52)	included in the turbulence closure
GFDL-ESM2M	MOM4.1	K-profile parameterization (33)	enhanced vertical diffusion
GISS-E2-H	HYCOM	K-profile parameterization (33)	enhanced vertical diffusion
GISS-E2-R	Russell	K-profile parameterization (33)	enhanced vertical diffusion
HadGEM2-CC	HadGOM2	Kraus-Turner/K-theory scheme (48,33)	convective adjustment (39)
HadGEM2-ES	HadGOM2	Kraus-Turner/K-theory scheme (48,33)	convective adjustment (39)
IPSL-CM5A-LR	NEMO3.2	Turbulent kinetic energy closure (46,47)	enhanced vertical diffusion
IPSL-CM5A-MR	NEMO3.2	Turbulent kinetic energy closure (46,47)	enhanced vertical diffusion
IPSL-CM5B-LR	NEMO3.2	Turbulent kinetic energy closure (46,47)	enhanced vertical diffusion
MIROC5	COCO4.5	Turbulent kinetic energy closure (53,54,55)	convective adjustment (39)
MPI-ESM-LR	MPI-OM	Richardson number dependent (56)	enhanced vertical diffusion
MPI-ESM-MR	MPI-OM	Richardson number dependent (56)	enhanced vertical diffusion
MRI-CGCM3	MRI.COM3	Turbulent kinetic energy closure (53,54,55)	convective adjustment (39)
CM2Mc	MOM4.1	K-profile parameterization (33)	enhanced vertical diffusion
BNU-ESM	MOM4.1	K-profile parameterization (33)	enhanced vertical diffusion
CanESM2	NCOM	K-profile parameterization (33)	enhanced vertical diffusion
CCSM4	POP2	K-profile parameterization (33)	enhanced vertical diffusion
CESM1-BGC	POP2	K-profile parameterization (33)	enhanced vertical diffusion
CESM1-CAM5	POP2	K-profile parameterization (33)	enhanced vertical diffusion
CESM1-WACCM	POP2	K-profile parameterization (33)	enhanced vertical diffusion
INMCM4	INMOM4	Richardson number dependent (56)	enhanced vertical diffusion
MIROC-ESM	COCO3.4	Turbulent kinetic energy closure (53,54,55)	convective adjustment (39)
MIROC-ESM-CHEM	COCO3.4	Turbulent kinetic energy closure (53,54,55)	convective adjustment (39)
NorESM1-M	MICOM/Bergen	Bulk mixed layer/Turbulent kinetic energy closure (57)	convective adjustment (39)
NorESM1-ME	MICOM/Bergen	Bulk mixed layer/Turbulent kinetic energy closure (57)	convective adjustment (39)

Table S3: Parameterizations of convection in CMIP5 models and CM2Mc.

The numerical treatment of mixed layer physics and convective instabilities is given for each model along with relevant references (numbers). The algorithm of ref. 39 is indicated as the reference for non-penetrative convective adjustment schemes though some models may use slightly different implementations. Information was collected from the ES-DOC model metadata

database available at http://earthsystemcog.org/projects/es-doc-models/comparator_demo, complemented by published model documentation.

Figure S1: Spatial pattern of Southern Ocean deep convection in 25 convecting CMIP5 models. For each model, the September mixed layer depth (shading) and 25% and 75% September sea ice concentration contours (light grey lines) are shown as averages over pre-industrial control years during which the convection area exceeds half of its overall maximum.

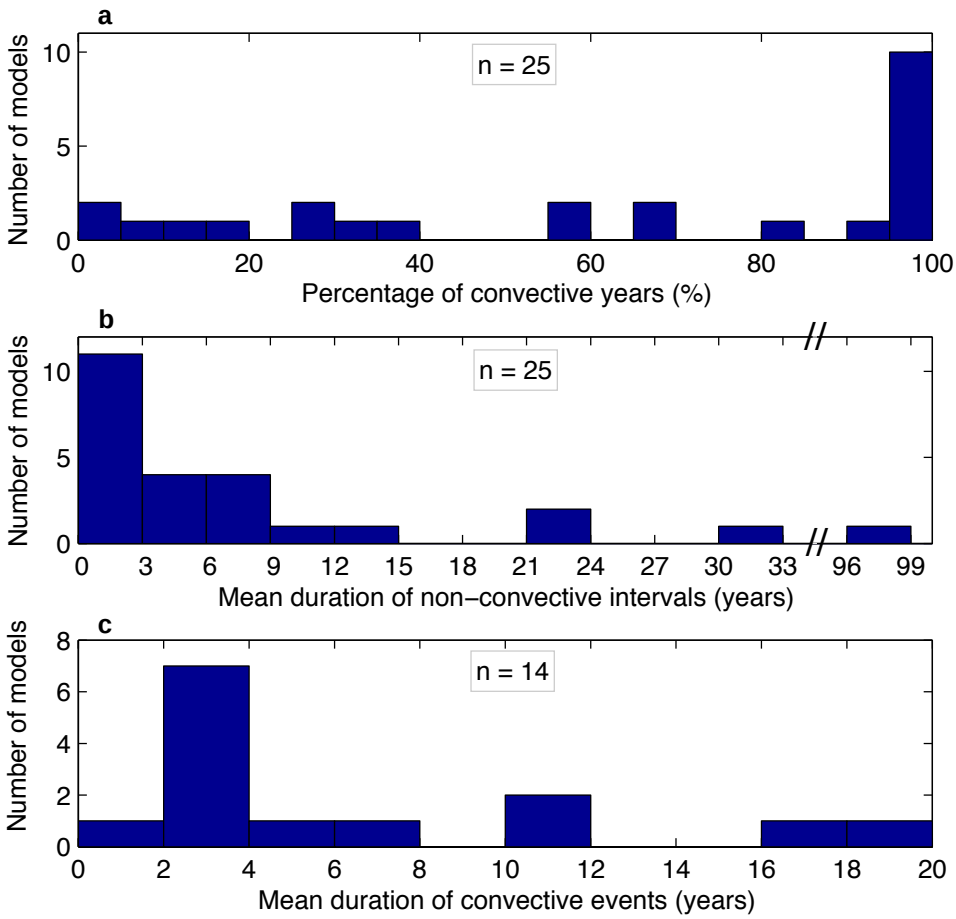

Figure S2: Frequency and duration of simulated Southern Ocean convective events under pre-industrial conditions. Distribution of the 25 convecting CMIP5 models according to (**a**) percentage of convective years and (**b**) mean duration of non-convective intervals, and (**c**) distribution of 14 intermittently convecting CMIP5 models according to duration of convection events. Note that both the frequency and the duration of convective events are highly variable across models. Eleven models simulate convection almost every winter. The 14 models that allow only intermittent convection show a mean duration of convective periods ranging between one and 19 consecutive winters, and a mean hiatus between events of three to 98 years.

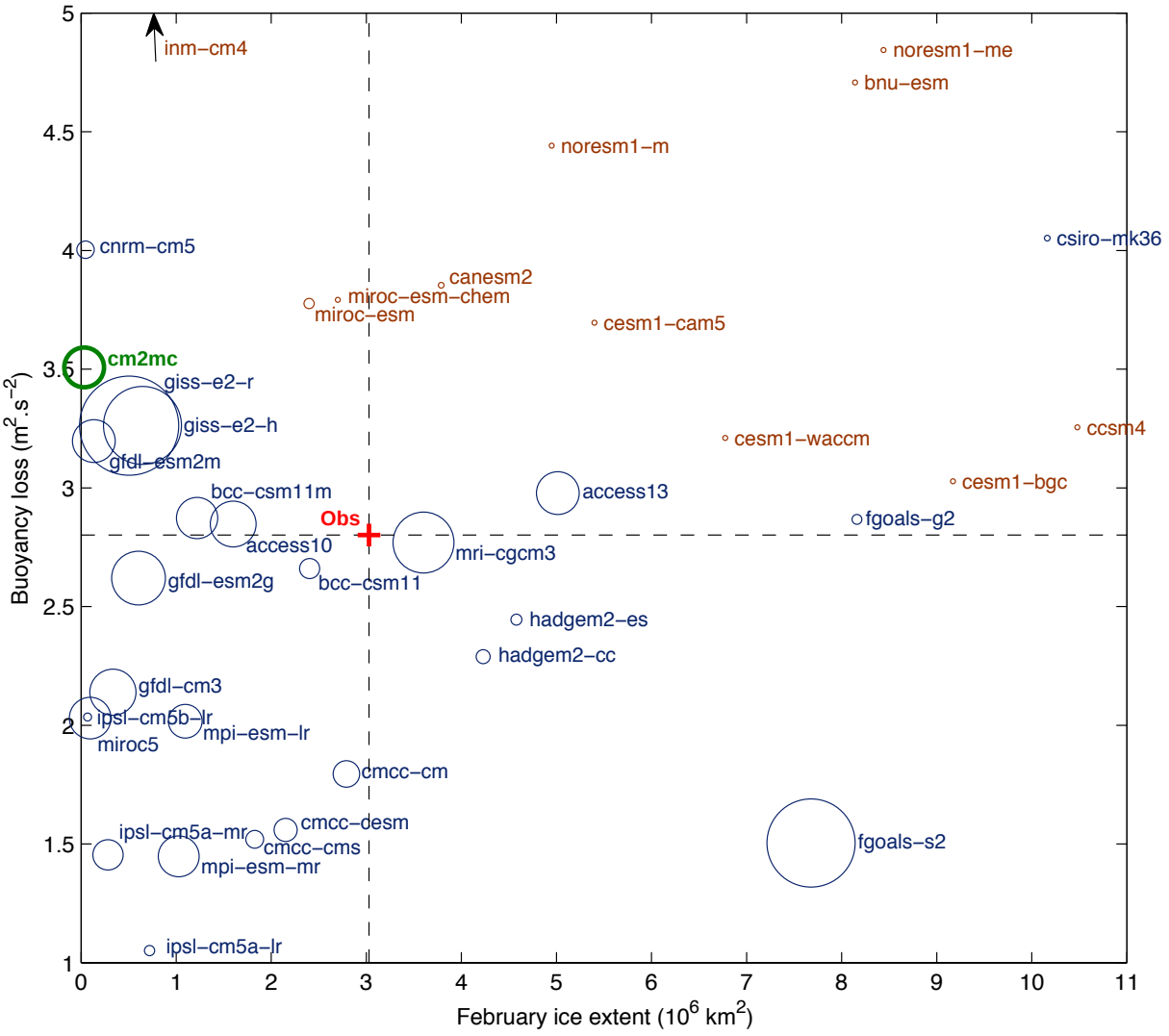

Figure S3: Southern Ocean stratification versus February ice extent in the CMIP5 model suite for the 1976-2005 period. Pre-industrial mean convection area reflected by the size of the circle for each model. The stratification is measured by the buoyancy loss necessary for convection to reach a depth of 3000 m in September, calculated as $\frac{g}{\rho_0}\int_0^{3000}\left[\sigma_\theta(3000m)-\sigma_\vartheta(z)\right]dz$, averaged over 55°S-90°S; σ_θ is the potential density referenced to the surface, and g, ρ_0 are constants. Sea ice extent refers to the area over which the sea ice concentration is larger than 15 %. All model variables are averaged over 1976-2005. A corresponding observational estimate (red cross) is

indicated, where the stratification is calculated from the CARS[28] September climatology and the observed February sea ice extent is the 1979-2005 average (data from the National Snow and Ice Data Center[58]). The 11 models with no significant convective activity (brown) tend to have either strong vertical stratification or large summer sea ice coverage or a combination of both relative to observations. The CM2Mc model (three-member ensemble mean) is shown in green.

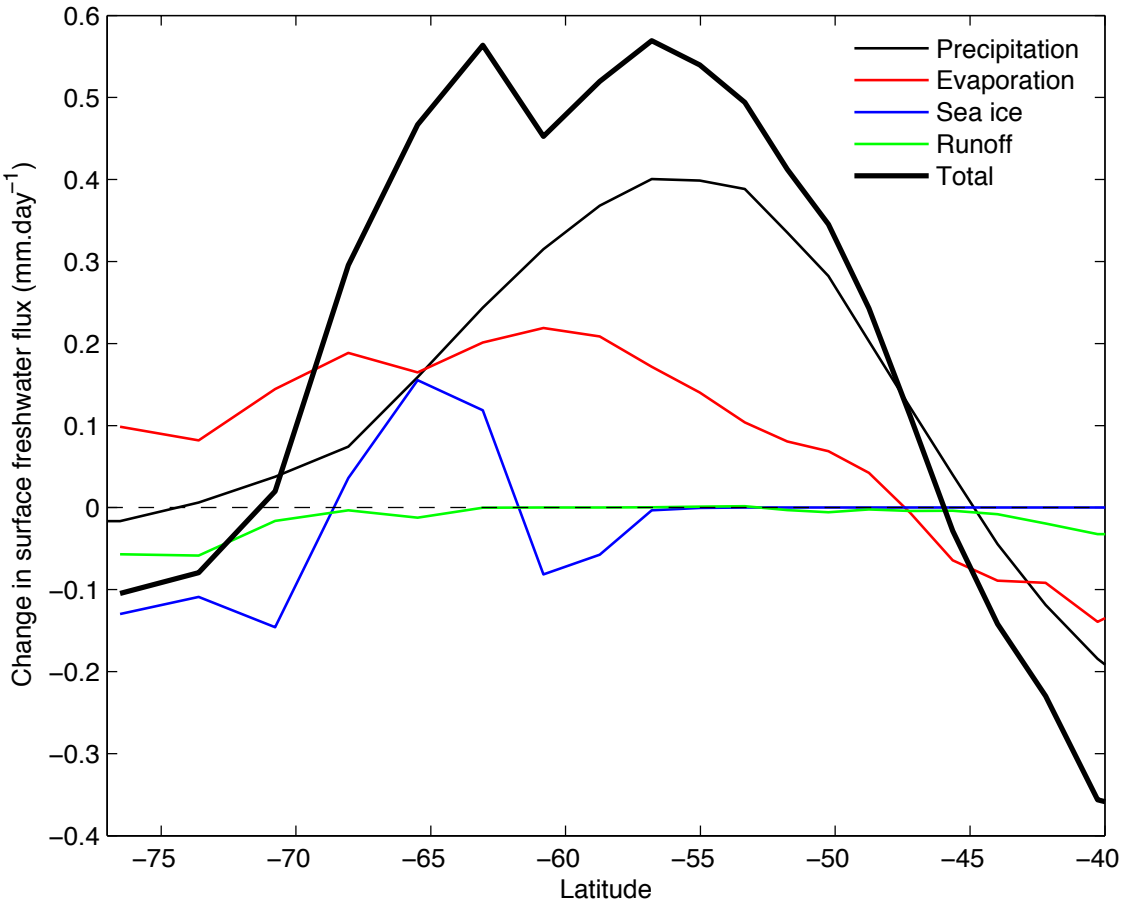

Figure S4: Changes in surface freshwater fluxes (mm.day^{-1}) in the CM2Mc *Climate Change* model simulations. Zonal mean total change (thick black line) and contributions due to precipitation (black), evaporation (red), sea ice melt (blue; negative values mean less melt or more ice growth) and runoff (green). Positive values correspond to an increase in freshwater input to the surface ocean. Ensemble multi-annual mean of three simulations presented for years 2070-2100 minus 1860-1890 (the same quantity calculated in the *Control* simulations showed the model drift to be negligible). Precipitative-evaporative freshening changes dominate between 68°S and 46°S.

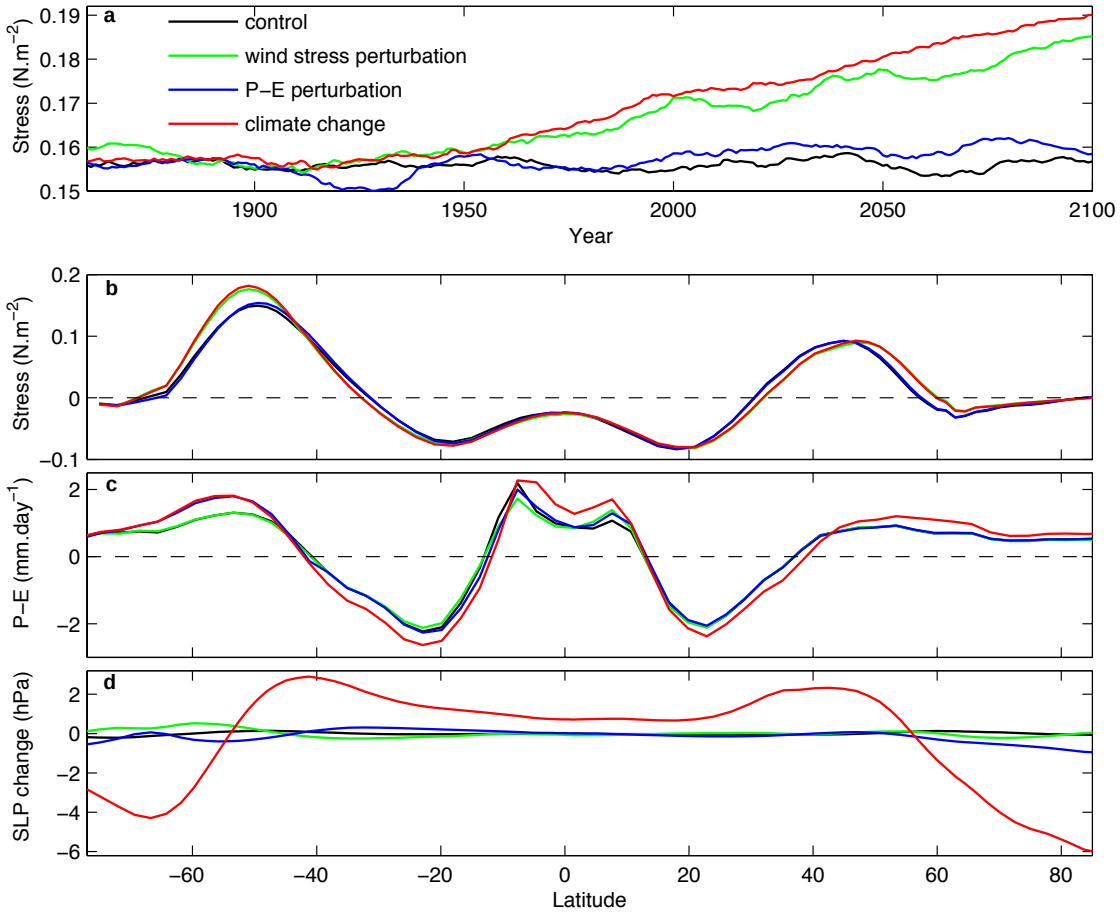

Figure S5: Changes in low-level atmospheric circulation and hydrological cycle in the CM2Mc ensemble experiments. **a**, Time evolution of the 20-year running mean maximum Southern Ocean zonal mean zonal wind stress. Zonal mean (**b**) zonal wind stress and (**c**) precipitation minus evaporation (P-E) averaged over 2070-2100. **d**, Difference in zonal mean sea level pressure (SLP) between years 2070-2100 and 1860-1890. All are averaged over (black) *Control*, (green) *Wind stress perturbation*, (blue) *P-E perturbation* and (red) *Climate Change* three-member ensembles. Under RCP8.5 (red curves), the P-E meridional gradients deepen and the high latitude maxima in P-E shift poleward (c). The deepening of the meridional gradient in SLP at about 53°S (d) signals the positive long-term change in the SAM index, which is accompanied by a strengthening and southward shift of the low-level atmospheric circulation (a,b).

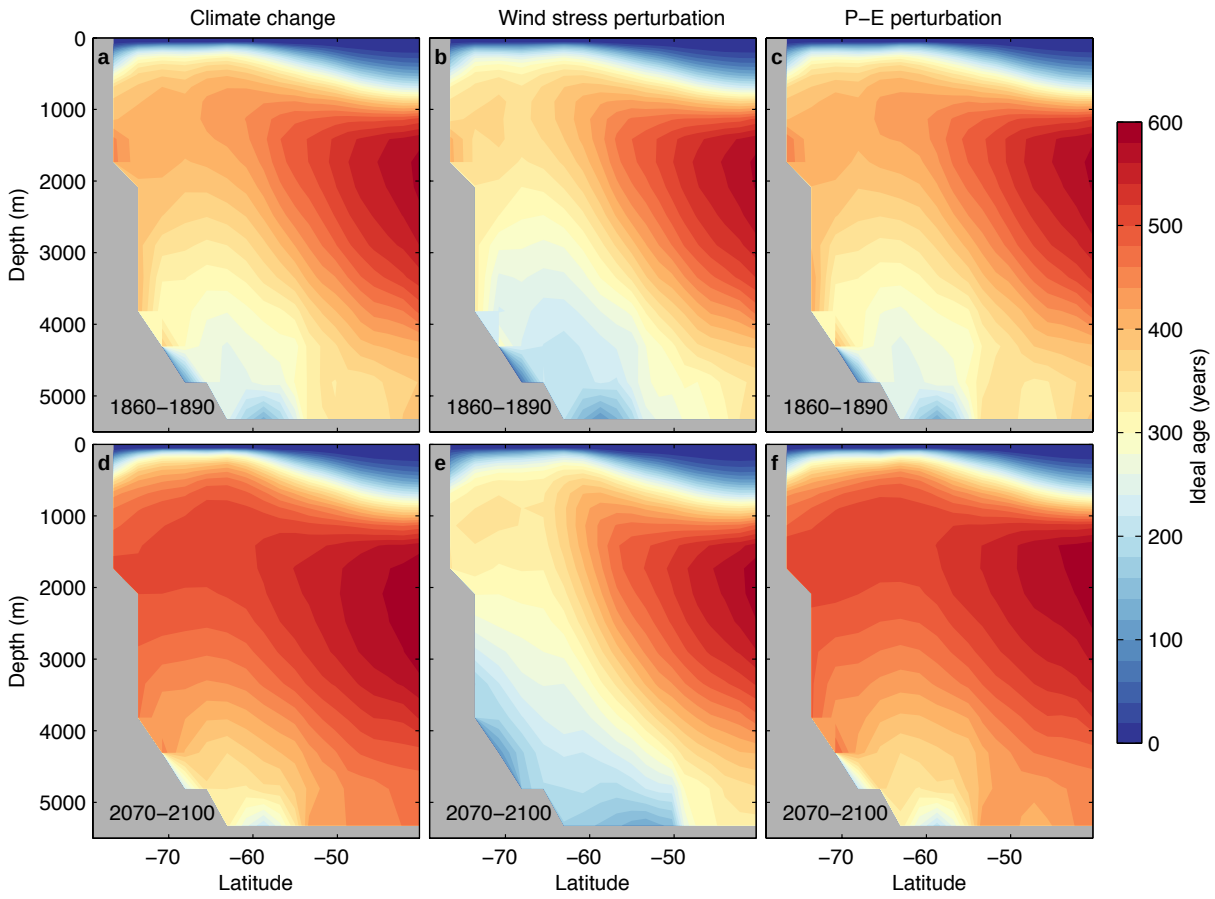

Figure S6: Zonal mean water age (since surface contact) in a depth versus latitude Southern Ocean profile for the CM2Mc model. Ensemble mean of three simulations shown for the 1860-1890 and 2070-2100 periods for the *Climate Change* (**a** and **d**, respectively), *Wind stress perturbation* (**b** and **e**) and *P-E perturbation* (**c** and **f**) experiments. The decrease in ventilation of intermediate and deep waters over 1860-2100 in the climate change experiments is not due to changes in wind stress, and hence must be explained by altered buoyancy fluxes. Changes in precipitation and evaporation south of 40°S alone cause a similar ventilation slowdown as that simulated under the full climate change forcing.

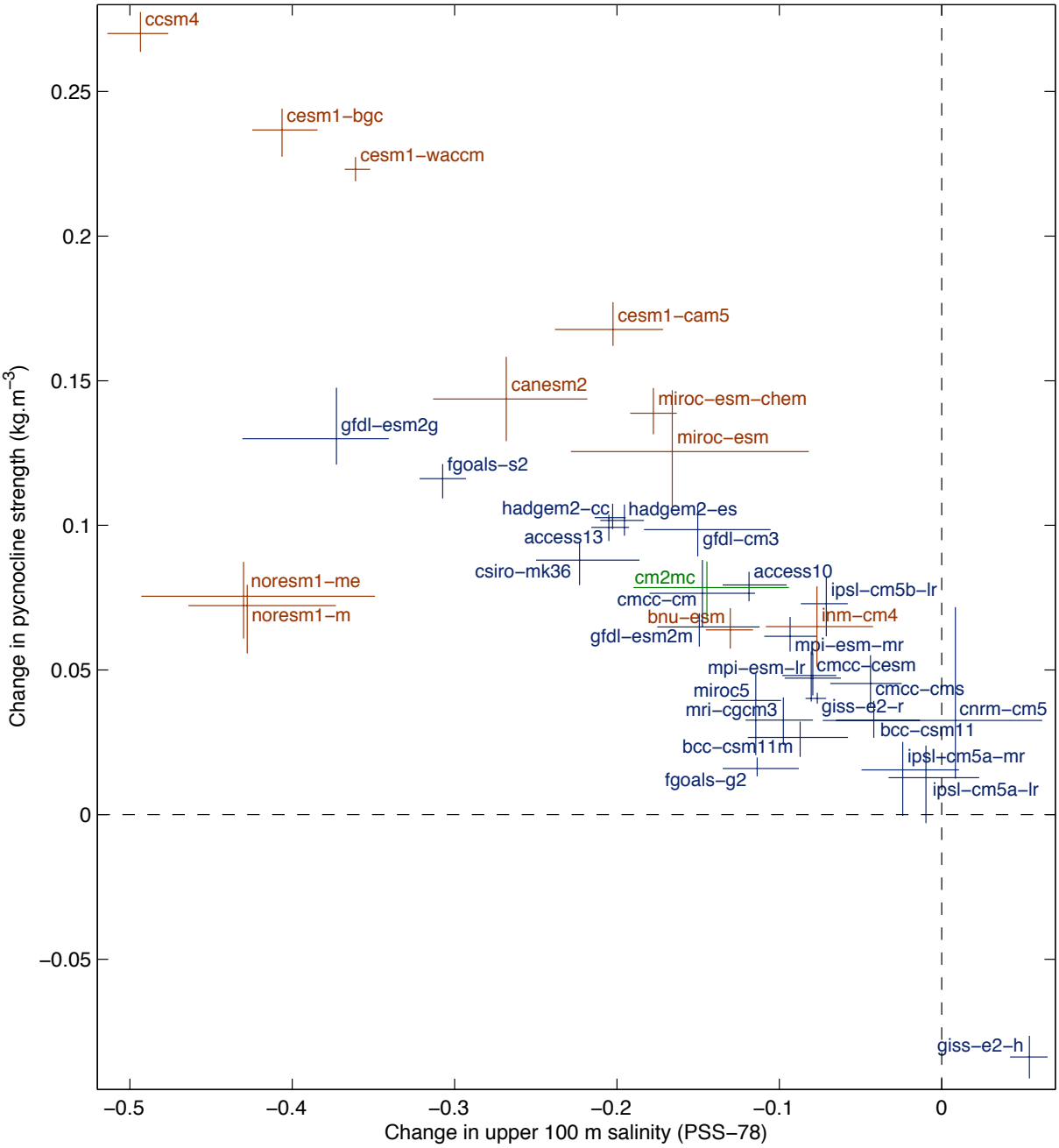

Figure S7: RCP8.5 changes and internal variability in southern polar ocean surface salinity and stratification in the CMIP5 model suite. Variables are annual averages over the region where the surface dynamic height relative to 1500 m is less than its minimum within Drake Passage, thus excluding both Antarctic Circumpolar Current and shelf waters. RCP8.5 changes (position of

crosses) refer to years 2050-2100 minus 1860-2005, and were corrected for drift by subtracting the linear pre-industrial control trends from the climate change time series. The range of unforced multidecadal variability is indicated by the vertical and horizontal bars, whose length is proportional to the maximum anomalies of all 50-year periods from the detrended pre-industrial control mean. Thus, RCP8.5 changes cannot be distinguished from unforced variability whenever these bars cross the origin, which is the case for the CNRM-CM5, IPSL-CM5A-LR and IPSL-CM5A-MR models only. Both convecting (blue) and non-convecting (brown) models are shown. The CM2Mc model ensemble is shown in green.

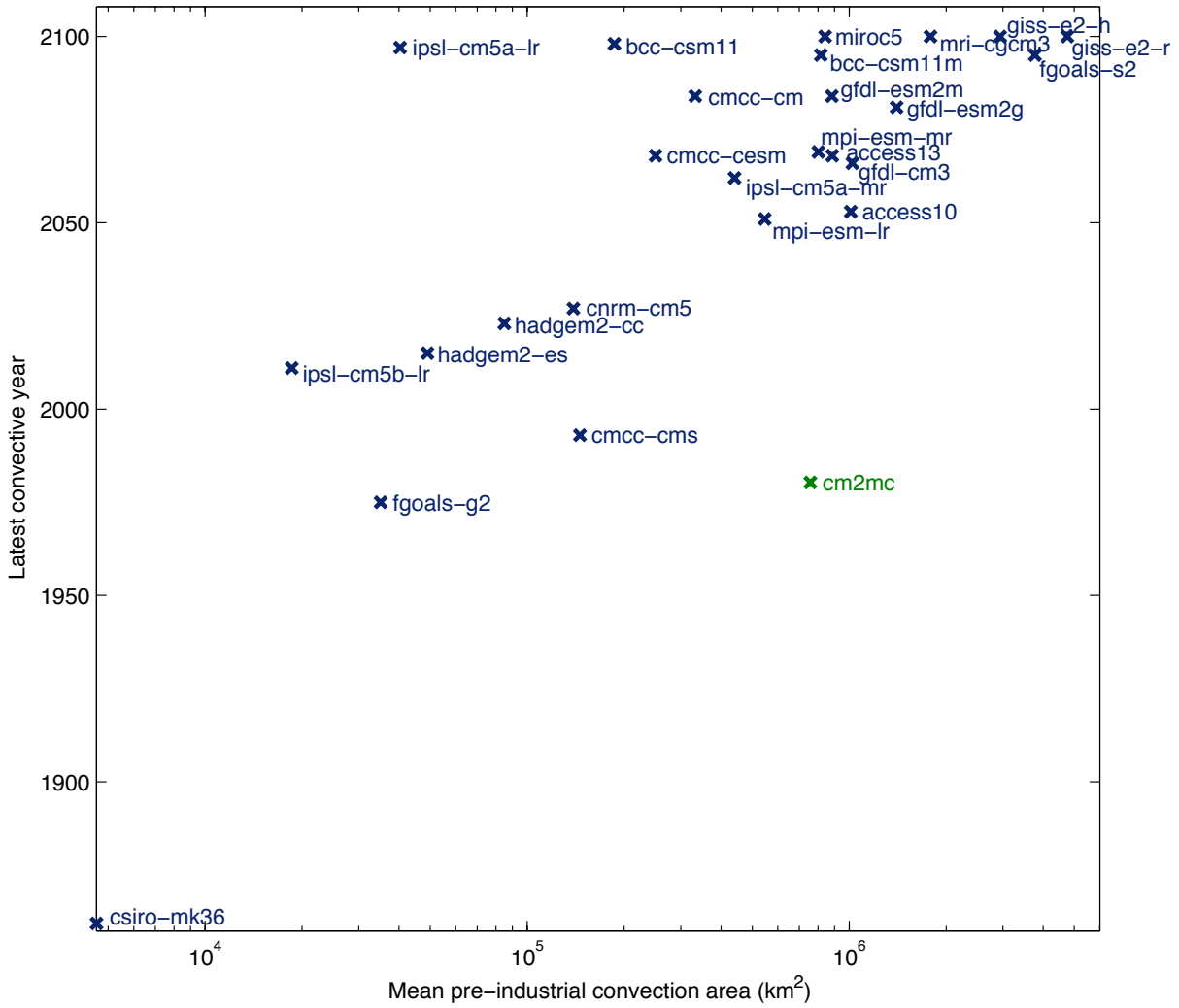

Figure S8: Latest convective year versus mean pre-industrial convection area in the 25 convecting CMIP5 models. Mean pre-industrial area is presented in log scale. The latest convective year corresponds to the last year of the climate change simulation (1860-2100) characterized by a convection area in excess of 100,000 km^2. Note that models with large convection areas tend to convect further in the 21st century. The three-member CM2Mc ensemble is shown in green.

Supplementary references:

31 Dunne, J. P. *et al*. GFDL's ESM2 global coupled climate-carbon Earth System Models. Part I: Physical formulation and baseline simulation characteristics. *J. Clim.* **25**, 6646-6665 (2012).

32 Martin, T., Adcroft, A. Parameterizing the fresh-water flux from land ice to ocean with interactive icebergs in a coupled climate model. *Ocean Model.* **34**, 111-124 (2010).

33 Large, W. G., McWilliams, J. C., Doney, S. C. Oceanic vertical mixing: a review and a model with a nonlocal boundary layer parameterization. *Rev. Geophys.* **32**, 363-403 (1994).

34 Bernardello, R. *et al*. Response of the ocean natural carbon storage to projected 21st century climate change. *J. Clim.* doi:10.1175/JCLI-D-13-00343.1, in press.

35 Meinshausen, M. *et al.* The RCP greenhouse gas concentrations and their extensions from 1765 to 2300. *Climatic Change* **109**, 213-241 (2011).

36 Delworth, T. L., Zeng, F. Simulated impact of altered Southern Hemisphere winds on the Atlantic meridional overturning circulation. *Geophys. Res. Lett.* **35**, L20708 (2008).

37 Yin, J. H. A consistent poleward shift of the storm tracks in simulations of 21st century climate. *Geophys. Res. Lett.* **32**, L18701 (2005).

38 Klinger, B. A., Marshall, J., Send, U. Representation of convective plumes by vertical adjustment. *J. Geophys. Res.* **101**, 18175-18182 (1996).

39 Rahmstorf, S. A fast and complete convection scheme for ocean models. *Ocean Model.* **101**, 9-11 (1993).

40 Hellmer, H. H. Impact of Antarctic ice shelf basal melting on sea ice and deep ocean properties. *Geophys. Res. Lett.* **31**, L10307 (2004).

41 Hellmer, H. H., Kauker, F., Timmermann, R., Determann, J., Rae, J. Twenty-first century warming of a large Antarctic ice-shelf cavity by a redirected coastal current. *Nature* **485**, 225-228 (2012).

42 Silva, T. A. M., Bigg, G. R., Nicholls, K. W. Contribution of giant icebergs to the Southern Ocean freshwater flux. *J. Geophys. Res.* **111**, C03004 (2006).

43 Bintanja, R., van Oldenborgh, G. J., Drijfhout, S. S., Wouters, B., Katsman, C. A. Important role for ocean warming and increased ice-shelf melt in Antarctic sea-ice expansion. *Nature Geosci.* **6,** 376-379 (2013).

44 Helm, K. P., Bindoff, N. L., Church, J. A. Changes in the global hydrological cycle inferred from ocean salinity. *Geophys. Res. Lett.* **37,** L18701 (2010).

45 Sen Gupta, A., Jourdain, N. C., Brown, J. N., Monselesan, D. Climate drift in CMIP5 models. *J. Clim.* **26**, 8597-8615 (2013).

46 Gaspar, P., Grégoris, Y., Lefevre, J-M. A Simple eddy kinetic energy model for simulations of the oceanic vertical mixing: tests at station Papa and Long-Term Upper Ocean Study site. *J. Geophys. Res.* **95**, 16179-16193 (1990).

47 Blanke, B., Delescluse, P. Variability of the tropical Atlantic Ocean simulated by a general circulation model with two different mixed-layer physics. *J. Phys. Oceanogr.* **23**, 1363-1388 (1993).

48 Kraus, E. B., Turner, J. S. A one-dimensional model of the seasonal thermocline II. The general theory and its consequences. *Tellus* **19**, 98-106 (1967).

49 Canuto, V. M., Howard, A., Cheng, Y., Dubovikov, M. S. Ocean turbulence. Part I: One-point closure model – momentum and heat vertical diffusivities. *J. Phys. Oceanogr.* **31**, 1413-1426 (2001).

50 Canuto, V. M., Howard, A., Cheng, Y., Dubovikov, M. S. Ocean turbulence. Part II: Vertical diffusivities of momentum, heat, salt, mass and passive scalars. *J. Phys. Oceanogr.* **32**, 240-264 (2002).

51 Thompson, L., Kelly, K. A., Darr, D., Hallberg, R. Buoyancy and mixed layer effects on the sea surface height response in an isopycnal model of the North Pacific. *J. Phys. Oceanogr.* **32**, 3657-3670 (2003).

52 Hallberg, R. In *Near-Boundary Processes and Their Parameterization: Proc. 'Aha Huliko'a Hawaiian Winter Workshop.* (Honolulu, HI, University of Hawaii at Manoa, 2003), pp. 187-203.

53 Mellor, G. L., Yamada, T. Development of a turbulence closure model for geophysical fluid problems. *Rev. Geophys.* **20**, 851-875 (1982).

54 Noh, Y., Kim, H. J. Simulations of temperature and turbulence structure of the oceanic boundary layer with the improved near-surface process. *J. Geophys. Res.* **104**, 15621-15634 (1999).

55 Noh, Y., Kang, Y. J., Matsuura, T., Iizuka, S. Effect of the Prandtl number in the parameterization of vertical mixing in an OGCM of the tropical Pacific. *Geophys. Res. Lett.* **32**, L23609 (2005).

56 Pacanowski, R. C., Philander, S. G. H. Parameterization of vertical mixing in numerical models of tropical oceans. *J. Phys. Oceanogr.* **11**, 1443-1451 (1981).

57 Oberhuber, J. M. Simulation of the Atlantic circulation with a coupled sea ice-mixed layer-isopycnal general circulation model. Part I: Model description. *J. Phys. Oceanogr.* **23**, 808-829 (1993).

58 Fetterer, F., Knowles, K., Meier, W., Savoie, M. Sea Ice Index. February 1979-2005. Boulder, Colorado USA: National Snow and Ice Data Center. (2002, updated 2009).

Assessing recent trends in high-latitude Southern Hemisphere climate

Julie. M. Jones[1]*, Sarah T. Gille[2], Hugues Goosse[3], Nerilie J. Abram[4], Pablo O. Canziani[5], Dan J. Charman[6], Kyle R. Clem[7], Xavier Crosta[8], Casimir de Lavergne[9], Ian Eisenman[2], Matthew H. England[10], Ryan L. Fogt[11], Leela M. Frankcombe[10], Gareth J. Marshall[12], Valérie Masson-Delmotte[13], Adele K. Morrison[14], Anaïs J. Orsi[13], Marilyn N. Raphael[15], James A. Renwick[7], David P. Schneider[16], Graham R. Simpkins[17], Eric J. Steig[18], Barbara Stenni[19], Didier Swingedouw[8] and Tessa R. Vance[20].

*Corresponding Author.

1. Department of Geography, University of Sheffield, Sheffield, S10 2TN, UK.

2. Scripps Institution of Oceanography, University of California San Diego, La Jolla, CA 92093, USA.

3. ELIC/TECLIM Université catholique de Louvain, Place Pasteur 3, 1348 Louvain-la-Neuve, Belgium.

4. Research School of Earth Sciences and Centre of Excellence for Climate System Science, The Australian National University, Canberra ACT 2601, Australia.

5. Unidad de Investigación y Desarrollo de las Ingenierías, Facultad Regional Buenos Aires, Universidad Tecnológica Nacional/CONICET, Argentina.

6. Department of Geography, College of Life and Environmental Sciences, University of Exeter, EX4 1RJ, UK.

7. School of Geography, Environment, and Earth Sciences, Victoria University of Wellington, Wellington, New Zealand, 6012.

8. Environnements et Paléoenvironnements Océaniques et Continentaux (UMR EPOC 5805), University of Bordeaux, Allée Geoffroy St Hilaire, 33615 Pessac, France.

9. Sorbonne Universités (Université Pierre et Marie Curie Paris 6)-CNRS-IRD-MNHN, LOCEAN Laboratory, F-75005 Paris, France.

10. ARC Centre of Excellence for Climate System Science, The University of New South Wales, Sydney, NSW 2052 Australia.

11. Department of Geography, Ohio University, Athens OH, 45701 USA.

12. British Antarctic Survey, High Cross, Madingley Road, Cambridge, CB3 0ET UK.

13. Laboratoire des Sciences du Climat et de l'Environnement, LSCE/IPSL, CEA-CNRS-UVSQ, Université Paris-Saclay, France.

14. Program in Atmospheric and Oceanic Sciences, Princeton University, 300 Forrestal Rd, Princeton, NJ, 08544, USA.

15. Department of Geography, University of California Los Angeles, 1255 Bunche Hall, Los Angeles CA 90095, USA.

16. National Center for Atmospheric Research, PO BOX 3000, Boulder, CO 80307-3000, USA.

17. Dept. Earth System Science, University of California, Irvine, Croul Hall, Irvine, CA 92697-3100, USA.

18. Department of Earth and Space Sciences, University of Washington, 70 Johnson Hall, Box 351310, Seattle, WA 98195, USA.

19. Department of Environmental Sciences, Informatics and Statistics, Ca' Foscari University of Venice, Italy, Via Torino 155, 30170 Venezia Mestre, Italy.

20. Antarctic Climate and Ecosystems Cooperative Research Centre, Private Bag 80, Hobart, Tasmania, Australia, 7001.

Abstract

Understanding the causes of recent climatic trends and variability in the high-latitude Southern Hemisphere is hampered by a short instrumental record. Here, we analyse recent atmosphere, surface ocean and sea-ice observations in this region and assess their trends in the context of palaeoclimate records and climate model simulations. Over the 36-year satellite era, significant linear trends in annual mean sea-ice extent, surface temperature and sea-level pressure are superimposed on large interannual to decadal variability. However, most observed trends are not unusual when compared with Antarctic paleoclimate records of the past two centuries. With the exception of the positive trend in the Southern Annular Mode, climate model simulations that include anthropogenic forcing are not compatible with the observed trends. This suggests that natural variability likely overwhelms the forced response in the observations, but the models may not fully represent this natural variability or may overestimate the magnitude of the forced response.

1. Introduction

The high latitude of the Southern Hemisphere (SH) is a highly complex and critically important component of the global climate system that remains poorly understood. The Antarctic Ice Sheet represents the greatest potential source of global sea level rise[1], and its response to climate change is a major source of uncertainty for future projections[2,3]. The Southern Ocean is important for its ability to uptake heat and carbon dioxide, and thereby mitigate human-induced atmospheric temperature and CO_2 rise[4,5,6,7,8]. Antarctic sea ice is important for its role in ocean-atmosphere exchange and provides an important climate feedback through its influence on albedo and atmospheric and oceanic circulation.

The leading mode of atmospheric circulation variability in the SH high latitudes is the Southern Annular Mode (SAM)[9]. It is a measure of the mid-to-high latitude atmospheric pressure gradient and reflects the strength and position of the westerly winds that circle Antarctica. This in turn impacts various aspects of Antarctic climate and controls the timing and distribution of rainfall received by the mid-latitude SH continents[10]. An almost equally important aspect of large-scale circulation variability in this region is the mid to high-latitude response to tropical variability, particularly the El Niño-Southern Oscillation (ENSO)[11].

Over recent decades, multiple changes have been observed in high-latitude SH climate. However, the brevity and sparse distribution of observational records poses a major challenge in understanding whether observed changes are anthropogenically forced or remain within the range of natural climate variability. We can improve our understanding of SH high latitude climate by combining information from instrumental, satellite, palaeoclimate and reanalysis data, along with climate model simulations. Here, we provide an assessment of recent changes in the atmosphere, ocean and sea ice systems of the southern high latitudes (south of 50°S), on timescales from decades to centuries. We describe SH climate trends using satellite information (1979-2014) and Antarctic station observations. These are compared with trends and multi-decadal variability from palaeoclimate data spanning the last 200 years, as well as control and forced climate simulations from the Fifth Climate Model Intercomparison Project (CMIP5)[12], to assess whether recent trends are unusual compared with natural variability. We conclude by identifying key knowledge gaps where strategically focussed research will improve understanding of the contribution of SH high latitudes to global climate variability and change.

2. Antarctic climate monitoring

Coordinated international efforts to monitor Antarctic climate began in the International Geophysical Year of 1957/58. However, few climate measurements are available over vast areas of the continent and the adjacent ice-shelves, sea ice and oceans. The advent of routine satellite sounder observations in 1979 revolutionised knowledge of climate over Antarctica and the surrounding oceans, although uncertainties remain due to satellite sensor changes[13]. More uncertain early satellite sea ice estimates extend back to 1972[14], with ongoing recovery of ice edge information for the 1964-1972 period[15,16]. Knowledge of recent sub-surface ocean trends remains more limited. The Argo profiling float program and conductivity-temperature-depth tags mounted on elephant seals have provided substantial numbers of subsurface ocean profiles only since 2004[7], and even now,

few ocean profiles are obtained within the sea-ice zone.

Antarctic annual mean climate trends over the 1979-2014 interval covered by satellite observations (Fig. 1, see Supplementary Fig. 1 for location map) are dominated by statistically significant ($p<0.05$) linear trends indicating: (1) an intensification of the mid-latitude westerly winds related to an increasing SAM index; (2) an overall sea surface temperature (SST) cooling, except in the southeast Indian Ocean sector, and in the Weddell, Bellingshausen and Amundsen Seas[17] (not visible in Fig. 1 due to sea-ice shading); (3) an overall expansion of sea ice, underpinned by a large increase in the Ross Sea sector, but partly offset by large decreases in the Amundsen-Bellingshausen sector, around the Antarctic Peninsula, and in the southeast Indian Ocean; (4) a strong surface air warming over the West Antarctic Ice Sheet and Antarctic Peninsula regions; and (5) surface air cooling above Adélie Land in East Antarctica. The surface air temperature (SAT) records from individual stations (inset panels in Fig. 1) demonstrate how considerable interannual to decadal variability underlies these long-term trends. In many cases, the annual-mean trends arise from strong trends in specific seasons (Supplementary Fig. 2).

Time series of summer anomalies in hemispherically averaged SST, zonal wind, and sea ice extent exhibit consistent multi-decadal variability since 1950[17], suggesting that recent changes in multiple variables are strongly coupled. Many of the observed changes in SH high-latitude climate can be related to changes in atmospheric circulation. Strengthening of the westerly winds associated with the positive SAM trend causes spatially coherent changes in surface air temperature over Antarctica[18], and in particular can account for the summer warming over the eastern Antarctic Peninsula[19,20]. Cooling of the surface ocean and warming of the subsurface ocean[21,22,23,24,25] throughout the Southern Ocean can also be partly attributed to a westerly wind-forced increase in northward Ekman transport of cold subantarctic surface waters. Summer trends in the SAM are distinct from natural variations[26], and are attributed to stratospheric ozone depletion, and the associated stratospheric cooling over Antarctica[10,27]. In addition, regional atmospheric circulation changes led to warming trends in winter and spring, distinct from the summertime warming associated with the SAM, particularly over the West Antarctic Ice Sheet (WAIS) and the western Antarctic Peninsula during the second half of the Twentieth Century[11,28,29,30,31,32]. However, in the last 10-15 years the rate of warming over the Peninsula has slowed markedly, in all seasons, but most strongly in summer (time series in Supplementary Fig. 2).

Regional atmospheric circulation changes are also a potential driver of the recent trends in Antarctic sea ice[33], in particular through the strengthening of the Amundsen Sea Low (ASL)[34]. Deepening of the ASL is linked to both changes in the SAM[35] and to atmospheric teleconnections with the tropical Pacific[11,29,34,36,37]. The ASL has intensified onshore warm air flow over the Amundsen-Bellingshausen sector, and colder air flow offshore in the Ross Sea sector[38]. This has contributed to the characteristic dipole of contrasting SAT and sea-ice concentration changes between the Ross Sea and the Amundsen-Bellingshausen/Antarctic Peninsula regions[11,36,39,40]. An additional mechanism that may partly explain the overall increasing trend in Antarctic sea-ice extent (SIE) involves the increased meltwater input, which has contributed to freshening of the Southern Ocean (e.g.[41]), stabilization of the water column[42] and thus potentially a reduction of the vertical ocean heat flux, enabling more prevalent sea ice formation[43,44].

Changes in SAT, atmospheric and ocean circulation have also affected the ice sheet itself, through surface melting of ice shelves around the Antarctic Peninsula[45], and melting of ice shelves from below owing to the intrusion of warm circumpolar deep water onto the continental shelf[46]. The importance of the latter process is particularly evident along the margin of the WAIS[47,48,49] and is associated with regional atmospheric circulation changes forced by teleconnections from the tropics[48,50].

The numerous interconnections between changes in the SH high latitude atmosphere-ocean-sea ice systems provide strong feedbacks that can amplify initial perturbations related for instance to winds or modifications in the hydrological cycle[42,51,52]. These connections also demonstrate the need to assess the significance and impacts of SH high latitude climate changes in a holistic way, using multiple variables.

3. Historical records and natural archives

To place these recent observed trends into a longer-term context, we compiled observational records of SAT longer than 55 years as well as proxy records for SAT, SST and sea ice, extracted from annually to multi-annually resolved ice and marine sediment cores, spanning the last 200 years (see Supplementary Table 1 for details of the datasets used, and Methods for data compilation). Datasets were grouped into four different sectors, which were designed to group observational and proxy records with similar patterns of variability while also working within the constraints of data availability. Our regions are comprised of three near-coastal zones spanning: (1) the Antarctic Peninsula region including the Bellingshausen and Scotia Seas, (2) the West Antarctic Ice Sheet and the Ross Sea region, and (3) a broad region spanning coastal East Antarctica and incorporating the adjacent oceans and the Weddell Sea. The final region is defined over the inland East Antarctic Plateau above 2000 m elevation (4). The separation of coastal from inland regions reflects known differences in atmospheric transport dynamics pathways for weather events that impact inland versus coastal sites in Antarctica[53]. Fig. 2 shows these sectors and the data available for this synthesis, and highlights the paucity of climate information currently available for many parts of Antarctica.

3.1. Antarctic Peninsula sector

Of the four sectors, the Antarctic Peninsula has the longest observed SAT record (1903-present); prior to the late 1940s, SAT is only available from the single Orcadas station, located northeast of the Peninsula itself. Instrumental data, proxy palaeotemperature records (ice cores and a moss bank core), and borehole temperature inversions show that the Antarctic Peninsula warming trend (Fig. 1) is part of a longer-term regional warming trend (Fig. 2a). The correspondence between instrumental and proxy data and between multiple proxy data sources may be stronger here than for any other region, suggesting this is a robust context for the late 20th century temperature trend. The James Ross Island (JRI) ice core suggests that local warming began in the 1920s and has been statistically-significant ($p<0.1$) since the 1940s[54]. Ice cores from the Gomez and Ferrigno sites and a moss bank core demonstrate that the 20th century rise in SAT on the northern Peninsula also extends south to the southwest Antarctic Peninsula[55,56] and was accompanied by increases in snow

accumulation[57,58] and increased biological productivity, suggesting temperature changes were likely year-round. Antarctic Peninsula warming has been related to intensification of the circumpolar westerlies in austral summer and autumn[19], associated deepening of the Amundsen Sea Low, and to central tropical Pacific warming in austral autumn, winter and spring[11].

None of the most recent 36-year trends in the proxy SAT records are unprecedented relative to trends of the same length from earlier portions of the palaeoclimate archives (Methods, Supplementary Fig. 3a). The most recent 100-year trends do exceed the upper 95% level of all earlier 100-year trends in three of the Antarctic Peninsula ice core isotope records (JRI, Gomez and Ferrigno; Supplementary Fig. 3c); for the JRI core the most recent 100-year warming trend falls within the upper 0.3% of the distribution of all 100-year trends over the last 2000 years[54,59].

Two marine SST proxy records from the northern Antarctic Peninsula show a warming trend over the 20th century that was most prominent over the ~1920s to 1950s (Fig. 2a). A cooling trend in the most recent decades of the proxy stack appears to be of similar magnitude to earlier episodes of decadal-scale variability. In this sector, sea-ice information is derived from one historical record, three ice core chemical records[60] and two marine diatom records spanning the Bellingshausen Sea and Scotia Sea/northern Weddell Sea. They depict a regionally coherent sea-ice decrease from the 1920s to the 1950s, coincident with proxy evidence for SST increases. The proxy composite does not clearly capture the Bellingshausen sea-ice decline observed by satellites since 1979, although individual studies have demonstrated that this recent observed sea-ice decline is embedded within a longer-term decreasing trend that persisted through the 20th century and was strongest at mid-century[61,62].

3.2. West Antarctica

In West Antarctica, SAT observations[28,30], a borehole temperature profile[63,64], and ice core water stable isotope records[65] all depict a consistent, statistically significant warming trend beginning in the 1950s. These trends are greatest in winter and spring, and closely associated with the rapid decline in sea ice observed in the Amundsen-Bellingshausen Seas[40,65,66]. The annual mean SAT trend over West Antarctica may be among the most rapid warming trends of the last few decades anywhere on Earth (2.2±1.3^{o}C increase during 1958-2010 at Byrd Station, mostly due to changes in austral winter and spring)[30,67]. Nevertheless, the natural decadal variability in this region is also large, owing to the strong variability of the ASL[68], amplified by teleconnections with the tropical Pacific also during winter and spring[11,29,69]. This differs markedly from the situation on the Antarctic Peninsula, where the summertime trends occur against a background of relatively small inter-annual variability[31]. As a consequence, the large recent trends cannot yet be demonstrated to be outside the range of natural variability (e.g. 100-year trend analysis in Supplementary Fig. 3c). An analysis of more than twenty ice core records from West Antarctica[65] concluded that the most recent decades were likely the warmest in the last 200 years, but with low confidence because of a similar-magnitude warming event during the 1940s associated with the major 1939-1942 El Niño event[70].

At present, no high-resolution reconstructions of SST or SIE are available for the Amundsen-Ross Sea sector to give context to the observed satellite-era trends there.

3.3. Coastal East Antarctica

No recent multi-decadal trend emerges from the compilation of SAT observations and proxy records in coastal East Antarctica. Recent fluctuations lie within the decadal variability documented from ice core water isotope records, and recent 36-year and 100-year trends remain within the 5-95% range of earlier trends within each record (Supplementary Fig. 3a, c). The only available long-term borehole temperature reconstruction suggests a recent warming trend. This apparent contradiction may arise from spatial gradients and differences in recent temperature trends (e.g. Fig. 1) across this geographically extensive but data sparse sector. Indeed, only seven meteorological stations, two ice core water isotope records of sufficient resolution (see methods) and one 100-year borehole profile occupy a longitudinal region spanning 150°E to 40°W (Fig. 2a). Networks of isotope records from shallow ice cores (not compiled in this study due to their limited temporal coverage) do provide evidence for a statistically significant increasing SAT trend in the past 30-60 years over the Fimbul Ice Shelf, East Antarctica[71] and over Dronning Maud Land[72], despite no observed warming at the nearby Neumayer station[71,72].

The single SST proxy record available from off the coast of Adélie Land[73] (Fig. 2) shows a strong increase post 1975, and, despite considerable decadal variability, the final 36-year trend exceeds the 95% range of trends in the full record (Supplementary Fig. 3a, c). Satellite observations, showing a regional SIE increase across this sector since 1979, are not mirrored by proxy records, which suggest an overall sea-ice decline since the 1950s[74], overlaid by strong decadal variability (Fig. 2). This also highlights the challenges in interpretation of sea-ice proxies, which can be sensitive to variations in sea-ice thickness, duration or local dynamics. For example, near the Mertz glacier sea-ice proxy records spanning the past 250 years depict large multi-decadal variations that are attributed to iceberg calving events and are comparable to, or larger than, the most recent 36-year or 100-year trends[73] (Supplementary Fig. 3b-c).

3.4. East Antarctic Plateau

The stable isotope records for the East Antarctic Plateau do not show statistically significant trends in the final 36 years of their record (Supplementary Figure 3a), unlike the observed SAT for the region (Fig. 1 inset b). Comparison of Figs. 1 and 2 indicates that the East Antarctic Plateau stable water isotope records come from locations spanning differing temperature trends in Fig. 1. The Plateau Remote core on the central Plateau is characterised by large decadal variability, and the most recent 100-year trend remains well within the 5-95 % range of earlier trends. Towards the margins of the East Antarctic Plateau, the EDML and Talos Dome ice cores display recent 100-year warming and cooling trends, respectively, that are significant with respect to earlier 100-year trends in these cores (Supplementary Fig. 3c). Temperature records from borehole inversions[75], which cannot resolve decadal variability, also show evidence for modest temperature increases on the Dronning Maud Land side of the East Antarctic Plateau during the late 20th Century, with warming apparently beginning earlier closer to the coast. The differing characteristics of long-term temperature variability and trends at sites across the Antarctic Plateau again

highlight the importance of increasing the spatial coverage of proxy records from this data sparse region.

3.5 The Southern Annular Mode

The history of the SAM over the last 200 years has been assessed in a number of previous reconstructions using syntheses of station observations[26,76,77] and palaeoclimate networks[18,78,79] (not shown). Reconstructions from station data display strong decadal variability and season-specific trends. The summer SAM exhibits the strongest post-1960s trend, which is assessed as unusual compared to trends in the earlier part of the century[26]. A summer SAM index reconstructed from mid-latitude tree rings also indicates that the recent positive phase of the SAM is unprecedented in the context of at least the past 600 years[79]. Similarly, an annual average SAM index reconstruction based on a network of temperature-sensitive palaeoclimate records spanning Antarctica and southern South America indicates that the SAM is currently in its most positive state over at least the last 1000 years[18]. Over the last 200 years, SAM index reconstructions display a steady[79] or declining[18] SAM index since the early 1800s, reaching a minimum in the early to mid-20th century[18,79], before commencement of the positive SAM trend that is seen in observations (Fig. 1).

4. Simulated Antarctic climate trends and variability

The satellite observations and longer historical and proxy-based climate records reviewed in preceding sections reveal significant regional and seasonal climatic trends of both positive and negative signs and with a range of amplitudes, together with substantial decadal to centennial variability in the high-latitude SH. To further assess whether recent climate variations may be attributed to externally forced changes, or can be explained by unforced multidecadal variability, we now examine statistics of 36-year trends in model simulations from CMIP5[12] and compare these to observed trends over the 1979-2014 period.

Trend distributions from pre-industrial control simulations provide an estimate of internally generated variability under fixed external forcing. The CMIP5 climate models display large internal multi-decadal variability in the high southern latitudes (Fig. 3), with satellite-era observational trends remaining within the 5-95% range of simulated internal variability for the annual means of all four examined variables – SIE, SST, SAT and the SAM index (Fig. 3a-d). Based on this comparison, the null hypothesis stating that the observed 1979-2014 trends are explained by internal climate system variability alone cannot be rejected at the 90% confidence level, with the underlying assumption that the simulated multi-decadal variability is of the correct magnitude. However, a seasonal breakdown of observed and simulated trends reveals that observed SAM trends in summer and autumn exceed the 95% level of control variability (Supplementary Fig. 5), consistent with a dominant role of stratospheric ozone depletion in the recent shift toward positive SAM[10,27]. The summer SAT trend also stands out as anomalously negative against the modelled preindustrial variability (Supplementary Fig. 5).

In order to estimate the combined influence of the intrinsic variability of the SH climate system and the response to known historical – natural and anthropogenic – forcings, we next compare statistics of modelled 1979-2014 trends in externally-forced simulations against observations (see Methods). With this measure of multi-model variability, the observed trends in SIE, SST and SAT appear only marginally consistent with the CMIP5 ensemble of simulated trajectories (Fig. 3a-c), in agreement with previous analyses[44,80,81]. For instance, only 15% of model simulations exhibit sea-ice expansion over 1979-2014, and only 3% a larger SIE increase than that observed by satellites. Similarly, only 8% of models predict a negative trend in average SAT south of 50°S. In contrast, the likelihood of positive trends in the SAM index is increased in the externally forced simulations compared to unforced simulations, resulting in an improved agreement with the observed SAM trend (Fig. 3d).

Thus the statistics of 36-year trends are consistent with the hypothesis that anthropogenic forcing contributes to the recent positive SAM trend. Our comparisons also highlight the mismatch between CMIP5 historical simulations and observed recent trends in SIE and surface temperatures. We suggest that internal variability alone is unlikely to be sufficient to explain this mismatch. Indeed, the recent observed expansion of Antarctic sea ice and average surface cooling south of 50^{o}S stand out as rare events when benchmarked against the ensemble of simulated trends for the 1979-2014 period (Fig. 3a-c).

Deficiencies in the model representation of SH climate are likely contributors to the disagreement between observations and forced climate simulations[82,83]. Inaccurate or missing Earth system feedbacks in the CMIP5 simulations, such as the absence of the freshwater input due to ice-sheet mass loss, and unresolved physical processes, related to sea-ice rheology, thin ice properties, stratospheric processes, katabatic winds, ocean-ice shelf interactions and sub-grid-scale ocean processes, can bias both the simulated internal variability and the model response to external forcing. For example, subsurface ocean warming around Antarctica in response to strengthening of the SH westerly winds has been found to occur at twice the magnitude in a high-resolution ocean model compared with coarser CMIP5 simulations[22]. Comparisons of CMIP5 last millennium simulations against palaeoclimate data have also shown deficiencies in the SH, suggesting that CMIP5 models may underestimate the magnitude of unforced variability in the SH or overestimate the SH climate response to external forcing[84]. Understanding the missing processes and the relationships between these processes and model skill will be crucial for future model developments in order to improve the model ability to simulate variability of the SH high-latitude climate and its response to forcing.

Within these limitations in the representation of SH high-latitude climate in the current generation of climate models, the available CMIP5 model output suggests that the observed and simulated 36-year (1979-2014) trends are not large enough to determine whether they are externally forced or merely a reflection of internal variability (Fig. 3a-d). Similarly, the most recent 36-year trends in the palaeoclimate records reviewed here are also too short to be considered unusual relative to the range of earlier 36-year trends in the last 200 years (Supplementary Fig. 3).

We further explore this by calculating the required duration of anthropogenically-driven trends under the RCP8.5 scenario for SH high-latitude climate variables to emerge as

statistically distinct from pre-industrial control variability. In a perfect model framework, this could be understood as estimating how long SH observations may need to be sustained before on-going trends can be definitively attributed to anthropogenic climate change (Fig. 3e-h and Table 1).

For each model and variable, we assess whether the simulated trend starting in 1979 falls outside of the matching 5-95% range of preindustrial variability and we calculate trends of length between 36 years (1979-2014) and 122 years (1979-2100). Our analysis reveals that, in 2015, over half of the models already simulate "unusual" post-1979 trends in SAT and the SAM. For SST, 50% of models have linear trends that emerge above unforced variability by 2021 (43-year trends), and for SIE the majority of CMIP5 models do not display trends emerging above the 95% significance level (relative to the preindustrial distribution) until 2031 (i.e. 53-year trends). For a trend emergence threshold of more than 90% of all CMIP5 models, trends do not emerge until between 2044 (66-year trends for SAM) and 2098 (120-year trends for SIE). Our results for the time of emergence of linear trends are in agreement with an earlier assessment using a different methodology[85], suggesting that the mid to high SH latitudes are among the last regions where the signal of anthropogenic forcing will be sufficiently large to differentiate it from the range of natural variability. These CMIP5-based estimates may in fact underestimate the true length of time required for statistically distinct trends to emerge, if CMIP5 models underestimate the magnitude of internal variability or overestimate the forced climate response. Hence, notwithstanding known limitations in CMIP5 models, our analysis suggests that 36-years of observations are simply insufficient to interrogate and attribute trends in SH high latitude surface climate.

5. Discussion

Climate change and variability over the high latitudes of the SH are characterized by strong regional and seasonal contrasts for all the variables investigated here. This is valid at interannual to decadal timescales, as illustrated in instrumental observations, as well as on longer time scales, as indicated in proxy-based reconstructions. The most unequivocal large-scale change over recent decades is the increase of the SAM index[19] and the freshening and subsurface warming of the ocean[23,24,41]. Regionally, a large warming has been observed over the Antarctic Peninsula and West Antarctic regions across the last 50 years. SIE has decreased in the Amundsen-Bellingshausen Seas while it has increased in the Ross Sea sector since 1979.

The large multi-decadal variations seen in high-resolution proxy-based reconstructions of temperature and SIE also have clear regional contrasts. Some estimates suggest common signals over the whole Southern Ocean, such as the decrease of the ice extent between the 1950s and the late 1970s deduced from whaling records (e.g.[86,87,88]), but this remains to be confirmed by the analysis of additional observations. The longer records independently support the conclusion that most of the recent changes for any single variable largely result from natural variability, and are not unprecedented over the past two centuries. This is consistent with results from state-of-the-art climate models showing that, except for the SAM index, most recent changes remain in the range of large-scale simulated internal variability. When analysing specifically the 1979-2014 period, including forced changes and internal variability, models struggle to track the observed trends in SST, SAT

and sea-ice cover. This suggests that either a singular event associated with internal variability has been able to overwhelm the forced response in observations, or that CMIP5 models overestimate the forced response (potentially partly due to key processes missing in the models), or a combination of both.

Recent observations and process understanding of the atmosphere, sea ice, ocean and ice sheets suggest strong coupling, which means that investigations need to encompass and understand the dynamics of the whole climate system. Statistics independently applied to a few large-scale metrics may not allow a robust comparison between observed and simulated trends. Regional and seasonal complexity[89] as well as physical relationships between different climate variables must be taken into account to evaluate the overall consistency of observed and modelled time-evolving climate states, and to identify caveats. We advocate process-oriented studies in which the primary mechanisms behind modelled behaviour are identified and their plausibility evaluated against available observations and theory.

In particular, the accelerating melting and calving of Antarctic ice shelves[46,90,91] could have a pronounced influence on the recent and future evolution of the high-latitude Southern Ocean[41,43,92-94]. Understanding and quantifying the role of changing glacial discharge in past and on-going climatic trends is an important unresolved question requiring attention.

To improve the sampling of forced and natural variability for the recent period, we also emphasize the importance of considering multiple models, as well as multiple realizations of different models. In this sense large ensembles, such as those recently released by some modelling groups[95], are particularly useful for improving estimates of internal variability compared with forced signals.

Atmospheric reanalyses are strongly dependent on the prescribed surface boundary conditions that are particularly uncertain before the 1970s in the Southern Ocean[96] and therefore have limited skills prior to the satellite era. Alternative approaches involve assimilation methods using proxy records and climate simulations in order to best reconstruct the past state of the Antarctic atmospheric circulation. Coupled ocean – sea ice – atmosphere reanalysis[97], with specific attention to the high latitudes of the Southern Ocean, should thus be a target for the future. Preliminary studies have demonstrated the feasibility of this approach for ensuring the consistency between the various components of the system and the study of their interactions[98].

Our synthesis has emphasized that less than 40 years of instrumental climate data is insufficient to characterize the variability of the high southern latitudes or to robustly identify an anthropogenic contribution, except for the changes in the SAM. Although temperature changes over 1950-2008 from the average of individual stations have been attributed to anthropogenic causes[99], only low confidence can be assigned due to observational uncertainties[100] and large-scale decadal and multidecadal variability. Detection and attribution studies depend on the validity of estimates of natural variability from climate model simulations. This is particularly the case for variables such as Antarctic sea ice which have problematic representation in climate models[36], and short observational time series from which to estimate real multi-decadal variability. The strong regional variability on all time scales implies that the sparsity of observations and proxy data is a

clear limitation, especially in the ocean, and that averaging climate properties over the entire Antarctic or Southern Ocean potentially aliases the regional differences.

The Antarctic climate system is strongly coupled, and future investigations need to combine information from different climate variables to identify the causes and mechanisms driving SH high-latitude climate variations. Process studies are essential to this task, along with a continued effort to maintain current observations from stations and satellites, and to expand the observational network in undocumented areas. The rescue of historical data is also critical to obtain a longer perspective. New high-resolution proxy data should be collected, both by expanding existing data types (e.g. lake sediments and deep sea sediments) and by investing in new records such as moss banks. Improved spatial coverage of ice core records and a requirement for a minimum suite of information from these archives (e.g. accumulation, water isotopes, borehole temperatures) are desirable, together with multiple records allowing improvement of the signal-to-noise ratio. Improved calibration of these proxy records (e.g. water stable isotopes against temperature) is critical for the uncertainties associated with past temperature reconstructions. Progress is expected from the use of historical data, but also through improved proxy modelling; for example by incorporating water stable isotopes in high-resolution atmospheric models and quantifying post-deposition effects. Not least important is the use of non-linear statistical analysis tools to improve the statistical analysis of observations and proxy data as well as model output evaluation. Gathering, utilising, combining, and improving the interpretation of data from all available sources are imperative to understand recent climate changes in this data sparse, but climatically important, region.

References

1 Church, J. A. *et al*. Sea Level Change. In: *Climate Change 2013: The Physical Science Basis.Contribution of Working Group I to the Fifth Assessment Report of the Intergovernmental Panel on Climate Change* (Stocker, T. F. et al. (eds)) (Cambridge University Press, Cambridge, United Kingdom, and New York, USA, 2013).

2 Bindschadler, R. A. *et al.* Ice-sheet model sensitivities to environmental forcing and their use in projecting future sea level (the SeaRISE project). *Journal of Glaciology* **59**, 195-224 (2013).

3 Ritz, C. *et al.* Potential sea-level rise from Antarctic ice-sheet instability constrained by observations. *Nature* **528**, 115-118 (2015).

4 Majkut, J. D. *et al.* An observing system simulation for Southern Ocean carbon dioxide uptake. *Philosophical Transactions of the Royal Society a-Mathematical Physical and Engineering Sciences* **372**, 20130046 (2014).

5 Landschutzer, P. *et al.* The reinvigoration of the Southern Ocean carbon sink. *Science* **349**, 1221-1224 (2015).

6 Rhein, M., et al. Observations: Ocean. In: In: *Climate Change 2013: The Physical Science Basis.Contribution of Working Group I to the Fifth Assessment Report of the Intergovernmental Panel on Climate Change* (Stocker, T. F. et al. (eds)) (Cambridge University Press, Cambridge, United Kingdom, and New York, USA, 2013).

7 Roemmich, D. *et al.* Unabated planetary warming and its ocean structure since 2006. *Nature Climate Change* **5**, 240-245 (2015).

8 Levitus, S. *et al.* World ocean heat content and thermosteric sea level change (0-2000 m), 1955-2010. *Geophysical Research Letters* **39**, doi:10.1029/2012gl051106 (2012).

9 Thompson, D. W. J. & Wallace, J. M. Annular modes in the extratropical circulation. Part I: Month-to-month variability. *Journal of Climate* **13**, 1000-1016 (2000).

10 Thompson, D. W. J. *et al.* Signatures of the Antarctic ozone hole in Southern Hemisphere surface climate change. *Nature Geoscience* **4**, 741-749 (2011).

11 Ding, Q., Steig, E. J., Battisti, D. S. & Kuettel, M. Winter warming in West Antarctica caused by central tropical Pacific warming. *Nature Geoscience* **4**, 398-403 (2011).

12 Taylor, K. E., Stouffer, R. J. & Meehl, G. A. An overview of CMIP5 and the experiment design. *Bulletin of the American Meteorological Society* **93**, 485-498 (2012).

13 Eisenman, I., Meier, W. N. & Norris, J. R. A spurious jump in the satellite record: has Antarctic sea ice expansion been overestimated? *Cryosphere* **8**, 1289-1296 (2014).

14 Cavalieri, D. J., Parkinson, C. L. & Vinnikov, K. Y. 30-Year satellite record reveals contrasting Arctic and Antarctic decadal sea ice variability. *Geophysical Research Letters* **30**, doi:10.1029/2003gl018031 (2003).

15 Meier, W. N., Gallaher, D. & Campbell, G. G. New estimates of Arctic and Antarctic sea ice extent during September 1964 from recovered Nimbus I satellite imagery. *Cryosphere* **7**, 699-705 (2013).

16 Gallaher, D. W., Campbell, G. G. & Meier, W. N. Anomalous Variability in Antarctic Sea Ice Extents During the 1960s With the Use of Nimbus Data. *Ieee Journal of Selected Topics in Applied Earth Observations and Remote Sensing* **7**, 881-887 (2014).

17 Fan, T., Deser, C. & Schneider, D. P. Recent Antarctic sea ice trends in the context of Southern Ocean surface climate variations since 1950. *Geophysical Research Letters* **41**, 2419-2426 (2014).

18 Abram, N. J. *et al.* Evolution of the Southern Annular Mode during the past millennium. *Nature Climate Change* **4**, 564-569 (2014).

19 Thompson, D. W. J. & Solomon, S. Interpretation of recent Southern Hemisphere climate change. *Science* **296**, 895-899 (2002).

20 Marshall, G. J. Half-century seasonal relationships between the Southern Annular Mode and Antarctic temperatures. *International Journal of Climatology* **27**, 373-383 (2007).

21 Sen Gupta, A. & England, M. H. Coupled ocean-atmosphere-ice response to variations in the Southern Annular Mode. *Journal of Climate* **19**, 4457-4486 (2006).

22 Spence, P. *et al.* Rapid subsurface warming and circulation changes of Antarctic coastal waters by poleward shifting winds. *Geophysical Research Letters* **41**, 4601-4610, doi:10.1002/2014gl060613 (2014).

23 Gille, S. T. Decadal-scale temperature trends in the Southern Hemisphere ocean. *Journal of Climate* **21**, 4749-4765 (2008).

24 Schmidtko, S., Heywood, K. J., Thompson, A. F. & Aoki, S. Multidecadal warming of Antarctic waters. *Science* **346**, 1227-1231 (2014).

25 Ferreira, D., Marshall, J., Bitz, C. M., Solomon, S. & Plumb, A. Antarctic Ocean and Sea Ice Response to Ozone Depletion: A Two-Time-Scale Problem. *Journal of Climate* **28**, 1206-1226 (2015).

26 Fogt, R. L. *et al.* Historical SAM Variability. Part II: Twentieth-Century Variability and Trends from Reconstructions, Observations, and the IPCC AR4 Models. *Journal of Climate* **22**, 5346-5365 (2009).

27 Gillett, N. P. & Thompson, D. W. J. Simulation of recent Southern Hemisphere climate change. *Science* **302**, 273-275 (2003).

28 Steig, E. J. *et al.* Warming of the Antarctic ice-sheet surface since the 1957 International Geophysical Year. *Nature* **457**, 459-462(2009).

29 Ding, Q., Steig, E. J., Battisti, D. S. & Wallace, J. M. Influence of the Tropics on the Southern Annular Mode. *Journal of Climate* **25**, 6330-6348 (2012).

30 Bromwich, D. H. *et al.* Central West Antarctica among the most rapidly warming regions on Earth. *Nature Geoscience* **6**, 139-145 (2013).

31 Ding, Q. & Steig, E. J. Temperature Change on the Antarctic Peninsula Linked to the Tropical Pacific. *Journal of Climate* **26**, 7570-7585 (2013).

32 Clem, K. R. & Fogt, R. L. South Pacific circulation changes and their connection to the tropics and regional Antarctic warming in austral spring, 1979-2012. *Journal of Geophysical Research-Atmospheres* **120**, 2773-2792 (2015).

33 Holland, P. R. & Kwok, R. Wind-driven trends in Antarctic sea-ice drift. *Nature Geoscience* **5**, 872-875 (2012).

34 Raphael, M. *et al.* The Amundsen Sea Low: Variability, Change and Impact on Antarctic Climate. *Bulletin of the American Meteorological Society* **97**, 111-121 (2016).

35 Turner, J., Phillips, T., Hosking, J. S., Marshall, G. J. & Orr, A. The Amundsen Sea low. *International Journal of Climatology* **33**, 1818-1829 (2013).

36 Turner, J., Hosking, J. S., Bracegirdle, T. J., Marshall, G. J. & Phillips, T. Recent changes in Antarctic Sea Ice. *Philosophical Transactions of the Royal Society a-Mathematical Physical and Engineering Sciences* **373** (2015).

37 Fogt, R. L. & Wovrosh, A. J. The Relative Influence of Tropical Sea Surface Temperatures and Radiative Forcing on the Amundsen Sea Low. *Journal of Climate* **28**, 8540-8555 (2015).

38 Hosking, J. S., Orr, A., Marshall, G. J., Turner, J. & Phillips, T. The Influence of the Amundsen-Bellingshausen Seas Low on the Climate of West Antarctica and Its Representation in Coupled Climate Model Simulations. *Journal of Climate* **26**, 6633-6648 (2013).

39 Stammerjohn, S. E., Martinson, D. G., Smith, R. C., Yuan, X. & Rind, D. Trends in Antarctic annual sea ice retreat and advance and their relation to El Nino-Southern Oscillation and Southern Annular Mode variability. *Journal of Geophysical Research-Oceans* **113**, doi:10.1029/2007jc004269 (2008).

40 Schneider, D. P., Deser, C. & Okumura, Y. An assessment and interpretation of the observed warming of West Antarctica in the austral spring. *Climate Dynamics* **38**, 323-347 (2012).

41 Rye, C. D. *et al.* Rapid sea-level rise along the Antarctic margins in response to increased glacial discharge. *Nature Geoscience* **7**, 732-735 (2014).

583 42 de Lavergne, C., Palter, J. B., Galbraith, E. D., Bernardello, R. & Marinov, I. Cessation of deep
584 convection in the open Southern Ocean under anthropogenic climate change. *Nature*
585 *Climate Change* **4**, 278-282 (2014).
586 43 Bintanja, R., van Oldenborgh, G. J., Drijfhout, S. S., Wouters, B. & Katsman, C. A. Important
587 role for ocean warming and increased ice-shelf melt in Antarctic sea-ice expansion. *Nature*
588 *Geoscience* **6**, 376-379 (2013).
589 44 Swart, N. C. & Fyfe, J. C. The influence of recent Antarctic ice sheet retreat on simulated sea
590 ice area trends. *Geophysical Research Letters* **40**, 4328-4332 (2013).
591 45 Scambos, T. A., Hulbe, C., Fahnestock, M. & Bohlander, J. The link between climate warming
592 and break-up of ice shelves in the Antarctic Peninsula. *Journal of Glaciology* **46**, 516-530
593 (2000).
594 46 Pritchard, H. D. *et al.* Antarctic ice-sheet loss driven by basal melting of ice shelves. *Nature*
595 **484**, 502-505 (2012).
596 47 Jenkins, A. *et al.* Observations beneath Pine Island Glacier in West Antarctica and
597 implications for its retreat. *Nature Geoscience* **3**, 468-472 (2010).
598 48 Dutrieux, P. *et al.* Strong Sensitivity of Pine Island Ice-Shelf Melting to Climatic Variability.
599 *Science* **343**, 174-178 (2014).
600 49 Jacobs, S. S., Jenkins, A., Giulivi, C. F. & Dutrieux, P. Stronger ocean circulation and increased
601 melting under Pine Island Glacier ice shelf. *Nature Geoscience* **4**, 519-523 (2011).
602 50 Steig, E. J., Ding, Q., Battisti, D. S. & Jenkins, A. Tropical forcing of Circumpolar Deep Water
603 Inflow and outlet glacier thinning in the Amundsen Sea Embayment, West Antarctica. *Annals*
604 *of Glaciology* **53**, 19-28 (2012).
605 51 Kirkman, C. H. & Bitz, C. M. The Effect of the Sea Ice Freshwater Flux on Southern Ocean
606 Temperatures in CCSM3: Deep-Ocean Warming and Delayed Surface Warming. *Journal of*
607 *Climate* **24**, 2224-2237 (2011).
608 52 Goosse, H. & Zunz, V. Decadal trends in the Antarctic sea ice extent ultimately controlled by
609 ice-ocean feedback. *Cryosphere* **8**, 453-470 (2014).
610 53 King , J. C. & Turner, J. T. *Antarctic Meteorology and Climatology*. (Cambridge, 1997).
611 54 Abram, N. J. *et al.* Acceleration of snow melt in an Antarctic Peninsula ice core during the
612 twentieth century. *Nature Geoscience* **6**, 404-411 (2013).
613 55 Thomas, E. R., Dennis, P. F., Bracegirdle, T. J. & Franzke, C. Ice core evidence for significant
614 100-year regional warming on the Antarctic Peninsula. *Geophysical Research Letters* **36**,
615 doi:10.1029/2009gl040104 (2009).
616 56 Thomas, E. R., Bracegirdle, T. J., Turner, J. & Wolff, E. W. A 308 year record of climate
617 variability in West Antarctica. *Geophysical Research Letters* **40**, 5492-5496 (2013).
618 57 Thomas, E. R., Marshall, G. J. & McConnell, J. R. A doubling in snow accumulation in the
619 western Antarctic Peninsula since 1850. *Geophysical Research Letters* **35**,
620 doi:10.1029/2007gl032529 (2008).
621 58 Thomas, E. R., Hosking, J. S., Tuckwell, R. R., Warren, R. A. & Ludlow, E. C. Twentieth century
622 increase in snowfall in coastal West Antarctica. *Geophysical Research Letters* **42**, 9387-9393,
623 doi:10.1002/2015gl065750 (2015).
624 59 Mulvaney, R. *et al.* Recent Antarctic Peninsula warming relative to Holocene climate and ice-
625 shelf history. *Nature* **489**, 141-144 (2012).
626 60 Abram, N. J., Wolff, E. W. & Curran, M. A. J. A review of sea ice proxy information from polar
627 ice cores. *Quaternary Science Reviews* **79**, 168-183 (2013).
628 61 Abram, N. J. *et al.* Ice core evidence for a 20th century decline of sea ice in the
629 Bellingshausen Sea, Antarctica. *Journal of Geophysical Research-Atmospheres* **115**,
630 doi:10.1029/2010jd014644 (2010).
631 62 Murphy, E. J., Clarke, A., Abram, N. J. & Turner, J. Variability of sea-ice in the northern
632 Weddell Sea during the 20th century. *Journal of Geophysical Research-Oceans* **119**, 4549-
633 4572 (2014).

63 Orsi, A. J., Cornuelle, B. D. & Severinghaus, J. P. Little Ice Age cold interval in West Antarctica: Evidence from borehole temperature at the West Antarctic Ice Sheet (WAIS) Divide. *Geophysical Research Letters* **39**, doi:10.1029/2012gl051260 (2012).

64 Steig, E. J. & Orsi, A. J. The heat is on in Antarctica. *Nature Geoscience* **6**, 87-88 (2013).

65 Steig, E. J. *et al.* Recent climate and ice-sheet changes in West Antarctica compared with the past 2,000 years. *Nature Geoscience* **6**, 372-375 (2013).

66 Kuettel, M., Steig, E. J., Ding, Q., Monaghan, A. J. & Battisti, D. S. Seasonal climate information preserved in West Antarctic ice core water isotopes: relationships to temperature, large-scale circulation, and sea ice. *Climate Dynamics* **39**, 1841-1857 (2012).

67 Bromwich, D. H. *et al.* Corrigendum: Central West Antarctica among the most rapidly warming regions on Earth. *Nature Geosci* **7**, 76-76 (2014).

68 Connolley, W. M. Variability in annual mean circulation in southern high latitudes. *Climate Dynamics* **13**, 745-756 (1997).

69 Lachlan-Cope, T. & Connolley, W. Teleconnections between the tropical Pacific and the Amundsen-Bellinghausens Sea: Role of the El Nino/Southern Oscillation. *Journal of Geophysical Research-Atmospheres* **111**, doi:10.1029/2005jd006386 (2006).

70 Schneider, D. P. & Steig, E. J. Ice cores record significant 1940s Antarctic warmth related to tropical climate variability. *Proceedings of the National Academy of Sciences of the United States of America* **105**, 12154-12158 (2008).

71 Schlosser, E. *et al.* Recent climate tendencies on an East Antarctic ice shelf inferred from a shallow firn core network. *Journal of Geophysical Research-Atmospheres* **119**, 6549-6562 (2014).

72 Altnau, S., Schlosser, E., Isaksson, E. & Divine, D. Climatic signals from 76 shallow firn cores in Dronning Maud Land, East Antarctica. *Cryosphere* **9**, 925-944 (2015).

73 Campagne, P. *et al.* Glacial ice and atmospheric forcing on the Mertz Glacier Polynya over the past 250 years. *Nature Communications* **6**, 1-9 (2015).

74 Curran, M. A. J., van Ommen, T. D., Morgan, V. I., Phillips, K. L. & Palmer, A. S. Ice core evidence for Antarctic sea ice decline since the 1950s. *Science* **302**, 1203-1206 (2003).

75 Muto, A., Scambos, T. A., Steffen, K., Slater, A. G. & Clow, G. D. Recent surface temperature trends in the interior of East Antarctica from borehole firn temperature measurements and geophysical inverse methods. *Geophysical Research Letters* **38**, doi:10.1029/2011gl048086 (2011).

76 Jones, J. M. *et al.* Historical SAM Variability. Part I: Century-Length Seasonal Reconstructions. *Journal of Climate* **22**, 5319-5345 (2009).

77 Visbeck, M. A Station-Based Southern Annular Mode Index from 1884 to 2005. *Journal of Climate* **22**, 940-950 (2009).

78 Jones, J. M. & Widmann, M. Instrument- and tree-ring-based estimates of the Antarctic oscillation. *Journal of Climate* **16**, 3511-3524 (2003).

79 Villalba, R. *et al.* Unusual Southern Hemisphere tree growth patterns induced by changes in the Southern Annular Mode. *Nature Geoscience* **5**, 793-798 (2012).

80 Zunz, V., Goosse, H. & Massonnet, F. How does internal variability influence the ability of CMIP5 models to reproduce the recent trend in Southern Ocean sea ice extent? *Cryosphere* **7**, 451-468 (2013).

81 Shu, Q., Song, Z. & Qiao, F. Assessment of sea ice simulations in the CMIP5 models. *Cryosphere* **9**, 399-409 (2015).

82 Purich, A. P., Cai, W., England, M. H., & Cowan, T. Evidence for link between modelled trends in Antarctic sea ice and underestimated westerly wind changes. *Nature Communications* **7**, 1-9 (2016).

83 Notz, D. How well must climate models agree with observations? *Philosophical Transactions of the Royal Society a-Mathematical Physical and Engineering Sciences* **373**, doi:10.1098/rsta.2014.0164 (2015).

84 Bothe, O. *et al.* Continental-scale temperature variability in PMIP3 simulations and PAGES 2k regional temperature reconstructions over the past millennium. *Climate of the Past* **11**, 1673-1699 (2015).
85 Hawkins, E. & Sutton, R. Time of emergence of climate signals. *Geophysical Research Letters* **39** (2012).
86 de la Mare, W. K. Whaling records and changes in Antarctic sea ice: Consistency with historical records. *Polar Record* **38**, 355-358 (2002).
87 de la Mare, W. K. Changes in Antarctic sea-ice extent from direct historical observations and whaling records. *Climatic Change* **92**, 461-493 (2009).
88 Cotte, C. & Guinet, C. Historical whaling records reveal major regional retreat of Antarctic sea ice. *Deep-Sea Research Part I-Oceanographic Research Papers* **54**, 243-252 (2007).
89 Hobbs, W. R., Bindoff, N. L. & Raphael, M. N. New Perspectives on Observed and Simulated Antarctic Sea Ice Extent Trends Using Optimal Fingerprinting Techniques. *Journal of Climate* **28**, 1543-1560 (2015).
90 Rignot, E., Jacobs, S., Mouginot, J. & Scheuchl, B. Ice-Shelf Melting Around Antarctica. *Science* **341**, 266-270 (2013).
91 Paolo, F. S., Fricker, H. A. & Padman, L. Volume loss from Antarctic ice shelves is accelerating. *Science* **348**, 327-331 (2015).
92 Swingedouw, D. *et al.* Antarctic ice-sheet melting provides negative feedbacks on future climate warming. *Geophysical Research Letters* **35**, doi:10.1029/2008gl034410 (2008).
93 Hellmer, H. H., Kauker, F., Timmermann, R., Determann, J. & Rae, J. Twenty-first-century warming of a large Antarctic ice-shelf cavity by a redirected coastal current. *Nature* **485**, 225-228 (2012).
94 Fogwill, C. J., Phipps, S. J., Turney, C. S. M. & Golledge, N. R. Sensitivity of the Southern Ocean to enhanced regional Antarctic ice sheet meltwater input. *Earths Future* **3**, 317-329 (2015).
95 Kay, J. E. *et al.* The Community Earth Sytem Model (CESM) Large Ensemble Project: A Community Resource for Studying Climate Change in the Presence of Internal Climate Variability. *Bulletin of the American Meteorological Society* **96**, 1333-1349 (2015).
96 Rayner, N. A. *et al.* Global analyses of sea surface temperature, sea ice, and night marine air temperature since the late nineteenth century. *Journal of Geophysical Research-Atmospheres* **108**, doi:10.1029/2002jd002670 (2003).
97 Laloyaux, P., Balmaseda, M., Dee, D., Mogensen, K., & Janssen, P. A coupled data assimilation system for climate reanalysis. *Quarterly Journal of the Royal Society* **142**, 65-78 (2016).
98 Goosse, H., Lefebvre, W., de Montety, A., Crespin, E. & Orsi, A. H. Consistent past half-century trends in the atmosphere, the sea ice and the ocean at high southern latitudes. *Climate Dynamics* **33**, 999-1016 (2009).
99 Gillett, N. P. *et al.* Attribution of polar warming to human influence. *Nature Geoscience* **1**, 750-754 (2008).
100 Bindoff, N. L. et al. Detection and Attribution of Climate Change: from Global to Regional. In: *Climate Change 2013: The Physical Science Basis.Contribution of Working Group I to the Fifth Assessment Report of the Intergovernmental Panel on Climate Change* (Stocker, T. F. et al. (eds)) (Cambridge University Press, Cambridge, United Kingdom, and New York, USA, 2013).

Acknowledgements

Ian Goodwin, Julie McClean, Judy Twedt, Jeff Severinghaus, Clive Wilkinson, Rob Wilson and Uriel Zajacazkovski are thanked for their contributions to the meeting where this paper was conceived and planned. The meeting and this project were undertaken with the support of the Climate and Cryosphere project of the World Climate Research Programme (through the Polar Climate Predictability Initiative) and the Government of Canada through the Federal Department of the Environment. Past Global Changes (PAGES) are also thanked for supporting this meeting. David McCutcheon is thanked for producing supplementary Figure 1.

NJA is supported by a QEII fellowship awarded by the Australian Research Council (ARC DP110101161) and MHE by an ARC Laureate Fellowship (FL100100214). VMD acknowledges support from Agence Nationale de la Recherche, project ANR-14-CE01-0001 (ASUMA). BS acknowledge PAGES Antarctica 2k. HG is Research Director with the Fonds National de la Recherche Scientifique (F.R.S.- FNRS-Belgium). This work is supported by the F.R.S.- FNRS. POC is supported by research grant ANPCyT PICT2012 2927. RLF is supported by NSF grant #1341621. EJS was supported by the Leverhulme Trust. STG is supported by NSF grant OCE-1234473. DPS was supported by NSF grant#1235231. NCAR is sponsored by the National Science Foundation. GRS was supported by NSF Grants AGS-1206120 and AGS-1407360. DS was supported by the French ANR CEPS project Green Greenland (ANR-10-CEPL-0008). GJM was supported by the UK Natural Environment Research Council (NERC) through the British Antarctic Survey research programme Polar Science for Planet Earth. AKM was supported by U.S. Department of Energy under Contract DE-SC0012457. KRC is supported by a VUW Doctoral Scholarship. LMF acknowledges support from the Australian Research Council (FL100100214). DJC was supported by NERC grant NE/H014896/1. CdL is supported by a UPMC doctoral scholarship. AJO was supported by the EU grant FP7-PEOPLE-2012-IIF 331615. XC was supported by the French ANR CLIMICE (ANR-08-CEXC-012-01) and the FP7 PAST4FUTURE (243908) projects. JAR is supported by Marsden grant VUW1408. IE is supported by NSF grant OCE-1357078. TRV is supported by the Australian Government's Cooperative Research Centres programme, through the ACE CRC.

Author Contributions

All authors conceived the paper. JMJ, HG and STG organised the contributions to the manuscript, and contributed to writing and editing the manuscript. NJA, undertook data analysis (Figs. 2 and 3), figure preparation, and contributed to writing and editing of the manuscript. GRS undertook data analysis and preparation of Fig.1 and associated supplementary material. DS undertook coordination, data analysis and preparation of Fig. 3, and editing/revision of the manuscript. CdL undertook data analysis, preparation and design of Fig. 3 and contributed to writing (especially Section 4 and related supplementary and methods) and editing of manuscript. BS undertook data preparation and analysis for Fig. 2, and contributed to editing and revision of the manuscript.

EJS undertook data analysis (Fig. 1), and contributed to writing (particularly West Antarctica and SAM/ENSO dynamics) and editing the manuscript. AKM and LMF undertook data analysis for Fig. 3, and editing/revision of the manuscript. AJO undertook data preparation for Fig. 2 (and related supplementary information), and editing/revision of the manuscript. XC provided paleo sea ice data, and undertook editing/revision of the manuscript, writing of methods section (diatoms). VMD contributed to discussion associated with Section 3, and selection of records for data analysis, provided advice on Fig. 2, and contributed to writing and editing/revision of the manuscript. MHE contributed to design of the analyses for Fig. 1 and Fig. 3, and to writing (Section 2), and editing/revision of the manuscript. TRV wrote the first draft of Section 3, and helped design Fig. 2.

POC contributed to writing (Section 2) and editing the manuscript. DJC provided data and commentary for Fig. 2, and contributed to editing/revision of the manuscript. JAR, RLF, MNR, GJM, DPS and IE contributed to discussion leading to Section 2/Figure 1, and to editing/revision of the manuscript. GJM also contributed SAM data. KRC contributed to writing of the methodology, and editing/revision of the manuscript.

Competing financial interests

The authors declare no competing financial interests.

Materials and Correpondence

Correspondence and requests for materials should be addressed to Julie Jones.

Tables

	50% of models exceeding control trends		90% of models exceeding control trends		
	end year	**trend length (y)**	**end year**	**trend length (y)**	**direction**
SIE	2031	53	2098	120	below
SST	2021	43	2056	78	above
SAT	<2014	<36	2050	72	above
SAM	2015	37	2044	66	above

Table 1: Summary of trend emergence analysis. Indicated are the end year (20YY) and trend length (in years) of 1979-20YY linear trends for which (left) 50% and (right) 90% of Historical-RCP8.5 simulated trends in CMIP5 models fall outside the 5-95% distribution (either above 95%, or below 5%) of pre-industrial trends of the same length in the same model.

Figure Legends

Figure 1 | Antarctic atmosphere-ocean-ice changes over the satellite-observing era. a) Total changes over 1979-2014 in annual mean surface air temperature (blue-red shading), station-based surface air temperature (SAT, blue-red shaded shapes), sea-ice concentration (contours, 10% intervals; red and blue contours, alongside light pink and blue shading beneath, denote negative and positive trends, respectively), sea surface temperature (SST, purple-red shading), and 10m winds (vectors). Only SST trends equatorward of the climatological September sea-ice extent (SIE, black contour) are shown. Hatching and teal vectors highlight trends significant at the 95% level according to two-tailed student t-tests. Note that SAT trends are calculated over 1979-2012 but scaled to represent trends over the 36-year period, 1979-2014. Surrounding figures show time-series of **b)** East Antarctic SAT (circles; red line denotes multi-station mean, grey lines those of individual East Antarctic stations), **c)** the Marshall Southern Annular Mode index (difference in station sea level pressure between 40° and 65°S), **d)** Southern Ocean zonal mean SST (averaged over 50°–70°S), **e)** Southern Hemisphere SIE, **f)** Ross-Amundsen SIE, **g)** West Antarctic SAT (square; Byrd Station), **h)** Amundsen-Bellingshausen SIE , and **i)** Antarctic Peninsula SAT (hexagons; red line denotes multi-station mean, grey lines those of individual Antarctic Peninsula stations). For all time-series, blue lines highlight the linear trend, and red asterisk where the trend is significant at the 95% level according to a two-tailed student t-test. See methods for details on datasets and trend significance calculation.

Figure 2 | Antarctic climate variability and trends over the last 200 years from long observational and proxy-derived indicators. Records were regionally compiled for (a) the Antarctic Peninsula, (b) West Antarctica, (c) coastal East Antarctica and (d) the Antarctic Plateau (Methods). Central map shows the location of records according to environmental indicator (colours) and record type (symbols), as well as the boundaries of the four geographic regions (black lines), the 2000m elevation contour (grey curve), and the trend in sea ice concentration over the 1979-2014 interval (shading). Within each region (a-d), records were compiled as 5y averages (dark lines) according to the environmental parameter that they represent; observed surface air temperature (SAT) (red); proxy for SAT (orange); borehole inversion reconstruction of surface temperatures (greens); proxy for sea surface temperature (blue); and proxy for sea ice conditions (cyan). Shadings (or thin vertical lines) denote range of estimates across records within each 5-year bin, with the exception of borehole temperature inversions. All records are expressed as anomalies (^{o}C units) or normalised data (σ units) relative to 1960-1990. With the exception of borehole temperature records which are are shown individually with uncertainty bounds (see Supplementary Figure 4 for additional details). Details of datasets used in this figure provided in Supplementary Table 1.

Figure 3 | Antarctic climate trends in CMIP5 simulations. (a-d) Distributions of (blue) 36-year linear trends in an ensemble of CMIP5 preindustrial simulations and (black/grey) 1979-2014 trends in an ensemble of CMIP5 historical (1979-2005)-RCP8.5 (2006-2014) simulations (see Methods). Red vertical lines correspond to observed 36-year linear trends (1979-2014). Horizontal bars depict (red) the 90 % confidence interval of the observed trend, (blue) the 5-95 % range of the simulated preindustrial distribution and (black) the 5-95% range of the simulated 1979-2014 trend distribution. The dark blue error bars on the pre-industrial histograms and horizontal ranges are 5-95% uncertainty intervals based on Monte Carlo analysis (see Methods) **(e-h)** Proportion of CMIP5 model experiments whose linear trends starting in 1979 are above the 95% level (below the 5% level for panel **e**) of the distribution of trends of the same length in their matching control simulation. Simulations follow the RCP8.5 scenario after year 2005. Dashed and solid red lines highlight the 50% and 90% levels of the cumulative distributions (Table 1). The orange bars are 5-95% uncertainty ranges based on Monte Carlo analysis of equal length segments from the preindustrial simulations (see Methods). Chosen climate variables are **(a, e)** Southern Hemisphere sea-ice extent, **(b, f)** mean SST south of 50°S, **(c, g)** mean SAT south of 50°S and **(d, h)** SAM index. Model details given in Supplementary Table 2. Observations used to compute observed sea ice extent and SST trends over the 1979-2014 period are referenced in Figure 1. The observed 1979-2014 SAT trend is derived from ERA-Interim 2-m air temperature fields. Modelled and observed SAM indices were calculated from annual mean time series using Empirical Orthogonal Function analysis applied on 500 hPa geopotential height fields over the 90°S-20°S region, with observation-based geopotential height fields taken from the ERA-Interim reanalysis.

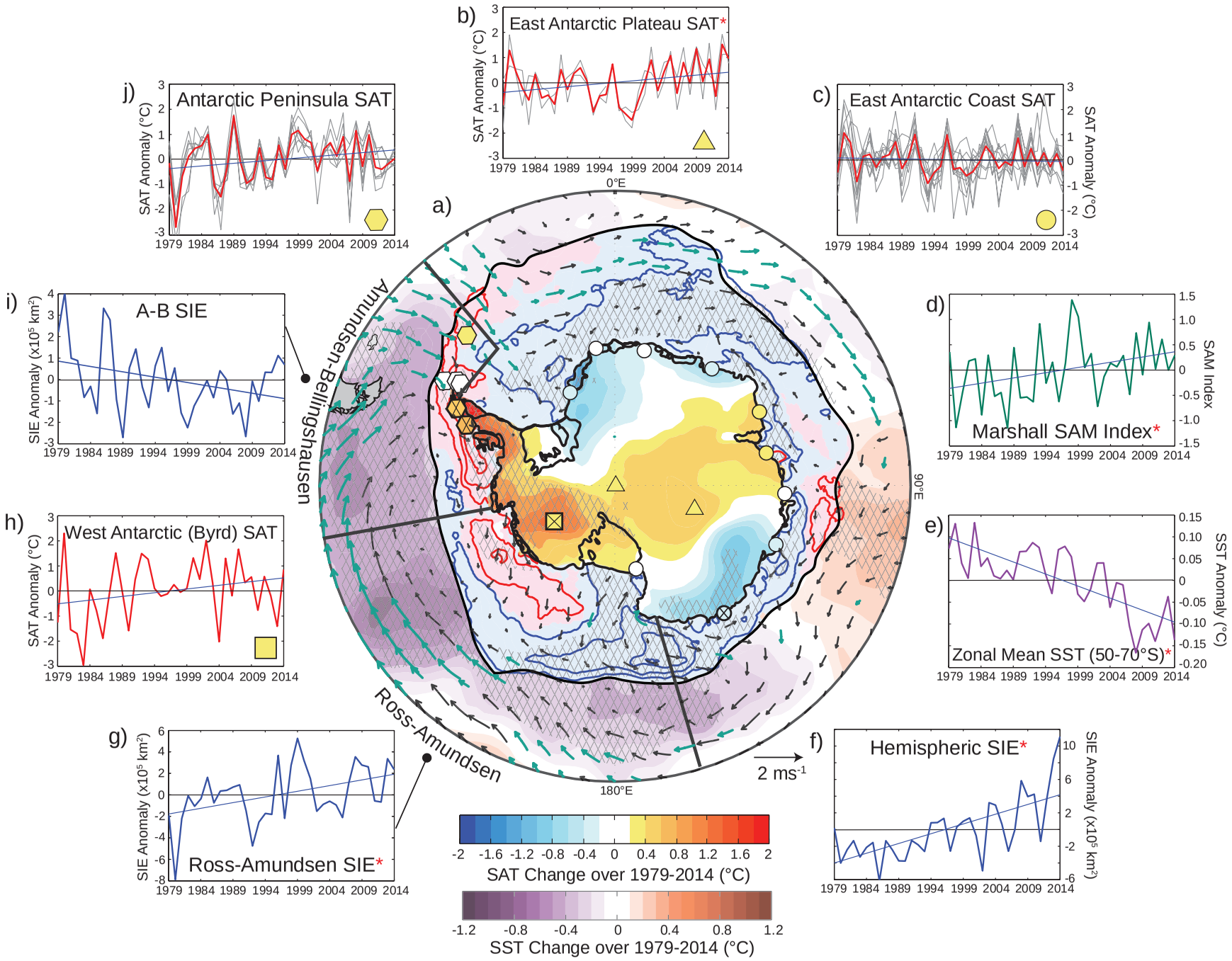
a)
b)
East Antarctic Plateau SAT*
SAT Anomaly (°C)
0°E
c)
East Antarctic Coast SAT
SAT Anomaly (°C)
d)
Marshall SAM Index*
SAM Index
e)
Zonal Mean SST (50-70°S)*
SST Anomaly (°C)
f)
Hemispheric SIE*
SIE Anomaly (x10⁵ km²)
g)
Ross-Amundsen SIE*
SIE Anomaly (x10⁵ km²)
h)
West Antarctic (Byrd) SAT
SAT Anomaly (°C)
i)
A-B SIE
SIE Anomaly (x10⁵ km²)
j)
Antarctic Peninsula SAT
SAT Anomaly (°C)
Amundsen-Bellingshausen
Ross-Amundsen
90°E
180°E
2 ms⁻¹
SAT Change over 1979-2014 (°C)
SST Change over 1979-2014 (°C)
1979 1984 1989 1994 1999 2004 2009 2014

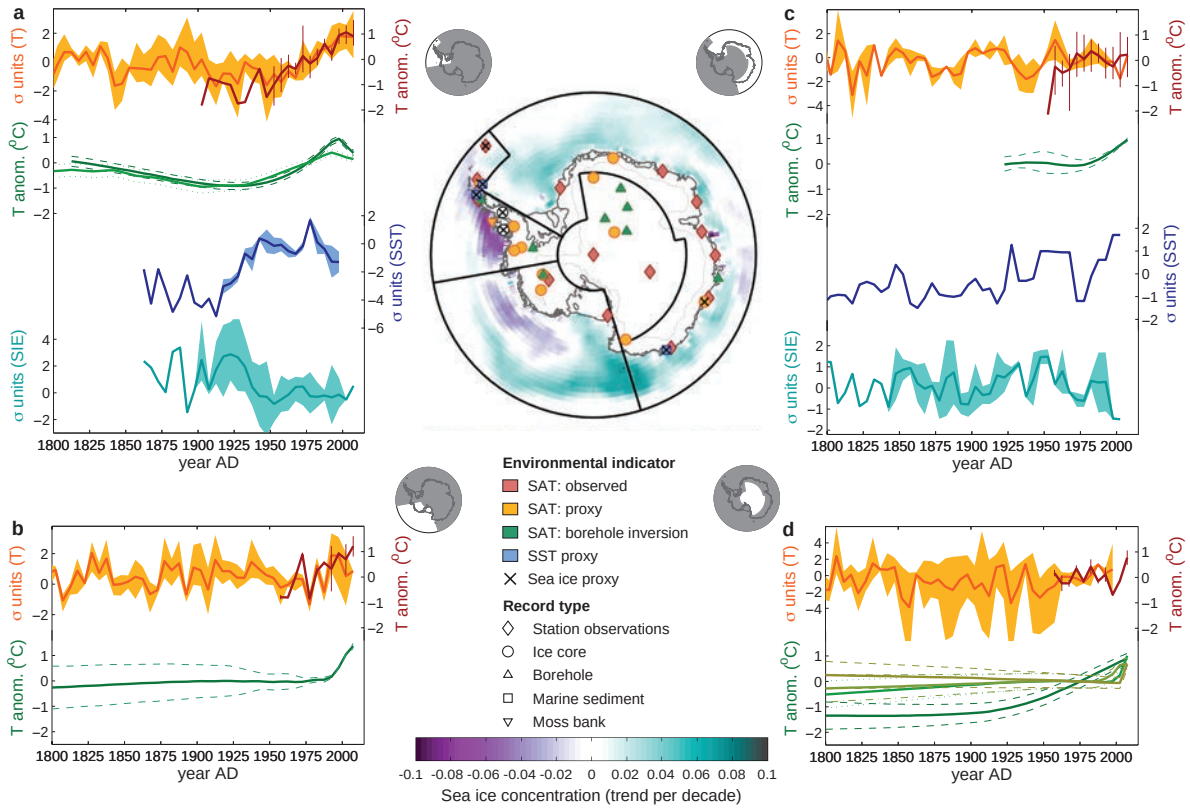
a
b
c
d
σ units (T)
T anom. (°C)
σ units (SST)
σ units (SIE)
1800 1825 1850 1875 1900 1925 1950 1975 2000
year AD
Environmental indicator
SAT: observed
SAT: proxy
SAT: borehole inversion
SST proxy
Sea ice proxy
Record type
Station observations
Ice core
Borehole
Marine sediment
Moss bank
-0.1 -0.08 -0.06 -0.04 -0.02 0 0.02 0.04 0.06 0.08 0.1
Sea ice concentration (trend per decade)

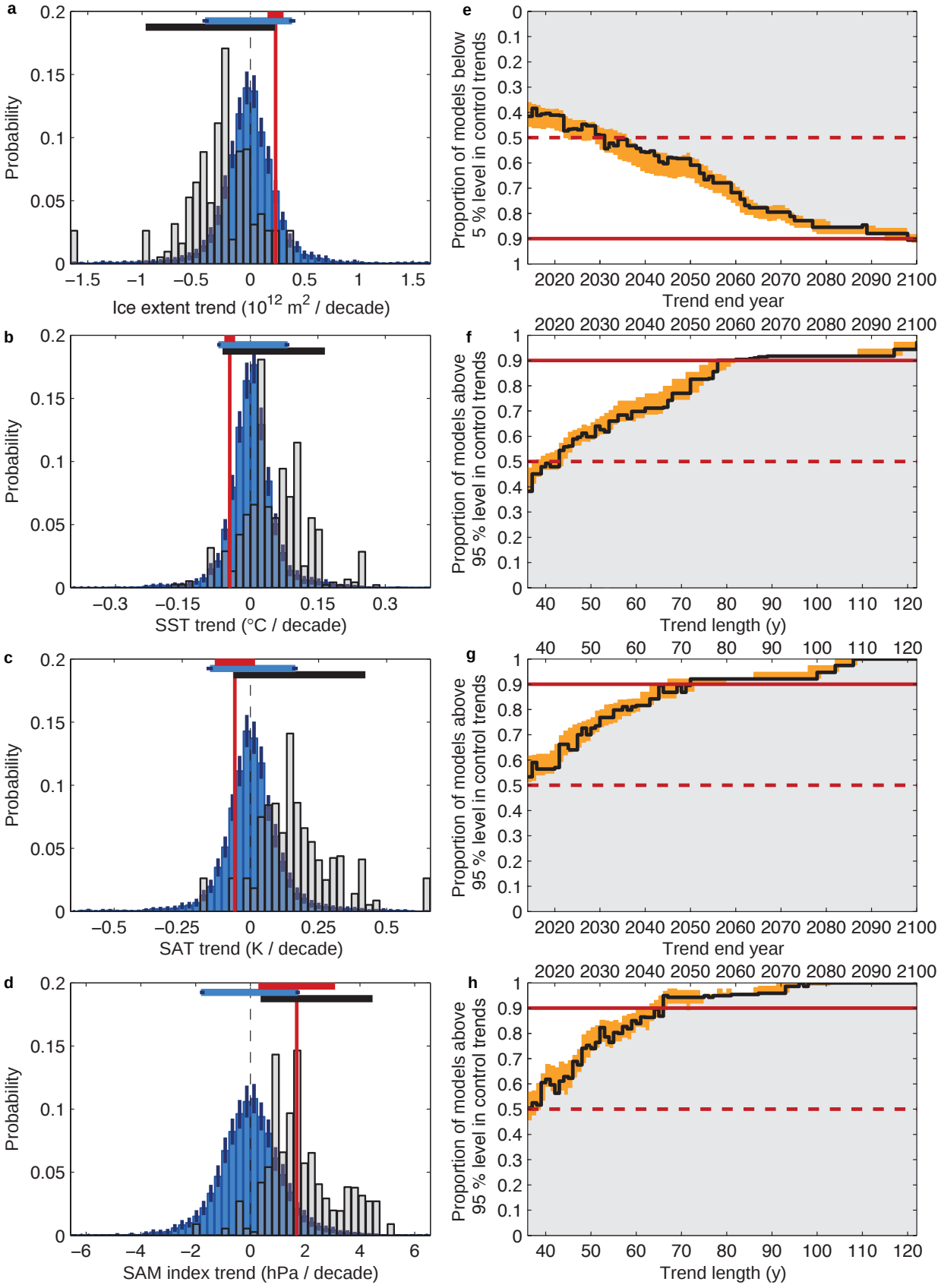
a
Probability
Ice extent trend (10^{12} m^2 / decade)
b
Probability
SST trend (°C / decade)
c
Probability
SAT trend (K / decade)
d
Probability
SAM index trend (hPa / decade)
e
Proportion of models below 5 % level in control trends
Trend end year
f
Proportion of models above 95 % level in control trends
Trend length (y)
g
Proportion of models above 95 % level in control trends
Trend end year
h
Proportion of models above 95 % level in control trends
Trend length (y)

Data and Methods

Antarctic Climate Monitoring
Figure 1 and Supplementary Figure 2

We used station-based (shaded shapes) and reconstruction-based (shading over Antarctica) temperature data to calculate Antarctic surface air temperature (SAT) trends over the period 1979-2014. Regional SAT was calculated by averaging the station-based temperatures for each respective region denoted by shaded shapes. Only Byrd station is available for West Antarctica; thus only one line is provided for that region. Station-based temperature data are from the quality-controlled SCAR READER Project[1] and the reconstructed data are from the Ohio State University Byrd Polar Research Center's Reconstruction of Antarctic near-surface temperature dataset[2]. Reconstructed temperature data span the period 1979-2012, and trends were scaled to represent the period 1979-2014.

Sea surface temperature (SST) trends (shading over the ocean) were calculated using the National Oceanic and Atmospheric Administration (NOAA) Extended Reconstructed SST version 3b dataset[3], employed at 2x2° latitude-longitude resolution. The zonal-mean SST is the average SST over the region 50-70°S. Sea ice concentration trends (contours over ocean) were calculated using the Bootstrap sea ice concentration dataset[4], which has approximately 25x25 km resolution and which was acquired from the National Snow and Ice Data Center (NSIDC). The regional sea-ice extent (SIE) is the sum of all grid points where ice concentration is greater than 15% in each respective region. The regions used are the entire Antarctic domain (shown in Fig. 1 and supplementary Fig. 2), and the Ross-Amundsen, and Amundsen-Bellingshausen regions (as marked in Fig. 1 and Supplementary Fig. 2). Ten-metre wind data (vectors) are from the ERA-Interim reanalysis dataset[5] employed at 1°x1° latitude-longitude resolution. The Southern Annular Mode (SAM) is defined using the observation-based Marshall SAM index[6].

Seasonal means for all metrics are defined with respect to the Southern Hemisphere: austral summer (December-February, DJF), austral autumn (March-May, MAM), austral winter (June-August, JJA), and austral spring (September-November, SON). Annual means are calculated over January-December. All trends are shown as the total linear trend over 1979-2014 (i.e. annual trend multiplied by 36). The statistical significance of trends (hatching and green vectors for wind) follows a Student's two-tailed t-test with threshold of significance set at the 95% confidence level taking into account autocorrelation by using the effective sample size[7].

Historical and palaeoclimate data analysis.
Figure 2 and Supplementary Figure 3

A full list of data used for this analysis, including references, is given in supplementary Table 1.

We use observations of SAT from Antarctic stations where long historical observations records exist. We use records beginning in 1959 (immediately following the International Geophysical

Year) or earlier. These data are sourced from the READER (REference Antarctic Data for Environmental Research) database maintained by the British Antarctic Survey[1]. Temperature information from natural archives comes primarily from the published, publicly available database of the PAGES (Past Global Changes) Antarctic2k working group[8]. The ice core water stable isotope records in this database have been assessed as suitable for high-resolution palaeotemperature reconstructions based on their temporal resolution and age control, and cover the last ~300 to 2000 years of climate history. We also use the Gomez[9] and Ferrigno[10] ice core isotope records to provide detailed climate information for the southwestern Antarctic Peninsula and a moss bank $\delta^{13}C$ record[11] as an additional palaeotemperature indicator from the northern Antarctic Peninsula. Sea ice indicators were derived from a historical record as well as from chemical records preserved within ice cores that are sensitive to sea ice extent [12] and from diatom assemblage data from marine sediment cores[13]. Diatom assemblages from marine sediment cores also provide indicators of past SST changes. Published temperature change reconstructed through inversion of borehole profiles[14,15] were also compiled. The locations of these borehole temperature profiles are shown in Supplementary Fig. 4). Note that because of temperature diffusion processes in snow and ice, borehole temperature profiles are unable to preserve signals of multi-decadal temperature fluctuations, and resolution is decreasing with time span.

We assess climate signals over four geographic regions (Fig. 2). These regions aim to group together records with similar signals informed by geographic constraints, cross correlation of records and spatial patterns of sea ice trends in the satellite era. The distribution of records was also taken into account when defining reconstruction regions, and in many cases the scarcity of available records necessitates the regions being very broad. The regions we use are: (1) the Antarctic Peninsula including the Bellingshausen Sea and Scotia Sea/northern Weddell Sea including the South Orkney Islands. It is defined by the region south of 55°S and extending to 65°S between 40°W and 60°W, and to 83°S between 60°W and 100°W. (2) The West Antarctic region covers the West Antarctic Ice Sheet, Ross Ice Shelf and the Amundsen and Ross Seas. It is bounded by the latitudes 55°S to 83°S, and the longitudes 100°W to 163°E. (3) The coastal East Antarctic region spans the margin of East Antarctic from the Victoria Land all the way to the Weddell Sea coast, and the adjacent Indian and Atlantic oceans. It is the region south of 55°S and extending to 72°S between 163°E and 80°E, to 74°S between 80°E and 10°W, and to 83°S between 10°W and 60°W (but excluding the region of the northern Weddell Sea assigned to the Antarctic Peninsula region). (4) The East Antarctic Plateau region approximately follows the 2000m elevation contour and is defined in this study as being south of 83°S between 10°W and 163°E, south of 72°S between 163°E and 80°E, and south of 74°S between 80°E and 10°W. The assignment of the historical and palaeoclimate records to these regions is shown in Supplementary Table 1.

In order to examine regional climate variability and trends over the past 200 years, all records were first binned as 5-year averages. Where records had less than annual resolution (e.g. marine sediment cores, moss bank), they were resampled as pseudo-annuals using a nearest neighbour interpolation method that distributes the measured value across all years that it represents. This ensures that data are attributed with the correct ratio between adjacent 5-year bins. The 5-year binned records were then converted to anomalies (SAT observations and

borehole inversions; ^{o}C units) or normalised (proxies for SAT, SST and sea ice; σ units) relative to the mean and standard deviation of data in the bins between 1960 and 1990. This normalization step assumes that temperature-proxy variance is the same in all locations within a region, but the validity of this assumption remains to be assessed. With the exception of borehole temperature records, the 5y binned records where then assigned to their respective geographic region and compiled as 5y averages. These regional compilations are presented in Figure 2.

Trend distributions were assessed for proxy records of SAT, SST and SIE using data at annual average or pseudo-annual resolution (Supplementary Fig. 3). To assess the significance of the most recent 36-year trends we calculate the linear trend across the final 36 years of each proxy record. These trends are comparable in length to the satellite-era trends presented in Fig. 1, but are not the same in timing as the proxy records end at varying times and none extend to the end of 2014. These are then compared to the distribution of all other earlier 36-year trends in the proxy record to assess the significance with each proxy record of the most recent 36-year trend. This trend assessment is also repeated using 100-year trends for proxy records that cover at least the past 200 years.

CMIP5 model analysis.

Fig. 3, Supplementary Fig. 5

We selected all CMIP5 models that have a minimum of 250 years' duration in their pre-industrial control simulation and at least one Representative Concentration Pathway 8.5 (RCP8.5) simulation (see Supplementary Table 2 for a list of the 38 models included). Prior to computing the trend distributions shown in Fig. 3, we corrected the modelled sea ice extent, SST, SAT and SAM time series for drift. When we found strong nonlinear drift near the start of pre-industrial simulations, we ignored the corresponding portion of the time series for subsequent analysis. We then calculated a linear trend over the full (remaining) length of pre-industrial control experiments and subtracted it from all time series.

From the detrended pre-industrial time series, we computed 36-year linear trends using a 36-year sliding window with a time step of 1 year. The analysed pre-industrial time series totalled a length of around 20000 years (depending on the variable considered, Supplementary Table 2). The distribution of all 36-year trends were compiled by model and then averaged to produce the distributions in Figure 3 (Fig. 3a-d, blue), a total of more than 15000 overlapping 36-year trends. To gain an estimate of uncertainty in the trend distributions, we applied a Monte Carlo methodology, whereby this process was repeated 1000 times, but with the individual model distributions based on random selections of 10% of all possible 36-year trends. The 5% and 95% levels across the 1000 replicate multi-model distributions produced were used to estimate uncertainty ranges around the pre-industrial 36-year trend distributions (dark blue error bars in Fig. 3a-d). The same process is repeated for Supplementary Figure 5, but using season-specific model data, and without applying the Monte Carlo uncertainty methodology, as we expect seasonal ranges to be very similar to the annual.

Since available historical experiments generally only cover up to year 2005, years 2006-2014 of RCP8.5 simulations were appended to historical 1979-2005 time series to obtain the modelled distributions of 1979-2014 trends (Fig. 3a-d, black/grey). Scenario forcing RCP8.5 was chosen because it is the best available match to the observed greenhouse gas emissions trajectory over 2006-2014. Between 1 and 12 historical-RCP8.5 simulations per model were available (Supplementary Table 2), giving a total of 90 sample 1979-2014 trends entering the satellite-era trend distributions. Despite the variable length of preindustrial simulations and the variable number of historical-RCP8.5 members across models, we enforced equal model weights in the ensemble distributions of Fig. 3a-d by normalizing each model's contribution by the corresponding number of available 36-year trends. Note also that 500hPa geopotential height fields were not available for the EC-EARTH model, reducing the total number of 36-year SAM index trends included in the control and 1979-2014 ensemble distributions of Fig. 3d to 3210 and 78, respectively.

The same models and experiments were employed for the trend emergence analysis presented in Fig. 3e-h. For each model and each variable, the 5-95% range of control trend distributions is first evaluated for trend lengths increasing from 36 to 122 years, using all possible trends of that length (i.e. stepped by 1 year). Historical-RCP8.5 trends starting in 1979 are then calculated for each trend length (i.e. 36-year trends represent the 1979-2014 interval; 122-year trends represent the 1979-2100 interval) and each model experiment. The historical-RCP8.5 trends are compared to the statistical distribution of trends of the same length in the corresponding model's control simulation, and we compute the proportion of models where the linear trend in the historical-RCP8.5 interval exceeds the 95% distribution of trends in the pre-industrial control (or falls below the 5% distribution in the case of negative sea ice extent trends). To gain an estimate of uncertainty in trend emergence, we again employ a Monte Carlo process, whereby we replicate this test 1000 times, but assess emergence for each model against a random selection of 10% of all possible trends of the same length in the control simulation of the same model. The 5% and 95% range of emergence profiles across the 1000 replicate emergence tests are shown as the orange bars around the black line in Figure 3e-h. As in Fig. 3a-d, we ensure that models have equal weights in the shown cumulative distributions: for a model with n member experiments, each experiment is given a weight of $1/n$ when calculating the cumulative multi-model trend emergence profile.

Supplementary Tables

Site Name	Record Type	Climate Parameter	Start Year	End Year	Lat. °N	Long. °E	Region	Ref.
Amundsen Scott	Observations	SAT	1957	2014	-90	0	East Antarctic Plateau	1
Casey	Observations	SAT	1959	2014	-66.3	110.5	Coastal East Antarctica	1
Davis	Observations	SAT	1957	2014	-68.6	78	Coastal East Antarctica	1
Dumont d'Urville	Observations	SAT	1956	2014	-66.7	140	Coastal East Antarctica	1
Esperanza	Observations	SAT	1945	2014	-63.4	-57	Antarctic Peninsula	1
Faraday	Observations	SAT	1951	2014	-65.4	-64.4	Antarctic Peninsula	1
Halley	Observations	SAT	1957	2014	-75.5	-26.4	Coastal East Antarctica	1
Mawson	Observations	SAT	1954	2014	-67.6	62.9	Coastal East Antarctica	1
McMurdo	Observations	SAT	1957	2014	-77.9	166.7	West Antarctica	1
Mirny	Observations	SAT	1956	2014	-66.5	90.3	Coastal East Antarctica	1
Orcadas	Observations	SAT	1904	2014	-60.7	-44.7	Antarctic Peninsula	1
Syowa	Observations	SAT	1957	2014	-69	39.6	Coastal East Antarctica	1
Vostok	Observations	SAT	1958	2014	-78.5	106.9	East Antarctic Plateau	1
Byrd	Observations	SAT	1957	2013	-80	-119.4	West Antarctica	16
Talos Dome	Ice core water isotopes	SAT	1232	1995	-72.5	159.1	East Antarctic Plateau	8,17
Law Dome DSS	Ice core water isotopes	SAT	174	2007	-66.8	112.8	Coastal East Antarctica	8,18
Plateau Remote	Ice core water isotopes	SAT	2	1986	-84	43	East Antarctic Plateau	8,19,20

Site Name	Record Type	Climate Parameter	Start Year	End Year	Lat. °N	Long. °E	Region	Ref.
IND-22 B4	Ice core water isotopes	SAT	1533	1994	-70.9	11.5	Coastal East Antarctica	8,21,22
EDML	Ice core water isotopes	SAT	166	1996	-75	0	East Antarctic Plateau	23, 8
WAIS 2005A	Ice core water isotopes	SAT	743	2005	-79.5	-112.1	West Antarctica	24,8
ITASE 00-1	Ice core water isotopes	SAT	1674	2000	-79.4	-111.2	West Antarctica	24,8,25
ITASE 00-5	Ice core water isotopes	SAT	1719	2000	-77.7	-124.0	West Antarctica	8,24,25
Siple Station	Ice core water isotopes	SAT	1417	1983	-75.9	-84.3	Antarctic Peninsula	8,25,26
JRI	Ice core water isotopes	SAT	0	2007	-64.2	-57.7	Antarctic Peninsula	27,28
Gomez	Ice core water isotopes	SAT	1857	2005	-73.6	-70.4	Antarctic Peninsula	9
Ferrigno	Ice core water isotopes	SAT	1703	2010	-74.6	-86.9	Antarctic Peninsula	10
Lazarav Bay	Moss bank $\delta^{13}C$	SAT	1863	2003	-69.4	-71.8	Antarctic Peninsula	11
WAIS Divide	Borehole temperature	SAT	8	2007	-79.5	-112.1	West Antarctica	14
Larissa	Borehole temperature	SAT	1810	2007	-66	-64	Antarctic Peninsula	29
DML NUS0702	Borehole temperature	SAT	1509	2008	-76.1	22.5	East Antarctic Plateau	30
DML NUS0705	Borehole temperature	SAT	1509	2008	-78.7	35.6	East Antarctic Plateau	30
DML NUS0707	Borehole temperature	SAT	1509	2008	-82.1	54.9	East Antarctic Plateau	30
DML NUS0805	Borehole temperature	SAT	1509	2009	-82.6	17.9	East Antarctic Plateau	30
Mill Island	Borehole temperature	SAT	1921	2011	-65.6	100.8	Coastal East Antarctica	31

Site Name	Record Type	Climate Parameter	Start Year	End Year	Lat. °N	Long. °E	Region	Ref.
Rutford	Borehole temperature	SAT	1700	2005	-78.1	-83.9	Antarctic Peninsula	[32]
MCT18a	Diatom assemblage	SST	1864	1999	-64.7	-62.8	Antarctic Peninsula	[13]
MCT38c	Diatom assemblage	SST	1916	2000	-64.7	-57.4	Antarctic Peninsula	[13]
CB2010	Diatom assemblage	SST	1740	2001	-66.9	142.4	Coastal East Antarctica	[33]
West Peninsula stack	Ice core MSA	Winter SIE	1902	1990	-71.9	-74.6	Antarctic Peninsula	[34]
Law Dome	Ice core MSA	Winter SIE	1841	1995	-66.8	112.8	Coastal East Antarctica	[35]
South Orkney Fast Ice	Observations	winter SIE	1903	2008	-60.7	-44.7	Antarctic Peninsula	[36]
MCT18a	Diatom assemblage	SI duration	1864	1999	-64.7	-62.8	Antarctic Peninsula	[13]
MCT38c	Diatom assemblage	SI duration	1916	2000	-64.7	-57.4	Antarctic Peninsula	[13]
CB2010	Diatom assemblage	SI duration	1740	2001	-66.9	142.4	Coastal East Antarctica	[33]

Supplementary Table 1: Details of the long observational records and palaeoclimate proxy records used in this study (Fig. 2, Supplementary Fig. 3)

Model	Analysed pre-industrial control length (years)	Number of historical-RCP8.5 member simulations
ACCESS1.0	500	1
ACCESS1.3	500	1
BCC-CSM1.1	500	1
BCC-CSM1.1m	400	1
BNU-ESM	550	1
CanESM2	1096	5
CCSM4	1051	6
CESM1-BGC	500	1
CESM1-CAM5	319	3
CMCC-CESM	276	1
CMCC-CM	330	1
CMCC-CMS	500	1
CNRM-CM5	850	5
CSIRO-Mk3.6	500	10
EC-EARTH	452	12
FGOALS-g2	700	1
FGOALS-s2	501	3
FIO-ESM	800	3
GFDL-CM3	500	1
GFDL-ESM2G	500	1
GFDL-ESM2M	500	1
GISS-E2-H	540	1
GISS-E2-H-CC	250	1
GISS-E2-R	550	2
GISS-E2-R-CC	250	1
HadGEM2-ES	340	4
INM-CM4	500	1
IPSL-CM5A-LR	1000	4
IPSL-CM5A-MR	300	1
IPSL-CM5B-LR	300	1
MIROC-ESM	630	1
MIROC-ESM-CHEM	254	1
MIROC5	700	5
MPI-ESM-LR	1000	3
MPI-ESM-MR	1000	1
MRI-CGCM3	630	1
NorESM1-M	601	1
NorESM1-ME	252	1
Total number of 36-year trends	**~ 19000**	**90**

Supplementary Table 2: CMIP5 experiments included in the analysis. The length of pre-industrial control experiments after removal of years characterized by nonlinear drift are indicated for each of the 38 selected models, along with the number of available historical-RCP8.5 members. Note that the SAM index could not be computed for the EC-EARTH model, reducing the total number of 36-year trends entering preindustrial and 1979-2014 ensemble distributions.

Supplementary Figures

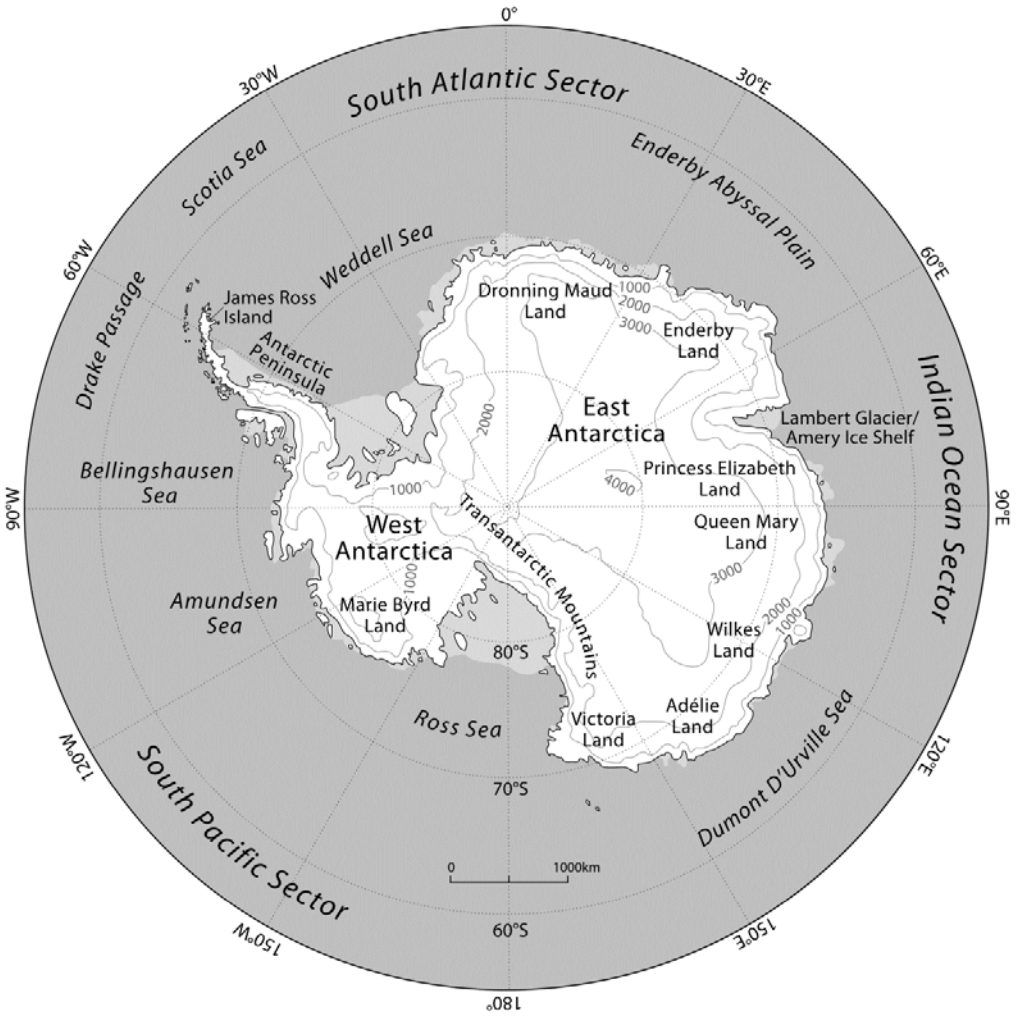

Supplementary Figure 1: Map of the high latitude Southern Hemisphere, including place names mentioned in the text.

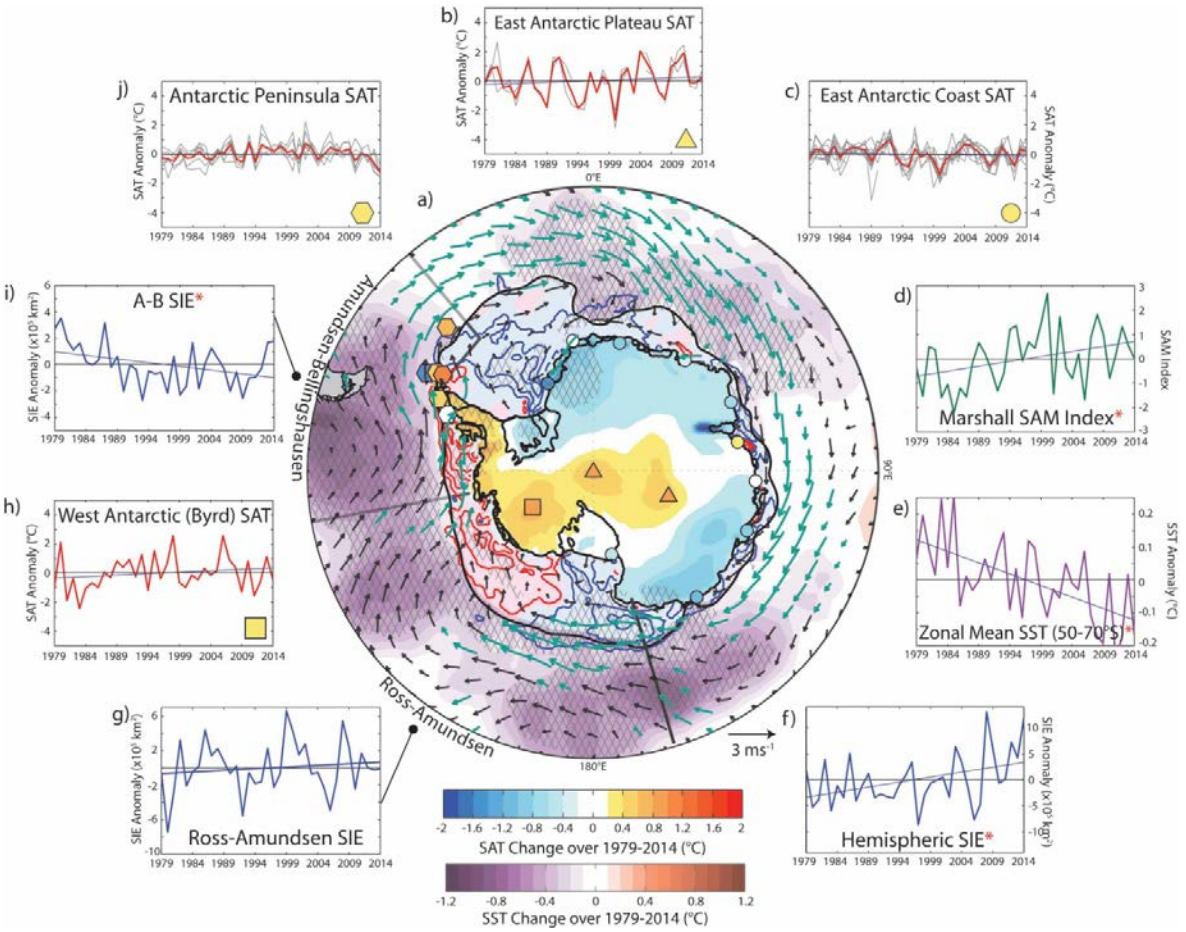

Supplementary Figure 2 a: Antarctic atmosphere-ocean-ice changes over the satellite-observing era for Summer (December, January, February). **a)** Total changes over 1979-2014 in remote sensing annual mean SAT (blue-red shading), station-based SAT (blue-red shaded shapes), sea ice concentration (contours, 10% intervals; red and blue contours, alongside light pink and blue shading beneath, denote negative and positive trends, respectively), SST (purple-red shading), and 10m winds (vectors). Remote sensing SST trends are only shown for areas equatorward of the climatological September SIE (black contour). Hatching and teal vectors highlight trends significant at the 95% level according to two-tailed student t-tests. Note that SAT trends are calculated over 1979-2012 but scaled to represent trends over the 36-year period, 1979-2014. Surrounding figures show time-series of **b)** East Antarctic SAT (circles; red line denotes multi-station mean, grey lines those of individual East Antarctic stations), **c)** the Marshall Southern Annular Mode index (difference in station sea level pressure between 40 and 65°S), **d)** Southern Ocean zonal mean SST (averaged over 50°–70°S), **e)** Southern Hemisphere SIE, **f)** Ross-Amundsen SIE, **g)** West Antarctic SAT (square; Byrd Station), **h)** Amundsen-Bellingshausen SIE, and **i)** Antarctic Peninsula SAT (hexagons; red line denotes multi-station mean, grey lines those of individual Antarctic Peninsula stations). For all time-series, blue lines highlight the linear trend, and red asterisks highlight trends that pass a 95% significance two-tailed student t-test. See methods for details on datasets and trend significance calculation.

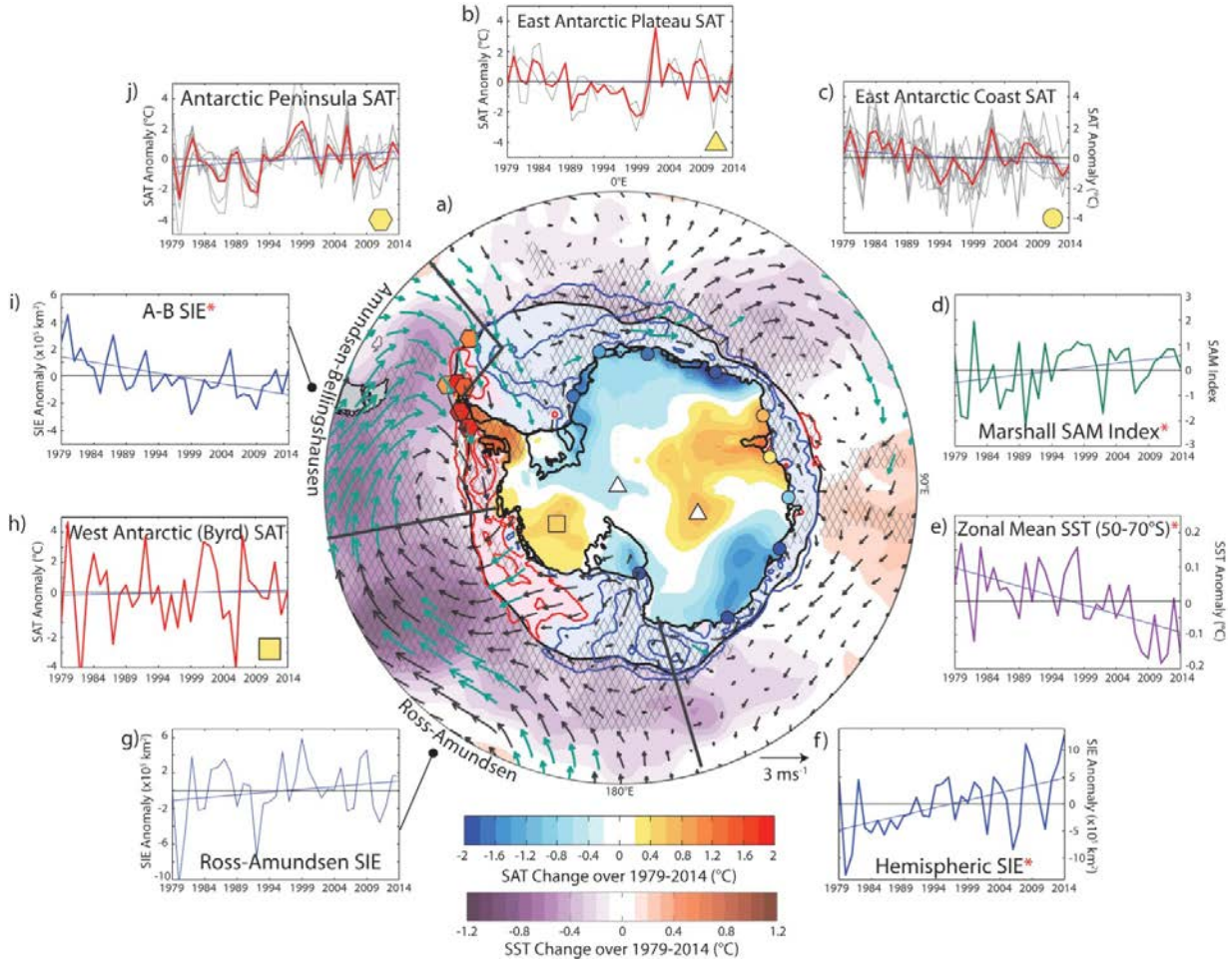

Supplementary Figure 2b: Antarctic atmosphere-ocean-ice changes over the satellite-observing era for Autumn (March, April, May). **a)** Total changes over 1979-2014 in remote sensing annual mean SAT (blue-red shading), station-based SAT (blue-red shaded shapes), sea ice concentration (contours, 10% intervals; red and blue contours, alongside light pink and blue shading beneath, denote negative and positive trends, respectively), sea surface temperature (purple-red shading), and 10m winds (vectors). Remote sensing SST trends are only shown for areas equatorward of the climatological September SIE (black contour). Hatching and teal vectors highlight trends significant at the 95% level according to two-tailed student t-tests. Note that SAT trends are calculated over 1979-2012 but scaled to represent trends over the 36-year period, 1979-2014. Surrounding figures show time-series of **b)** East Antarctic SAT (circles; red line denotes multi-station mean, grey lines those of individual East Antarctic stations), **c)** the Marshall Southern Annular Mode index (difference in station sea level pressure between 40 and 65°S), **d)** Southern Ocean zonal mean SST (averaged over 50°–70°S), **e)** Southern Hemisphere SIE, **f)** Ross-Amundsen SIE, **g)** West Antarctic SAT (square; Byrd Station), **h)** Amundsen-Bellingshausen SIE, and **i)** Antarctic Peninsula SAT (hexagons; red line denotes multi-station mean, grey lines those of individual Antarctic Peninsula stations). For all time-series, blue lines highlight the linear trend, and red asterisks highlight trends that pass a 95% significance two-tailed student t-test. See methods for details on datasets and trend significance calculation.

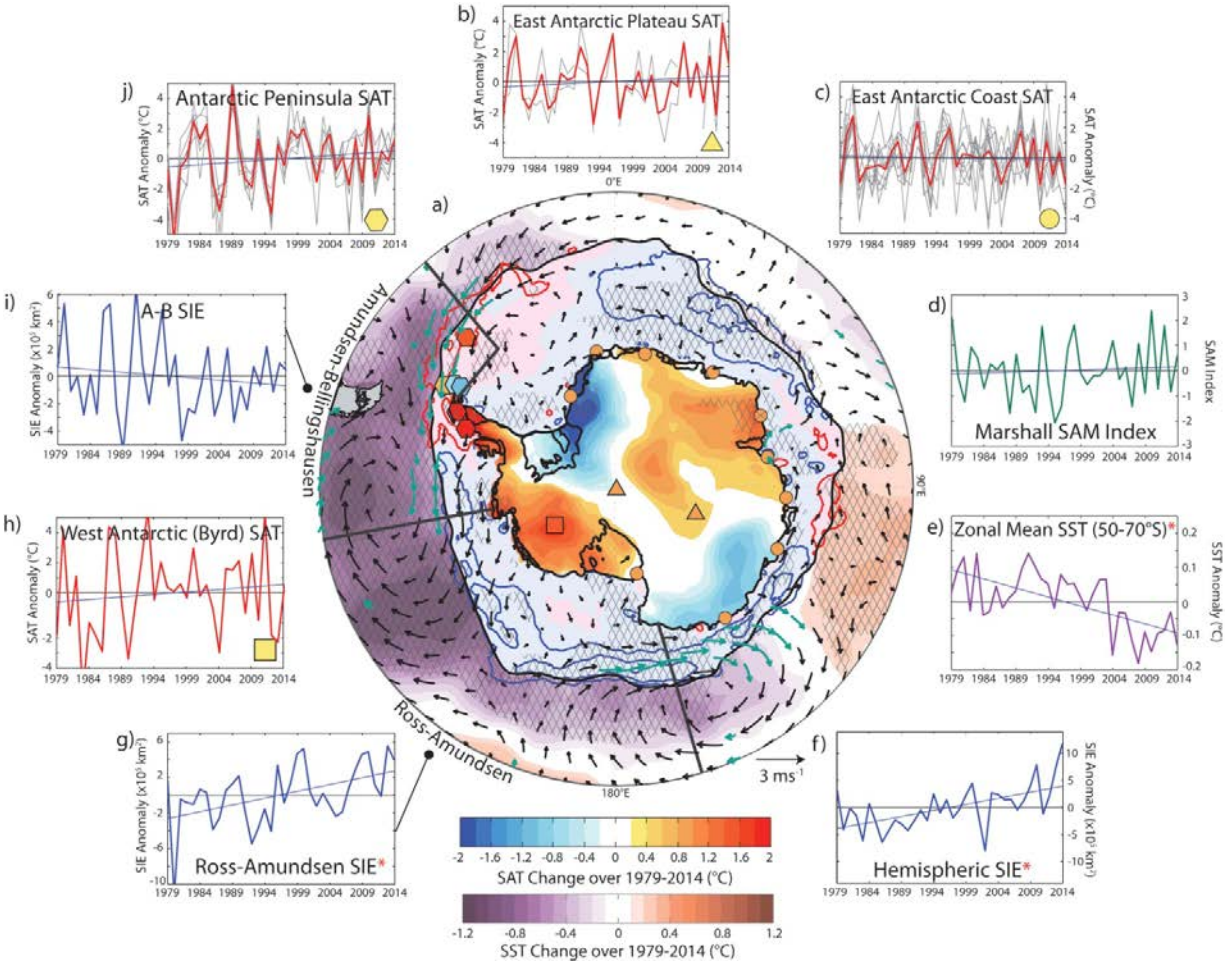

Supplementary Figure 2c: Antarctic atmosphere-ocean-ice changes over the satellite-observing era for Winter (June, July, August). **a)** Total changes over 1979-2014 in remote sensing annual mean SAT (blue-red shading), station-based SAT (blue-red shaded shapes), sea ice concentration (contours, 10% intervals; red and blue contours, alongside light pink and blue shading beneath, denote negative and positive trends, respectively), sea surface temperature (purple-red shading), and 10m winds (vectors). Remote sensing SST trends are only shown for areas equatorward of the climatological September SIE (black contour). Hatching and teal vectors highlight trends significant at the 95% level according to two-tailed student t-tests. Note that SAT trends are calculated over 1979-2012 but scaled to represent trends over the 36-year period, 1979-2014. Surrounding figures show time-series of **b)** East Antarctic SAT (circles; red line denotes multi-station mean, grey lines those of individual East Antarctic stations), **c)** the Marshall Southern Annular Mode index (difference in station sea level pressure between 40 and 65°S), **d)** Southern Ocean zonal mean SST (averaged over 50°–70°S), **e)** Southern Hemisphere SIE, **f)** Ross-Amundsen SIE, **g)** West Antarctic SAT (square; Byrd Station), **h)** Amundsen-Bellingshausen SIE, and **i)** Antarctic Peninsula SAT (hexagons; red line denotes multi-station mean, grey lines those of individual Antarctic Peninsula stations). For all time-series, blue lines highlight the linear trend, and red asterisks highlight trends that pass a 95% significance two-tailed student t-test. See methods for details on datasets and trend significance calculation.

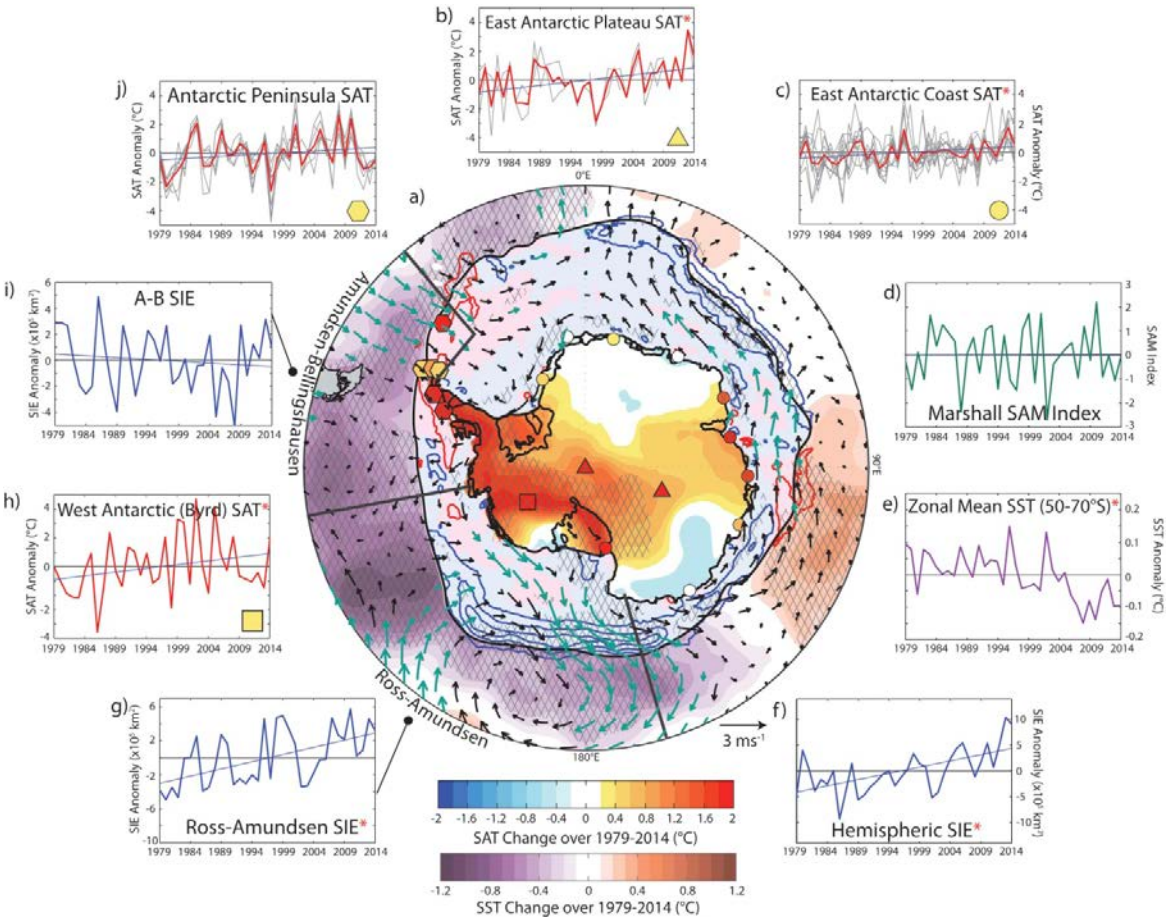

Supplementary Figure 2d: Antarctic atmosphere-ocean-ice changes over the satellite-observing era for Spring (September, October, November)**. a)** Total changes over 1979-2014 in remote sensing annual mean SAT (blue-red shading), station-based SAT (blue-red shaded shapes), sea ice concentration (contours, 10% intervals; red and blue contours, alongside light pink and blue shading beneath, denote negative and positive trends, respectively), sea surface temperature (purple-red shading), and 10m winds (vectors). Remote sensing SST trends are only shown for areas equatorward of the climatological September SIE (black contour). Hatching and teal vectors highlight trends significant at the 95% level according to two-tailed student t-tests. Note that SAT trends are calculated over 1979-2012 but scaled to represent trends over the 36-year period, 1979-2014. Surrounding figures show time-series of **b)** East Antarctic SAT (circles; red line denotes multi-station mean, grey lines those of individual East Antarctic stations), **c)** the Marshall Southern Annular Mode index (difference in station sea level pressure between 40 and 65°S), **d)** Southern Ocean zonal mean SST (averaged over 50°–70°S), **e)** Southern Hemisphere SIE, **f)** Ross-Amundsen SIE, **g)** West Antarctic SAT (square; Byrd Station), **h)** Amundsen-Bellingshausen SIE, and **i)** Antarctic Peninsula SAT (hexagons; red line denotes multi-station mean, grey lines those of individual Antarctic Peninsula stations). For all time-series, blue lines highlight the linear trend, and red asterisks highlight trends that pass a 95% significance two-tailed student t-test. See methods for details on datasets and trend significance calculation.

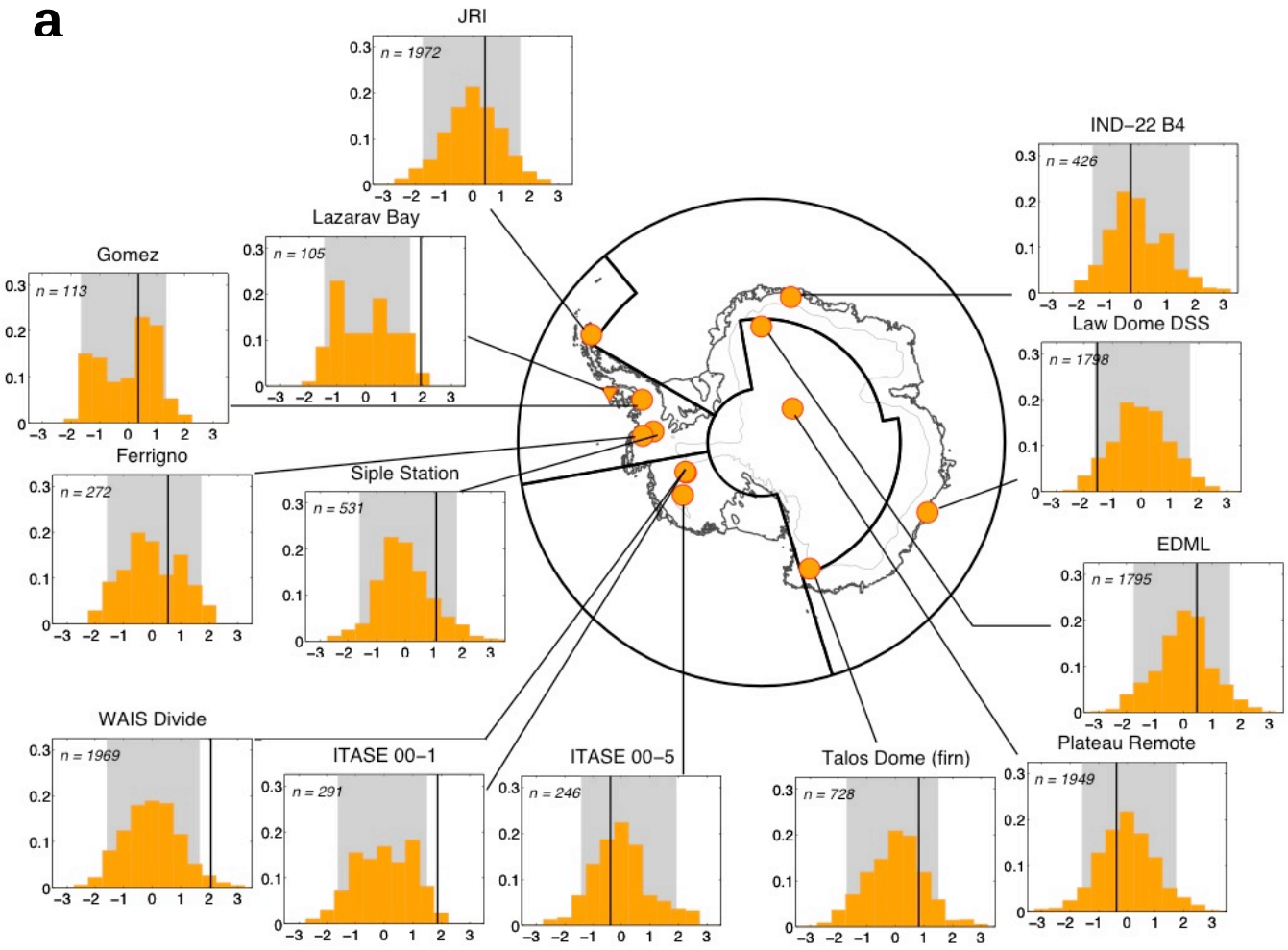

Supplementary Figure 3 (a-c): Significance of recent trends in paleoclimate records. (a) Comparison of the most recent 36y linear trend (black vertical line) in SAT proxy records, compared with all other 36y linear trends in the same SAT proxy record (orange histograms). Grey shading shows the 5-95% range of all 36y trends and n-values denote the total number of 36y trends, excluding the most recent trend. To aid visualisation, the x-axes for all histograms are in normalised trend units (calculated across all trends for a record), and trend occurrence (y-axes) is expressed as a proportion of the total number of trends (n). (b) As in (a) but for SST (blue) and sea ice (cyan) proxy records. (c) As in (a-b) but with trend analysis based on 100y linear trends and shown for SAT (orange), SST (blue) and sea ice (cyan) proxies where records are at least 200 years long.

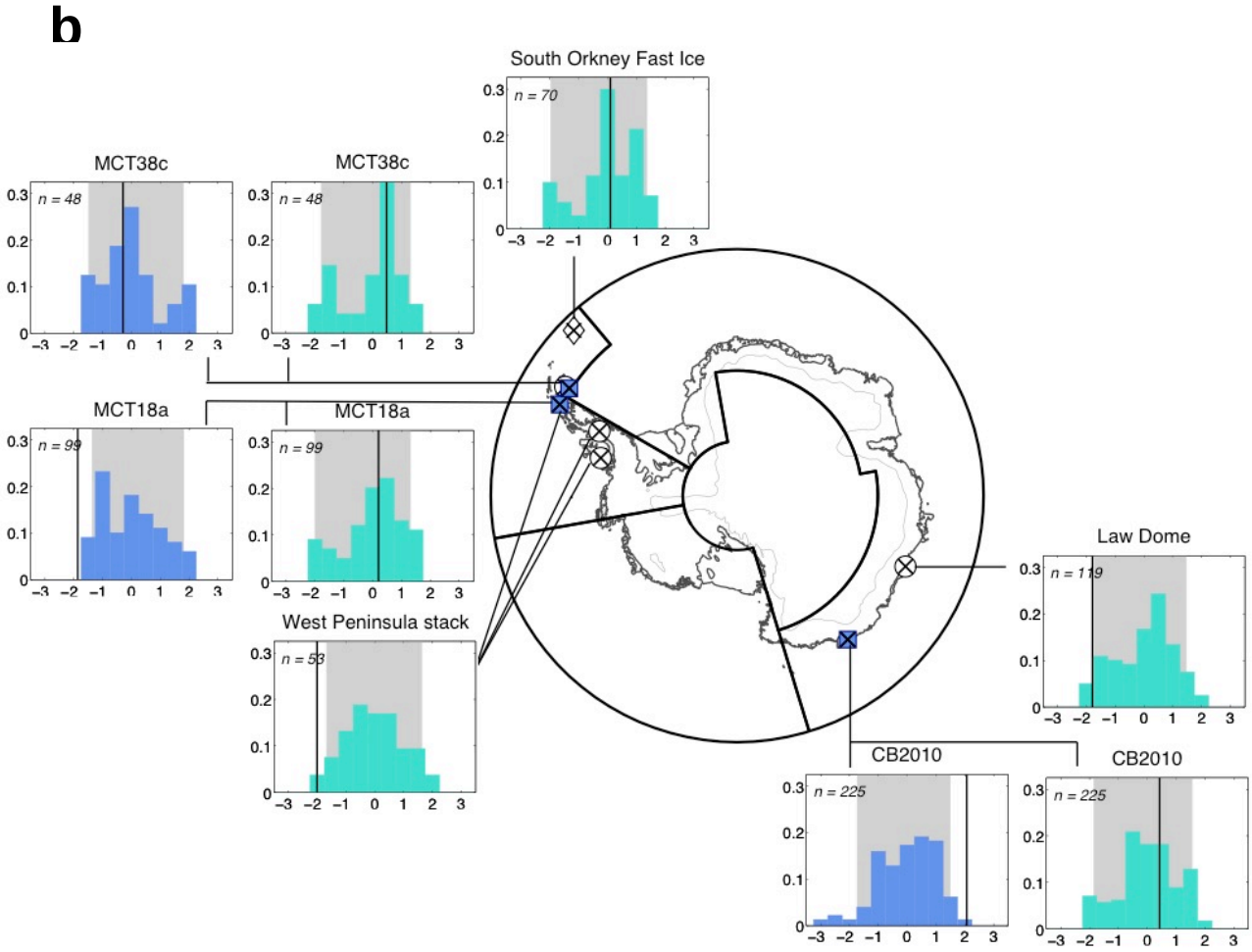

Supplementary Figure 3 (a-c) continued: Significance of recent trends in paleoclimate records. (a) Comparison of the most recent 36y linear trend (black vertical line) in SAT proxy records, compared with all other 36y linear trends in the same SAT proxy record (orange histograms). Grey shading shows the 5-95% range of all 36y trends and n-values denote the total number of 36y trends, excluding the most recent trend. To aid visualisation the x-axes for all histograms are in normalised trend units (calculated across all trends for a record) and trend occurrence (y-axes) is expressed as a proportion of the total number of trends (n). (b) As in (a) but for SST (blue) and sea ice (cyan) proxy records. (c) As in (a-b) but with trend analysis based on 100y linear trends and shown for SAT (orange), SST (blue) and sea ice (cyan) proxies where records are at least 200 years long.

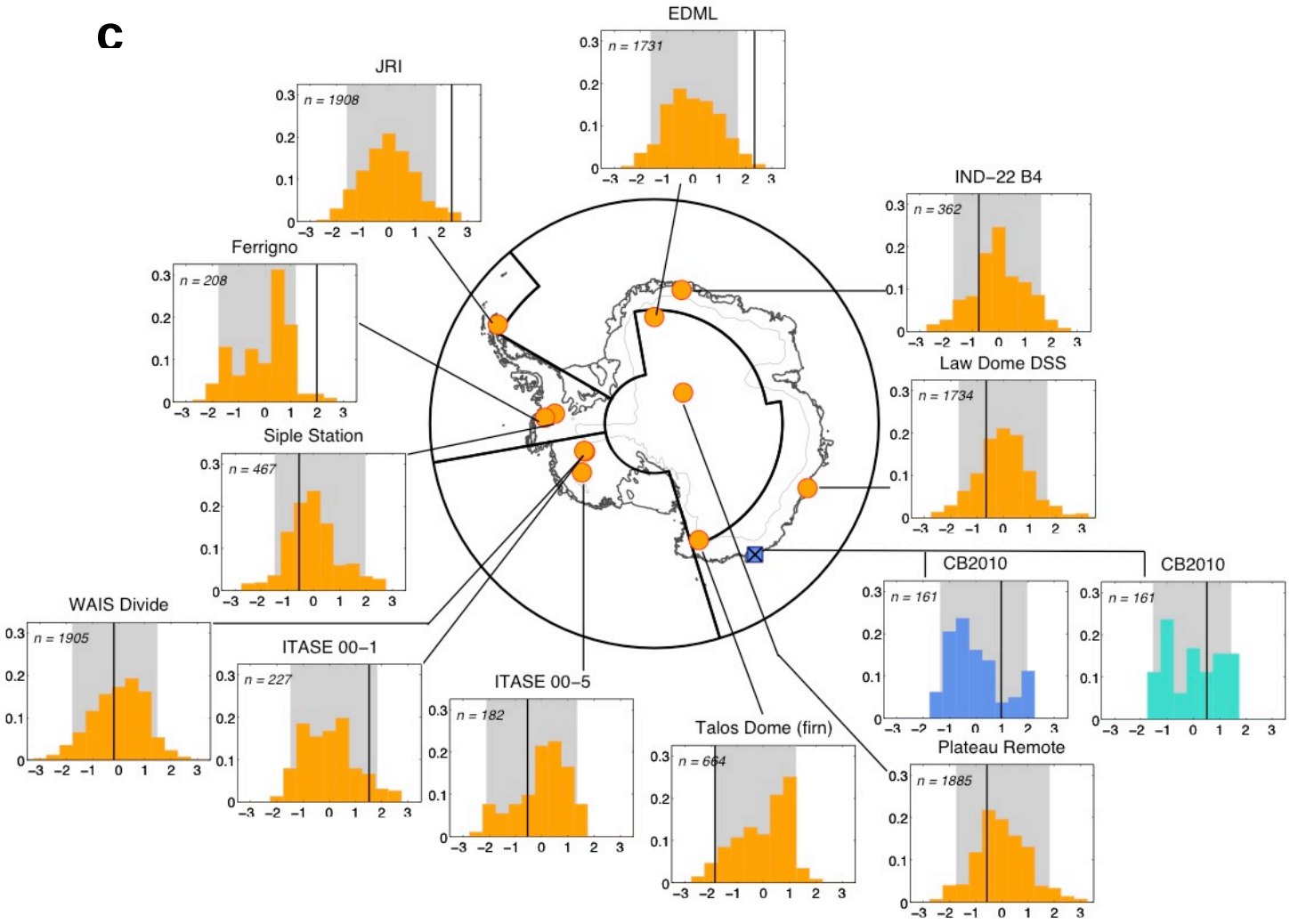

Supplementary Figure 3 (a-c) continued: Significance of recent trends in paleoclimate records. (a) Comparison of the most recent 36y linear trend (black vertical line) in SAT proxy records, compared with all other 36y linear trends in the same SAT proxy record (orange histograms). Grey shading shows the 5-95% range of all 36y trends and n-values denote the total number of 36y trends, excluding the most recent trend. To aid visualisation the x-axes for all histograms are in normalised trend units (calculated across all trends for a record) and trend occurrence (y-axes) is expressed as a proportion of the total number of trends (n). (b) As in (a) but for SST (blue) and sea ice (cyan) proxy records. (c) As in (a-b) but with trend analysis based on 100y linear trends and shown for SAT (orange), SST (blue) and sea ice (cyan) proxies where records are at least 200 years long.

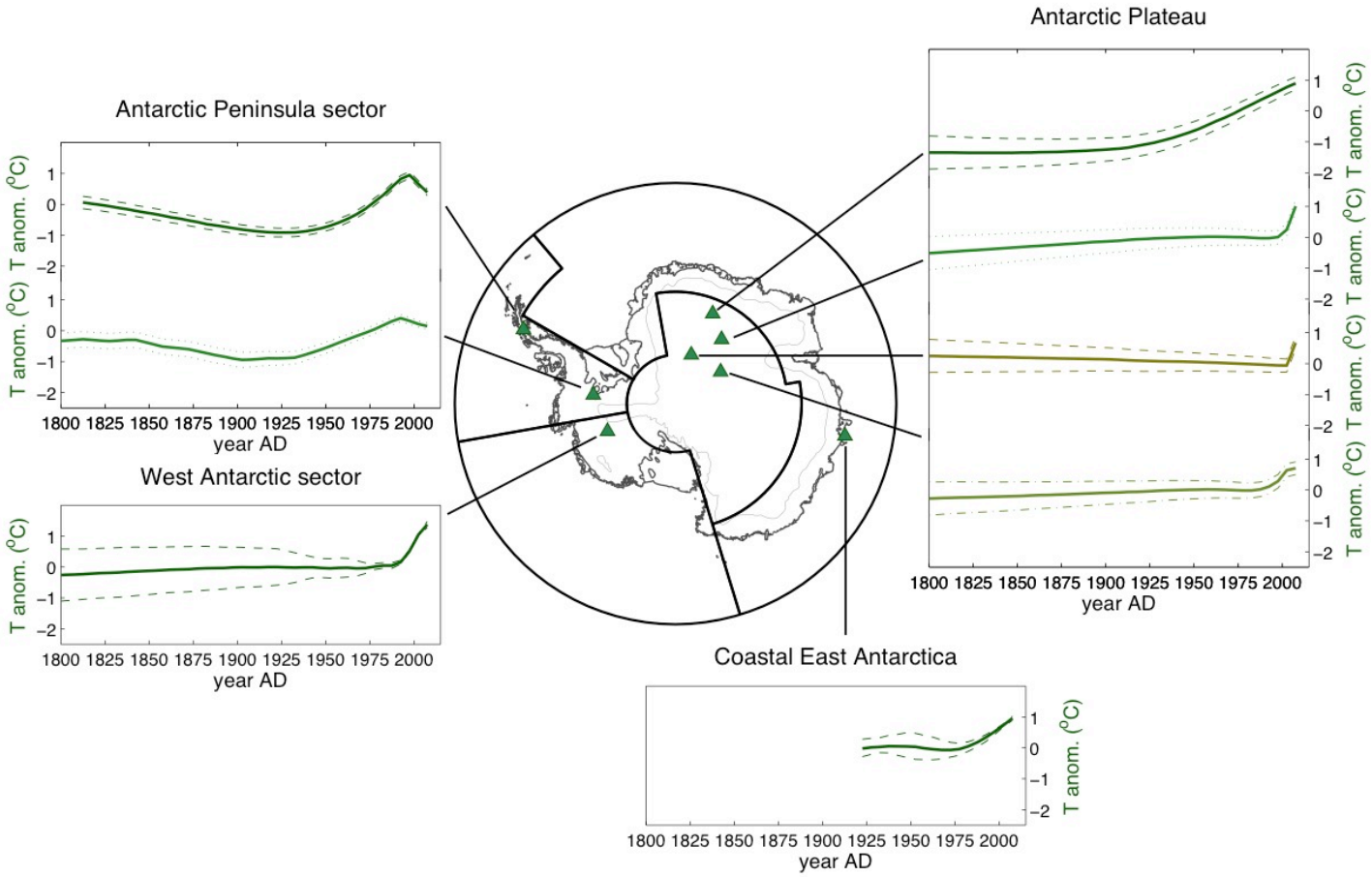

Supplementary Figure 4: Antarctic borehole temperature inversion records. Individual borehole temperature inversions (solid lines) are shown along with their uncertainty bounds (dashed/dotted lines). Colours for each record correspond to those used in Figure 2, but are shown here so that the location of each borehole temperature inversion record can be identified. Details of the individual records provided in Supplementary Table 1.

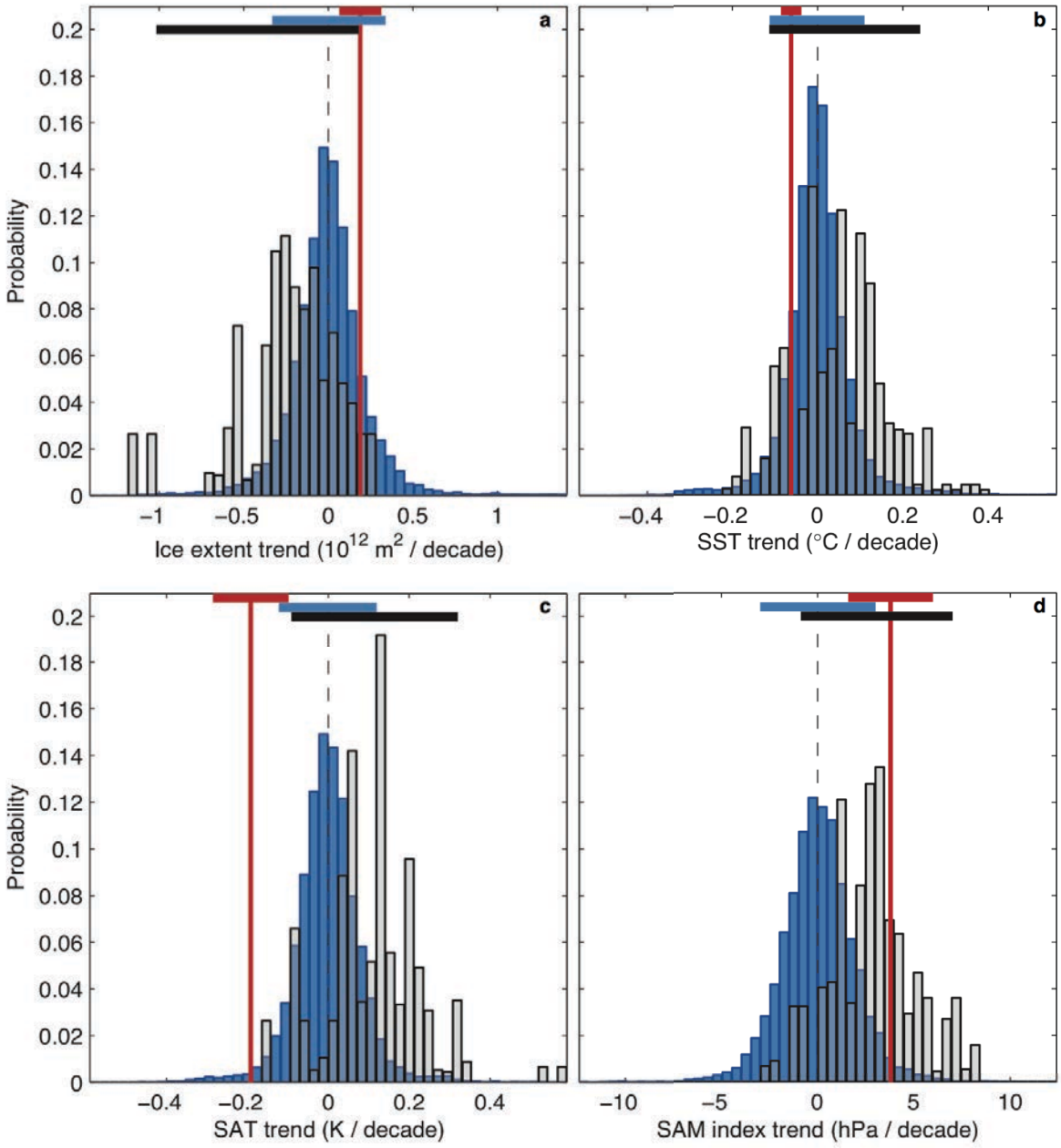

Supplementary Figure 5 DJF: CMIP5 ensemble distributions of 36-year summer (DJF) linear trends in (blue) the ensemble of preindustrial simulations and (black/grey) the ensemble of 1979-2014 historical-RCP8.5 simulations. Panels show **(a)** Southern Hemisphere sea-ice extent, **(b)** mean SST south of 50°S, **(c)** mean SAT south of 50°S and **(d)** SAM index. The red vertical lines correspond to the recent observed 36-year linear trends (1979-2014). Horizontal bars depict (red) the 90% confidence interval of the observed trend, (blue) the 5-95% range of the preindustrial distribution and (black) the 5-95% range of the 1979-2014 trend distribution. Trend calculation methods and data sources are identical to those of Fig. 3a-d.

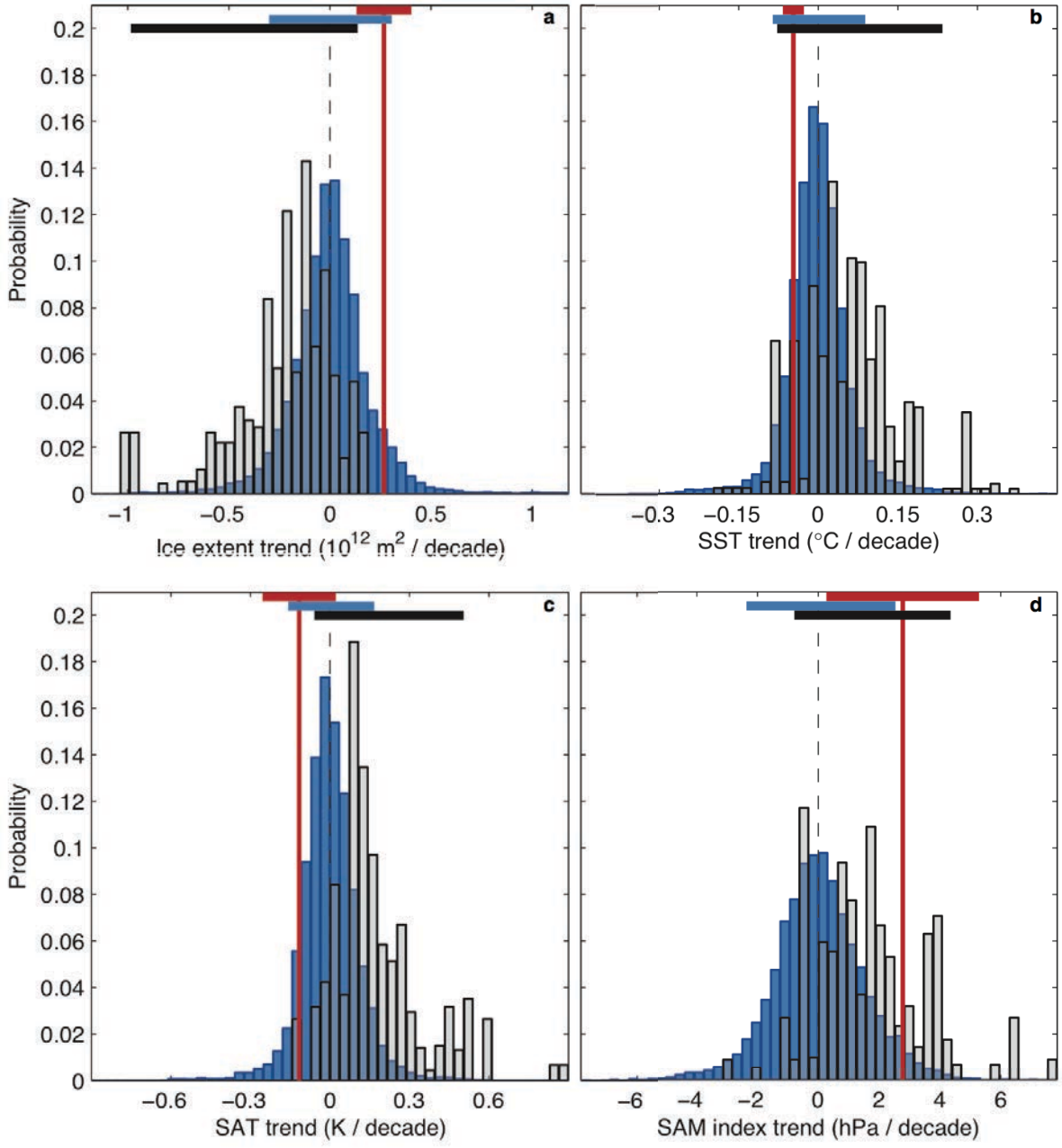

Supplementary Figure 5 MAM: CMIP5 ensemble distributions of 36-year autumn (MAM) linear trends in (blue) the ensemble of preindustrial simulations and (black/grey) the ensemble of 1979-2014 historical-RCP8.5 simulations. Panels show **(a)** Southern Hemisphere sea-ice extent, **(b)** mean SST south of 50°S, **(c)** mean SAT south of 50°S and **(d)** SAM index. The red vertical lines correspond to the recent observed 36-year linear trends (1979-2014). Horizontal bars depict (red) the 90% confidence interval of the observed trend, (blue) the 5-95% range of the preindustrial distribution and (black) the 5-95% range of the 1979-2014 trend distribution. Trend calculation methods and data sources are identical to those of Fig. 3a-d.

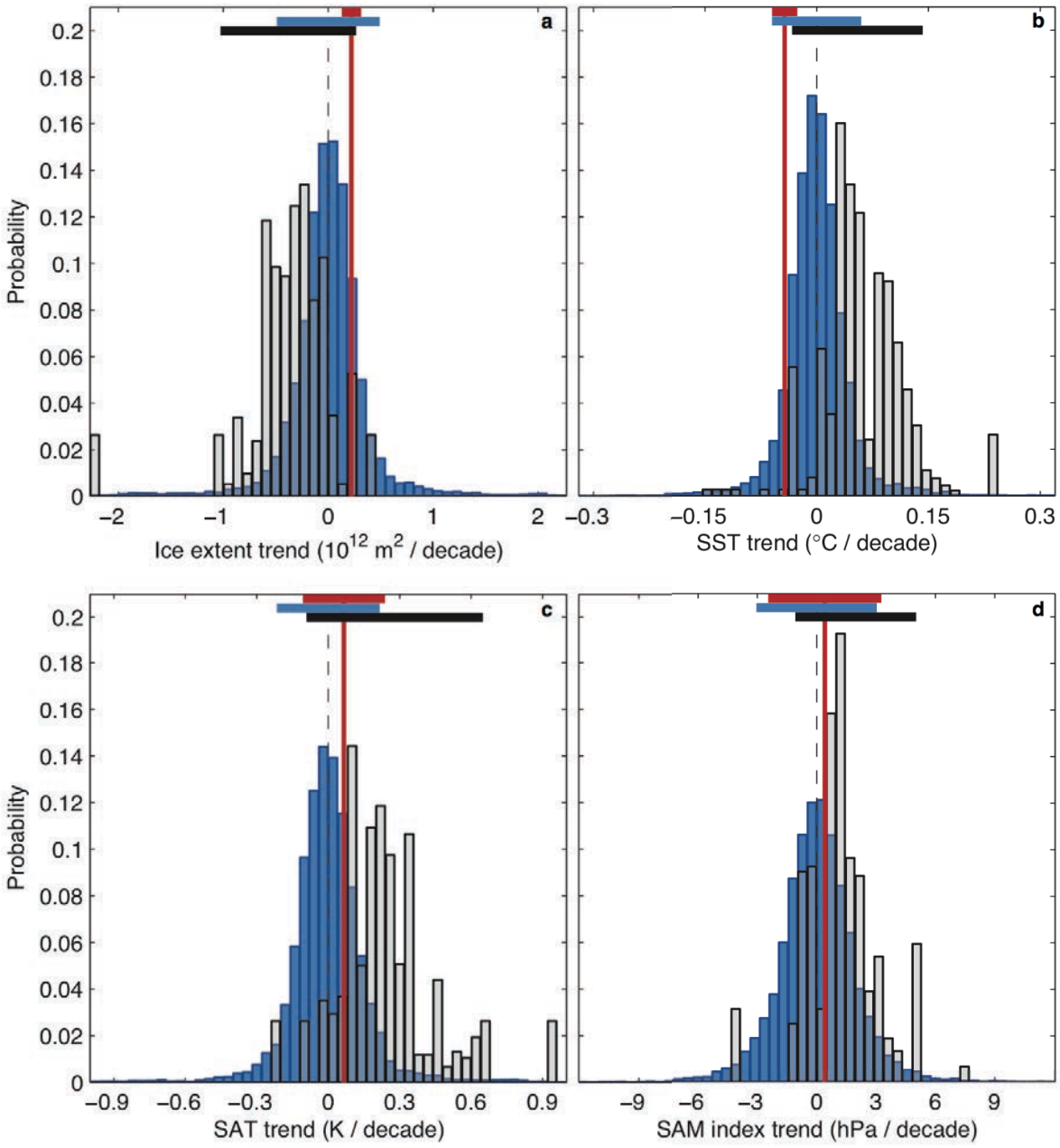

Supplementary Figure 5 JJA: CMIP5 ensemble distributions of 36-year winter (JJA) linear trends in (blue) the ensemble of preindustrial simulations and (black/grey) the ensemble of 1979-2014 historical-RCP8.5 simulations. Panels show **(a)** Southern Hemisphere sea-ice extent, **(b)** mean SST south of 50°S, **(c)** mean SAT south of 50°S and **(d)** SAM index. The red vertical lines correspond to the recent observed 36-year linear trends (1979-2014). Horizontal bars depict (red) the 90% confidence interval of the observed trend, (blue) the 5-95% range of the preindustrial distribution and (black) the 5-95% range of the 1979-2014 trend distribution. Trend calculation methods and data sources are identical to those of Fig. 3a-d.

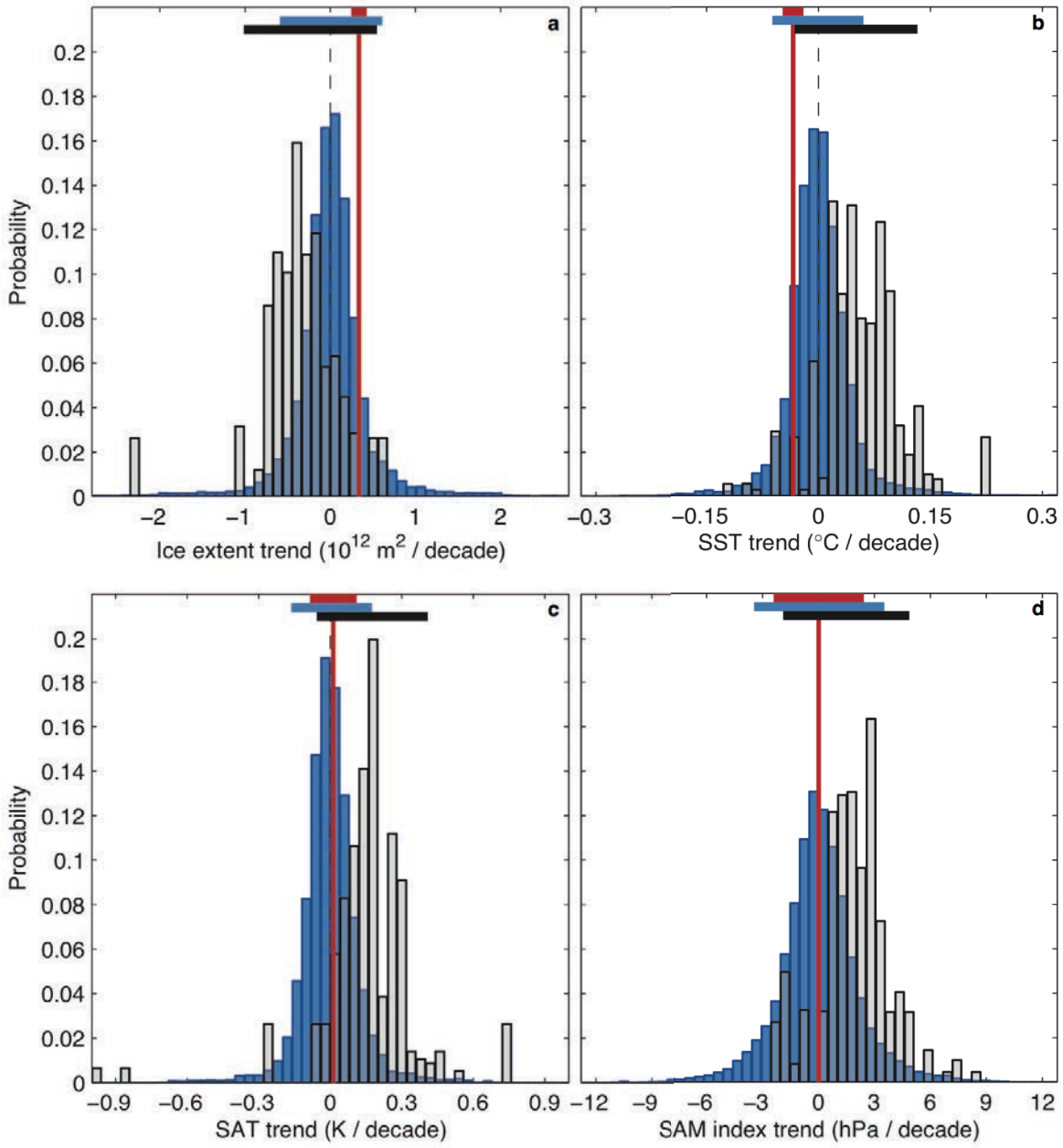

Supplementary Figure 5 SON: CMIP5 ensemble distributions of 36-year spring (SON) linear trends in (blue) the ensemble of preindustrial simulations and (black/grey) the ensemble of 1979-2014 historical-RCP8.5 simulations. Panels show **(a)** Southern Hemisphere sea-ice extent, **(b)** mean SST south of 50°S, **(c)** mean SAT south of 50°S and **(d)** SAM index. The red vertical lines correspond to the recent observed 36-year linear trends (1979-2014). Horizontal bars depict (red) the 90% confidence interval of the observed trend, (blue) the 5-95% range of the preindustrial distribution and (black) the 5-95% range of the 1979-2014 trend distribution. Trend calculation methods and data sources are identical to those of Fig. 3a-d.

References

1 Turner, J. *et al.* The SCAR READER project: Toward a high-quality database of mean Antarctic meteorological observations. *Journal of Climate* **17**, 2890-2898, doi:10.1175/1520-0442(2004).

2 Nicolas, J. P. & Bromwich, D. H. New Reconstruction of Antarctic Near-Surface Temperatures: Multidecadal Trends and Reliability of Global Reanalyses. *Journal of Climate* **27**, 8070-8093, doi:10.1175/jcli-d-13-00733.1 (2014).

3 Smith, T. M., Reynolds, R. W., Peterson, T. C. & Lawrimore, J. Improvements to NOAA's historical merged land-ocean surface temperature analysis (1880-2006). *Journal of Climate* **21**, 2283-2296, doi:10.1175/2007jcli2100.1 (2008).

4 Comiso, J. C. Bootstrap Sea Ice Concentrations from Nimbus-7 SMMR and DMSP SSM/I-SSMIS, Version 2 [NSIDC-0-79]. National Snow and Ice Data Center Distributed Active, Boulder, Colorado, doi: http://dx.doi.org/10.5067/J6JQLS9EJ5HU. (2000, 2015 update).

5 Dee, D. P. *et al.* The ERA-Interim reanalysis: configuration and performance of the data assimilation system. *Quarterly Journal of the Royal Meteorological Society* **137**, 553-597, doi:10.1002/qj.828 (2011).

6 Marshall, G. J. Trends in the southern annular mode from observations and reanalyses. *Journal of Climate* **16**, 4134-4143, doi:10.1175/1520-0442 (2003).

7 Santer, B. D. *et al.* Statistical significance of trends and trend differences in layer-average atmospheric temperature time series. *Journal of Geophysical Research-Atmospheres* **105**, 7337-7356, doi:10.1029/1999jd901105 (2000).

8 PAGES 2K Consortium. Continental-scale temperature variability during the past two millennia. *Nature Geoscience* **6**, 339-346, doi:10.1038/ngeo1797 (2013).

9 Thomas, E. R., Marshall, G. J. & McConnell, J. R. A doubling in snow accumulation in the western Antarctic Peninsula since 1850. *Geophysical Research Letters* **35**, doi:10.1029/2007gl032529 (2008).

10 Thomas, E. R., Bracegirdle, T. J., Turner, J. & Wolff, E. W. A 308 year record of climate variability in West Antarctica. *Geophysical Research Letters* **40**, 5492-5496, doi:10.1002/2013gl057782 (2013).

11 Royles, J. *et al.* Plants and Soil Microbes Respond to Recent Warming on the Antarctic Peninsula. *Current Biology* **23**, 1702-1706, doi:10.1016/j.cub.2013.07.011 (2013).

12 Abram, N. J., Wolff, E. W. & Curran, M. A. J. A review of sea ice proxy information from polar ice cores. *Quaternary Science Reviews* **79**, 168-183, doi:10.1016/j.quascirev.2013.01.011 (2013).

13 Barbara, L., Crosta, X., Schmidt, S. & Masse, G. Diatoms and biomarkers evidence for major changes in sea ice conditions prior the instrumental period in Antarctic Peninsula. *Quaternary Science Reviews* **79**, 99-110, doi:10.1016/j.quascirev.2013.07.021 (2013).

14 Orsi, A. J., Cornuelle, B. D. & Severinghaus, J. P. Little Ice Age cold interval in West Antarctica: Evidence from borehole temperature at the West Antarctic Ice Sheet (WAIS) Divide. *Geophysical Research Letters* **39**, doi:10.1029/2012gl051260 (2012).

15 Clow, G. D. The extent of temporal smearing in surface-temperature histories derived from borehole temperature measurements. *Palaeogeography Palaeoclimatology Palaeoecology* **98**, 81-86, doi:10.1016/0031-0182(92)90189-c (1992).
16 Bromwich, D. H. *et al.* Central West Antarctica among the most rapidly warming regions on Earth. *Nature Geoscience* **6**, 139-145, doi:10.1038/ngeo1671 (2013).
17 Stenni, B. *et al.* Eight centuries of volcanic signal and climate change at Talos Dome (East Antarctica). *Journal of Geophysical Research-Atmospheres* **107**, doi:10.1029/2000jd000317 (2002).
18 Plummer, C. T. *et al.* An independently dated 2000-yr volcanic record from Law Dome, East Antarctica, including a new perspective on the dating of the 1450s CE eruption of Kuwae, Vanuatu. *Climate of the Past* **8**, 1929-1940, doi:10.5194/cp-8-1929-2012 (2012).
19 Cole-Dai, J. H., Mosley-Thompson, E., Wight, S. P. & Thompson, L. G. A 4100-year record of explosive volcanism from an East Antarctica ice core. *Journal of Geophysical Research-Atmospheres* **105**, 24431-24441, doi:10.1029/2000jd900254 (2000).
20 Mosley-Thompson, E. Holocene Climate Changes Recroded in an East Antarctica Ice Core, in *Climatic Variations and Forcing Mechanisms of the Last 2000 years* (eds P. D Jones, R. S. Bradley, & J. Jouzel) 263-269 (Springer-Verlag, 1996).
21 Thamban, M. *et al.* Aerosol perturbations related to volcanic eruptions during the past few centuries as recorded in an ice core from the Central Dronning Maud Land, Antarctica. *Current Science* **91**, 1200-1207 (2006).
22 Laluraj, C. M. *et al.* Nitrate records of a shallow ice core from East Antarctica: Atmospheric processes, preservation and climatic implications. *Holocene* **21**, 351-356, doi:10.1177/0959683610374886 (2011).
23 Graf, W. *et al.* Stable-isotope records from Dronning Maud Land, Antarctica. Supplement to Annals of Glaciology, 35, 195-201, doi:10.1594/PANGAEA.104862 (2002).
24 Steig, E. J. *et al.* Recent climate and ice-sheet changes in West Antarctica compared with the past 2,000 years. *Nature Geoscience* **6**, 372-375, doi:10.1038/ngeo1778 (2013).
25 Schneider, D. P. *et al.* Antarctic temperatures over the past two centuries from ice cores. *Geophysical Research Letters* **33**, doi:10.1029/2006gl027057 (2006).
26 Mosley-Thompson, E., Thompson, L. G., Grootes, P. M., & Gundestrip, N. Little Ice Age (neoglacial) palaeoenvironmental conditions at Siple Station. *Annals of Glaciology* **14**, 199-204 (1990).
27 Mulvaney, R. *et al.* Recent Antarctic Peninsula warming relative to Holocene climate and ice-shelf history. *Nature* **489**, 141-144, doi:10.1038/nature11391 (2012).
28 Abram, N. J. *et al.* Acceleration of snow melt in an Antarctic Peninsula ice core during the twentieth century. *Nature Geoscience* **6**, 404-411, doi:10.1038/ngeo1787 (2013).
29 Zagorodnov, V. *et al.* Borehole temperatures reveal details of 20th century warming at Bruce Plateau, Antarctic Peninsula. *Cryosphere* **6**, 675-686, doi:10.5194/tc-6-675-2012 (2012).
30 Muto, A., Scambos, T. A., Steffen, K., Slater, A. G. & Clow, G. D. Recent surface temperature trends in the interior of East Antarctica from borehole firn temperature measurements and geophysical inverse methods. *Geophysical Research Letters* **38**, doi:10.1029/2011gl048086 (2011).

31 Roberts, J. L. *et al.* Borehole temperatures reveal a changed energy budget at Mill Island, East Antarctica, over recent decades. *Cryosphere* **7**, 263-273, doi:10.5194/tc-7-263-2013 (2013).

32 Barrett, B. E., Nicholls, K. W., Murray, T., Smith, A. M. & Vaughan, D. G. Rapid recent warming on Rutford Ice Stream, West Antarctica, from borehole thermometry. *Geophysical Research Letters* **36**, doi:10.1029/2008gl036369 (2009).

33 Campagne, P. *et al.* Glacial ice and atmospheric forcing on the Mertz Glacier Polynya over the past 250 years. *Nature Communications* **6**, doi:10.1038/ncomms7642 (2015).

34 Abram, N. J. *et al.* Ice core evidence for a 20th century decline of sea ice in the Bellingshausen Sea, Antarctica. *Journal of Geophysical Research-Atmospheres* **115**, doi:10.1029/2010jd014644 (2010).

35 Curran, M. A. J., van Ommen, T. D., Morgan, V. I., Phillips, K. L. & Palmer, A. S. Ice core evidence for Antarctic sea ice decline since the 1950s. *Science* **302**, 1203-1206, doi:10.1126/science.1087888 (2003).

36 Murphy, E. J., Clarke, A., Abram, N. J. & Turner, J. Variability of sea-ice in the northern Weddell Sea during the 20th century. *Journal of Geophysical Research-Oceans* **119**, 4549-4572, doi:10.1002/2013jc009511 (2014).

Eléments du cycle de vie de l'Eau Antarctique de Fond

Résumé : L'Eau Antarctique de Fond constitue la principale masse d'eau océanique par son volume, et nourrit la composante la plus profonde et la plus lente de la circulation océanique. Les processus qui régissent son cycle de vie sont donc clé pour la capacité de stockage de l'océan en carbone et chaleur aux échelles centennales à multi-millénaires. Cette thèse tente de caractériser et quantifier les principaux processus responsables de la destruction (synonyme d'allègement et de remontée) de l'Eau Antarctique de Fond dans l'océan abyssal. A partir d'une estimée issue d'observations de la structure thermohaline de l'océan mondial et de diagnostics fondés sur le budget de densité des eaux profondes, les rôles respectifs du chauffage géothermal, du mélange turbulent par déferlement d'ondes internes et de la géométrie des bassins sont évalués. Il est montré que la géométrie de l'océan gouverne la structure de la circulation de l'Eau Antarctique de Fond. La contribution du déferlement des ondes internes, bien que mal contrainte, est estimée insuffisante pour maintenir un rythme de destruction de l'Eau Antarctique de Fond comparable à celui de sa formation. Le chauffage géothermal a quant à lui un rôle important pour la remontée des eaux recouvrant une large surface du lit océanique. Les résultats suggèrent une réévaluation de l'importance du mélange au niveau des détroits et seuils profonds, mais aussi du rôle fondamental de la forme des bassins, pour l'allègement et le transport des eaux abyssales.

Mots clés : Masses d'eau, Océan abyssal, Circulation thermohaline, Chauffage géothermal, Mélange, Ondes internes, Turbulence, Paramétrisation, Modélisation, NEMO

On the lifecycle of Antarctic Bottom Water

Abstract : Antarctic Bottom Water is the most voluminous water mass of the World Ocean, and it feeds the deepest and slowest component of ocean circulation. The processes that govern its lifecycle are therefore key to the ocean's carbon and heat storage capacity on centennial to multi-millennial timescales. This thesis aims at characterizing and quantifying processes responsible for the destruction (synonymous of lightening and upwelling) of Antarctic Bottom Water in the abyssal ocean. Using an observational estimate of the global ocean thermohaline structure and diagnostics based on the density budget of deep waters, we explore the roles of basin geometry, geothermal heating and mixing by breaking internal waves for the abyssal circulation. We show that the shape of ocean basins largely controls the structure of abyssal upwelling. The contribution of mixing powered by breaking internal waves, though poorly constrained, is estimated to be insufficient to destroy Antarctic Bottom Water at a rate comparable to that of its formation. Geothermal heating plays an important role for the upwelling of waters covering large seafloor areas. The results suggest a reappraisal of the role of mixing in deep straits and sills, but also of the fundamental role of basin geometry, for the lightening and transport of abyssal waters.

Keywords : Water masses, Abyssal ocean, Thermohaline circulation, Geothermal heating, Mixing, Internal waves, Turbulence, Parameterization, Modelling, NEMO